

# Structure-Property Relationships in Isotactic Polypropylene

D.W. van der Meer

2003

Ph.D. thesis  
University of Twente



Twente University Press

Also available in print:  
<http://www.tup.utwente.nl/>

---

**STRUCTURE-PROPERTY RELATIONSHIPS  
IN ISOTACTIC POLYPROPYLENE**



The research described in this thesis was financially supported by the Dutch Polymer Institute (DPI), The Netherlands.

#### Committee

Chairman/ Secretary	prof. dr. P.J. Gellings	Univ. of Twente, The Netherlands
Promotor:	prof. dr. G.J. Vancso	Univ. of Twente, The Netherlands
Members:	prof. dr. B. Pukánszky	Techn. Univ. of Budapest, Hungary
	prof. dr. G. Weickert	Univ. of Twente, The Netherlands
	prof. dr. J. Feijen	Univ. of Twente, The Netherlands
	prof. dr. P.J. Lemstra	Techn. Univ. of Eindhoven, The Netherlands
	dr. S. Rastogi	Techn. Univ. of Eindhoven, The Netherlands



#### Twente University Press

Publisher: Twente University Press  
P.O. Box 217, 7500 AE Enschede, the Netherlands  
[www.tup.utwente.nl](http://www.tup.utwente.nl)

Print: Océ Facility Services, Enschede

© D.W. van der Meer, Enschede, 2003

No part of this work may be reproduced by print, photocopy or any other means without the permission in writing from the publisher.

ISBN 9036519144

Cover: S.J. van der Meer-de Jong  
Artistic impression of crystallized isotactic polypropylene as seen under a light microscope equipped with polarizers.

**STRUCTURE-PROPERTY RELATIONSHIPS  
IN ISOTACTIC POLYPROPYLENE**

THE INFLUENCE OF  
CHAIN ARCHITECTURE AND NUCLEATION ON  
CRYSTALLIZATION, MORPHOLOGY AND MECHANICAL PROPERTIES

PROEFSCHRIFT

ter verkrijging van  
de graad van doctor aan de Universiteit Twente,  
op gezag van de rector magnificus,  
prof.dr. F.A. van Vught,  
volgens besluit van het College voor Promoties  
in het openbaar te verdedigen  
op vrijdag 13 juni 2003 om 13.15 uur

door

Douwe-Wiebe van der Meer

geboren op 14 juli 1975  
te Sneek

Dit Proefschrift is goedgekeurd door:

Promotor: prof. dr. G.J. Vancso

# Contents

<b>1</b>	<b>GENERAL INTRODUCTION AND SCOPE</b>	<b>1</b>
1.1	General introduction	2
1.2	Scope of this thesis	4
1.3	References	6
<b>2</b>	<b>POLYMER MORPHOLOGY AND ANALYSIS: A REVIEW</b>	<b>7</b>
2.1	Introduction	8
2.2	Morphology of isotactic polypropylene	8
2.2.1	<i>The primary level of macromolecular structure: Molecular characteristics</i>	8
2.2.2	<i>The secondary level of macromolecular structure: Crystal phases of iPP</i>	11
2.2.3	<i>The tertiary level of macromolecular structure: Lamellar structure</i>	14
2.2.4	<i>The quaternary level of macromolecular structure: Spherulites and row structures</i>	15
2.3	Crystallization and melting of the $\beta$ -phase in relation to the $\alpha$ -phase	17
2.3.1	<i>Crystallization</i>	17
2.3.2	<i>Melting characteristics</i>	17
2.4	Impact properties in relation to morphology	18
2.4.1	<i>Introduction</i>	18
2.4.2	<i>Impact tests</i>	18
2.4.3	<i>Linear elastic fracture mechanics (LEFM)</i>	19
2.4.4	<i>Relationships between morphology and impact properties</i>	20
2.5	Experimental methods	23
2.5.1	<i>Wide angle x-ray scattering (WAXS)</i>	23
2.5.2	<i>Infrared dichroism</i>	28
2.5.3	<i>Polarized light microscopy</i>	30
2.6	References	30

<b>3</b>	<b>THE INFLUENCE OF CHAIN ARCHITECTURE ON THE CRYSTALLIZATION OF ISOTACTIC POLYPROPYLENE</b>	<b>37</b>
<b>3.1</b>	<b>Introduction</b>	<b>39</b>
<b>3.2</b>	<b>Experimental</b>	<b>41</b>
	3.2.1 <i>Samples</i>	41
	3.2.2 <i>Morphology studies</i>	42
	3.2.3 <i>Crystallization studies</i>	45
<b>3.3</b>	<b>Results</b>	<b>47</b>
	3.3.1 <i>Introduction</i>	47
	3.3.2 <i>Description of defects</i>	47
	3.3.3 <i>Crystal morphology as observed by WAXS</i>	49
	3.3.4 <i>Crystal morphology as observed by SAXS</i>	56
	3.3.5 <i>Growth rate observations by LM</i>	65
	3.3.6 <i>The shear induced formation of the <math>\beta</math>-phase</i>	73
<b>3.4</b>	<b>Discussion</b>	<b>76</b>
	3.4.1 <i>Crystallization of homo-polymers</i>	78
	3.4.2 <i>Crystallization of copolymers</i>	79
	3.4.3 <i>Analysis of the crystallization behavior of <math>\alpha</math>- and <math>\beta</math>-phases of polypropylene</i>	81
	3.4.4 <i>The influence of secondary crystallization</i>	86
<b>3.5</b>	<b>Conclusions</b>	<b>87</b>
<b>3.6</b>	<b>References</b>	<b>88</b>
<b>3.7</b>	<b>Acknowledgements</b>	<b>92</b>
<b>3.8</b>	<b>Appendix 1</b>	<b>93</b>
<b>4</b>	<b>THE INFLUENCE OF CHAIN DEFECTS ON THE FUSION BEHAVIOR OF <math>\alpha</math>-, <math>\beta</math>-, AND <math>\gamma</math>-PHASES OF ISOTACTIC POLYPROPYLENE</b>	<b>95</b>
<b>4.1</b>	<b>Introduction</b>	<b>96</b>
<b>4.2</b>	<b>Experimental</b>	<b>97</b>
	4.2.1 <i>Samples</i>	97
	4.2.2 <i>Melting</i>	98
<b>4.3</b>	<b>Results</b>	<b>98</b>
	4.3.1 <i>Introduction</i>	98
	4.3.2 <i>Main sample characteristics</i>	99
	4.3.3 <i>Melting characteristics of the <math>\alpha</math>-, <math>\beta</math>- and <math>\gamma</math>-phases as revealed by LM and DSC</i>	99
	4.3.4 <i>Melting points (<math>\alpha</math>-, <math>\beta</math>-, <math>\gamma</math>-phase) as function of type and concentration of defects</i>	104

---

<b>4.4</b>	<b>Discussion</b>	<b>110</b>
	4.4.1 <i>Comparison with theory</i>	110
	4.4.2 <i>Discussion of the melting point determination by DSC</i>	118
<b>4.5</b>	<b>Conclusions</b>	<b>121</b>
<b>4.6</b>	<b>References</b>	<b>122</b>
<b>5</b>	<b>STRUCTURE-PROPERTY RELATIONS IN DIFFERENT NUCLEATED POLYPROPYLENES</b>	<b>127</b>
<b>5.1</b>	<b>Introduction</b>	<b>128</b>
<b>5.2</b>	<b>Experimental</b>	<b>129</b>
<b>5.3</b>	<b>Theory</b>	<b>131</b>
	5.3.1 <i>LEFM and Young's dislocation theory</i>	131
<b>5.4</b>	<b>Results and Discussion</b>	<b>132</b>
	5.4.1 <i>Crystalline morphology</i>	132
	5.4.2 <i>Tensile properties</i>	134
	5.4.3 <i>Impact tests</i>	135
	5.4.4 <i>Stress intensity factor</i>	136
	5.4.5 <i>Strain energy release rate</i>	138
<b>5.5</b>	<b>Conclusions</b>	<b>139</b>
<b>5.6</b>	<b>References</b>	<b>140</b>
<b>5.7</b>	<b>Acknowledgements</b>	<b>142</b>
<b>6</b>	<b>ORIENTED CRYSTALLIZATION AND MECHANICAL PROPERTIES OF IPP ON FIBRILLATED POLYTETRAFLUOROETHYLENE</b>	<b>143</b>
<b>6.1</b>	<b>Introduction</b>	<b>144</b>
<b>6.2</b>	<b>Experimental</b>	<b>145</b>
<b>6.3</b>	<b>Results</b>	<b>147</b>
	6.3.1 <i>PTFE particle morphology</i>	147
	6.3.2 <i>Morphology of injection molded bars</i>	148
	6.3.3 <i>Crystallization behavior of iPP on fibrillated PTFE</i>	153
	6.3.4 <i>Fibrillation</i>	161
	6.3.5 <i>Discussion of iPP-PTFE blend morphology</i>	161
	6.3.6 <i>Crystallization</i>	164
	6.3.7 <i>Mechanical properties</i>	164
<b>6.4</b>	<b>Conclusions</b>	<b>170</b>
<b>6.5</b>	<b>References</b>	<b>171</b>



<b>7</b>	<b>SPECIMENS WITH CONTROLLED THERMO-RHEOLOGICAL HISTORY FOR MECHANICAL TESTS</b>	<b>175</b>
7.1	<b>Introduction</b>	<b>176</b>
7.2	<b>Design of a dedicated compression mold</b>	<b>177</b>
	7.2.1 <i>Introduction</i>	177
	7.2.2 <i>Design</i>	177
7.3	<b>Experimental</b>	<b>180</b>
7.4	<b>Results and Discussion</b>	<b>183</b>
	7.4.1 <i>Introduction</i>	183
	7.4.2 <i>Validation of mold design</i>	183
	7.4.3 <i>Mechanical properties</i>	185
7.5	<b>Conclusions</b>	<b>187</b>
7.6	<b>References</b>	<b>188</b>
7.7	<b>Acknowledgements</b>	<b>188</b>
7.8	<b>Appendix: Design calculations</b>	<b>189</b>
	7.8.1 <i>Detailed calculation of the cooling time for the part</i>	189
	7.8.2 <i>Pump and coolant</i>	191
<b>8</b>	<b>SUMMARY</b>	<b>193</b>
<b>9</b>	<b>SAMENVATTING</b>	<b>197</b>

# **Chapter 1**

## **General Introduction and Scope**



## 1.1 General introduction

Structure-property relationships are well known in nature. For example, proteins have the most diverse functions that are related to the chain microstructure, i.e. sequences of amino acids. As enzymes and hormones, proteins catalyze and regulate reactions that occur in the body; as muscles and tendons they provide the body with means of movement; as skin and hair they give it an outer covering; as hemoglobin's they transfer all-important oxygen to its remote corners; as antibodies they provide it with means of protection against diseases. Given such a diversity of functions, it should not be surprising to find that proteins exist in all sizes and shapes. Their shapes or structure cover a range from globular (hemoglobin) to helical coils (hair, nails) and the pleated sheets of silk fibrion. The function of a protein is thus strictly follows its structure. The shape of proteins exhibits a structural hierarchy and consists of a primary, secondary, tertiary, and quaternary level. When the primary structure, which corresponds to the exact sequences of amino acids, is "correct", the polyamide chain folds in certain particular ways to gives rise to the higher levels of structure. In many cases an alteration of any amino acid in the sequence will result in a loss of function for the protein (e.g. sickle cell anemia) [1].

The above example of structure-property relationships in proteins finds its analogy (although maybe not as neat as "designed" by nature) in structure-property relationships of isotactic polypropylene (iPP). Isotactic polypropylene (iPP) is an important engineering plastic used in many different application areas like furniture, toys, and parts for the automotive industry. Daily we use products that are made of iPP, and new products are still under development. New areas of technology and science are explored to meet the new requirements set by the need for better mechanical, optical, thermal, and environmental properties [2].

The *morphology* of a polypropylene product, like in the case of proteins, is of great importance since it ultimately determines the macroscopic properties of the material. Crystalline polymers (among which is iPP) in the solid state show a very complex morphology in which various levels of hierarchy can be distinguished. Four levels of morphology can be identified: chain characteristics (primary level), crystal unit-cell (secondary level), lamellae structure (tertiary level), and crystal aggregates or super-molecular structures (quaternary level). Modifying morphology in order to modify required properties can take place on all four levels of the structural hierarchy.

The invention of industrial metallocene catalysis, introduced during the mid 1980s, offered a direct way to broaden the horizon of required properties. In contrary to conventional Ziegler-Natta (ZN) iPPs, metallocene catalysts produce molecularly very uniform homo- and co-polymers, with narrow molar mass

distribution (MMD). Metallocene catalysts have the ability to incorporate many different monomers leading to completely different chain architectures. For example, co-polymerization with ethylene may lead to ‘super soft’ PP, while incorporation of cyclic olefins may yield ‘super stiff’ material by ways of internal cross-linking.

Reactor-technology offers another way of adjusting polymer-properties. By having two or more different reactors in series, multiple reactor conditions become available for one catalyst particle. This results in for example bimodality (or higher order modalities) of the MMD. Reactor blends can also be made by introducing catalyst particles with two different reactive species. In this way otherwise thermodynamically immiscible polymers can be blended on the nano-scale, without the necessity of expensive process-technology.

In addition to the direct ways to change polymer properties by ‘designing chains’, via catalyst combined with reactor technology, several other, non-direct ways exists to broaden the wide product range of iPP. One example is post-reactor process-technology. After production the polymer is melt blended with an additional components. For example, we can think of the higher toughness of polypropylene nucleated with a highly selective  $\beta$ -nucleating agent. But also fiber reinforcement, ‘nano’-composites with layered silicate minerals, and in-situ composites are also ways to tune or improve the material properties of iPPs.

The above paragraphs give an idea of the many possibilities for tailoring polymer-properties by the expertise areas of catalysis, reactor engineering, and processing. The influence on the morphology of iPP is far-reaching and very complex. Understanding the influence of catalysis, reactor engineering, and processing on the resulting morphology needs an in-depth knowledge of the various parts and aspects of the relationships. Such an understanding is best achieved by following the “chain of knowledge”. The term is inextricably connected with the relationships and interaction between the various disciplines in polymer science. A thorough understanding of the basic principles of polymer-properties and morphology is therefore indispensable. It is of much scientific and technological interest to understand the relationships between polymer properties and morphology. In this thesis we present in various situations insights into novel relationships between polymer-morphology and polymer-properties using polypropylene as an representative example.

The following figure schematically presents the approach introduced for this thesis. The upper three boxes show the general concepts technology-morphology-properties, which were described above. The lower boxes highlight several topics taken from the main themes that are used in this thesis.

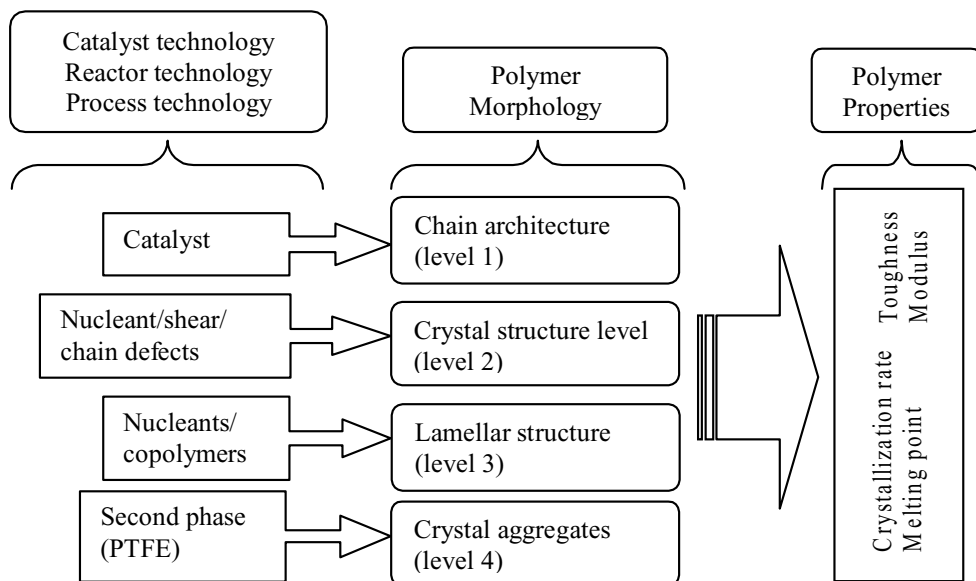


Figure 1.1. Schematic representation of the approach used in this thesis. The upper three text blocks give the general concepts: technology, morphology, and properties. Below these three blocks, details from each of the main themes are given which are used in this thesis.

## 1.2 Scope of this thesis

This thesis highlights several subjects taken from the various levels of structural hierarchy as described in Figure 1.1, starting from the chain characteristics (Chapter 3), via crystal unit cell (Chapter 4) and lamellar structure (Chapter 5) to polymer texture and orientation (Chapter 6). Central are crystallization kinetics and melting, toughness and modulus of nucleated polymers.

Chapter 2 gives a general description of the morphological characteristics of isotactic polypropylene. For each of the structural levels the specific characteristics are mentioned. Subsequently, the influence of the morphology on the impact behavior of polypropylene is discussed and a method to accurately determine impact resistance is given. The last sections of this chapter discuss the background concerning some of the experimental methods used in this thesis, like infrared dichroism and the representation of orientation structure by pole figures (wide angle x-ray scattering).

Central in Chapter 3 are structure-property relationships between polymer microstructure, crystallization behavior, and morphology. This chapter typically describes the transition from primary level (chain architecture), via secondary level (crystal unit cell), to tertiary level (lamellar structure). The basis for this study is given by a collection of well-defined and well-characterized polypropylene samples obtained by metallocene catalysis. With these samples we perform a fundamental

study on the influence of regio- and stereo-defects on the crystallization growth rate and the resulting morphology. Especially the internal differences in crystallization behavior and morphology between the crystal phases of isotactic polypropylene are highlighted. The profound influence of the presence of defects will be qualitatively expressed by an analysis of the measured data with a current crystallization theory.

Chapter 4 deals with the characteristic melting point depression of the samples studied in chapter 3. In this chapter relationships between the melting properties and the structure on the primary level (chain architecture) and tertiary level (lamellar structure) are established. The results describe the separate influence of stereo- and regio-defects on the fusion behavior of isotactic polypropylene. As in chapter 3, a comparison for the various crystal phases is given. A comparison is made between predictions from a current melting point depression theory and our data. A detailed discussion follows.

Central in Chapter 5 are correlations between impact resistance and crystalline morphology. The crystalline morphology was varied using three different polypropylene homo- and copolymers and several different nucleating agents. In contrast to chapters 3 and 4 where the influence of the primary and secondary level on several properties stood central, in Chapter 5 the influence of the tertiary level of morphology (lamellar level) on the mechanical properties is the main subject of research. Linear elastic fracture mechanics (LEFM) was used to characterize toughness.

Chapter 6 gives a discussion of the quaternary level (polymer texture and orientation) of morphology in interesting “in-situ” blends. In this chapter PTFE was blended with isotactic polypropylene in order to explore the parallel influence of fibrillation and nucleation on the morphology and impact properties of these materials. The combination of the ability of PTFE to fibrillate and to act as a nucleant results in a self-reinforced material with highly improved mechanical properties. We melt-blended small amounts of various PTFE powder particles (with different particle diameter and molar mass) with iPP. In the present study, results obtained from impact and tensile measurements of injection-molded specimen are summarized and a discussion of (fibrillar) phase morphology of the corresponding blends is given.

Chapter 7 provides an outlook for a new approach to establish structure-property relationships. Accurate structure property studies of polymers necessitate the use of samples with well defined and well characterized molecular characteristics and a reproducible, well controlled thermo-rheological history. For studies of microstructure, thermal properties, and crystallization characteristics specimen sizes can be as small as several tens of milligrams (Chapter 3 and 4). However, for mechanical studies, e.g. for impact test, standard specimen size

significantly exceeds these limits (Chapter 5 and 6). Hence, there is need to prepare isothermally crystallized samples with large enough sizes and compare these materials processed by practice, such as injection molding. In this chapter we investigate the possibilities to achieve the goal of producing well-defined samples of sufficient size. For that purpose we designed a compression mold which enabled us to make homogeneous samples isothermally.

The last chapter (Chapter 8) provides an overview of the entire research project, i.e. of every chapter a short summary is given.

## 1.3 References

- (1) Solomons, T. W. G. *Organic Chemistry*; 5th ed.; John Wiley & Sons, Inc.: New York, 1992.
- (2) Ratzsch, M. J. *Macromol. Sci.-Pure Appl. Chem.* **1999**, A36, 1587.

# **Chapter 2**

## **Polymer Morphology and Analysis: A Review**





## 2.1 Introduction

This chapter serves as an introduction to topics that are relevant for the work described in this thesis. Only general aspects are discussed here, specific topics relevant for the particular chapters are dealt with in the corresponding chapters.

In section 2.2, the various morphological levels in isotactic polypropylene (iPP) are introduced. The topics in this section are arranged according to the characteristic size of the system. Firstly the primary level of structure is described. Central in this treatment is the chain architecture, i.e. structural isomerism and monomer connectivity. Accurate characterization of chain architecture receives particular attention. Secondly, the forms of chain packing in the crystalline phase (secondary level) of polypropylene are discussed. For each crystalline phase the main characteristics are mentioned. The third part (tertiary level) describes how elements of the secondary structure of polypropylene can be ordered into larger assemblies, like lamellae. The last part describes the morphological characteristics of the polymer on the quaternary level, e.g. the texture of the material. The influence of thermal rheological history on the formation of these configurations is essential and is described in detail.

Section 2.3 gives a short summary of the crystallization and melting of the  $\beta$ -phase of polypropylene. Next (section 2.4), a discussion of impact properties in relation to morphology is given, together with a description of the various methods to accurately measure toughness. The discussion on the influence of morphology on toughness is arranged according to the aforementioned characteristic morphological levels. The last section of this chapter (section 2.5) deals with some of the analysis techniques used in this thesis. Subsequently, wide-angle x-ray scattering (WAXS), infrared dichroism and polarized light microscopy receive attention. Special attention is focused on the representation of WAXS-data in pole-figures for texture analysis

## 2.2 Morphology of isotactic polypropylene

### 2.2.1 The primary level of macromolecular structure: Molecular characteristics

The primary level, i.e. the chain characteristics follow directly from the chemistry of the particular polymerization reactions. Stereo regular polypropylene can be obtained by using various catalysts that promote regular insertion of monomers in the growing chain. Thus, the type of catalyst used, together with the support of the catalyst [1] has a profound influence on the primary chain architecture. In this chapter we do not discuss the reaction mechanisms that determine the chain characteristics, but rather take the polymer chain as starting

point for the discussion.

The main chain-characteristics of linear PP are the molar mass (MM), molar mass distribution (MMD), and chain regularity. Gel permeation chromatography (GPC) is typically used to measure the MM and MMD. The full representation of the continuous MM distribution of a polymer sample as measured by GPC is usually expressed in averages, see equations (2.1a/b/c).

$$\bar{M}_n = \frac{\sum_i N_i M_i}{\sum_i N_i}, \quad \bar{M}_w = \frac{\sum_i N_i M_i^2}{\sum_i N_i M_i}, \quad \bar{M}_z = \frac{\sum_i N_i M_i^3}{\sum_i N_i M_i^2}, \quad (2.1a/b/c)$$

where  $N_i$  is the number of molecules with molar mass  $M_i$ . The width of the MM distribution is usually expressed as  $\bar{M}_w / \bar{M}_n$  or  $\bar{M}_z / \bar{M}_w$ .

The regularity in the configuration of successive stereo centers determines the overall order (= tacticity) of the polymer chain. A stereo center is defined as an atom bearing several groups whose identities are such that an interchange of two of the groups produces a stereo isomer [2]. The carbon atom carrying the substituent (a methyl group in PP) is a stereogenic center and the microstructure of the polyolefin is described in terms of the *meso* [*m*] or *racemo* [*r*] enchainment neighboring substituents. Isotactic polypropylene is characterized by a high fraction of [*m*] position of the methyl groups as depicted in Figure 2.1, whereas syndiotactic polypropylene and atactic polypropylene are characterized by an high fraction of [*r*] positions and a random amount of [*r*] and [*m*] positions, respectively (structures not shown).

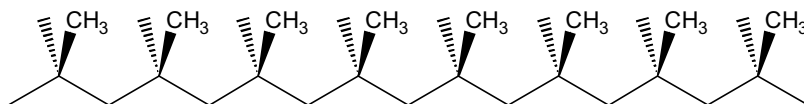


Figure 2.1. Part of an isotactic polypropylene chain.

From  $^{13}\text{C}$ -NMR spectra it is possible to extract information about the configuration of five neighboring substituents (pentad level) [3]. Ten different pentads exist, i.e. [*mmmm*], [*mmmr*], [*rmmr*], [*mmrr*], [*mrmm*], [*rmrr*], [*mrrr*], [*rrrr*], [*rrrm*], [*mrrm*] [4]. A few of these pentads are shown as illustrated in the modified Fischer projection of isotactic polypropylene in Figure 2.2. Structures I and II of Figure 2.2 show two pentads with a different defect structure.

Several relationships between dyads, triads, etc. can be established [5]. A few of these relations are given below (for clarity the square brackets are omitted):

$$r = rr + \frac{1}{2} mr \quad (2.2a)$$

$$mm = mmmm + mmmr + rmmr \quad (2.3b)$$

$$mr = mmrr + mrmr + rmmr + rmmr \quad (2.4c)$$

$$rr = rrrr + rrrm + mrrm \quad (2.5d)$$

Besides stereo defects, the chain may also contain regio-defects. A regio-defect in polypropylene is defined as a “mis” insertions of a polypropylene unit during polymerization, e.g. a ‘2-1’ insertion takes place during a repeated ‘1-2’ insertion or vica versa. Possible regio defects are indicated in Figure 2.2 (structures III and IV).

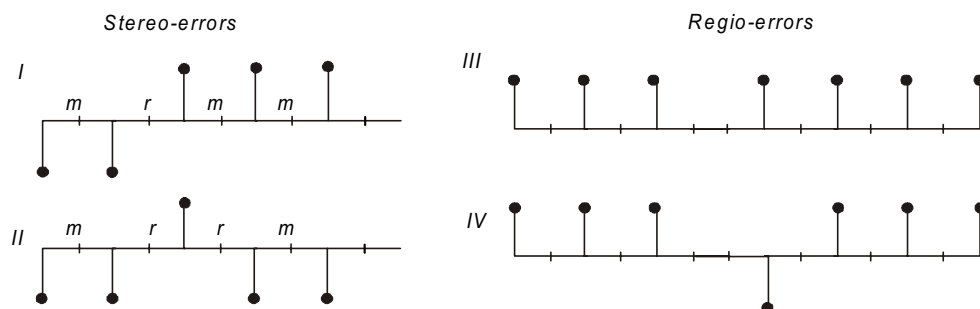


Figure 2.2 (Modified) Fischer projections of possible polypropylene defects: I, II: two pentads with stereo defects, III and IV: two pentads with regio defects. The methyl groups of the iPP chain are indicated as black spheres.

## 2.2.2 The secondary level of macromolecular structure: Crystal phases of iPP

### Introduction

Isotactic polypropylene is a polymer with a number of crystal modifications [6]. In all of the crystal structures the chain is packed in the lattice as a left or right handed (or both)  $2^*3_1$ -helix conformation with either an 'up' or 'down' position of the methyl groups (see Figure 2.3 for a helix with 'down' position of the methyl groups). Figure 2.3 shows the contours of the helix as a triangular bar. This representation is used in the description of the crystal phases of polypropylene.

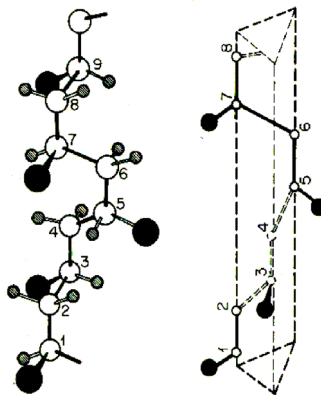


Figure 2.3. Left: helical structure of isotactic polypropylene with 'down' positions of the methyl groups (black spheres). Right: representation of the same helix in a triangular bar. After Cowie [7].

### The $\alpha$ -phase of polypropylene

The  $\alpha$ -phase of iPP is described by an alternation, in the b-axis direction, of layers parallel to the ac-plane and composed of only left handed (L) or right-handed (R) helices, indicated in Figure 2.4 by white and gray triangles, respectively. The position of the methyl groups in both the left or right-handed helix can be positioned 'up' or 'down' (up or dw) (see Figure 2.3 for a helix with 'dw' position of the methyl groups). Due to the possibility of the chains to be situated 'up' or 'down', two limiting  $\alpha$ -phases ( $\alpha_1$ : disordered,  $\alpha_2$ : ordered) can be recognized (see Figure 2.4). The ordered  $\alpha_2$  phase (Figure 2.4 right) can be obtained by re-crystallizing or annealing [8]. The monoclinic unit cell has the following parameters  $a = 6.65\text{\AA}$ ,  $b = 20.96\text{\AA}$ ,  $c = 6.5\text{\AA}$  [9,10], and  $\beta = 99.62^\circ$ . The overall density is  $0.946\text{ g/mol}$  [10] (room temperature).

The value of the thermodynamic equilibrium melting point,  $T_m^\circ$ , of the  $\alpha$ -phase has been studied by many authors [6]. However, corresponding attempts resulted in different values, which can be grouped in values around  $186^\circ\text{C}$  and values around  $220^\circ\text{C}$ .  $T_m^\circ$  can be determined by various extrapolation methods, like the Hoffman-Weeks and Gibbs-Thomson extrapolations [12,13]. Values determined by Hoffman-Weeks plots are usually in the higher temperature range, while Gibbs-Thomson plots give lower values [6]. The values of the heat of fusion ( $\Delta H_f^\circ$ ) are also scattered. Data obtained from calorimetry show values around  $\Delta H_f^\circ = 8.7 \pm 0.8$

kJ/mol [6], while the value determined by the method of the melting point depression by diluents is  $\Delta H_f^\circ = 9.1 \pm 1.6$  kJ/mol [6]. In this thesis we adopt the values of  $T_m^\circ = 186^\circ\text{C}$  [6,14] and  $\Delta H_f^\circ = 8.7$  kJ/mol [6].

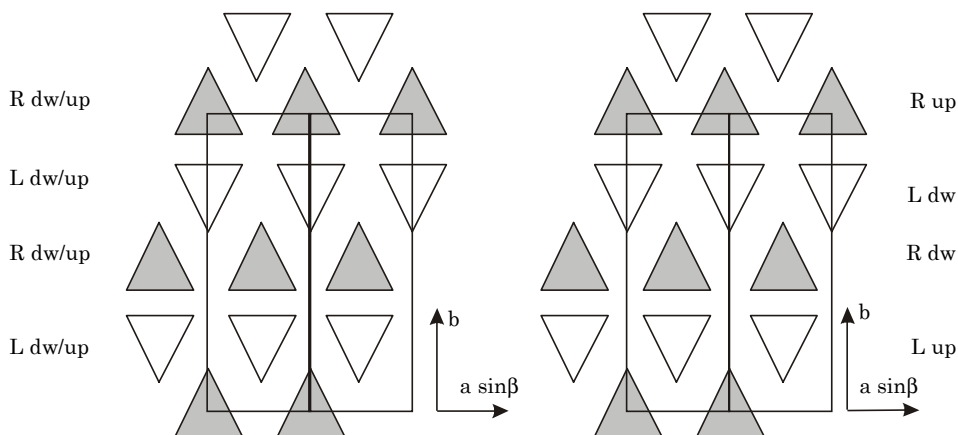


Figure 2.4. Two limiting forms of the  $\alpha$ -phase. Left:  $\alpha_1$ ; Right:  $\alpha_2$ . The horizontal arrows indicate the projection of the  $a$ -axis, the vertical arrow indicates the  $b$ -axis. The  $c$ -axis is perpendicular to the plane of view [11].

### The $\beta$ -phase of polypropylene

Under proper crystallization conditions (shear, large temperature gradients, or use of  $\beta$ -nucleating agents like quinacridone [15], the anhydrous calcium salt of suberic acid [16], and other agents), polypropylene samples with a high content of the  $\beta$ -phase can be made [15-17]. In samples that have been subjected to high shear in the melt the  $\beta$ -phase can be found, as well [15].

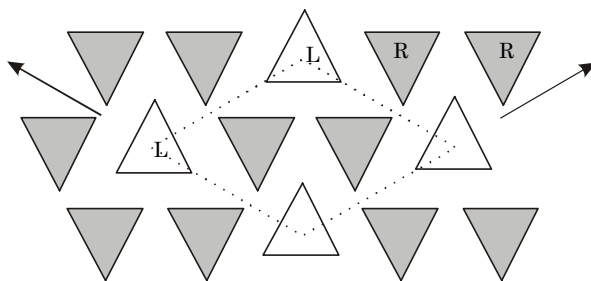


Figure 2.5. Schematic representation of the arrangement of *iPP*-helices in the  $\beta$ -phase. The arrows indicates the  $b$ -axes, the  $c$ -axis is perpendicular to the plane of view.

The  $\beta$ -phase has a trigonal unit-cell with lattice parameters  $a = b = 11.0 \text{ \AA}$ ,  $c = 6.5 \text{ \AA}$ ,  $\beta = 120^\circ$  [#471][#472]. The  $\beta$ -phase is metastable relative to the  $\alpha$ -phase. The values published in literature of  $T_m^\circ$  for  $\beta$ -phase isotactic polypropylene are scattered for the same reasons as mentioned for the  $\alpha$ -phase [6]. The values of  $\Delta H_f^\circ$

vary from 4.2 kJ/mol, 4.7 kJ/mol, to 8.1 kJ/mol [6]. In the thesis we adopt the value of  $T_m^\circ = 177^\circ\text{C}$  [6,14] and  $\Delta H_f^\circ = 5.0$  kJ/mol [6]. The values of  $T_m^\circ$  and  $\Delta H_f^\circ$  are always found to be lower than the corresponding values for the  $\alpha$ -phase.

### The $\gamma$ -phase of polypropylene

The  $\gamma$ -phase is usually associated with the  $\alpha$ -phase, although individual single crystals of the  $\gamma$ -phase have also been observed. The  $\gamma$ -modification may be formed in degraded, low molecular weight isotactic polypropylene and in samples crystallized under high pressures [19,20]. Also, considerable amounts of the  $\gamma$ -modification were obtained under atmospheric pressure, both in systems with low tacticity or made by homogeneous metallocene catalysts [17,21]. The value of the thermodynamic equilibrium melting point,  $T_m^\circ$ , of the  $\gamma$ -phase is  $187.2^\circ\text{C}$  [21]. The value of the heat of fusion ( $\Delta H_f^\circ$ ) was determined as  $\Delta H_f^\circ = 6.1$  kJ/mol [21].

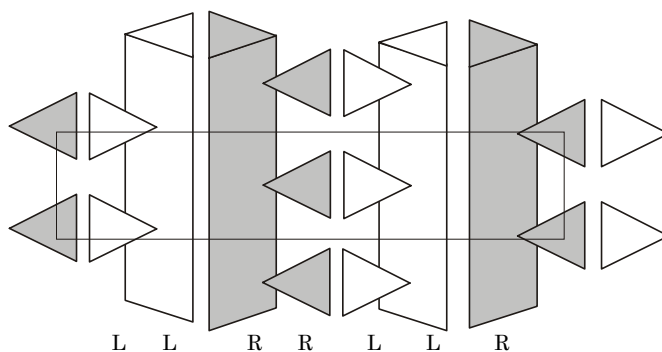


Figure 2.6. Schematic representation of the arrangement of *iPP*-helices in the  $\gamma$ -phase [24] [20].

The crystalline structure of the  $\gamma$ -modification was first denoted as triclinic [17,18]. However, it was shown that the structure is orthorhombic with parameters  $a = 8.54\text{\AA}$ ,  $b = 9.93\text{\AA}$ , and  $c = 42.41\text{\AA}$  [20], with the aforementioned triclinic cell as a sub-cell [22]. The structure is composed of sheets of parallel chains, in which the molecular orientation in adjacent sheets is inclined to one another at  $80^\circ$  angle [23]. In this unit cell the  $c$ -axis is not parallel with chain axis direction.

### Other-phases of polypropylene

Rapid quenching of molten isotactic polypropylene fails to produce a totally amorphous polymer, but rather leads to an intermediate crystalline order. The interpretation of the structure formed is still disputed in literature [17]. Some attempts have been made to elucidate the structure. For example, Caldas, et al. [25] measured, in addition to the pure amorphous matrix, crystalline regions of about 10 to 20 nm in size, which possessed the  $\alpha$ -crystal modification. In addition,

regions of lower crystalline order containing the  $\alpha$ -phase could be found, but with much larger crystal unit cell dimensions. In this thesis, no attention is paid to such phases of iPP.

### 2.2.3 The tertiary level of macromolecular structure: Lamellar structure

The most common basic structural feature of melt crystallized iPP is the lamellar like crystallite. The chains in the lamellae are ordered in crystal cells as described in the previous section (section 2.2.2). In the  $\alpha$ - and  $\beta$ -phases of iPP, the polymer chains are oriented perpendicular (in *c*-direction) to the *ab*-plane of the crystals, i.e. the wide face or basal plane of the crystallite. In the  $\gamma$ -phase, the chains have an angle of + or - 40° with the normal direction of the lamellae. The usual shape of  $\gamma$ -phase crystals is lenticular.  $\gamma$ -Phase crystals grow epitaxially on  $\alpha$ -phase crystals, similar to the epitaxial growth of secondary lamellae (crosshatches) on the  $\alpha$ -phase (see chapter 3). As a consequence of the association of  $\gamma$ -phase with the  $\alpha$ -phase,  $\alpha$ -spherulites contain, under proper conditions,  $\gamma$ -phase crystals as well.

In general, lamellae in polypropylene have thicknesses varying from approximately 4 nm for the crosshatched lamellae to several tens of nanometers for primary grown lamellae. Lateral dimensions may reach several micrometers. The lamellae are separated by amorphous layers. The thickness of the layer is usually in the order of the thickness of lamellae. Above the glass transition ( $T_g$ ), which is around 0°C [26], the amorphous phase shows visco-elastic (rubbery) behavior, while below  $T_g$  the amorphous phase behaves as a rigid solid. Between the pure amorphous- and crystalline-regions, a rigid-amorphous or disordered crystalline phase can be distinguished. The polymer chains in this region are restricted in their movement by the ordered crystal phase. The inter-phase contains also the fold surface of the lamellae. Two or more lamellae separated by amorphous layers may be arranged in stacks [27,28], which are also called fibrils [29].

Naturally, many more aspects of the lamellar habit of PP (like branch points, screw dislocations, structure of the fold-surface, lateral size and shape, etc.) can be highlighted. Moreover, the exact structure of the lamellar crystals depends largely on the conditions of formation. A detailed description of these characteristics is beyond the scope of this thesis. For more information see reference [29].

## 2.2.4 The quaternary level of macromolecular structure: Spherulites and row structures

### Introduction

The morphology on the quaternary level of polypropylene is complex. Depending on crystallization conditions (isothermal, non-isothermal), flow conditions (quiescent or shear induced crystallization), molecular constitution, pressure and the presence of nucleating agents many different features exist like spherulites, cylindrites, or trans-crystalline structures.

### Quiescent crystallization: Spherulites

The term “spherulite” indicates an aggregate of primary crystallites of spherical shape, consisting of individual lamellae or bundles of lamellae growing from a central nucleus [6,30]. Branching and splaying provide complete filling of space [6]. Spherulites of iPP show the general characteristics of typical spherulitic morphologies of semi-crystalline materials, some special features exist, which are highlighted.

Four different types of spherulites can be distinguished for polypropylene, which are marked with Roman numerals. The classification is determined by their birefringence (see section 2.5.3). The spherulites consisting of the  $\alpha$ -phase may be divided into three different types: positive ( $\alpha_I$ ), negative ( $\alpha_{II}$ ), and mixed ( $\alpha_m$ ).  $\alpha_I$  is formed below 134°C and  $\alpha_{II}$  is formed above 137°C [6,29,31]. The difference in birefringence for spherulites consisting of the  $\alpha$ -phase can be interpreted by the unique cross hatched structure of  $\alpha$ -phase iPP. Initially ‘mother’ lamellae crystallize, on which subsequently ‘daughter’ lamellae can grow homo-epitaxially on the lateral (010) planes. This results in an interchange of a- and c-axes orientations in the mother and daughter lamellae across the contact plane, while the b-axis orientation is preserved [6,29,31]. Assuming a quadratic arrangement of the mother and daughter lamellae, the relative amount of radial and tangential lamellae in the various types of  $\alpha$ -spherulites determines the sign of birefringence [10]. Also, increasing the tacticity decreases the formation of tangential lamellae and an almost 100%  $\alpha_{II}$  form was obtained, with a very stereoregular isotactic polypropylene [32].

Spherulites consisting of the  $\beta$ -phase follow the general characteristics of spherulitic growth in semi-crystalline materials. The development of  $\beta$ -spherulites (from a point like nucleus via hedrites to the final form) is covered by [6] and is not repeated here. Two types of  $\beta$ -spherulites may be formed, separated with a broad-defined transition temperature ( $\pm 128^\circ\text{C}$ ): negatively birefringed radial ( $\beta_{III}$ ) types and negative birefringed ringed ( $\beta_{IV}$ ) type.  $\beta$ -spherulites do not exhibit cross-



hatching [6].

The  $\gamma$ -phase is usually associated with the  $\alpha$ -phase [33], although individual single crystals of the  $\gamma$ -phase also were observed [23]. Therefore, no separate classification exists for spherulites exhibiting the  $\gamma$ -phase.

### Crystallization under shear: Skin-core morphology

Injection-molded iPP samples display distinct skin-core morphologies as a result of processing [35], see Figure 2.7. The core is usually spherulitic, however may still exhibit an overall chain orientation [36]. The skin usually shows three [37] or more distinct layers [38] (not shown in Figure 2.7). The structure of the skin is non-spherulitic and consists of highly oriented structures. The underlying reason for this typical skin-core morphology is that due to processing, the polymer is subjected to strong flows before and during crystallization. Moreover the polymer crystallizes under strong temperature gradients. This results in a strong orientation of both the crystalline and amorphous phases [37,39].

The morphological entities in the skin are often referred to as row-structures [40]. Highly extended polymer chains crystallize in an oriented way resulting in iPP row-nuclei on which lamellae may grow perpendicular. Other morphological entities, which may be present in the skin of typical injection molded specimen result from shearing partially crystallized material [41]. The resulting morphologies are very diverse and may influence mechanical properties strongly, see section 2.4.4.

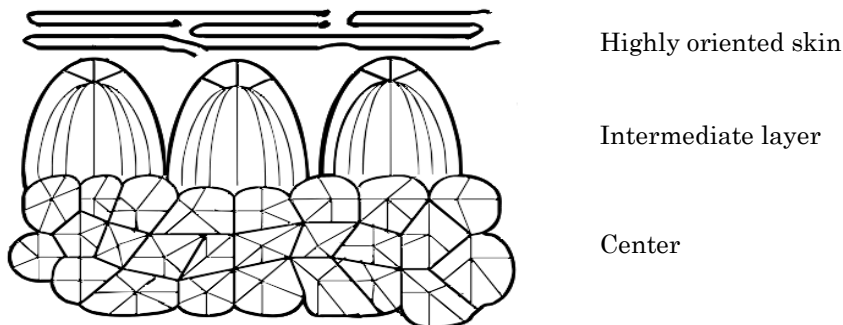


Figure 2.7. Simplified schematic representation of a skin-core morphology from an injection molded sample. After A. E. Woodward [35].

## 2.3 Crystallization and melting of the $\beta$ -phase in relation to the $\alpha$ -phase.

### 2.3.1 Crystallization characteristics

It was established that the  $\beta$ -phase of isotactic polypropylene produced with conventional Ziegler-Natta (ZN) catalysts shows two critical temperatures. The critical temperatures are characterized by the relative growth rates of the  $\alpha$ - and  $\beta$ -phase. As is known from literature [42], the ratio of the growth rate of the  $\beta$ -phase with the growth rate of the  $\alpha$ -phase ( $G_\beta/G_\alpha$ ) increases steadily with decreasing crystallization temperature. When the  $\beta$ -phase is crystallized below  $T_{\beta\alpha}$  (but above  $T_{\alpha\beta}$ ), the growth rate of the  $\beta$ -phase exceeds that of the  $\alpha$ -phase ( $G_\beta > G_\alpha$ ). In all other cases the growth rate of the  $\alpha$ -phase is larger than that of the  $\beta$ -phase. The two temperatures thus border the growth rate of the  $\beta$ -phase, within this temperature range  $G_\beta > G_\alpha$ .

Formation of the  $\beta$ -phase can also be enhanced by shearing the melt prior to crystallization. The relative growth rates of the  $\alpha$ - and  $\beta$ -phase are important for the formation of the  $\beta$ -phase under shear. Samples rich in  $\beta$ -phase are formed when  $T_{\alpha\beta} < T_c \leq T_{\text{pull}} < T_{\beta\alpha}$ , where when  $T_{\alpha\beta}$  and  $T_{\beta\alpha}$  are the lower ( $T_{\alpha\beta} = 100\text{-}105^\circ\text{C}$ ) and upper (bifurcation) critical temperatures ( $T_{\beta\alpha} \approx 141^\circ\text{C}$ ) for the formation of the  $\beta$ -phase.

### 2.3.2 Melting characteristics

The melting characteristics of the  $\beta$ -phase highly depend on thermal history of the sample and are influenced by many factors. Studies of the melting of  $\beta$ -phase-spherulites by polarized optical microscopy (POM) showed that the spherulites recrystallized into the  $\alpha$ -modification ( $\beta\alpha$ -recrystallization) when heated and finally melt from this form [44]. This recrystallization only occurs when cooled below the critical temperature  $T_{\alpha\beta}$  ( $= 100\text{-}105^\circ\text{C}$ ). Samples not cooled below this temperature show separate melting of the  $\beta$ -phase without recrystallization. The recrystallization effect is attributed to  $\alpha$ -phase growing on the  $\beta$ -phase during cooling (secondary crystallization) [6,15,45]. During partial melting of the  $\beta$ -phase, the  $\alpha$ -phase nuclei act as  $\alpha$ -nucleating agents and therefore induce a  $\beta\alpha$ -recrystallization.  $\alpha$ -Phase formed by  $\beta\alpha$ -bifurcation of growth does not induce  $\beta\alpha$ -recrystallization. These nucleation effects are caused only by the  $\alpha$ -phase, which is very finely distributed on the intra and inter spherulitic regions [45]. The tendency for  $\beta\alpha$ -recrystallization is influenced by the crystallization temperature, rate of crystallization, and cooling/heating rate and time.

## 2.4 Impact properties in relation to morphology

### 2.4.1 Introduction

One of the mechanical characteristics of a material is its resistance to impact, or toughness. Toughness is typically measured by standard tests as Izod or Charpy impact-tests or according to the method of linear elastic fracture mechanics (LEFM) [46,47]. The strain rates in impact tests are generally high (several meters per second) compared with tensile tests (millimeters per second or slower).

The discussion of morphology in relation to toughness starts with a general description of impact-tests (section 2.4.2). Subsequently, a method is described for obtaining the size-independent critical stress-intensity factor ( $K_{Ic}$ ) and critical strain energy release rate ( $G_{Ic}$ ). Next, an overview of the morphological parameters, which influence the toughness of a material, is given (section 2.4.4). This discussion is divided according to the morphological hierarchy described in the introduction of this thesis, i.e. molecular characteristics (primary level), crystal structure (secondary level), lamellae (tertiary level), and crystal aggregates and textures (quaternary level).

### 2.4.2 Impact tests

In a typical impact test (Izod or Charpy) a bar with standard dimensions and optional with a notch of different size and shape, is hit by a hammer. Instrumented impact-apparatuses [48] are able to measure the force during fracture, resulting in a stress vs. strain curve. The toughness of a material may be defined in terms of such a resistance curve. Figure 2.8 A and B show such (idealized) stress-strain curves.

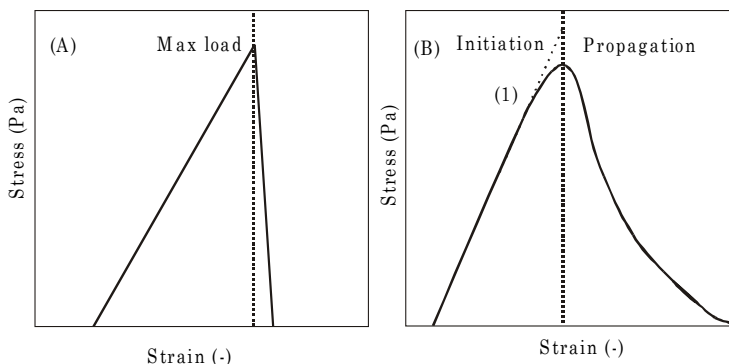


Figure 2.8. Idealized stress-strain curves of A) a brittle material, B) a ductile (semi-brittle) material.

The total energy absorption is the area under a stress-strain curve, this is the total energy necessary to produce two new fracture surfaces. After an initial linear

increase of the force the impact curves show a maximum. At the (near) maximum a crack may form, which is often accompanied by a certain amount of localized yielding (i.e. crazing) over a restricted area near the crack tip [49]. The maximum load is the boundary between crack initiation and crack propagation [50]. Preceding the maximum load sometimes some short range ligament yielding may take place, this is seen as a curvature in the otherwise straight curve (see (1) in Figure 2.8B). Brittle fracture is characterized by a negligible propagation energy (see the area under the steep straight line after the maximum load in Figure 2.8A). In contrary to brittle fracture, the curve in Figure 2.8B shows pronounced crack propagation energy. The presence of this propagation energy is defined here as a sign for ductile fracture.

Ductile/brittle behavior can be defined in two ways; from a stress-strain curve (see above) and phenomenologically from the study of fracture zones and surfaces [49,51]. A highly deformed fracture zone indicates a ductile fracture mechanism, while a less, more locally deformed zone indicates brittle fracture. Since brittle fracture is one of the prerequisites to apply linear elastic fracture mechanics (LEFM) (see section 2.4.3), it is important to know if a specimen fractures brittle or ductile.

Whether a material behaves brittle or ductile under impact conditions (high strain rates) depends on many factors, like temperature [52], strain-rate [53,54], stress-state (plain strain or plain stress) [47], and the presence of a notch (including shape and size) [49,55]. It is outside the scope of this thesis to give a survey of the influence of test-conditions on the impact behavior.

Many ‘artifacts’ or effects may be introduced during fracture, which one must keep in mind in interpreting the impact results. For example, the dissipation of the mechanical energy as heat can raise the temperature in the deformation zone, causing temperature effects, such as the lowering of the yield stress [49,56]. Other parameters are size and shape of the notch, size of specimen [57] (in traditional Izod and Charpy impact tests [47]).

### 2.4.3 Linear elastic fracture mechanics (LEFM)

Fracture resistance of polymers can be characterized by standard test methods (Charpy, Izod), but these supply values, which depend on the size of the specimen and on loading conditions [50,58]. On the other hand, linear elastic fracture mechanics (LEFM) give size independent fracture characteristics. One of the quantities, which can be determined by this technique, is the critical strain energy release rate ( $G_{lc}$ ), defined by equation. (2.11):

$$U = U_0 + G_{lc}BD\phi, \tag{2.6}$$

where  $U$  is the measured total fracture energy,  $U_0$  is kinetic energy loss,  $B$  is the

specimen thickness,  $D$  labels the width of the specimen, and  $\phi$  is a geometric factor related to the compliance of the specimen [46]. In this thesis, we used the technique of Plati and Williams [46] to determine  $G_{Ic}$ . The other quantity, which can be derived from the load vs. displacement traces measured in instrumented impact testing, is the critical stress intensity factor ( $K_{Ic}$ ), defined by equation (2.12):

$$K_{Ic} = f(a) \frac{F_Q}{BD^{1/2}}, \quad (2.7)$$

where  $f(a)$  is a geometric factor depending on the depth of the notch ( $a$ ) and  $F_Q$  is the force measured before crack initiation (maximum force).

In order to be able to apply LEFM, specimens must be in plane-strain condition, which requires a certain minimum thickness ( $B$ ) and ligament length ( $D-a$ ), i.e.

$$B > 2.5 \left( \frac{K_{Ic}}{\sigma_y} \right)^2 \text{ and } (D - a) > 2.5 \left( \frac{K_{Ic}}{\sigma_y} \right)^2, \quad (2.8a/b)$$

where  $\sigma_y$  is the yield stress of the polymer. The extent of plastic deformation (plastic zone size,  $r_p$ ), defined as:

$$r_p = \frac{1}{2\pi} \left( \frac{K_{Ic}}{\sigma_y} \right)^2, \quad (2.9)$$

must be significantly smaller than the characteristic dimensions ( $B$ ,  $D-a$ ) of the specimen [47]. In equations (2.8a/b) and (2.9) yield stress values measured under static conditions are considered, as the yield stress is lower at smaller strain rates [49]. Thus rather conservative values are obtained for the minimum thickness  $B$ , ligament length, and  $r_p$ . Under these conditions, when the failed specimen satisfies the conditions for plain strain set by equation (2.8a/b), LEFM can be applied and  $K_{Ic}$  and  $G_{Ic}$  can be determined accordingly.

## 2.4.4 Relationships between morphology and impact properties

### Introduction

In order to have a material that has a good resistance to impact, the material must have the ability to dissipate energy during loading. The more energy a material can absorb the higher the impact resistance. Various mechanisms may occur in (pure) polypropylene, which can lead to energy dissipation and thus to a higher toughness e.g. yielding, crazing, and phase transitions [58].

In the stress-strain curve of semi-crystalline polymers, the yield point corresponds to the onset of irreversible morphological deformation [59]. Yielding in semi-crystalline polymers involves considerable disruption of the crystalline

morphology. As plastic flow continues, the polymer becomes highly oriented and the resistance to further extension increases correspondingly. The lamellae and spherulites increasingly lose their identity and a new fibrillar structure is formed [49]. Localized yielding over a restricted region, near points of high stress concentration, is associated with crazing (and the formation of a crazed network). A craze is a wedge of deformed polymer, with a tip that is sharp on a scale of tens of nano-meters, broadening out over a distance of about 0.1 mm [49]. Load bearing fibrils are present which are formed by drawn, highly deformed polymer [49]. Both mechanisms (yielding/crazing) involve large plastic deformation, although yielding takes place macroscopically and crazing microscopically.

From a molecular point of view no distinction needs to be made between yielding and crazing, however the distinction macroscopically is obvious. In this thesis we make use of the molecular description of yielding and crazing to discuss the influence of the morphological parameters on the fracture behavior. This discussion is arranged according to the morphological levels introduced in section 2.2, i.e. molecular characteristics (primary level), crystal phases: phase transformations (secondary level), lamellar structure (tertiary level), and spherulites and polymer texture (quaternary level).

### **Role of molecular characteristics in deformation (primary level)**

As mentioned in section 2.2.1, the most important molecular characteristics of a linear chain polymer (like polypropylene) are the molar mass (MM), molar mass distribution (MMD), and chain architecture.

In general, an increase in MM strongly enhances the impact properties of the polymer [56,60]. For example the brittle-to-ductile transition temperature decreases with increasing MM [56,60]. The MM influences the maximum obtainable degree of crystallinity, as well. The degree of crystallinity in injection molded specimen decreases slightly with increasing MM [61]. In turn, a decrease in crystallinity usually gives an increase in toughness. Increasing the MM of the polymer causes a larger amount of entanglements and amorphous tie chains in the inter-lamellar and inter-spherulitic regions. This leads to the tendency of an enhanced stabilization and extension of a crazed network with increasing molecular weight, resulting in higher toughness [62].

Tacticity, or regularity of the chain, greatly influences higher order levels of morphology, e.g. at the lamellar level, and the spherulitic level. Upon incorporation of chain defects, the development into super-molecular structures is changing from ordered (spherulitic) to completely disordered (single crystal domains) [63]. The changes on the higher structural levels obviously have influence on the deformation behavior (see subsequent sections). The influence of tacticity on the resulting properties is thus often indirect.

### **Role of crystal phase in deformation: phase transformations (secondary level)**

An increase in toughness is usually found when phase transformations are possible, and occur, during deformation. Isotactic polypropylene exhibits a  $\beta\alpha$ -transition [64,65] when the  $\beta$ -phase is present. The  $\beta$ -phase is mechanically stable up to the yield point, but after yielding the  $\beta$ -phase can transform to the  $\alpha$ -phase. The  $\beta\alpha$ -transformation depends on the time of loading, and the thermal history [64]. The phase transformation in polypropylene is likely when the sample is subject to large strains [66]. Thus the  $\beta$ -phase has better impact properties than the  $\alpha$ -modification

### **Role of lamellar structure in deformation (tertiary level)**

Lamellae with the surrounding amorphous layers are the smallest entities usually considered in the deformation behavior of polymers. Deformation of the lamellar structure was mainly studied at lower strain rates and results of the corresponding studies are used for higher strain rates [54]. The plastic deformation of polymer crystals at medium strains ( $< 2\%$ ), is generally expected to be crystallographic in nature and to take place without destroying the crystalline order [67]. However at higher strains, the crystals may completely break down and new crystals may form with no specific crystallographic relation to the original structure. Several mechanisms have been proposed [67]: slip in the chain direction, fine and coarse chain-direction slip, inter-fibrillar slip, transverse slip, twinning, stress-induced martensitic transformation, chain disentanglement, and dislocations in polymer crystals [67-71]. Crystallographic slip along planes parallel to the chain axis is probably the main active process of plasticity of PP's for various deformation modes [72], namely tensile drawing, simple shear, and compressive testing.

Two main theories exist in the literature for the explanation of the relation between yield stress and crystal thickness [73]. One claims that the dominating mechanism of yielding is partial or local melting, stretching of amorphous chains, and subsequent re-crystallization [67]. The other uses the more conventional approaches of crystal plasticity. This includes stress induced crystal-crystal transformation, twinning, and slip. This approach was reviewed by Bowden and Young [67]. The plasticity was regarded as a thermally activated process involving nucleation and propagation of screw dislocations under the influence of an applied stress. Young's theory was shown to have several drawbacks [67,74], e.g. a too weak dependence on temperature and problems with the morphological reasoning behind it. The correlation of crystal structure and yielding was extensively studied for polyethylene and the available information indicates that at, or near, room temperature crystal plasticity, i.e. the *onset* of plastic deformation, is controlled by dislocations [73], while *post*-yield deformation, involving neck formation and stabilization, is assumed to occur by "quasi-melting" or "de-crystallization" [73].

### **Role of spherulites in deformation (quaternary level)**

The discussion on the role of spherulites on impact behavior is usually restricted to the influence of inter-spherulitic boundaries. During spherulitic crystallization, there is a tendency for low molecular weight and other less crystallizable entities to be rejected from the body of the spherulites [75]. As a result, the boundaries between adjacent spherulites contain a higher concentration of non-crystallizable material composed of low(er) molecular weight chains, atactic (parts of) chains, and possible impurities. This segregation often results in mechanical weakness in these regions of the polymer. This may change mechanical properties like yield stress and toughness [58,75-77]. It is expected, however, that below a certain spherulite size the influence of boundaries weakening can be neglected and other factors become important [76]. Inter-spherulitic adhesion is improved by increasing the MM [75].

Another aspect of the role that spherulites play in impact is the internal arrangement of lamellae. As discussed in section 2.2.4, iPP shows two distinctly different types of spherulites consisting of the  $\alpha$ -phase (possibly accompanied with the  $\gamma$ -phase) and  $\beta$ -phase. Spherulites consisting of the  $\alpha$ -phase show, depending on the crystallization temperature, crosshatches, while these are absent in the  $\beta$ -phase. The crosshatched structure exhibits an inherently lower ductility than spherulites without crosshatches [64].

### **Role of process induced structures in deformation (quaternary level)**

The mechanical properties of samples with process induced structures depend, in general on the processing parameters and molding techniques used to produce them. As briefly discussed in section 2.2.4 the processing induced structure in injection molded is a typical skin-core morphology. The preferred crystallite orientation introduces anisotropy and accordingly the skin and intermediate layers exert profound effects on the mechanical properties [39,78]. It was found that mechanical properties, like tensile impact strength, yield strength, and E-modulus, increased in the direction of orientation [79].

## **2.5 Experimental methods**

### **2.5.1 Wide angle x-ray scattering (WAXS)**

Wide angle x-ray scattering (WAXS) experiments can be used to qualify and quantify the crystal phases present in isotactic polypropylene. Moreover, with WAXS it is possible to obtain information about the unit cell orientation in the material.

The use of x-ray in materials science is well known. From wide-angle x-ray scattering (WAXS) and small-angle x-ray scattering a wide variety of morphological



characteristics for structural features with different sizes can be elucidated. In a x-ray experiment a monochromatic x-ray beam (with a wavelength  $\lambda$ ) is scattered (diffracted) by the material at a specific angle  $\theta$  [80], due to the presence of regular (crystal) planes in the material separated a distance ( $d$ ). The scattering angle ( $2\theta$ ) is related to the inter-planar distance ( $d$ ) by the Bragg equation (see also (2.10)),

$$2d = \frac{n\lambda}{\sin\theta}, \quad (2.10)$$

where  $n$  is an integer. The equation indicates a reciprocal relationship between the characteristic length  $d$  and  $\sin\theta$ .

### WAXS and polymorphism

Inter planar distances ( $d$ ) for crystal facets measured with WAXS are in the order of unit cell dimensions. The unit cell is described by the axes  $a$ ,  $b$ ,  $c$ , and the angles between them:  $\alpha$ ,  $\beta$ , and  $\gamma$  (see Figure 2.12). Within an assembly of unit-cells, repeating crystallographic planes are present, which are indexed as  $(hkl)$  (Miller indices).

$(hkl)_\alpha$	$(hkl)_\beta$	$(hkl)_\gamma$	$d$ (Å)	$2\theta$ ( $\lambda=1$ Å)
		(111)	6.39	8.98
(110)			6.26	9.16
		(113)	5.86	9.79
	<b>(300)</b>		5.50	10.43
(040)		(008)	5.24	10.95
<b>(130)</b>			4.78	12.01
		<b>(117)</b>	4.38	13.11
(111)	(311)	(202)	4.17	13.77
(13 $\bar{1}$ )/(041)		(026)	4.05	14.18
		(206)	3.63	15.83
(150)/(060)			3.51	16.38
		(00 12)	3.47	16.57
(200)			3.28	17.54

Table 2.1. Miller-indices and corresponding  $d$ -spacings of the three crystal modifications of isotactic-polypropylene [33,81]. Diffraction angles are given for  $\lambda = 1\text{Å}$  as this wavelength is used in the WAXS experiments. Characteristic reflections are indicated in bold.

For each type of unit cell, relationships are given between the  $d$ -spacing and the indexes  $h$ ,  $k$ , and  $l$ . Several crystallographic planes [80] of the crystal lattice give rise to peaks in a WAXS spectrum. Figure 2.9 shows the WAXS spectra (intensity versus  $2\theta$ ) of the pure  $\alpha$ -,  $\beta$ -, and  $\gamma$ -phases, respectively. Table 2.1 gives the Miller indices of the main reflections [33,81].

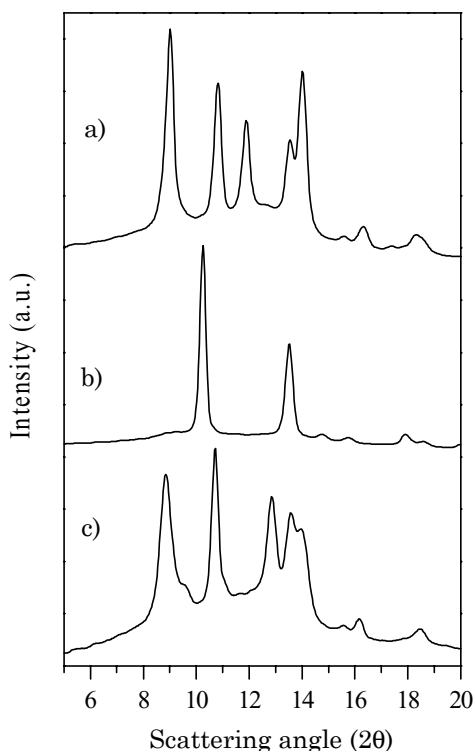


Figure 2.9. WAXS-patterns of pure  $\alpha$ -,  $\beta$ - and  $\gamma$ -phase, indicated by a, b, and c, respectively.

### WAXS and crystallinity

Non-oriented semi-crystalline polymers can be ideally represented by a two-phase model of alternating parallel and flat crystalline (lamellae) and amorphous layers arranged in stacks. In the case that the scattering from the crystalline and amorphous phases can be separated [82], the mass crystallinity ( $\omega_m$ ) can be estimated from the integrated crystalline scattering ( $I_c$ ) divided by the total coherent scattering ( $I_{tot}$ ), i.e. crystalline plus amorphous scattering ( $I_a$ ):

$$\omega_m = \frac{I_c}{I_{tot}} = \frac{I_c}{I_c + KI_a}, \quad (2.11)$$

where  $K$  is a calibration factor. The calibration factor can be set to unity for

comparative purposes [83]. However, for absolute measurements the  $K$  factor can be determined by e.g. the Ruland method [84] or density measurements [80].

The volume crystallinity can be calculated by using the following equation:

$$\omega_c = \frac{\rho_a \omega_m}{\rho_c (\omega_m + 1) - \rho_a \omega_m}, \quad (2.12)$$

where  $\rho_c$  and  $\rho_a$  are the density of the pure crystalline- and pure amorphous-phase of the material, respectively. Profile fitting can be used to determine the crystallinity. The crystalline peaks can be fitted with a Lorentzian function after subtracting the background, taken as a straight line. The background is the incoherent scattering and other mainly not crystallinity-dependent, coherent scattering contributions [29]. The amorphous scattering can be approximated by a Lorentzian function as well. The application of this two-phase model has limitations [84]. The crystalline regions are not ideally perfect and their imperfections contribute to the non-crystalline scattering as well as reducing the intensity scattered from crystalline regions at higher angles. Moreover, the interfacial layers i.e. the rigid-amorphous or the amorphous-crystalline layers are not taken into account [85].

### WAXS and pole figures

The preferred orientation of selected crystallographic planes in a sample may be revealed by pole-figures. A pole is the point of intersection of the normal to a crystal plane with the surface of a sphere having the crystal at its center (see Figure 2.10).

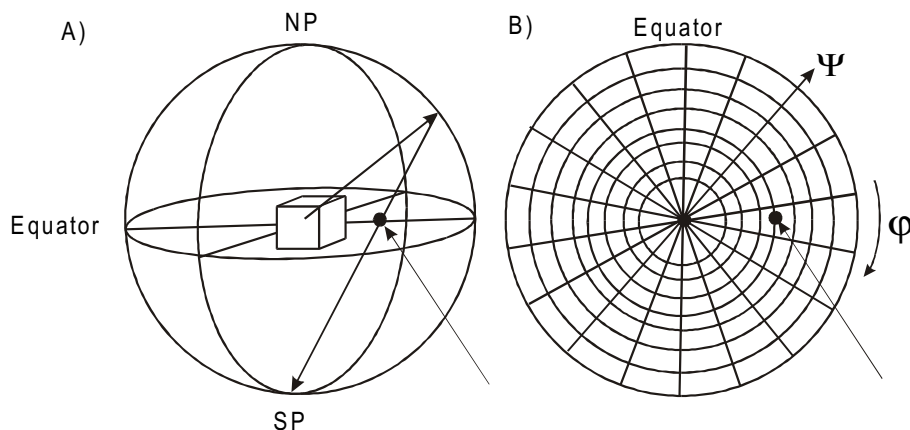


Figure 2.10. A) Derivation of the stereographic projection from the spherical projection. B) Pole stereographic net with a point corresponding to a point in the figure left (both points are indicated with an arrow). Angles in B) are the same as the angles seen in Figure 2.11. NP and SP label the north pole and south pole, respectively.

Pole figures are stereographic projections showing the density of poles of certain crystallographic planes as a function of orientation [83]. It is customary to plot the spherical polar-map by means of planar, stereographic projections. The stereographic projection can be obtained from the northern hemisphere of a spherical polar map by drawing straight lines from the various (hkl)-poles to the south pole of the sphere. The stereographic projection then is composed of the points of intersection of these lines with the equatorial plane of the sphere [80]. Figure 2.10, gives a schematic representation of the method of projection.

Experimentally, pole figures are constructed by positioning the x-ray detector at a fixed angle  $\theta$ , see Figure 2.11, that corresponds to a chosen diffraction plane (for example (110)-plane). The specimen is rotated about two perpendicular axes to permit the measurement of the intensities diffracted by this selected plane oriented at various angles within the specimen. The rotations around the two axes are denoted by the two angles  $\Psi$  and  $\phi$ , see Figure 2.11, corresponding to the angles on the pole-figure.

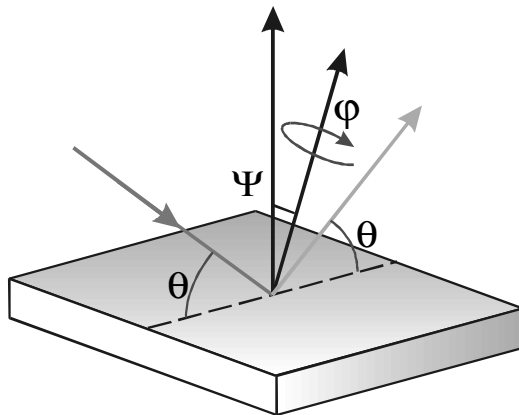


Figure 2.11. Measurement geometry in a WAXS experiment used to construct pole-figures. Indicated angles are explained in the text.

Several different types of orientation modes can be defined (in addition to the isotropic mode) [80,86]. The orientation modes are specified by describing the orientation of (see Figure 2.12A and B): a crystallographic axis with respect to a reference plane (planar) (2); a plane with respect to a plane (uniplanar) (3); an axis with respect to an axis (axial) (4); a plane with respect to an axis (plan-axial) (5); and a combination of (3) and (4) (uniplanar-axial).

The aforementioned orientation modes can be represented by idealized pole figures (see Figure 2.13). Measured pole figures can be compared with these idealized pole figures in order to facilitate the analysis of the orientation in a material. More complex, as well as mixed, orientation modes can be observed, but they can usually be characterized as combinations of the basic modes.

In the construction of the pole figures a crystal symmetry as indicated in Figure 2.12A (with  $\alpha = \beta = 90^\circ \neq \gamma$ ) is supposed. The reference axes in the sample, (M, T, and N) designate respectively the machine, transfer, and normal directions, respectively (Figure 2.12B). For more details, we refer to the publication of Heffelfinger and Burton [86].

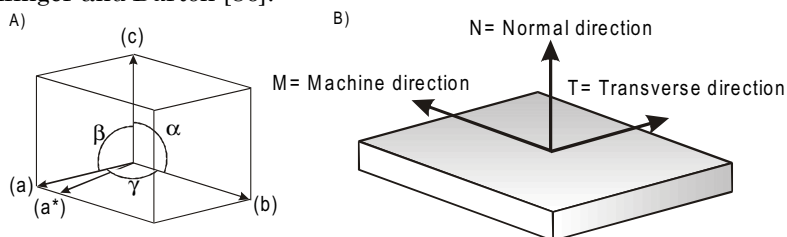


Figure 2.12. A) Crystal axes in a unit cell, B) Axes of reference.

	Orientation mode	Geometry	Reference element	Representative pole figures with indicated Miller indices.
1	Random	None	None	
2	Planar	A crystal axis (c) lying in a reference plane (MT)	Plane MT	
3	Uniplanar	A crystal plane (010) parallel to a reference plane (MT)	Plane MT	
4	Axial	A crystal axis (c) parallel to a reference axis (M)	Axis M	
5	Plan-axial	A crystal plane (010) parallel to a reference axis (M)	Axis M	
6	Uniplanar-axial	A given crystal axis (c) parallel to a reference axis (M) and a given plane (010) parallel to a reference plane (MT)	Axis M and plane MT	

Figure 2.13. Classification of orientation modes according to Heffelfinger and Burton [86].

### 2.5.2 Infrared dichroism

Infrared-dichroism (IR-D) measurements are suitable for the determination of the orientation of individual components or phases (crystalline or amorphous domains in semi-crystalline polymers or an average of the two domains), see Table 2.2. The method is based on the principle of selective absorption of polarized IR

radiation parallel and perpendicular to a certain reference direction (z-direction). The dichroic ratio ( $D$ ) is defined as:

$$D = \frac{A_{\parallel}}{A_{\perp}}, \quad (2.13)$$

where  $A_{\parallel}$  and  $A_{\perp}$  are the absorbances of the IR band under consideration when the electric field vectors are parallel and perpendicular to the reference direction.

The absorbance ( $A$ ) depends strongly on the angle ( $\varphi$ ) between the electric vector of the polarized IR-radiation ( $E$ ) and the transition dipole moment vector ( $\mu$ ) associated with an active IR-mode (e.g. stretching of c-c bond):

$$A \cong |E|^2 \cdot |\mu|^2 \cdot \cos^2 \varphi. \quad (2.14)$$

The transition dipole moment vector ( $\mu$ ) is oriented at an angle ( $\nu$ ) with regard to the chain direction ( $C$ ). The following figure shows the position of the vectors  $\mu$ ,  $E$ , and  $C$  with respect to the reference direction (z-axis).

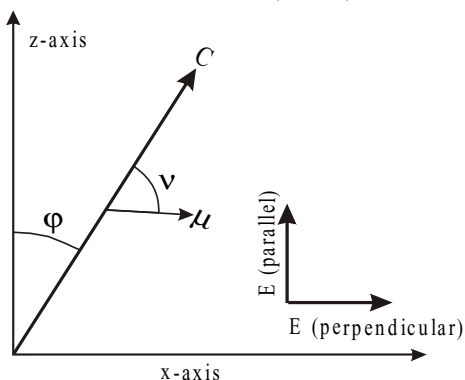


Figure 2.14. A schematic representation of a chain containing a group whose transition moment  $\mu$  makes an angle  $\nu$  with respect to the chain direction  $C$ . The chain itself makes an angle  $\varphi$  with respect to the reference z-axis. The two measurement directions are given by the electric vector of the polarized IR-direction ( $E_{\text{parallel}}$  and  $E_{\text{perpendicular}}$ ).

Several IR-bands exist that can be used for the determination of orientation. The following table summarizes the properties of the four IR-bands used:

Nr.	Wave Number (cm <sup>-1</sup> )	Type	Transition moment angles (°)
1	1045	Average	0
2	898	⊥ Average	34.7
3	841	Crystalline	0
4	809	⊥ Average	17.8

Table 2.2. Characteristics of the IR-bands used in this chapter. The symbols || and ⊥ denote parallel and orthogonal infrared bands, respectively. This table is taken from reference [87].

### 2.5.3 Polarized light microscopy

Polarized light microscopy is a versatile and relatively simple method to study the super molecular structure of semi-crystalline polymers. In a typical microscopy set-up, the sample is placed between two crossed polarizers and white light is transmitted. Polarized microscopy is usually used to measure birefringence. The birefringence ( $\Delta n$ ) is defined as:

$$\Delta n = n_1 - n_2,$$

where  $n_1$ ,  $n_2$  are the refractive indices parallel and perpendicular to the slow direction of the first-order red filter, respectively [6]. A first-order red filter, which is placed diagonally between the two crossed polarizers, can define the sign of birefringence [6]. In polymeric materials several different types of birefringence can be distinguished, e.g. orientation birefringence, strain birefringence, and form birefringence. A spherulite can be considered as an optically birefringent object with two refractive indices: the radial ( $n_r = n_1$ ) and the tangential ( $n_t = n_2$ ). In case of a 'positive' spherulite,  $n_r$  is larger than  $n_t$  and for 'negative' spherulites  $n_t > n_r$ . The classification of the different types of spherulites in isotactic polypropylene is based on the birefringence.

## 2.6 References

- (1) Paukkeri, R.; Vaananen, T.; Lehtinen, A. Microstructural analysis of polypropylenes produced with heterogeneous Ziegler-Natta catalysts. *Polymer* **1993**, *34*, 2488.
- (2) Odian, G. *Principles of Polymerization*; 3rd ed.; John Wiley & Sons, Inc.: New York, 1991.
- (3) Randall, J. C. Carbon-13 nuclear magnetic resonance quantitative measurements of average sequence lengths of like stereochemical additions in polypropylene and polystyrene. *J. Polym. Sci.* **1976**, *14*, 2083.
- (4) Randall, J. C. A review of high-resolution liquid C-13 nuclear magnetic resonance characterizations of ethylene based polymers. *J. Macromol. Sci.-Rev. Macromol. Chem. Phys.* **1989**, *C29*, 201.
- (5) Bovey, F. A.; Mireau, P. A.; Blümich, B. NMR of polymers. *Angew. Chem.* **1997**, *109*, 2637.
- (6) Varga, J. Supermolecular structure of isotactic polypropylene. *J. Mat. Sci.* **1992**, *27*, 2557.
- (7) Cowie, J. M. G. *Polymers: Chemistry & Physics of Modern Materials*; 2nd ed.; Chapman & Hall: New York, 1991.

- (8) De Rosa, C.; Auriemma, F.; Circelli, T.; Waymouth, R. M. Crystallization of the alpha and gamma forms of isotactic polypropylene as a tool to test the degree of segregation of defects in the polymer chains. *Macromolecules* **2002**, *35*, 3622.
- (9) Lotz, B.; Wittmann, J. C. Structure and morphology of polypropylenes: A molecular analysis. *Polymer* **1996**, *37*, 4979.
- (10) Awaya, H. Morphology of different types of isotactic polypropylene spherulites crystallized from the melt. *Polymer* **1988**, *26*, 591.
- (11) Auriemma, F.; de Ballesteros, O. R.; De Rosa, C.; Corradini, P. Structural disorder in the alpha form of isotactic polypropylene. *Macromolecules* **2000**, *33*, 8764.
- (12) Marand, H.; Xu, J.; Srinivas, S. Determination of the equilibrium melting temperature of polymer crystals: linear and non-linear Hoffman-Weeks extrapolations. *Macromolecules* **1998**, *31*, 8219.
- (13) Xu, J.; Srinivas, S.; Marand, H. Equilibrium melting temperature and undercooling dependence of the spherulitic growth rate of isotactic polypropylene. *Macromolecules* **1998**, *31*, 8230.
- (14) Juhász, P.; Varga, J.; Belina, K.; Marand, H. Determination of the equilibrium melting point of the beta-form of polypropylene. *J. Therm. Anal. Calorim.* **2002**, *69*, 561.
- (15) Vleeshouwers, S. Simultaneous in-situ WAXS/SAXS and DSC study of the recrystallization and melting behaviour of the alpha and beta form of iPP. *Polymer* **1997**, *38*, 3213.
- (16) Trifonova, D.; Varga, J.; Vancso, G. J. AFM study of lamellar thickness distributions in high temperature melt-crystallization of beta-polypropylene. *Polym. Bull.* **1998**, *41*, 341.
- (17) Perez, E.; zucchi, D.; Sacchi, M. C.; Forlini, F.; Bello, A. Obtaining the gamma-phase in isotactic polypropylene: Effect of catalyst system and crystallization conditions. *Polymer* **1999**, *40*, 675.
- (18) Lovinger, A. J. Microstructure and unit-cell orientation in alpha-propylene. *J. Polym. Phys.* **1983**, *21*, 97.
- (19) Mezghani, K.; Phillips, P. J. The gamma-phase of high molecular weight isotactic polypropylene. II: The morphology of the gamma-form crystallized at 200 MPa. *Polymer* **1997**, *38*, 5725.
- (20) Campbell, R. A.; Philips, P. J. The gamma phase of high-molecular-weight polypropylene: 1. Morphological aspects. *Polymer* **1993**, *34*, 4809.
- (21) Mezghani, K.; Philips, P. J. The gamma-phase of high molecular weight isotactic polypropylene: III. The equilibrium melting point and the phase diagram. *Polymer* **1998**, *39*, 3735.
- (22) Suhm, J. New molecular and super molecular polymer architectures via transition metal catalysed alkene polymerization. *J. Mater. Chem.* **1998**, *8*, 553.



- (23) Thomann, R.; Wang, C.; Kressler, J.; Mulhaupt, R. On the gamma-phase of isotactic polypropylene. *Macromolecules* **1996**, *29*, 8425.
- (24) Lotz, B.; Graff, S.; Straupé, C.; Wittmann, J. C. Single crystals of gamma phase isotactic polypropylene: Combined diffraction and morphological support for a structure with non-parallel chains. *Polymer* **1991**, *32*, 2903.
- (25) Caldas, V.; Brown, G. R. The structure of the mesomorphic phase of quenched isotactic polypropylene. *Polymer* **1994**, *35*, 899.
- (26) Moore, E. P. *Polypropylene Handbook*; Hauser Publishers: Munich, 1996.
- (27) Zhou, H.; Wilkes, G. L. Comparison of the lamellar thickness and its distribution determined from DSC, SAXS, TEM and AFM for high-density polyethylene films having a stacked lamellar morphology. *Polymer* **1997**, *38*, 5735.
- (28) Nitta, K.-H.; Tekayanagi, M. Tensile yield of isotactic polypropylene in terms of a lamellar-cluster model. *J. Polym. Sci.: Polym. Phys. Ed.* **2000**, *38*, 1037.
- (29) Wunderlich, B. *Macromolecular Physics*; Academic Press: New York, 1973; Vol. 1.
- (30) Bassett, D. C. Polymer morphology: Pure and applied. *J. Macromol. Sci.-Phys.* **1996**, *B35*, 277.
- (31) Yan, S.; Katzenberg, F.; Petermann, J.; Yang, D.; Shen, Y.; Straupe, C.; Wittmann, J. C.; Lotz, B. A novel epitaxy of isotactic polypropylene (alpha phase) on PTFE and organic substrates. *Polymer* **2000**, *41*, 2613.
- (32) Radhakrishnan, J.; Ichikawa, K.; Yamada, K. Nearly pure alpha2 form crystals obtained by melt crystallization of high tacticity isotactic polypropylene. *Polymer* **1998**, *39*, 2995.
- (33) Lotz, B.; Graff, S.; Wittmann, J. C. Crystal morphology of the gamma (triclinic) phase of isotactic polypropylene and its relation to the alpha-phase. *J. Polym. Sci.: Polym. Phys. Ed.* **1986**, *24*, 2017.
- (34) Thomann, R.; Wang, C.; Kressler, J.; Mulhaupt, R. On the gamma-phase of isotactic polypropylene. *Macromolecules* **1996**, *29*, 8425.
- (35) Woodward, A. E. *Understanding Polymer Morphology*; Hanser Publishers: Munich, 1995.
- (36) Trotignon, J. P.; Lebrun, J. L.; Verdu, J. Crystalline polymorphism and orientation in injection-moulded polypropylene. *Plast. Rubber Comp.* **1982**, *2*, 247.
- (37) Mencik, Z.; Fitchmun, D. R. Texture of injection-molded polypropylene. *J. Polym. Sci.* **1973**, *11*, 973.
- (38) Karger-Kocsis, J. Skin-core morphology and failure of injection-molded specimen of impact polypropylene blends. *Polym. Eng. Sci.* **1987**, *27*, 241.
- (39) Kantz, M. R.; Newman, H. D.; Stigale, F. H. The skin-core morphology and structure-property relationships in injection-molded polypropylene. *J. Appl. Polym. Sci.* **1972**, *16*, 1249.

- (40) Fujiyama, M.; Wakino, T. Structure of the skin layer in injection-molded polypropylene. *J. Polym. Sci., Polym. Phys. Ed.* **1988**, *35*, 29.
- (41) Kalay, G.; Bevis, M. J. Processing and physical property relationships in injection-molded isotactic polypropylene: 2. Morphology and crystallinity. *J. Polym. Sci.* **1997**, *35*, 265.
- (42) Varga, J. Crystallization, Melting and Supermolecular Structure of Isotactic Polypropylene; Karger-Kocsis, J., Ed.; Chapman & Hall: London, 1995; Vol. 1.
- (43) Strobl, G. R.; Schneider, M. Direct evaluation of the electron density correlation function of partially crystalline polymers. *J. Polym. Sci., Polym. Phys. Ed.* **1980**, *18*, 1343.
- (44) Padden, F. J. J.; Keith, H. D. Spherulitic crystallization in polypropylene. *J. Applied Phys.* **1959**, *30*, 1479.
- (45) Lotz, B. Alpha and beta phases of isotactic polypropylene: A case of growth kinetics 'phase reentry' in polymer crystallization. *Polymer* **1998**, *39*, 4561.
- (46) Plati, E.; Williams, J. G. Determination of the fracture parameters for polymer impact. *Polym. Eng. Sci.* **1975**, *15*, 470.
- (47) McClintock, F. A.; Irwin, G. R. Plasticity aspects of fracture mechanics. *ASTM STP* **1965**, *381*, 84.
- (48) Pukánszky, B.; Mudra, I.; Staniek, P. Relation of crystalline structure and mechanical properties of nucleated polypropylene. *J. Vinyl Addit. Techn.* **1997**, *3*, 53.
- (49) McCrum, N. G.; Buckley, C. P.; Bucknall, C. B. *Principles of Polymer Engineering*; Oxford University Press Inc.: New York, 1994.
- (50) Hertzberg, R. W.; Manson, J. A. *Fracture and Fatigue*; 2 ed.; Kroschwitz, J. I., Mark, H. F., Bikales, N. M., Overberger, C. G. and Menges, G., Ed.; John Wiley & Sons, Ltd: New York, 1986; Vol. 7, pp 328.
- (51) Bartczak, Z.; Argon, A. S.; Cohen, R. E.; Weinberg, M. Toughness mechanisms in semi-crystalline polymer blends: II. High-density polyethylene toughened with calcium carbonate filler particles. *Polymer* **1999**, *40*, 2347.
- (52) Brooks, N. W. J.; Mukhtar, M. Temperature and stem length dependence of the yield stress of polyethylene. *Polymer* **2000**, *41*, 1475.
- (53) Arruda, E. M.; Ahzi, S.; Li, Y.; Ganesan, A. Rate dependent deformation of semi-crystalline polypropylene near room temperature. *J. Eng. Mater. Technol.-Trans. ASME* **1997**, *119*, 216.
- (54) Brooks, N. W.; Duckett, R. A.; Ward, I. M. Temperature and strain-rate dependence of the yield stress of polyethylene. *J. Polym. Sci., Polym. Phys. Ed.* **1998**, *36*, 2177.
- (55) Kausch, H. H.; Hassell, J. A.; Jaffee, R. I. *Deformation and Fracture of High Polymers*; Plenum Press: New York, 1973.

- (56) Wal, A. v. d.; Mulder, J. J.; Thijs, H. A.; Gaymans, R. J. Fracture of polypropylene: 1. The effect of molecular weight and temperature at low and high test speeds. *Polymer* **1998**, *39*, 5467.
- (57) ASTM-standard Standard test methods for impact resistance of plastics and electrical insulating materials. *ASTM Committee on Standards* **1992**, *ASTM; D256-90b*.
- (58) Kinloch, A. J.; Young, R. J. *Fracture Behavior of Polymers*; Elsevier Applied Science Publishers: New York, 1983.
- (59) Nitta, K.-H.; Takayanagi, M. Role of tie molecules in the yielding deformation of isotactic polypropylene. *J. Polym. Phys: Part B: Polym. Phys.* **1999**, *37*, 357.
- (60) Wal, A. v. d.; Mulder, J. J.; Gaymans, R. J. Fracture of polypropylene: 2. The effect of crystallinity. *Polymer* **1998**, *39*, 5477.
- (61) Narisawa, I.; Ishikawa, M. Crazing and shear deformation of polymer alloys. *Macromol. Chem-M. Symp.* **1991**, *41*, 87-107.
- (62) Patel, R. M.; Sehanobish, K.; Knight, G. W. Theoretical prediction of tie-chain concentration and its characterization using post-yield response. *J. Appl. Polym. Sci.* **1996**, *60*, 749.
- (63) Isai, J. R.; Graham, J. A.; Mandelkern, L.; Alamo, R. G. Some aspects of the crystallization of ethylene copolymers. *Polymer* **2000**, *41*, 8813.
- (64) Karger-Kocsis, J.; Varga, J. Effects of beta-alfa transformation on the static and dynamic tensile behaviour of isotactic polypropylene. *J. Appl. Polym. Sci.* **1996**, *62*, 291.
- (65) Li, J. X.; Cheung, W. L. On the deformation mechanisms of beta-polypropylene I. Effect of necking on the beta-phase PP crystals. *Polymer* **1998**, *39*, 6935.
- (66) Karger-Kocsis, J. How does "phase transformation toughening" work in semi-crystalline polymers? *Polym. Eng. Sci.* **1996**, *36*, 203.
- (67) Bowden, P. B.; Young, R. J. Deformation mechanisms in crystalline polymers. *J. Mat. Sci.* **1974**, *9*, 2034.
- (68) Li, J. X.; Cheung, W. L.; Chan, C. M. On the deformation mechanisms of beta-polypropylene 3. Lamella structures after necking and cold drawing. *Polymer* **1999**, *40*, 3641.
- (69) Peterson, J. M. Thermal initiation of screw dislocations in polymer crystal platelets. *J. Appl. Phys.* **1966**, *37*, 4047.
- (70) Young, R. J. A dislocation theory for yield in polyethylene. *Philos. Mag.* **1974**, *30*, 85.
- (71) Peterlin, A. Molecular model of drawing polyethylene and polypropylene. *J. Mater. Sci.* **1971**, *6*, 490.
- (72) Seguela, R.; Staniek, E.; Escaig, B.; Fillon, B. Plastic deformation of polypropylene in relation to crystalline structure. *J. Appl. Polym. Sci.* **1999**, *71*, 1873.

- (73) Crist, B. *Plastic Deformation of Polymers*; Thomas, E. L., Ed.; VCH: Weinheim, 1993; Vol. 12, pp 428.
- (74) Kennedy, M. A.; Peacock, A. J.; Mandelkern, L. Tensile properties of crystalline polymers - linear polyethylene. *Macromolecules* **1994**, *27*, 5297.
- (75) Lustiger, A.; Marzinsky, C. N.; Mueller, R. R. Spherulite boundary strengthening concept for toughening polypropylene. *J. Polm. Sci., Polm. Phys.* **1998**, *36*, 2047.
- (76) Ouederni, M.; Phillips, P. J. Influence of morphology on the fracture toughness of isotactic polypropylene. *J. Polym. Sci.: Polym. Phys. Ed.* **1995**, *33*, 1313.
- (77) Way, J. L.; Atkinson, J. R.; Nutting, J. The effect of spherulite size on the fracture morphology of polypropylene. *J. Mat. Sci.* **1974**, *9*, 293.
- (78) Kalay, G.; Bevis, M. J. Processing and physical property relationships in injection-molded isotactic polypropylene: 1. Mechanical properties. *J. Polm. Sci.* **1997**, *35*, 241.
- (79) Fujiyama, M.; Awaya, H. Mechanical anisotropy in injection-molded polypropylene. *J. Polym. Sci., Polym. Phys. Ed.* **1977**, *21*, 3291.
- (80) Alexander, L. E. *X-ray Diffraction Methods in Polymer Science*; John Wiley & Sons, Inc.: New York, 1969.
- (81) Turner-Jones, A.; Aizlewood, J. M.; Beckett, D. R. Crystalline forms of isotactic polypropylene. *Makrom. Chem.* **1964**, *75*, 134.
- (82) Hindeleh, A. H.; Johnson, D. J. Crystallinity and crystallite size measurement in polyamide and polyester fibres. *Polymer* **1978**, *19*, 27.
- (83) Kakudo, M.; Kasai, N. *X-ray Diffraction by Polymers*; Elsevier: Amsterdam, 1972.
- (84) Ruland, W. X-ray determination of crystallinity and diffuse disorder scattering. *Acta Cryst.* **1961**, *14*, 1180.
- (85) O'Kane, W. J.; Young, R. j.; Ryan, A. J. Simultaneous SAXS/WAXS and DSC analysis of the melting and recrystallization behaviour of quenched polypropylene. *Polymer* **1994**, *35*, 1352.
- (86) Heffelfinger, C. J.; Burton, R. L. X-Ray determination of the crystallite orientation distributions of polyethylene terephthalate films. *J. Polym. Sci.* **1960**, *47*, 289.
- (87) Bruce, G. D.; Weatherly, G. C.; Vancso, G. J. Solid-state orientation studies on polypropylene disks, 1. *Angew. Makromol. Chem.* **1993**, *205*, 161.



# Chapter 3

## The influence of chain architecture on the crystallization of isotactic polypropylene

The crystallization characteristics and morphology of isotactic polypropylene concerning the  $\alpha$ -,  $\beta$ -, and  $\gamma$ -phases were studied for well-defined and fully characterized polymers samples with varying amounts of stereo- and regio-defects. The set of samples enabled us to study separately the influence of the type of defect on the parameters of interest. A combined defect fraction (CDF) was introduced to describe arbitrary iPP samples with a varying amount of stereo- and regio-defects and a combination thereof. Small-angle and wide-angle x-ray scattering (SAXS/WAXS), supplemented with differential scanning calorimetry (DSC), were used to characterize the morphology after isothermal crystallization. The percentage of the  $\gamma$ -phase was strongly enhanced in the samples exhibiting regio-defects, reaching almost 100% for the samples with highest amounts of defects. The long period, as well as the lamellar-thickness, were found to be larger for the  $\beta$ -phase as compared with the  $\alpha$ -phase. Moreover the long-period of the  $\beta$ -phase increased with increasing amount of defects. The determination of the long-period of the  $\alpha$ -phase and the estimation of the lamellar thickness, was impeded by the occurrence of  $\gamma$ -phase crystals and cross-hatched lamellae, respectively.

Crystal growth rates as measured by polarized light microscopy (LM) were found to decrease linearly with the defect fraction and is much stronger influenced by regio-defects as compared with stereo-defects. We found that the deceleration of the growth rate of the  $\beta$ -phase is higher compared to the  $\alpha$ -phase with increasing defect fraction. We also found a critical defect fraction ( $X_{\text{crit}}$ ) for which the growth rates of the  $\alpha$ - and  $\beta$ -phase are equal. The value of  $X_{\text{crit}}$  was found to be depended on temperature. For samples with this specific critical defect fraction the upper recrystallization temperature is lowered to 130°C. Shear induced crystallization of

the samples was studied and compared with quiescent crystallization. The growth rates of the shear induced cylindrites followed the spherulitic growth rates. It was evidenced that due to the lowering of the upper recrystallization temperature no  $\beta$ -cylindrites could be formed above the critical defect concentration ( $X_{crit}$ ).

Analysis of the crystallization was done with the model of Sanchez and Eby. Results of the analysis were found to be in good agreement with the results found for the samples with a variation in the number of stereo-defects, however a less satisfactory agreement was found in case of regio-defects. From the analysis it followed that regio-defects are more difficult to incorporate in the crystalline regions than stereo-defects. The excess free energy for incorporating a stereo-defect into the trigonal crystal lattice of  $\beta$ -phase is lower as compared with the  $\alpha$ -phase, which results in a higher defect partitioning coefficient for the  $\beta$ -phase. The results of the analysis showed that the bulk free energy for the complete defect-free (homo) polymer is the main factor which determines the difference in growth rate dependence on the defect fraction for the  $\alpha$ - and  $\beta$ -phase, respectively. The theory rightly predicts the earlier mentioned critical defect fraction for which the growth rate of the  $\alpha$ - and  $\beta$ -phase is equal.

---

## 3.1 Introduction

The various forms of the crystalline morphology of polymers can be directly derived from the mechanisms and kinetics of crystallization, which -in turn- depend on the primary chemical structure and chain topology of macromolecules [1]. Therefore, it is of great importance to understand the influence of the primary structure on the different aspects of crystallization and on the resulting morphology.

Modifications in the morphology due to incorporation of defects in the chain take place on the secondary and higher levels of the morphological hierarchy, i.e. on the lamellar level and spherulitic level [2,3]. Several studies addressed the effects of chain architecture on the various levels of the morphology and crystallization behavior of iPPs [2-5]. Yet as the availability of PP macromolecules with well-defined primary structure has been limited, no definite conclusions have been reached.

In isotactic polypropylene, which exhibits polymorphism, the relative amounts of the different crystal phases ( $\alpha$ ,  $\beta$ , and  $\gamma$ ) may change as function of chain regularity. Especially in metallocene catalyzed polymers, an enhancement in the formation of the  $\gamma$ -phase can be seen [4,6]. This was ascribed to a decrease in crystallizable sequence length as a consequence of an increase in the fraction stereo- and regio-defects [7], or morphological effects which render the chain-folding in lamellae more difficult [8].

Upon increasing irregularity of the chain usually an increase in unit-cell dimensions is detected, which indicates a less regular packing of the macromolecules in the crystal lattice due to incorporation of defects [2]. Chain regularity also influences the relative amounts of 'up' and 'down' helices in the  $\alpha$ -phase of iPP. A continuous change from the limiting ordered ( $\alpha_2$ ) modification to the limiting disordered ( $\alpha_1$ ) modification was found [3,9].

With increasing defect fraction, the lamellar thickness and lamellar lateral size are decreasing [2], for the same degree of undercooling. Together with a decrease in the lamellar size, the crystallinity also decreases with decreasing isotacticity [2,10].

Morphology changes on the spherulitic level for iPP involve variations in the crosshatched structure of the  $\alpha$ -phase and the frequency of branching in the  $\beta$ -phase. The radial lamellar fraction in  $\alpha$ -spherulites, estimated from refractive indices, increases with an increase in isotacticity [5,9]. Naturally, changes in the morphology on the spherulitic level take place due to variations in the relative amounts of the  $\beta$ - and  $\gamma$ -phases compared to the commonly existing  $\alpha$ -phase.



The influence of chain architecture on the crystallization behavior of the  $\beta$ -phase was not extensively studied, i.e. certainly not at the extent as it has been as was done for the  $\alpha$ -phase. We are particular interested in the  $\beta$ -phase as this structure has better impact properties than that typical for the  $\alpha$ -phase [11,12]. Thus the influence of one deficiency, i.e. mediocre toughness, at PP, can in principle be improved by increasing the amount of the  $\beta$ -polymorph.

Varga, *et al.* found that the formation of the  $\beta$ -phase was strongly inhibited in co-polymers of propylene and ethylene [13]. Growth rates of the  $\beta$ -phase in co-polymers of propylene and ethylene were found to be lower for all temperatures studied [14] as compared to pure homopolymers. In these studies selective nucleating agents were used to induce the nucleation of the  $\beta$ -phase. Formation of the  $\beta$ -phase can also be enhanced by shearing the melt prior to crystallization. Shear stress generated for example by pulling a fiber through an under-cooled melt produces row nuclei of  $\alpha$ -phase, inducing the growth of a cylindrical growth front consisting of the  $\beta$ -phase. Many studies [15-20] were dealing with parameters that influence the formation of such  $\beta$ -cylindrites, like the temperature of pulling ( $T_{\text{pull}}$ ), crystallization temperature ( $T_c$ ), time of pulling ( $t_{\text{pull}}$ ), speed of fiber pull ( $v_{\text{pull}}$ ), etc. The conclusion from these studies was that samples rich in  $\beta$ -phase are formed when  $T_{\alpha\beta} < T_c \leq T_{\text{pull}} < T_{\beta\alpha}$ , where  $T_{\alpha\beta}$  and  $T_{\beta\alpha}$  are the lower and upper (recrystallization) critical temperatures for the formation of the  $\beta$ -phase, respectively. As described in reference [21], a lowering of the upper critical temperature ( $T_{\beta\alpha}$ ) due to the presence of chain defects is predicted. In this study we will investigate the influence of chain defects on  $T_{\beta\alpha}$  and on the formation of  $\beta$ -cylindrites.

In order to perform rigorous analyses of (chain) structure-property relationships, well defined and well characterized samples are needed. Most of the aforementioned studies lack a complete characterization of the chain microstructure of the polymer specimen used and the studies are usually restricted to the mentioning of the percentage *m*-pentads ( $\%[mmmm]$ ). Moreover, in most cases the polymers used were polypropylenes produced with Ziegler-Natta catalysts. As polymers obtained by Ziegler-Natta stereospecific polymerizations exhibit heterogeneous chemical and stereo-chemical distributions within one batch and within a single polymer chain, these macromolecules are not very well suitable for structure-property studies.

With the advent and widespread availability of isotactic polypropylenes obtained by metallocene polymerizations (m-iPPs) it is now possible to perform rigorous scientific studies aiming at the influence of the chain architecture on the polymer morphology. Metallocene catalysts are composed of essentially a single type of catalytically active centers, which produce uniform homo- and co-polymers. Structural uniformity in these polymers is far superior compared with Ziegler-

Natta catalyzed chains [6,22]. Possible defects are distributed homogeneously in the chain and all chains possess practically equal number and distribution of defects [22]. In addition to the conventional Ziegler-Natta catalyzed iPPs, which contain only stereo-defects, metallocene catalyzed iPPs contain also regio-defects. Furthermore, the length (molar mass) distribution of polymers obtained by metallocene catalysis is much narrower as compared with Ziegler-Natta catalyzed polymers.

In this study we collected a number of iPPs obtained by metallocene catalysis from different manufacturers, made by using various specific catalysts. The samples were fully characterized by  $C^{13}$  nuclear magnetic resonance ( $C^{13}$ -NMR). In this study two distinguishable groups of polymer samples will be used. The first group of polymer samples exhibits a variation in the number of regio-defects, however with a constant amount of stereo-defects. The second group of polymer samples possesses a varying amount of stereo-defects but virtually no regio-defects. Especially the latter group is interesting as these m-iPPs without regio-defects are not widely available. This collection of polymers provides us with the possibility to investigate independently the influence of regio- and stereo-defects on the crystallization behavior and morphology of polypropylene. Such comprehensive and comparative studies, to our knowledge, have not been presented.

The present chapter discusses the crystallization behavior of the  $\alpha$ -,  $\beta$ -, and  $\gamma$ -phases and the variation in the morphology as function of stereo- and regio-defects in the polymer chain. An elaborate description of the samples used is given. Morphology is studied by synchrotron small- and wide angle x-ray scattering complemented by atomic force microscopy and polarized light microscopy. Spherulitic growth rates are measured for the different polymorphs of iPP by a combined use of light microscopy and hot-stage. We investigate systematically the separate influence of the amount and type of defects on the nucleation and crystallization behavior of the  $\beta$ -phase using a highly selective nucleating agent and the fiber-pull technique. A discussion about the structural origin of the growth rate difference between the  $\alpha$ - and  $\beta$ -phase as function of defect fraction is provided. Results obtained from the crystallization experiments are evaluated and compared with results from literature.

## 3.2 Experimental

### 3.2.1 Samples

A collection of samples including one Ziegler-Natta catalyzed polymer (ZN), 15 different metallocene-catalyzed polymers (Mx), and 5 blends (BLx) were used in this study. Table 3.1 gives the relevant characteristics of the individual polymers. The blends (BLx) were made by solution blending of M6 and ZN. Solutions of M6

and ZN in tetrachloroethene were prepared (10 wt%) at the solvent boiling point (121.1°C) and stabilized with 0.1 wt% 2,6-Di-tert.-butyl-4-methylphenol 99% antioxidant (Aldrich). The hot solutions were mixed in the desired ratios. After 10 min stirring, the polymer solution was quenched in ice-water, filtered over a glass-filter, and subsequently washed with ethanol. After drying for 48 hours in a vacuum oven the blends were ready for use.

In order to determine the tacticity of the samples,  $C^{13}$  nuclear magnetic resonance ( $C^{13}$ -NMR) measurements were performed. The samples were prepared and measured according to the procedure described in the literature [23,24]. Peak assignment was done by using the results described in reference [25]. An representative example of a  $C^{13}$ -NMR spectrum (M6) is given in Appendix 1. Number average and weight average molar masses ( $\bar{M}_n$  and  $\bar{M}_w$ ) and polydispersity index values ( $\bar{M}_w/\bar{M}_n$ ) were determined by using gel permeation chromatography (GPC) measurements using a Walters-GPC set-up equipped with a differential refractometer (Walter model 410) detection system. Narrow polystyrene standards were used for calibration. Prior to the measurements, samples were dissolved in trichlorobenzene (TCB) at 130°C and stabilized with 0.1wt% 2,6-di-tert.-butyl-4-methylphenol 99% (Aldrich) [24].

### 3.2.2 Morphology studies

Simultaneous small angle x-ray scattering (SAXS) and wide angle x-ray scattering (WAXS) measurements were performed on the beam-line ID2 at the European Synchrotron Radiation Facility (ESRF). In the SAXS experiments the sample to detector distance was 5 m and the wavelength of the x-ray radiation was 1Å ( $\lambda = 1\text{\AA}$ ). Air-scattering and detector response were subtracted from the two-dimensional (2D) diffraction pattern. Integration over the azimuthal angle yielded the one-dimensional (1D) plot of intensity (I) versus scattering vector ( $q$ ). Integrated SAXS-data was Lorentz corrected [26]. The values of  $d$ -spacings (also called long-periods, LP) could be directly determined from the scattering curve by reading the  $q$  and calculating the  $d$  (= LP) values by using the following equation (3.1):

$$LP = d = \frac{1}{q}, \quad (3.1)$$

where  $q = (2/\lambda)\sin(\theta)$ ,  $2\theta$  is the scattering angle and  $\lambda$  is the x-ray wavelength. Profile fitting of the WAXS patterns (within the range of scattering angles  $4^\circ < 2\theta < 30^\circ$ ) was used to determine the degree of (mass) crystallinity ( $\omega_m$ ). The crystalline peaks could be fitted with a Lorentzian function after subtracting the background, taken as a straight line. The background includes the incoherent scattering and other largely not crystallinity-dependent, coherent scattering contributions [27].

a) Molecular characteristics of samples with varying amounts of stereo defects.

Polymer Sample	$\overline{M}_n$ (*10 <sup>-4</sup> ) (g/mol)	$\overline{M}_w$ (*10 <sup>-4</sup> ) (g/mol)	$\overline{M}_w / \overline{M}_n$ (-)	Percentage [mmmm] (%)	Fraction regio defects (-)	Fraction stereo defects [r] (-)
<sup>1</sup> ZN/BL0	-	-	-	98.0	<0.0001	0.0020
<sup>2</sup> M1	1.80	3.80	2.11	83.1	<0.0001	0.1390
<sup>2</sup> M2	4.00	8.10	2.03	84.2	<0.0001	0.1460
<sup>2</sup> M3	9.90	20.0	2.02	97.6	<0.0001	0.0222
<sup>2</sup> M4	6.80	20.0	2.94	97.6	<0.0001	0.0223
<sup>2</sup> M5	2.90	8.30	2.86	97.4	<0.0001	0.0234

b) Molecular characteristics of samples with varying amounts of regio defects, and approximately constant amount of stereo defects.

Polymer Sample	$\overline{M}_n$ (*10 <sup>-4</sup> ) (g/mol)	$\overline{M}_w$ (*10 <sup>-4</sup> ) (g/mol)	$\overline{M}_w / \overline{M}_n$ (-)	Percentage [mmmm] (%)	Fraction regio defects (-)	Fraction stereo defects [r] (-)
<sup>3</sup> M6/BL100	-	15.0	-	98.5	0.0034	0.0200
<sup>3</sup> M7	-	-	-	98.0	0.0034	0.0200
<sup>2</sup> M8	28.0	83.0	2.96	97.3	0.0055	0.0010
<sup>2</sup> M9	7.50	26.0	3.47	97.3	0.0055	0.0010
<sup>2</sup> M10	-	-	-	97.3	0.0055	0.0010
<sup>2</sup> BL15	-	-	-	98.0	0.0011	0.0026

c) Molecular characteristics of samples with both varying amounts of regio- and stereo defects.

Polymer Sample	$\overline{M}_n$ (*10 <sup>-4</sup> ) (g/mol)	$\overline{M}_w$ (*10 <sup>-4</sup> ) (g/mol)	$\overline{M}_w / \overline{M}_n$ (-)	Percentage [mmmm] (%)	Fraction regio defects (-)	Fraction stereo defects [r] (-)
BL20	-	-	-	98.0	0.0018	0.0036
BL30	-	-	-	98.0	0.0026	0.0054
BL50	-	-	-	98.0	0.0030	0.0092
BL70	-	-	-	98.0	0.0032	0.0128
<sup>2</sup> M11	2.00	3.90	1.95	84.6	0.0065	0.0920
<sup>3</sup> M12	6.00	12.0	2.00	95.8	0.0027	0.0500
<sup>3</sup> M13	-	18.0	-	95.0	0.0027	0.0500
<sup>3</sup> M14	10.0	23.0	2.30	95.0	0.0027	0.0500
<sup>3</sup> M15	-	-	-	-	-	-

Table 3.1a, b, c. Relevant characteristics of the polymers used. Explanations can be found in text. <sup>1</sup>DSM, Geleen, The Netherlands; <sup>2</sup>Basell, Ferrara, Italy; <sup>3</sup>Fina Research, Feloy, Belgium.

The amorphous scattering could be approximated by a Lorentzian function, as well. In case the crystalline and amorphous scattering can be separated [28], then the mass crystallinity ( $\omega_m$ ) is given by the integrated crystalline scattering ( $I_c$ ) intensity divided by the total coherent scattered ( $I_{tot}$ ) intensity, i.e. crystalline plus amorphous scattering ( $I_a$ ):

$$\omega_m = \frac{I_c}{I_{tot}} = \frac{I_c}{I_c + KI_a}, \quad (3.2)$$

where  $K$  is a calibration factor. The calibration factor was set to unity for comparative purposes [29]. The volume crystallinity can be calculated by using the following equation:

$$\omega_c = \frac{\rho_a \omega_m}{\rho_c (\omega_m + 1) - \rho_a \omega_m}, \quad (3.3)$$

where  $\rho_c$  and  $\rho_a$  are the density of the pure crystalline- and pure amorphous-phases of iPP, respectively. The following values for the densities were adopted:  $\rho_c = 0.936$  g/mol ( $\alpha$ -phase),  $\rho_c = 0.922$  g/mol ( $\beta$ -phase),  $\rho_c = 0.939$  g/mol ( $\gamma$ -phase) and  $\rho_a = 0.854$  g/mol, respectively [30,31]. The lamellar thickness (LT) was calculated by multiplying the long-period (LP) with the volume degree of crystallinity ( $\omega$ ).

The relative amount of the  $\gamma$ -phase was determined by WAXS. The amount of the  $\gamma$ -phase compared with the  $\alpha$ -phase is best expressed using the intensity ratio of the reflections  $(130)_\alpha$  ( $2\theta \approx 12.0^\circ$ ) and  $(117)_\gamma$  ( $2\theta \approx 13.1^\circ$ ), respectively [32]. The areas indicated in Figure 3.1 for the  $(130)_\alpha$  reflection ( $A_\alpha$ ) and  $(117)_\gamma$  reflection ( $A_\gamma$ ) are used in the calculation for  $\omega_\gamma$ .

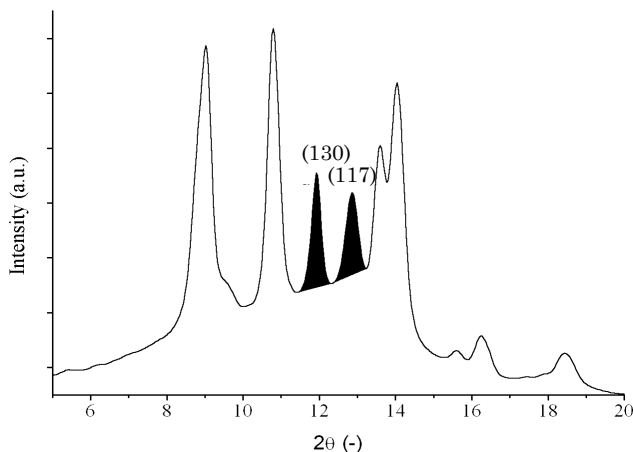


Figure 3.1. WAXS-trace of the polymer M5 with medium amount of the  $\alpha$ - and  $\gamma$ -phases, respectively. The areas indicated are used in the calculation for  $\omega_\gamma$ .

Non-overlapping areas are taken as the overlapping reflection may introduce extra uncertainties in the determination of the mass  $\gamma$ -fraction. The mass fraction of the  $\gamma$ -phase (denoted as  $\omega_\gamma$ ) was then calculated by the empirical relation [33]:

$$\omega_\gamma = \frac{A_\gamma}{A_\alpha + A_\gamma}. \quad (3.4)$$

In the rest of the thesis we will denote mass fractions of the various polymorphic forms simply as fraction.

Samples for AFM experiments were prepared by melt pressing the polymer between two mica sheets (or between two pieces of silicon) in a thermally controlled microscope hotstage (Mettler FP82). The polymer was kept at 220°C for 5 min to remove the thermal-rheological history of the material and then cooled to the temperature of crystallization (130°C) within approximately 1 min. After completion of the crystallization the substrate was removed, leaving a polymer film of an estimated thickness value of 0.7  $\mu\text{m}$ . AFM experiments were performed in air using a NanoScope III setup (Digital Instruments). The instrument was equipped with a J-scanner (maximum scan size 100  $\mu\text{m}^2$ ). Commercially available tapping mode Si-cantilevers were used. Height and phase images were acquired simultaneously.

### 3.2.3 Crystallization studies

Crystallization was followed using a polarized light microscope (LM) (Olympus BX60) equipped with a CCD camera (Sony HyperHAD) and computer. Micrographs were captured automatically by commercially available software (Image SXM, Scion Corp.) and kept for subsequent image processing. Growth rates were determined by measuring the length of the crystalline structures (i.e. a growth front of a spherulite) with time using the captured micrographs. From the slope of the length vs. time plot growth rate values were determined. In order to reduce the statistical error, growth rate experiments were repeated at least two times and per experiment at least 5 structures were measured.

The corresponding crystallization rates of both the  $\alpha$ - and  $\beta$ -phases were studied. Crystallization of the  $\alpha$ -phase was observed in non-nucleated samples. To induce the  $\beta$ -phase, a selective  $\beta$ -nucleating agent, the calcium salt of suberic acid [34], was used, kindly supplied by Prof. J. Varga, Technical University Budapest. The nucleant was manually dispersed into the melt. Although the  $\beta$ -phase could be easily distinguished from the  $\alpha$ -phase in most of the cases, the presence of  $\beta$ -phase crystals was always confirmed by selective melting of the  $\beta$ -phase prior to analyzing measured growth rates. For a detailed description of the melting behavior of the  $\beta$ -phase see chapter 2.

For a typical crystallization experiment, the polymer was pressed between two glass cover-slides in a thermally controlled microscope hotstage (Mettler FP82). The polymer was kept at 220°C for 5 min to remove the thermal-rheological history and then cooled to the temperature of crystallization (130°C) within approximately 1 min. Subsequently, the polymer is cooled down to 110°C and heated up from 110°C to 180°C with 10 °C/min in order to study the aforementioned selective melting of the  $\beta$ -phase.

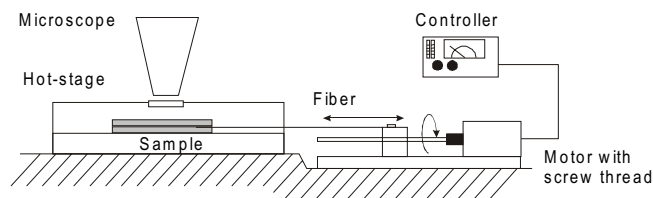


Figure 3.2. Schematic drawing of the fiber pull device employed for shear induced crystallization experiments.

Shear-induced crystallization experiments were performed with the help of a fiber pull device (see Figure 3.2). In this device a fiber was pulled at a controlled rate ( $v_{\text{pull}}$ ) for a predetermined time ( $t_{\text{pull}}$ ). The fiber was sandwiched between two thin solid polymer films. The two polymer films together with the fiber are placed between two cover-slides and melted. As in normal quiescent crystallization experiments, the polymer was kept at 220°C for 5 min to remove the thermal-rheological history and then cooled to the temperature of crystallization ( $T_c = 130^\circ\text{C}$ ) within approximately 1 min. Upon reaching  $T_c$  the fiber was pulled. The temperature of pulling ( $T_{\text{pull}}$ ) was set to be equal to  $T_c$ . The course of crystallization was followed by LM as in the case of quiescent crystallization.

Furthermore crystallization was studied by Differential Scanning Calometry (DSC). The DSC (a Perkin-Elmer calorimeter Pyris 1) was calibrated using gallium and indium before use. The sample chamber was kept under a constant flux of nitrogen. All samples were melted for 5 min at 220°C and subsequently cooled to the crystallization temperature (130°C). The samples were cooled down to only 110°C in order to prevent  $\beta\alpha$ -recrystallization of the  $\beta$ -phase during heating. All DSC melting scans were recorded at a heating rate value of 10 °C/min.

## 3.3 Results

### 3.3.1 Introduction

In this section the results of this research are arranged as follows. The section starts with a short description of the samples. We will go into the possible defect structures present in the samples and the representation of the amount of defects by defect-fractions. Next, we will describe the morphology of the samples after isothermal crystallization and cooling to room temperature. The formation of the  $\beta$ -phase and  $\gamma$ -phase as function of the number and type of defects will be addressed, in addition to long-periods, degrees of crystallinity, and lamellar-thicknesses. The section proceeds with the presentation of the results obtained from crystallization experiments. A description of the growth rates of both the  $\alpha$ -phase and  $\beta$ -phase as a function of the number and type of defects is given. The section ends with a discussion on the results regarding the formation of the  $\beta$ -phase under shear.

### 3.3.2 Description of defects

Table 3.1 shows the main characteristics of the samples used in this research. The polymer samples show a large diversity in chain regularity. The regularity or the configuration of successive stereo centers (chiral carbon atoms) in the isotactic polypropylene chain determines the overall order (tacticity) of the polymer. During polymerization, tacticity can be disturbed by the incorporation of chain-defects. Possible irregularities can be divided into a category of stereo-defects and regio-defects, respectively (see Figure 3.3).

It was pointed out that the distribution of defects within one chain and among the chains play an important role in the crystallization behavior of the polymer. Theoretical predictions were made mainly for polymers with randomly distributed defects. Therefore it is important to make use of polymers with only randomly distributed defects. The samples mentioned in Table 3.1 are predominantly metallocene catalyzed iPPs with different chain-architectures in which the defects are distributed evenly and randomly in the chains.

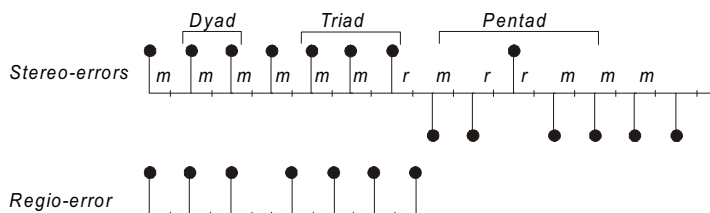


Figure 3.3. Modified Fisher-projections of two selected arbitrary parts of a polypropylene polymer chain showing stereo- and regio-defects, respectively. Indicated are a dyad, triad and, pentad.



The fraction *meso- or racemic*-sequences for pairs of consecutive stereo-centers is denoted as  $[m]$  or  $[r]$ , respectively (see Figure 3.3). Identification and quantification of the defects are necessary in order to investigate the influence of chain architecture on the melting and crystallization of the polymer. With help of  $C^{13}$ -NMR the sequence length on the pentad level (four pairs of consecutive stereo-centers, see Figure 3.3) [22] was determined. The number of pentads can be expressed as fractions by dividing the  $C^{13}$ -NMR signal intensity of the concerning pentad by the total intensity obtained from all pentads. Since we are interested in the fraction of stereo-defects, denoted as the dyad  $[r]$ , we need to calculate  $[r]$  from the measured pentad fractions. This can be done by establishing relationships between pentads, triads, and diads. [35]. A few of these relations are given below (for clarity the square brackets are omitted):

$$r = rr + \frac{1}{2}(mr) \quad (3.5)$$

$$mm = (m m m m + m m m r + r m m r) \quad (3.6)$$

$$mr = (m m r r + m m r m + r m r r + r m r m) \quad (3.7)$$

$$rr = (r r r r + r r r m + m r r m) \quad (3.8)$$

We calculated the number fraction of  $[r]$  in the chain from  $C^{13}$ -NMR measurements with help of the given relations. The results are given in Table 3.1. We assume a similar influence of the many possible stereo sequence defects on crystallization and melting behavior of iPP, therefore we decided to take the fraction *racemic*  $[r]$  additions as a measure for the number of stereo-defects. The fraction of stereo-defects presented in Table 3.1, is thus a collection of all the possible stereo errors, no discrimination was made for the possible variations of possible stereo-sequences in the chain. Although this may be a oversimplification, it is a very powerful way of dealing with all given polymer samples in a combined fashion.

In addition to the stereo-defects, the polymer chain may also contain regio-defects. Regio-defects are defined as a misinsertion of the polypropylene unit in the chain [35], usually denoted as a 2,1 addition. The results of the quantification of the regio-defect fraction as measured by  $C^{13}$ -NMR is also given in Table 3.1.

In order to facilitate the analyses, the samples in Table 3.1 were sorted in three groups. The first group of samples (Group 1) contains polymers with only stereo-defects (ZN, M1-M5). No regio-defects are present in these samples. The second group (Group 2) contains polymers with a low amount of stereo-defects, but with a strong varying amount of regio-defects (M3-M10). The third group (Group 3) contains polymers with both a significant amount of stereo- and regio-defects (BL15-M15). By dividing the polymers in the 3 groups as described above, it is possible to *separately* investigate the influence of stereo and regio-defects on the crystallization behavior and morphology.

### 3.3.3 Crystal morphology as observed by WAXS

#### Polymorphism and chain architecture ( $\gamma$ -phase)

As mentioned in the introduction of this chapter, the formation of the  $\gamma$ -phase is enhanced with the incorporation of defects within the chain. Especially in metallocene catalyzed iPPs an increase in the amount of the  $\gamma$ -phase can be found. In order to investigate the influence of stereo- and regio-defects on the formation of the  $\gamma$ -phase, WAXS experiments were performed. Each of the polymers was crystallized isothermally at 130°C and rapidly cooled to room temperature, as described in the Experimental section. The WAXS measurements were done at room temperature.

To qualitatively show the influence of chain defects on the formation of the  $\gamma$ -phase, WAXS diffractograms are given for a given number of polymers with increasing defect fraction (ZN, BL70, BL30, BL15, and M11), see Figure 3.4. Included in the figure are the most (M11) and least (ZN) defected polymers (upper and lower curves, respectively).

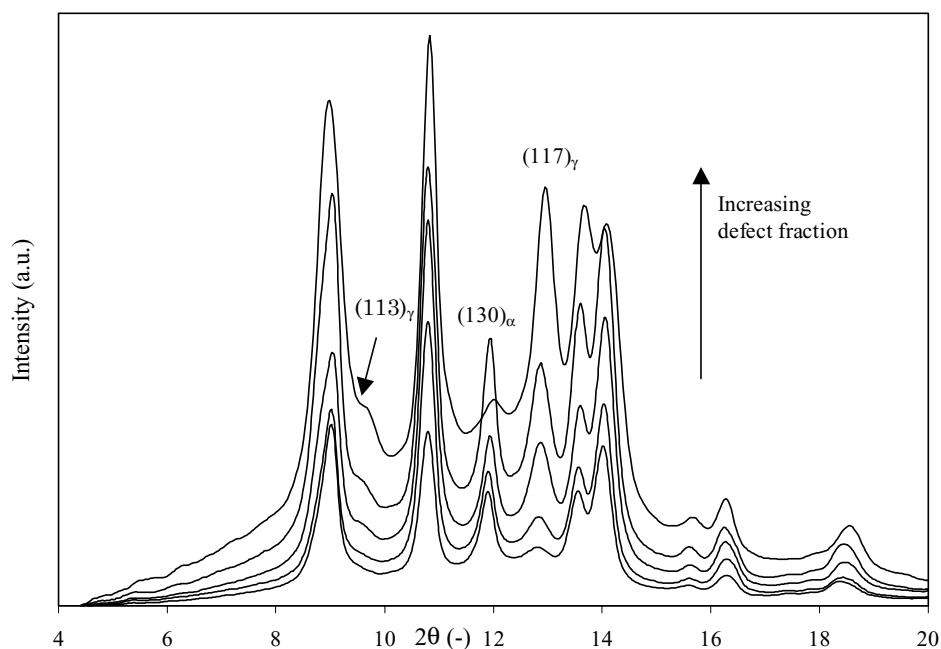


Figure 3.4. WAXS diffractograms of several iPP polymers ( $\alpha/\gamma$ -phase) with increasing defect (stereo- and regio-) fraction (from bottom to top) obtained after complete crystallization. Explanation of peaks indicated can be found in the text.

For all polymers the characteristic  $(117)_\gamma$  reflection is present, even for the least defected Ziegler-Natta catalyzed iPP, although for the latter with very weak intensity. As expected, the intensity of the  $(117)_\gamma$  reflection strongly increases with

defect fraction, while the intensity of the  $(130)_\alpha$  reflection decreases. The increase in the amount of the  $\gamma$ -phase can also be seen in the increasing intensity of the small  $(113)_\gamma$  peak indicated by the arrow.

As described in the Experimental section, the amount of  $\gamma$ -phase ( $\omega_\gamma$ ) is quantified by the ratio of the relative areas of the  $(117)_\gamma$  and  $(130)_\alpha$  reflections. The percentage of crystals exhibiting the  $\gamma$ -phase ( $\omega_\gamma$ ) is plotted as a function of defect fraction, in Figure 3.5. The different specimens were grouped (see section 3.3.1) and plotted according to the specific defect type as function of the type of the given defect fraction, i.e. the amount of the  $\gamma$ -phase of the polymers:

- (1) with only *stereo*-defects (ZN, M1-M5) ( $\blacktriangle$ ) is plotted as function of the fraction *stereo*-defects (group 1);
- (2) with varying fraction *regio*-defects (M3-M10) ( $\blacksquare$ ) but with approximately the same fraction of stereo-defects is plotted as function of fraction *regio*-defects (group 2);
- (3) with *both* stereo- and regio-defects (BL15-M15) ( $\circ$ ) is plotted as function of fraction *stereo*-defects [36] (group 3).

We saw already qualitatively (see Figure 3.4) that the fraction of the  $\gamma$ -phase increases with increasing number of defects. Data from Figure 3.5 quantifies this result.

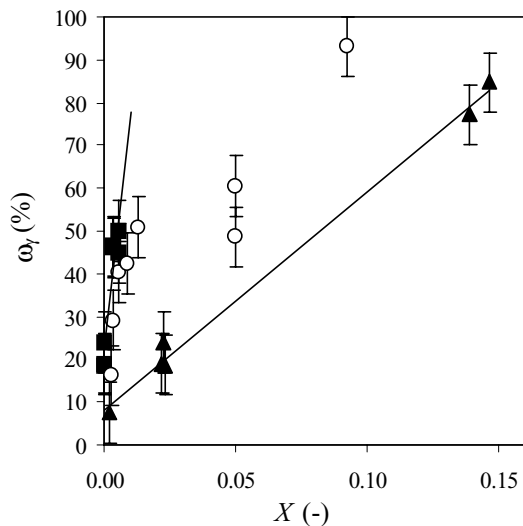


Figure 3.5. Fraction of the  $\gamma$ -phase of the polymer sample studied as a function of defect fraction. Assignments of the symbols are given in the text. The error bars are estimated errors of 5%.

As Figure 3.5 shows, a much stronger increase of the  $\gamma$ -phase as a function of increasing regio-defect fraction is found as compared to the amount of stereo-defects. This conclusion is in disagreement with an earlier published result that the

two types of defects (regio/stereo) have the same influence in the formation on the  $\gamma$ -polymorphic form of iPP [37].

Under the crystallization conditions employed, the  $\gamma$ -phase percentage increases up to  $93 \pm 5\%$  [38] for the polymer with the highest fraction of defects. The polymer with the lowest fraction of defects, i.e. is the polymer synthesized by a Ziegler-Natta catalyst (ZN), contains approximately  $7 \pm 5\%$  [38]  $\gamma$ -phase, which is still considerable. As one can see, Figure 3.5 shows two approximately linear dependences on the number of regio- and stereo-defects, respectively. The observed relationships between the percentage of the  $\gamma$ -phase as a function of the two different types of defects (regio/stereo) were fitted with a linear relationship using a standard least-squares fit procedure. The following numerical equations were obtained:

$$(\omega_{\gamma,s})_{X_r=0} = (8.3 \pm 1.6) + (5.1 \pm 0.2) \cdot 10^2 X_s, \quad (3.9a)$$

$$(\omega_{\gamma,r})_{X_s=0} = (22.2 \pm 3.0) + (5.3 \pm 0.9) \cdot 10^3 X_r, \quad (3.9b)$$

where  $(\omega_{\gamma,s})_{X_r=0}$  corresponds to the percentage of the  $\gamma$ -phase as function of stereo-defects, while the fraction of the regio-defects was kept zero.  $X_s \approx 0$  in the subscript of equation 3.9b refers to approximately zero fraction of stereo-defects for the equation fitted with the amount of regio-defects fraction used as independent variable (equation 3.10b). A linear combination of equation 3.10a/b yields the following equations:

$$\omega_{\gamma,s/r} = (8.3 \pm 1.6) + (5.1 \pm 0.2) \cdot 10^2 \tilde{X} \quad \text{where} \quad \tilde{X} = X_s + (10.3 \pm 1.5) X_r. \quad (3.10a/b)$$

The combined defect fraction ( $\tilde{X}$ ) is the sum of the number of stereo-defects and the number of regio-defects multiplied by a given weighting factor with a value of 10.3.

Equation 3.10a/b predicts a linear relationship between the amount of the  $\gamma$ -phase with the combined defect fraction ( $\tilde{X}$ ). Figure 3.6 shows the percentage  $\gamma$ -phase as a function of  $\tilde{X}$  for all polymers mentioned in Table 3.1. We see that the formation of the  $\gamma$ -phase is approximately linear with the combined defect fraction ( $\tilde{X}$ ). Equations 3.10a and b predict that the percentage of the  $\gamma$ -phase will be 100% at a combined defect fraction of  $\tilde{X} \approx 0.17$  (-). Equations 3.9a/b and 3.10a/b are strictly valid for small values of  $\tilde{X} < 0.17$  (-) or for  $\omega_{\gamma,s} < 100\%$ .

Although a linear fit is used to describe the observed percentage of the  $\gamma$ -phase as function of the combined defect fraction, a higher order (e.g. a second order) polynomial would describe the trend more accurately (see the dashed trend line in Figure 3.6). In the calculation of equation 3.11a/b we assumed a linear dependence

of the amount of the  $\gamma$ -phase for both the regio- and stereo-defects. Probably this assumption is not entirely valid and a higher order dependence describing the relationship between the fraction of *regio*-defects (or stereo-defects) and the percentage of the  $\gamma$ -phase would yield a closer fit with the observed data. Nevertheless, the data presented in Figure 3.6 clearly shows that the amount of the  $\gamma$ -phase strongly depends on the amount of regio- and stereo-defects, exhibiting a stronger function on the fraction of regio-defects.

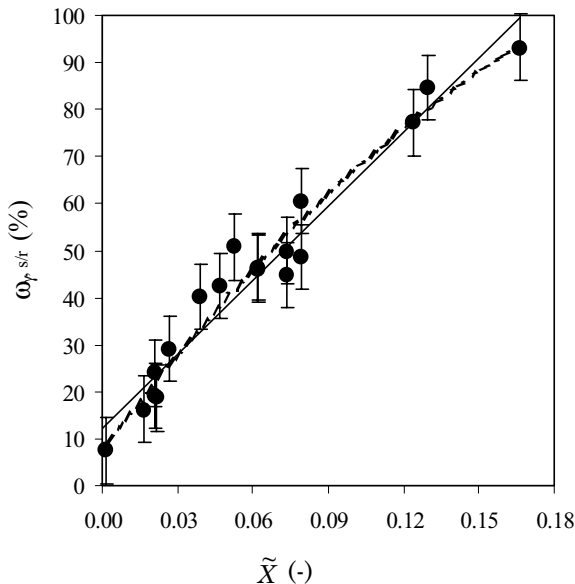


Figure 3.6. Fractions of the  $\gamma$ -phase of the used polymers as a function of combined defect fraction. Assignments of the symbols are given in the text. Error bars correspond to estimated errors of 5%.

### The formation of the $\gamma$ -phase: Structural origins

In the discussion about the structural origins for the formation of the  $\gamma$ -phase, we adopted for our situation the theory presented by Mandelkern et al. [37,39]. For clarity we briefly summarize the most important characteristics of the  $\gamma$ -phase (see also chapter 2).

The usual shape of the crystals in the  $\gamma$ -phase is lenticular. The unit cell is orthorhombic with the parameters  $a = 8.54 \text{ \AA}$ ,  $b = 9.93 \text{ \AA}$ , and  $c = 42.41 \text{ \AA}$  [6]. In this structure the PP helices are tilted with respect to each other. The angle of tilt is  $+40^\circ$  or  $-40^\circ$  to the normal of the lamella ( $80^\circ$  with respect to each other). The fast direction of growth is along the  $b^*$ -axis [40]. The growth and occurrence of the  $\gamma$ -phase is usually associated with the  $\alpha$ -phase [41], although individual single crystals of the  $\gamma$ -phase were also observed [7]. The  $\gamma$ -phase is associated with the  $\alpha$ -phase as the  $\gamma$ -crystals are considered to grow epitaxially onto  $\alpha$ -crystals [41]. The

angle of branching is approximately  $40^\circ$  corresponding to the angle of  $\gamma$ -phase relative to the  $\alpha$ -lamellae [41] (see Figure 3.7).

The coexistence of two different non parallel chain directions within one unit cell resembles the branch point in a  $\alpha$ -quadrates (cross-hatch cross-over point). The  $\alpha$ -phase of iPP shows, for the cross-hatched structure, lamellae oriented at  $\approx 80^\circ$  to each other. A second  $\alpha$ -phase lamella can initiate on the lateral (010) face of the primary  $\alpha$ -phase elongated lath-like crystal. This is called crosshatching and takes place via homo-epitaxy (see Figure 3.7). As shown in literature [5], the number of crosshatched crystals increases with increasing number of (stereo- and regio-) defects. Thus, it is not surprising that if similar crystallization mechanisms are involved, the amount of the  $\gamma$ -phase would also increase with increasing number of defects.

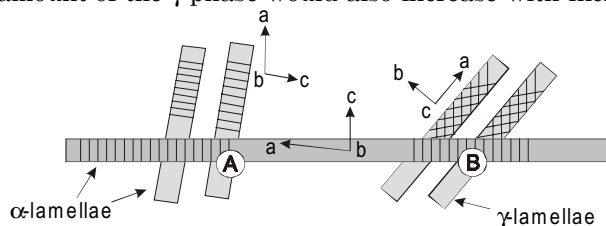


Figure 3.7. Schematic representations (upper graph: side or 'edge on' view, lower graph 3D view) of  $\alpha$ -phase cross-hatched lamellae (A) and  $\gamma$ -phase lamellae (B) epitaxially grown on an  $\alpha$ -phase lamellae. Indicated are the unit-cell orientations of the individual lamellae [42].

For a lamellar structure to evolve, the large flux of chains that emanate from the crystallite needs to be dissipated. Chain folding, of one type or the other, is one mechanism by which this flux in many semi-crystalline polymers is dissipated. Therefore, in order for a crystallite to grow laterally, a significant amount of chain bending or folding must occur, which will necessarily involve an expenditure of free energy [39]. Because the energy penalty of a regio-defect, when inserted into a crystal lattice, would be large and the surrounding stacked layers strongly suppresses chain diffusion, the chain can not fold back easily, or be inserted back into the crystal lattice. Therefore long chains containing defects will remain (for a longer time) in the melt [5]. Upon formation of the initial crystals (the  $\alpha$ -phase) there will thus be an increase in concentration of chain entanglements and defects in the melt [42].

At some point, long sequences lengths of *non*-crystallizable units will preclude any significant folding with (adjacent) re-entry. Another way, in addition to folding, by which the chain flux can be dissipated, such that crystallization can proceed with the development of lamellar crystals, is chain tilting. The interphase density of chains in the first layer of the interphase would be reduced by tilting. As a consequence the need for (adjacent) re-entry to reduce the flux of chains will be decreased [39]. Thus the enhanced formation of the  $\gamma$ -phase with anti-parallel

chains can be considered as the consequence of reducing the flux of chains that arise from the (001) plane and accommodating the chain defects outside the crystal [37].

### **Polymorphism and chain architecture ( $\beta$ -phase)**

From the literature it is known that only negligible amounts of the  $\beta$ -phase forms in random (ethylene/propylene) copolymers with low (1.8-2.5%) ethylene content [13]. Based on these observations, it was suggested that the tendency to  $\beta$ -crystallization is suppressed by the disturbance of the chain regularity [14,43]. As we have access to a large set of PP samples with various types and amounts of chain defects, the opportunity arose to perform a comprehensive structure-property study on the formation of the  $\beta$ -phase and its dependence on the chain architecture.

From DSC experiments, which were done to determine the melting characteristics, we found as expected a strong decrease in the heat of fusion corresponding to the  $\beta$ -phase and thus on the relative concentration of the  $\beta$ -form with decreasing tacticity. In order to further demonstrate the decline in the tendency for  $\beta$ -crystallization with the incorporation of defects in the chain, WAXS measurements were performed. Moreover, knowledge of the amount of the  $\beta$ -phase is important for the interpretation of the results of SAXS data (see section 3.3.4).

Two peaks in the WAXS diffractograms of iPP are characteristic for the  $\beta$ -phase, i.e.  $(300)_\beta$  at  $2\theta = 10.4^\circ$  and  $(311)_\beta$  at  $2\theta = 13.8^\circ$  diffraction angle, respectively. Figure 3.8 shows the WAXS diffractograms for a selective number of polymers with increasing defect fraction (ZN, BL70, BL30, BL15, M12). In accordance with the findings from DSC measurements, the amount of the  $\beta$ -phase strongly decreases with increasing fraction of defects. The arrows in Figure 3.8 show the strong decrease in intensity of the characteristic peaks. Only in polymers with relatively low amount of defects (ZN, M1-M4, and BL15-BL30) the  $\beta$ -phase was present in relative high amounts. In the next section we will see that separate peaks from SAXS can be detected only for the polymers with considerable  $\beta$ -phase formation.

Several reasons exist why the amount of the  $\beta$ -phase strongly decreases with increasing concentration of defects. The amount of the  $\beta$ -phase is kinetically determined and depends on the relative growth rates of the  $\alpha$ -phase<sup>1</sup> and the  $\beta$ -phase ( $G_\alpha$ , and  $G_\beta$ ), respectively. At the crystallization temperature of 130°C,  $G_\alpha/G_\beta$  is smaller than unity for conventional Ziegler-Natta catalyzed iPPs [44]. However,

---

<sup>1</sup> In the previous section it was shown that the amount of  $\gamma$ -phase strongly increases with the amount of defects. As the  $\gamma$ -phase is intimately connected with the  $\alpha$ -phase, it is not possible to quantify the growth rate of the  $\gamma$ -phase separately. Therefore, we denote the growth rate of the  $\alpha$ - and  $\gamma$ -phases simply as  $G_\alpha$ .

this ratio is rapidly increasing with increasing fraction of defects and becomes even larger than unity above some critical defect concentration (see section 3.3.5 of this chapter). Once nucleated, the  $\beta$ -phase is easily overgrown by the  $\alpha$ -phase in case the growth rate of the  $\alpha$ -phase is higher ( $G_\alpha > G_\beta$ ). Consequently, the growth of the  $\beta$ -phase is increasingly inhibited with increasing defect fraction.

One of the other reasons which determine the fraction of the  $\beta$ -phase originates from the use of a  $\beta$ -nucleant. Assuming that the  $\beta$ -phase epitaxially nucleates [45] on the surface of the nucleant, it is expected that epitaxial nucleation will be disturbed by the presence of defects. An increase in the amount of defects, therefore, reduces the efficiency of the nucleant. In addition to a lower efficiency of the nucleant, a lower amount and a poor dispersion of the  $\beta$ -nucleant decreases the number of possible sites for nucleation of the  $\beta$ -form and hence the amount of the  $\beta$ -phase. Due to the specific experimental procedure applied in this thesis the amount and dispersion of the nucleant could not be precisely controlled. As the amount and degree of dispersion of the nucleation agent has strong influence on the amount of the  $\beta$ -phase as well, it is not useful to correlate the fraction of the  $\beta$ -phase with the number of defects, as was done for the  $\gamma$ -phase.

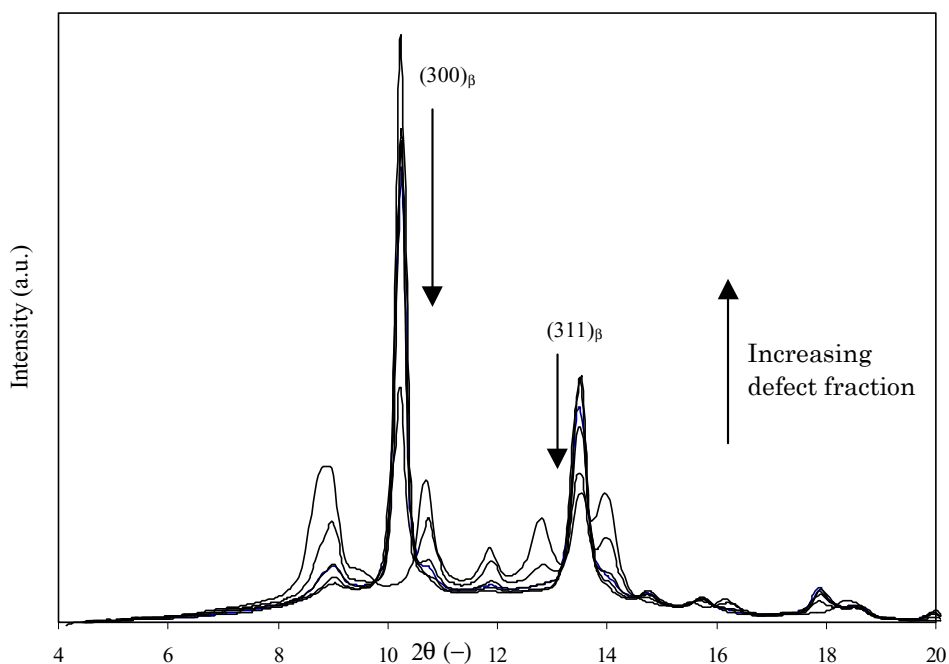


Figure 3.8. WAXS diagrams of several iPP polymers (characteristic reflections for the  $\beta$ -phase are labeled) with increasing defect fraction obtained after complete crystallization. Explanation of the peaks indicated can be found in the text.



### 3.3.4 Crystal morphology as observed by SAXS

#### Introduction

SAXS measurements were performed in order to investigate the influence of the fraction of defects on the resulting morphology on the lamellar level after isothermal crystallization. For clarity, first SAXS-curves from a limited number of samples will be presented in order to demonstrate the changes in scattering curves with increasing defect fraction. Consecutively, results for the long-period (LP), crystallinity ( $\omega_c$ ), and lamellar thickness (LT) will be discussed. Special attention will be paid to the differences in morphology for the  $\alpha$ -,  $\beta$ -, and  $\gamma$ -polymorphs, respectively.

#### SAXS-curves of the $\alpha$ - and $\gamma$ -phases

SAXS-curves obtained from the non-nucleated samples (only  $\alpha$ - and  $\gamma$ -phase present) show one main peak (assigned by 1) and a higher-angle second peak (assigned by 2), as can be seen in Figure 3.9. The maximum of the main peak shifts to higher values of the scattering vector ( $q$ ), and broadens considerably with increasing defect fraction (regio labeled by 3). The width of the distribution of long-periods can be expressed by the width at half height [46]. Estimated values of the half-width of the main peak increases from 1.6 (ZN) to 3.2 (M6)  $\text{nm}^{-1}$  with increasing defect fraction. The second peak (assigned by 2) is initially medium strong, but reduces in intensity with increasing defect-fraction. However, with even more increasing amount of defects, a second peak at higher values of  $q$  arises again (assigned by 4).

The assignments of the main and the secondary peaks is complicated since the sample contains both the  $\alpha$ - and  $\gamma$ -phases. Therefore it is useful to analyze the sample with the highest  $\alpha$ -phase content (highest curve in Figure 3.9) and the sample with the highest amount  $\gamma$ -phase (lowest curve in Figure 3.9), respectively. The former sample exhibits the lowest amount of stereo-defects and no regio-defects, the latter sample contains the highest amount of stereo- and regio-defects.

The curve with the lowest defect fraction (sample ZN) contains almost exclusively the  $\alpha$ -phase. Therefore, we expect that the main peak (assigned by 1) of the scattering curve is only associated with the  $\alpha$ -phase. A possible origin of the second peak (assigned by 2) in the most upper curve (almost pure  $\alpha$ -phase) could be related to a second order reflection [47]. The ratio of the angles of the second and first maxima ( $\theta_1/\theta_2$ ) observed is approximately 2 ( $\theta_1/\theta_2 = 1.96$ ) (the values of scattering vector are  $q \cong 0.34 \text{ nm}^{-1}$  and  $0.66 \text{ nm}^{-1}$ , respectively). The deviation from the ideal value of 2 for  $\theta_1/\theta_2$  may be ascribed to the presence of non-symmetric lattice statistics [48,49] or curvature in the lamellar stacks [50]. Similar second order

reflections have been reported in the literature for polyoxymethylene (LM) and linear polyethylene (PE) [48].

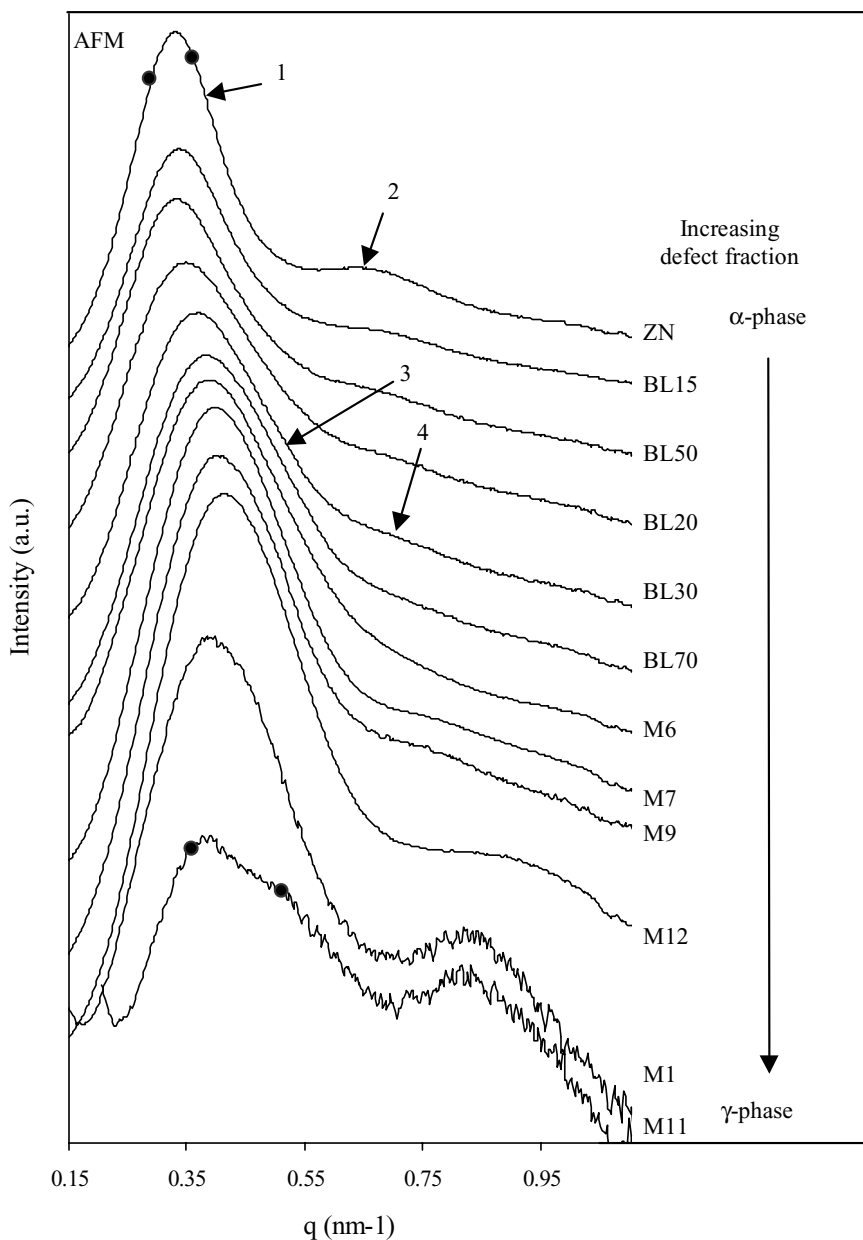


Figure 3.9. SAXS curves of PP samples without added nucleating agents ( $\alpha/\gamma$ -phases). The numbered arrows as well as the points indicated are explained in the text.

Another possible reason for the second peak (assigned by 2), which was proposed in literature [51], is the presence of a bimodal distribution of long-periods. In the case of polypropylene this would mean that the main peak originates from the initially grown ‘mother’ lamellae and the origin of the smaller peak (high values of  $q$ ) may lay in the existence of crosshatched ‘daughter’ lamellae, or secondary crystallized lamellae, respectively. As the number of cross-hatched lamellae is expected to increase with increasing defect fraction, the second peak would also increase in intensity. However, in our experiments this is not the case, therefore we believe that the peak at the higher  $q$  value is a second order reflection. In order to support this assumption, AFM and DSC measurements were performed.

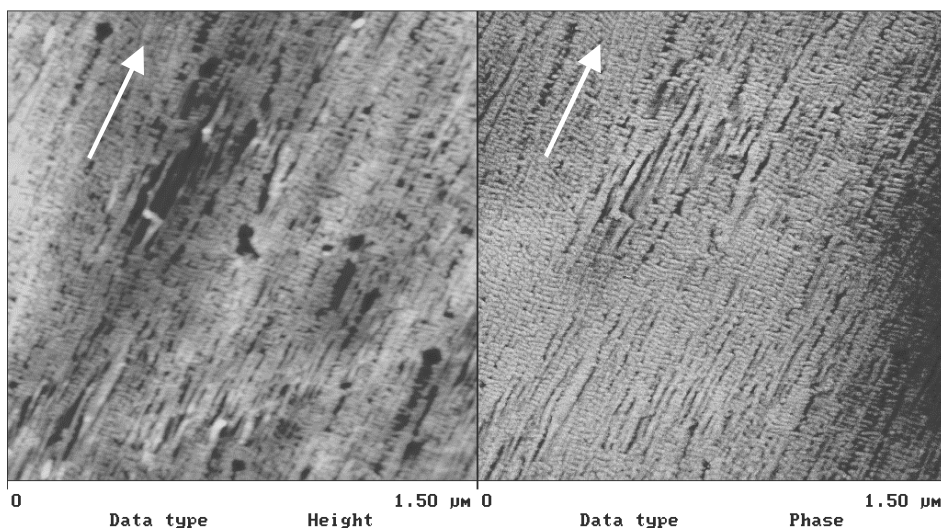


Figure 3.10. AFM tapping mode height image (A) and phase (B) image of iPP isothermally crystallized at 130°C on mica.

Measuring individual lamellar thicknesses with AFM involves many difficulties, however determination of LPs is possible without serious limitations [52]. In the particular experiment we crystallized the sample with the lowest defect fraction (ZN) between to mica plates, as described in the section Experimental. The substrate could possibly influence the crystallization and as a consequence the measured values of the LPs, however other substrates like silicon and glass yielded similar values for the LPs. Thus we assume that the LP value is dominated by the crystallization process. Figure 3.10 shows the surface of iPP (ZN-sample) crystallized on mica at 130°C. The arrow indicates the direction of the center of the spherulite (radial direction). Clearly, radial ‘mother’ and tangential ‘daughter’ lamellae are visible. The values of the LP were directly measured from the AFM micrographs. Estimated values are  $22 \pm 2$  nm and  $16 \pm 2$  nm for the radial- and tangential lamellae, respectively. The most probable value of the LP determined from SAXS is  $18 \pm 1$  nm. A conversion of the AFM long-period values into scattering

vectors yield  $q = 0.28 \text{ nm}^{-1}$  and  $q = 0.35 \text{ nm}^{-1}$ , respectively, for the radial and tangential lamellae in terms of scattering vectors. These calculated values of  $q$  are indicated in Figure 3.9 on the curve of the ZN-sample with filled circles (dots). AFM does not indicate the existence of a LP-population with a repeat length of  $9 \pm 1 \text{ nm}$ , which is the value of LP from the second peak in the SAXS-curve. This is a supportive indication that peak indicated by 2 is a second order reflection

Another supportive argument for the existence of a second order reflection we obtained from DSC experiments. With help of the Gibbs-Thomson relation we can estimate the melting points of crystals with finite thickness ( $l_c$ ) values (but with infinite lateral dimensions).

$$T_m = T_m^0 \left( 1 - \frac{2\sigma_e}{\Delta H_f^0 l_c} \right). \quad (3.11)$$

Where  $T_m^0$  is the equilibrium melting temperature,  $\Delta H_f^0$  the equilibrium heat of fusion, and  $\sigma_e$  denotes the surface energy, respectively.

Assuming a crystallinity of 75%, we calculate a value of 11.7 nm and a value of 16.1 nm for the lamellar thickness of the tangential and radial lamellae, respectively. With the values for the constants:  $T_m^0 = 186^\circ\text{C}$ ,  $\Delta H_f^0 = 8700 \text{ kJ/mol}$ , and  $\sigma_e = 62 \text{ erg/cm}^2$  [2], we calculated the melting points of these populations as  $162.5^\circ\text{C}$  and  $168.9^\circ\text{C}$ , respectively. In case the second peak (high  $q$ ) would originate from a separate population of lamellae, this population would have a melting point around  $142^\circ\text{C}$  (calculated with equation 3.11). DSC measurements of this sample (ZN-sample isothermally crystallized at  $130^\circ\text{C}$ , heating rate  $10^\circ\text{C/min}$ ) does not show any indication of a melting peak at this temperature. Thus the AFM and DSC measurements support that the peak at  $q = 0.66 \text{ nm}^{-1}$  can be with high confidence assigned to a second order reflection.

As we discussed the origin of the peak at higher values of  $q$  (assigned by 2) we can now proceed with a discussion on the broadening indicated by arrow 3 in Figure 3.9.

The broadening of the main SAXS peak with increasing defect fraction occurs mainly at the high angle side (large  $q$ ) of the peak indicated by arrow 3. Simultaneously with the broadening a distinct shift of the maximum to higher values of  $q$  occurs. Ultimately, the main peak from the SAXS curve of the highest defected sample splits into two peaks (lowest curve in Figure 3.9). Results from AFM showed a bimodal distribution of lamellae and the SAXS-curve originating from the sample with the highest defect fraction (lowest curve in Figure 3.9) suggests a bimodal distribution of crystal planes, as well (see the indicated places in Figure 3.9). Therefore, it is reasonable to assume a bimodal distribution for each sample with intermediate defect fraction.

The main peak thus can be considered as a convolution of two long-period distributions, i.e. a distribution at higher values of  $q$  (smaller values of the LP) and a distribution at lower  $q$  values. The shift of the peak maximum and the broadening of the peak to high values of  $q$  can be explained by an increase of the distribution at higher  $q$ . The position of the peak maximum is determined by the most probable population of long-periods LPs [42] and a relative change in the distribution will cause the observed shift in the maximum.

Although speculative, we believe that the distribution at lower values of  $q$  originates from primary ‘mother’ lamellae, while the distribution at higher values of  $q$  initially originates from cross-hatched lamellae and with increasing defect fraction from  $\gamma$ -lamellae, as well. The structural similarity between the  $\alpha$ - and  $\gamma$ -phases (see Figure 3.7) supports this statement. We found, from WAXS analysis, that the amount of  $\gamma$ -phase strongly increases with increasing defect fraction. As the sample with the highest defect fraction contains  $93 \pm 5\%$   $\gamma$ -phase [38], we expect that a large part of the scattered intensity (SAXS) of the sample with the highest fraction of defects originates from the  $\gamma$ -phase. It is also known that with increasing defect fraction the population cross-hatched lamellae increases [5,9]. The increase in both the cross-hatched lamellae and fraction of  $\gamma$ -phase lamellae occurs in line with the increase in the distribution at higher values of  $q$  explaining the observed trends in the SAXS-scattering curves.

### SAXS-curves of the $\beta$ -phases

Figure 3.11 shows the SAXS curves for the  $\beta$ -nucleated samples. Multiple peaks can be seen in the SAXS curves of the  $\beta$ -nucleated samples, as well. As shown by WAXS measurements the amount of the  $\beta$ -phase in the sample with the lowest defect fraction (ZN) exhibits almost 100%  $\beta$ -phase. The SAXS intensity is thus only from the  $\beta$ -phase. Therefore, we define the first peak (low  $q$ ) as originating from the  $\beta$ -phase. The origin of the second peak in the  $\beta$ -nucleated samples (assigned by arrow 2,  $q \cong 0.57 \text{ nm}^{-1}$ ) is probably, like in the  $\alpha$ -phase, a second order reflection. The value of the scattering vector at the maximum of that peak is approximately twice the value of the first maximum ( $q \cong 0.27$  and  $0.57 \text{ nm}^{-1}$ ) [50].

The volume fraction of the  $\beta$ -phase drastically decreases with increasing number of defects corresponding to the peak at  $q \cong 0.25 \text{ nm}^{-1}$  (assigned by arrow 1). Almost no  $\beta$ -phase could be detected by WAXS for the sample BL100 (= M6). This curve (lowest curve in Figure 3.11) has the same appearance as the curve of the corresponding sample in Figure 3.9 with  $\alpha$ -phases only. With increasing defect-fraction two shoulders appear (assigned by arrows 3 and 4, see also Figure 3.9). The  $q$ -values of the shoulder maxima exactly correspond with the  $q$  values from the non-nucleated sample with the same number of defects. The shoulders can thus be assigned to the scattering originating from the  $\alpha$ - and  $\gamma$ -phases, respectively.

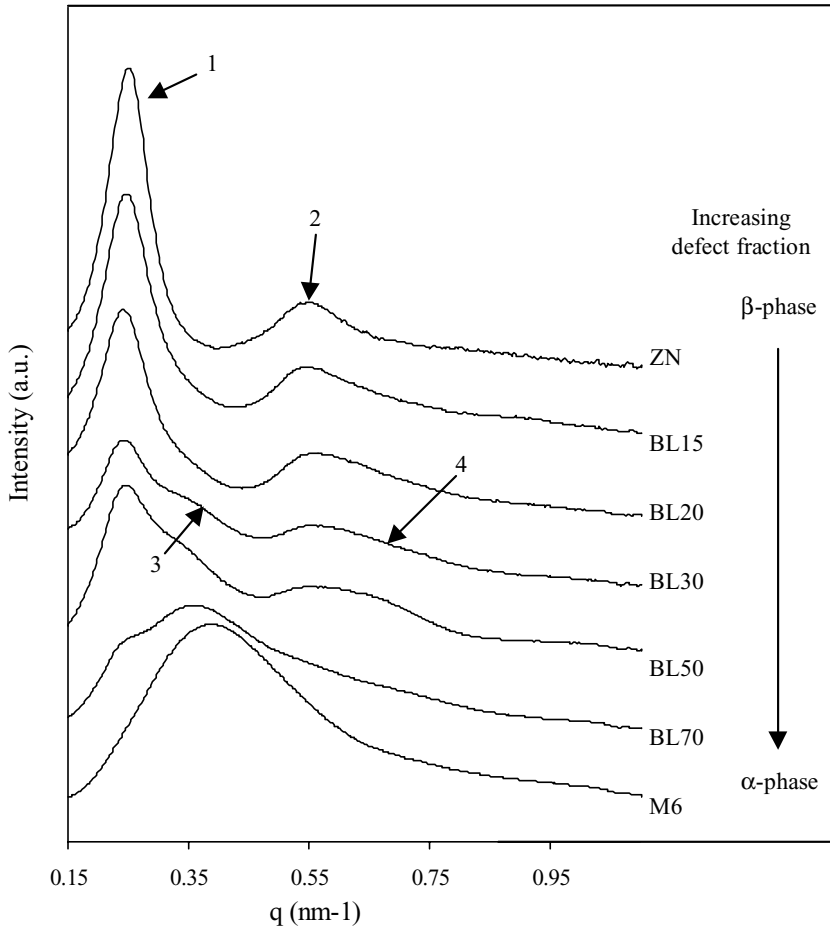


Figure 3.11. SAXS curves for the samples BL100 to BL0 (from bottom to top). The figure gives the results for the  $\beta$ -nucleated samples. The diminishing peak at  $q \approx 0.25 \text{ nm}^{-1}$  (labeled by 1) originates from the  $\beta$ -phase.

### Long-period

To obtain an overview on the influence of defects on the morphology, the values of the long-period as calculated from equation 3.1 (see section Experimental) were plotted as a function of the combined defect fraction ( $\tilde{X}$ ) using equation 3.10b, see Figure 3.12. The LP was calculated from the maximum of the SAXS peaks.

The first observation one can make from this plot is that the LP of the  $\beta$ -phase ( $\blacksquare$ ) is higher as compared with the  $\alpha$ - and  $\gamma$ -phases and increases slightly over the range of defect-fractions of the samples used. The values of LP coming from the second order reflection ( $\square$ ) obey approximately the same trend.

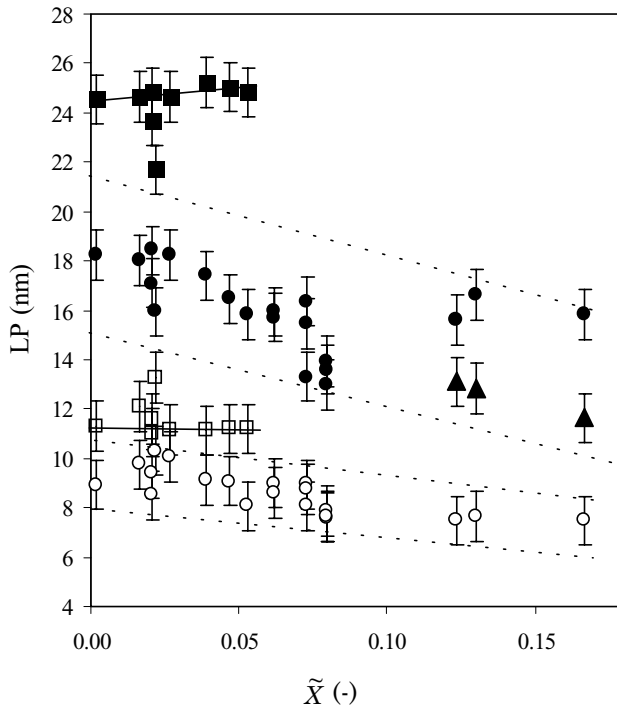


Figure 3.12. Values of the long-periods (LPs) of polymers described in Table 3.1 as a function of the combined defect-fraction.  $\beta$ -phase: ( $\blacksquare$  = peak 1), ( $\square$  = peak 2);  $\alpha$ -phase: ( $\bullet$  = peak 1), ( $\circ$  = peak 2);  $\gamma$ -phase: ( $\blacktriangle$ ). The error in the long-period is estimated as  $\pm 1$  nm.

The situation for the  $\alpha$ -phase is slightly different, and more difficult to interpret due to the complications discussed in the previous section, i.e. the bimodality of the SAXS peaks and the occurrence of the  $\gamma$ -phase. Two linear decreasing dashed lines are drawn to guide the eye. The lines are drawn such that within the two lines the LPs for both distributions are positioned.

The value of the LP as calculated from the maximum of the SAXS curve decreases steadily. For the three most defected polymers two LPs are indicated (see the samples labeled by the symbols ( $\blacktriangle$ ) and ( $\bullet$ )). The three points indicated with ( $\blacktriangle$ ), most probably correspond to reflections originating from the  $\gamma$ -phase, as the samples contain a high  $\gamma$ -phase content. As discussed previously, the overall decrease in the values of the LPs is at least partly a result of the underlying bimodal distribution of the first SAXS peak.

In addition to the LP, the value of the lamellar thickness (LT) is an important parameter characterizing the morphology of semi-crystalline materials. We also anticipate that this parameter plays an important role in morphology-mechanical (impact) properties relationships. As mentioned in the section Experimental the value of the LT can be estimated by multiplying the LP with the (volume)

crystallinity ( $\omega_c$ ). Therefore, we first present the results of the crystallinity measurements by WAXS before proceeding with the results on the calculated LTs.

## Crystallinity

Figure 3.13 shows the values of the degree of (volume) crystallinity for the samples mentioned in Table 3.1 as function of the combined defect fraction ( $\tilde{X}$ ). As the scattering in the measured values obscures a clear trend, two lines are indicated, which border the values measured for the degree of crystallinity.

The values for the degree of crystallinity of the  $\beta$ -phase are indicated for the three  $\beta$ -nucleated samples exhibiting negligible amounts of  $\alpha$ -phase (see the WAXS curves of these samples in Figure 3.8). The  $\beta$ -phase has a higher degree of crystallinity after isothermal crystallization (and cooling to room temperature) as compared to the  $\alpha$ -phase (for samples with a low defect content).

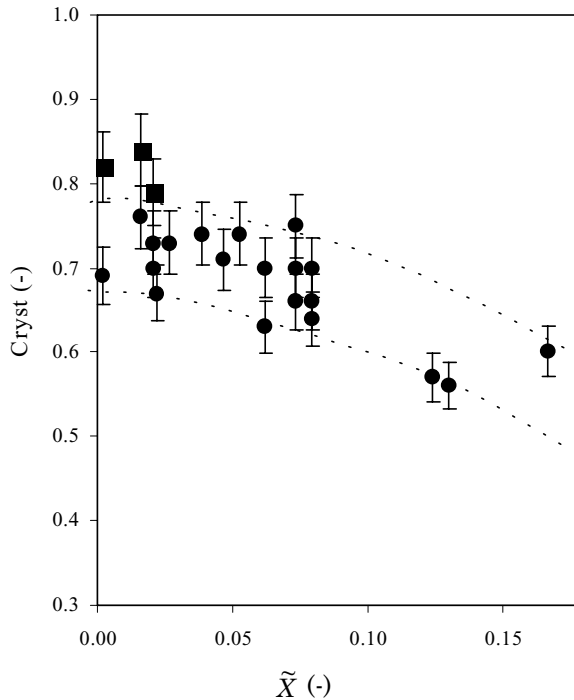


Figure 3.13. Degree of (volume) crystallinity ( $\omega_c$ ) after isothermal crystallization (and cooling to room temperature) for the polypropylene samples described in Table 3.1. ( $\bullet$ ) =  $\alpha$ -phase, ( $\blacksquare$ ) =  $\beta$ -phase. The relative error in the value of the degree of crystallinity is estimated as  $\pm 10\%$ .

Initially, the degree of crystallinity for the  $\alpha$ -phase is a weak function of the number of defects, however at higher defect-fractions the crystallinity decreases considerably. We can conclude that due to the incorporation of defects the amount of amorphous phase in the polymer increases. However, we can not conclude at this



stage whether the increase in amorphous phase is due to an increase in inter lamellar spacing or due to a break-up of the lamellar structure. The former, assuming a constant LP, would have a distinct influence on the lamellar thickness, while the latter would only decrease the lateral size of the lamellae. We should note that variations in crystallinity and lamellar thickness do not represent equilibrium structure in the thermodynamic sense and are determined by crystallization kinetics. Detailed analysis of the lamellar structure e.g. by transmission electron microscopy (TEM) would likely yield more insight into the origin of the decrease in crystallinity and the exact lamellar morphology. However, we have not completed such investigations in our work in view of a different experimental focus.

### **Lamellar thickness**

The lamellar thickness (LT) plays an important role in crystallization and fusion theories and is, for example, an important parameter determining the mechanical properties of the material. Therefore, the value of the LT is considered as one of the main parameters characterizing the morphology of semi-crystalline polymers. Assuming an ideal two-phase model in which crystalline and amorphous layers are regularly alternating, we may multiply the LPs with the volume fraction crystallinity as obtained from WAXS ( $\omega_c$ ) to estimate the values for the LT.

Results of the calculated LT values as function of defect-fraction are summarized in Figure 3.14. We included two dashed lines that border the values for the LT. One can see that after isothermal crystallization the value of the LT of the  $\beta$ -phase is higher compared with the  $\alpha$ -phase (strictly for samples with  $\tilde{X} < 0.03$  (-)). The values of the LTs of the  $\alpha$ - and  $\gamma$ -phases decrease with increasing values of the combined defect fraction. The average value of the LT of the  $\alpha$ -phase lamellae is approximately 13.8 nm for the polymer with negligible amount of defects.

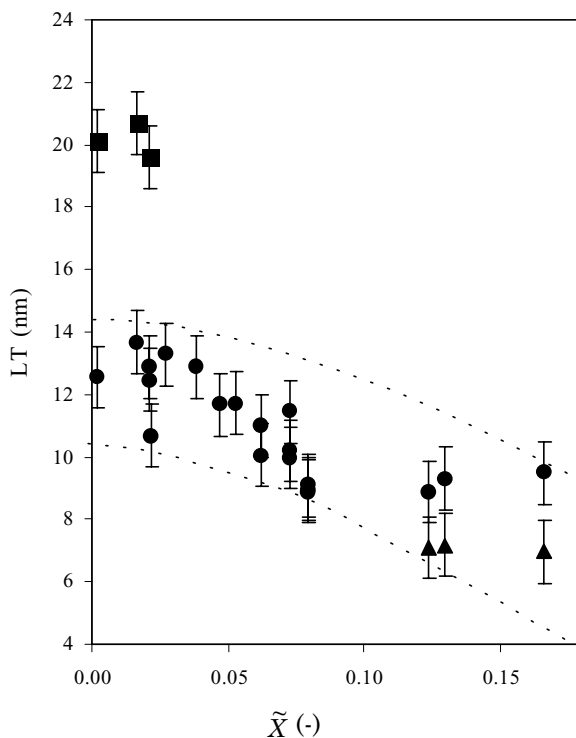


Figure 3.14. Lamellar thicknesses ( $LT$ s) of polymers mentioned in Table 3.1 as a function of combined defect-fraction.  $\beta$ -phase: (■);  $\alpha$ -phase: (●);  $\gamma$ -phase: (▲). The error is estimated as  $\pm 1.2$  nm.

### 3.3.5 Growth rate observations by LM

The previous section described the morphology of the samples listed in Table 3.1 after isothermal crystallization as a function of the number and type of defects. As mentioned in the introduction, the morphology of polymers is directly derived from the mechanism and kinetics of crystallization, which in turn depend on the primary chemical structure and chain topology of the macromolecules [1]. This section describes the isothermal growth kinetics of the samples used. The crystallization kinetics were characterized by the spherulitic growth rates measured by polarized light microscopy (LM).

The growth rate of crystallization ( $G$ ) was monitored by measuring the increase of the spherulitic diameter in the radial direction as a function of time. The spherulite size increased linearly with time and remained linear over the measured time. The growth rates of both  $\alpha$ - and  $\beta$ -phases of the Ziegler-Natta sample (indicated by 1, Figure 3.15) are larger compared with the growth rates ( $\alpha$ - and  $\beta$ -phases) measured for the more defected sample M9 (indicated by 2). We see that

the growth rate of the  $\beta$ -phase clearly exceeds the growth rate of the  $\alpha$ -phase for the ZN-sample. Furthermore, for the sample M9 the growth rates of the  $\beta$ - and  $\alpha$ -phases are approximately the same. These results indicate that the absolute growth rates depend on the number (and type) of defects and that the  $\beta$ -phase shows a stronger dependence on the number (and type) of defects than the  $\alpha$ -phase.

No influence of the molar mass on the spherulitic growth rate could be detected for the molar mass range studied here. For example, the polymers M9 and M10 with similar chain characteristics but different molar masses ( $8.25 \cdot 10^5$  g/mol and  $2.55 \cdot 10^5$  g/mol, respectively) show very similar growth rates ( $0.037$   $\mu\text{m/s}$  and  $0.035$   $\mu\text{m/s}$ , respectively).

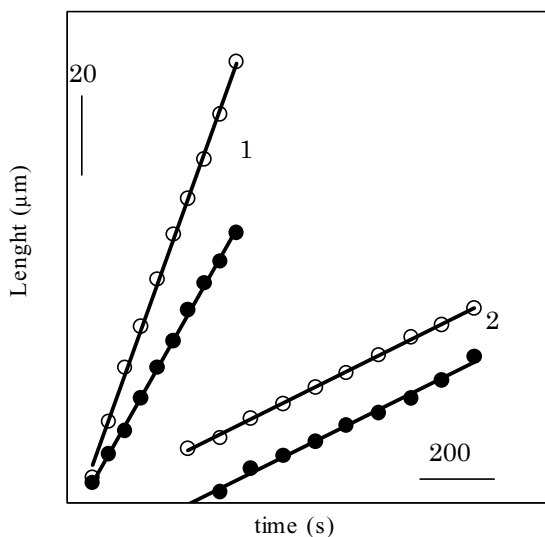


Figure 3.15. Variations of the spherulitic diameter with time for the samples ZN (1) and M9 (2) at crystallization temperature of  $130^\circ\text{C}$ . Open circles ( $\circ$ ) represent the  $\beta$ -phase, closed circles ( $\bullet$ ) originate from the  $\alpha$ -phase. Growth rates of the  $\alpha$ - and  $\beta$ -phases

Growth rates ( $G$ ) were determined for all samples mentioned in Table 3.1 at the crystallization temperature of  $130^\circ\text{C}$ . Linear growth rates with time were found for all polymers. Figure 3.16 shows the values of  $\ln(G)$  of isotactic-polypropylene ( $\alpha$ -phase) as a function of defect fraction. In principle, we measured the growth rates of spherulites consisting of the  $\alpha$ -phase, but at the same time an increase in the amount of  $\gamma$ -phase was detected in samples with increasing defect fraction (see section 3.3.3). As the formation of the  $\gamma$ -phase is related to the presence of the  $\alpha$ -phase, it was not possible to separately measure the growth rates of the  $\alpha$ - and  $\gamma$ -phases. Therefore, in the rest of this section we denote the growth rate of spherulites exhibiting both the  $\alpha$ - and  $\gamma$ -phases as  $G_\alpha$  (growth rate of the  $\alpha$ -phase).

The different specimens were grouped as described in section 3.3.1. The  $\ln(G)$  of specimen with the different types of dominating defects (regio- or stereo-defects)

were plotted according to a specific defect type as function of that defect fraction. The growth rates of the polymers:

- (1) with only *stereo*-defects (ZN, M1-M5) ( $\blacktriangle$ ) are plotted as function of the fraction *stereo*-defects (group 1);
- (2) which show a variation in the fraction *regio*-defects (M3-M10) ( $\blacksquare$ ) but with approximately the same fraction of *stereo*-defects are plotted as function of fraction *regio*-defects (group 2);
- (3) with *both* *stereo*- and *regio*-defects (BL15-M15) ( $\circ$ ) are plotted as function of fraction *stereo*-defects<sup>2</sup> (group 3).

Figure 3.16 shows a decrease in growth rate for all samples with increasing defect fraction. The growth rates of samples with a varying amount of *regio*-defects but constant amount of *stereo*-defects (group 2) show a much stronger dependence on the number of defects than the growth rates of the samples with only a varying amount of *stereo*-defects.

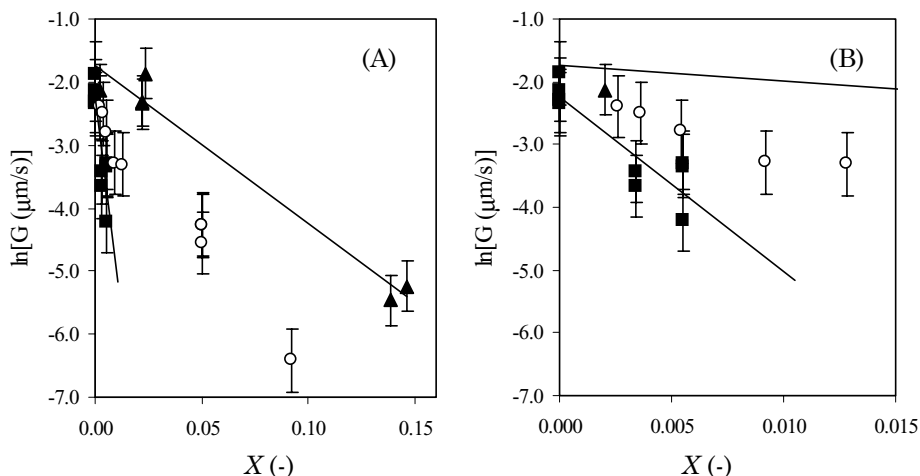


Figure 3.16. (A) Growth rates as a function of the defect fraction. (B) Magnification of a section showed in (A) for low defect fractions. The solid lines are fitted lines using a least squares fit through the data points. Assignments of symbols are given in the text.

As can be seen in Figure 3.16, two trend lines are given. One trend line shows the linear dependence of the growth rate as function of *stereo*-defects, while the other shows the linear dependence of the growth rate as function of *regio*-defects, respectively. The two trend lines can be presented as two linear equations:

$$\ln(G_{\alpha,s})_{X_s=0} = -(2.5 \pm 0.2) \cdot 10^1 X_s - (1.74 \pm 0.22) \quad \text{and} \quad (3.12a)$$

<sup>2</sup> In principle the growth rates of the polymers with both types of defects could be plotted also as function of *regio*-defects as well, however such analysis would not have any influence on the results.

$$\ln(G_{\alpha,r})_{X_s=0} = -(2.8 \pm 0.5) \cdot 10^2 X_r - (2.23 \pm 0.19), \quad (3.12b)$$

where  $\ln(G_{\alpha,s})_{X_r=0}$  corresponds to the logarithm of the growth rate of the  $\alpha$ -phase as function of stereo-defects with zero fraction of regio-defects.

In order to describe also the group of polymers which exhibit a variation in both stereo- and regio-defects ( $\circ$ ) a linear combination of equations 3.6a and 3.6b was made. The linear combination results in the following equation:

$$\ln(G_{\alpha,s/r}) = -(2.5 \pm 0.2) \cdot 10^1 X_s - (2.8 \pm 0.5) \cdot 10^2 X_r - (1.74 \pm 0.22), \quad (3.13a/b)$$

which can be simplified further:

$$\ln(G_{\alpha,s/r}) = -(2.5 \pm 0.2) \cdot 10^1 \tilde{X} - (1.74 \pm 0.22) \text{ where } \tilde{X} = X_s + (11.1 \pm 3.1)X_r. \quad (3.14a/b)$$

Similarly as described in section 3.3.3 a combined defect fraction ( $\tilde{X}$ ) is introduced.  $\tilde{X}$  is the sum of the number of stereo-defects and the number of regio-defects multiplied by a given *regio-error coefficient* with a certain value. The value of regio-error coefficient ( $11.1 \pm 3.1$ ) was calculated using an error propagation estimation. The combined defect fraction provides us with the possibility to describe any sample with an arbitrary amount of stereo- and regio-defects with a single parameter. The regio-error coefficient is a measure for (stronger) influence of regio-defects on the rate of crystallization.

The growth rate of the  $\beta$ -phase ( $G_\beta$ ) as function of the number and type of defects was measured, as well. Similar to Figure 3.16 for the  $\alpha$ -phase Figure 3.17 gives the natural logarithm of the growth rate of the  $\beta$ -phase ( $\ln(G_\beta)$ ) as a function of defect fraction. The polymers with different types of defects were grouped as it was done for the  $\alpha$ -phase.

The linear dependence of  $\ln(G_\beta)$  on the amount of *regio*-defects can be written in the following form:

$$\ln(G_{\beta,r})_{X_s=0} = -(4.4 \pm 0.8) \cdot 10^2 X_r - (2.1 \pm 0.3). \quad (3.15)$$

As one can see from equation 3.12b and 3.15, the values of the slopes are  $-2.8 \cdot 10^2$  and  $-4.4 \cdot 10^2$  for the  $\alpha$ - and  $\beta$ -phase, respectively. In addition to the general larger influence of the regio-defects on the growth rate, the influence of regio-defects on the growth rate of the  $\beta$ -phase is much larger as compared with the growth rate the  $\alpha$ -phase.

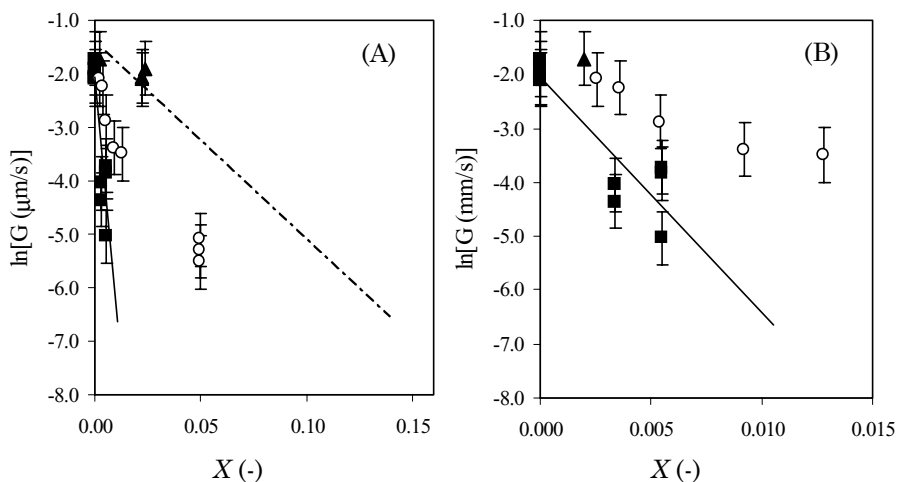


Figure 3.17. (A)  $\ln(G)$  of the  $\beta$ -phase for various samples as a function of the fraction of defects. The figure to the right (B) shows the dependence of the defect fractions with enlarged  $x$ -scale. The solid lines are fitted through the data points. Assignments of symbols are given in the text.

Unfortunately, the growth rates of the polymers with the highest defect concentrations could not be determined at the crystallization temperature of  $130^\circ\text{C}$ . The lowest growth rate for the  $\beta$ -phase, which was possible to directly measure was approximately  $0.0039 \mu\text{m/s}$ . For the samples with the highest defect fractions the relative growth rate of the  $\alpha$ -phase compared with the  $\beta$ -phase was much higher. Therefore, a growing  $\beta$ -phase crystal was readily surrounded and overgrown by surrounding  $\alpha$ -phase crystals. Moreover, the nucleating ability of the  $\beta$ -nucleant to induce the  $\beta$ -phase decreased with an increasing amount of defects, which resulted in practically undetectable amounts of the  $\beta$ -phase for these samples (see also section 3.3.3).

This imposes some practical problems if one wants to develop a similar analysis for the  $\beta$ - polymorph as for the  $\alpha$ -phase (see equations 3.12 - 3.15). Because of the missing data, we could not construct a trend line, which describes the correlation of the growth-rate dependence on only stereo-defects (for the  $\beta$ -phase). From the previous analysis of the  $\alpha$ -phase we found that  $\ln(G_\alpha)$  has a linear dependence on  $X_s$ . Therefore, a linear dependence of  $\ln(G_\beta)$  on  $X_s$  is expected, as well (see the dashed line Figure 3.17A). Assuming a linear relationship between  $\ln(G_\beta)$  and  $X_s$  we can write:

$$\ln(G_{\beta,s})_{X_s=0} = -C_1 X_s - 1.69. \quad (3.16)$$

Assuming that the constant ( $C_i$ ) is known, then a linear combination of equations 3.16 and 3.17 would describe the group of polymers with both stereo- and regio-defects ( $\circ$ ) as well as the samples exhibiting only stereo- or regio-defects. The

linear combination of equation 3.16 and 3.17 results in:

$$\ln(G_{\beta,s/r})_{\text{calculated}} = -C_1 X_s - 4.4 \cdot 10^2 X_r - 2.01. \quad (3.17)$$

We can obtain the value of  $C_1$  by plotting  $\ln(G_{\beta})_{\text{measured}}$  vs.  $\ln(G_{\beta,s/r})_{\text{calculated}}$  and maximizing the correlation coefficient. The figure below shows the result of the fitting procedure. The result of the fitting gives a value of  $3.8 \cdot 10^1$  for  $C_1$ . Figure 3.18 shows that all samples including the samples exhibiting stereo- and regio-defects, indicated with ( $\circ$ ), fall on the fitted line, which supports the assumption of linear additivity of the number of stereo- and regio-defects.

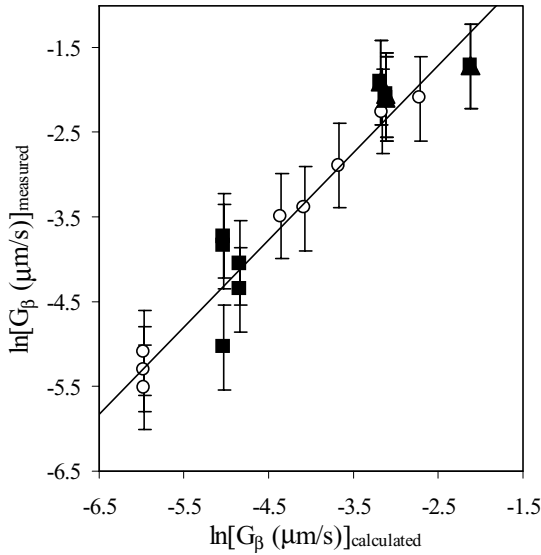


Figure 3.18. Plot of measured and calculated growth rates of the  $\beta$ -phase. Assignments of symbols are the same in Figure 3.17.

Another, complementary method to determine the value of  $C_1$  is given by an *indirect* determination of the  $\beta$ -phase growth rate at  $130^\circ\text{C}$  for samples with the highest defect concentrations (M1). The indirect method involves the measurement of the crystal growth rates of the  $\beta$ -phase at lower crystallization temperatures ( $105^\circ\text{C} < T_c < 120^\circ\text{C}$ ) followed by an extrapolation to the crystallization temperature of  $130^\circ\text{C}$ .

Figure 3.19A shows the results of the growth rates as function of various crystallization temperatures. The line through the measurement points is extrapolated to  $130^\circ\text{C}$  and gives value of  $\ln(G) = -6.6$  at  $130^\circ\text{C}$ . This value of the growth rate is plotted in Figure 3.19B and indicated by an arrow. In the figure also two lines are indicated; the solid line is a fitted line through the data points. The slope of the solid line has a value  $3.7 \cdot 10^1$ , which is the value of  $C_1$  (see equation 3.16). The dashed line is the graphical representation of equation 3.16 with the

previously determined value of  $3.8 \cdot 10^1$  for  $C_l$ . Since the slopes of the two lines are similar, support is given for the validation of the former applied method for the determination of  $C_l$ .

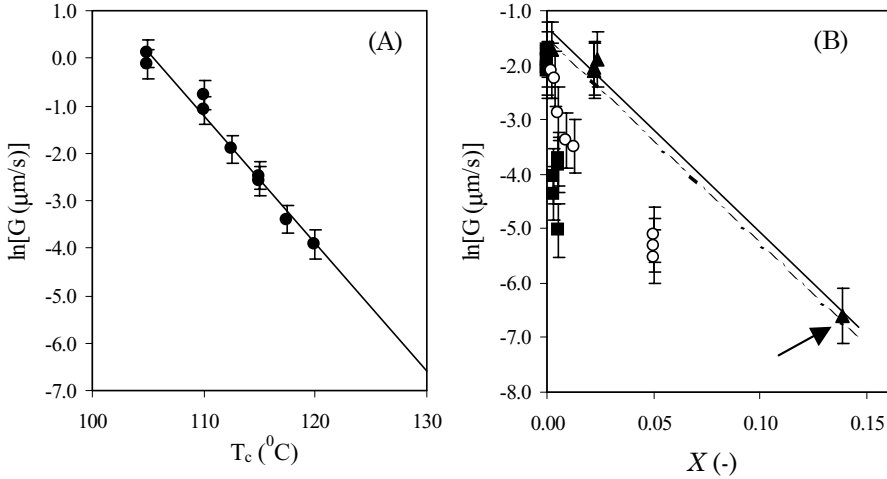


Figure 3.19. (A)  $\ln(G)$  of the  $\beta$ -phase for sample M1 as a function of crystallization temperature ( $T_c$ ). The figure to the right (B) shows  $\ln(G)$  of the  $\beta$ -phase for various samples as a function of the fraction of defects (= Figure 3.17). The solid lines are fitted through the data points, the dashed line obtained by using equation 3.16 and the value of  $C_l$  obtained from figure 3.18. Assignments of symbols are given in the text.

Since we estimated the value of  $C_l$  we can write equation 3.18 in a similar way as equation 3.14a/b:

$$\ln(G_{\beta,slr}) = -3.8 \cdot 10^1 \tilde{X} - 2.01, \quad \text{where} \quad \tilde{X} = X_s + 11.6X_r. \quad (3.18a/b)$$

The combined defect fractions of the  $\alpha$ - and  $\beta$ -phases show a remarkable resemblance. In both equations the influence of the regio-defects on the growth rate is approximately 11-12 times higher than the stereo-defects.

Comparing equation 3.12a and 3.18a we can draw the conclusion that the influence of *stereo*-defects on the growth rate of the  $\beta$ -phase is larger as compared to the influence of *stereo*-defects on the  $\alpha$ -phase. We already drew the conclusion that the influence of *regio*-defects on the growth rate of the  $\beta$ -phase is larger as compared to the influence of *regio*-defects on the  $\alpha$ -phase.

Although regio-defects have a *larger* influence on the crystallization rate of  $\beta$ -phase as compared to the  $\alpha$ -phase, regio-defects *compared* with stereo-defects exert a *similar* influence on the growth rate of the  $\alpha$ - and  $\beta$ -phases, respectively. In other words, the influence of the number of (stereo- and regio-) defects on the growth rate of the  $\beta$ -phase is a constant factor larger as compared with the  $\alpha$ -phase.



As mentioned before, the definition of the combined defect fraction ( $\tilde{X}$ ) provides us with the possibility to describe any sample with an arbitrary amount of stereo- and regio-defects. Utilizing this possibility the growth rate data of all samples mentioned in Table 3.1 (for both the  $\alpha$ - and  $\beta$ -phases) was plotted as function of the combined defect fraction. This procedure resulted in the following figure (Figure 3.20).

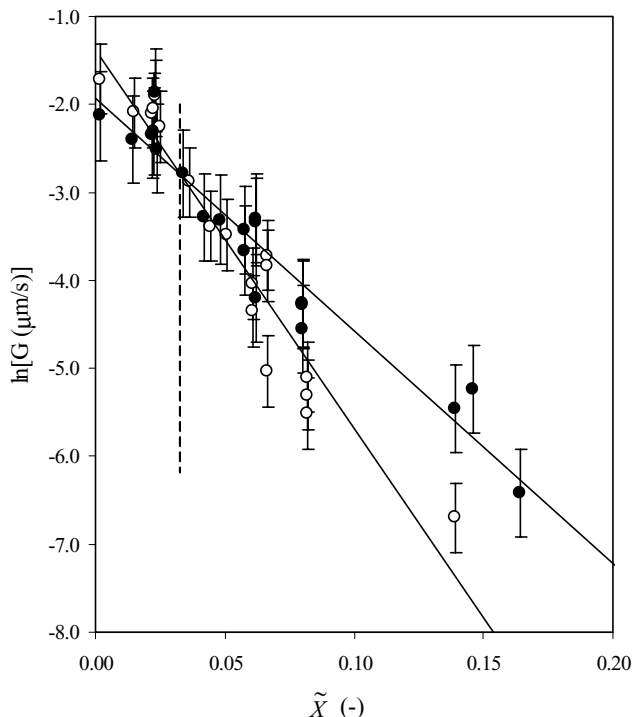


Figure 3.20. Growth rates as a function of the combined defect fraction. Open symbols (○): growth data for the  $\beta$ -phase. Closed symbols (●): growth data for the  $\alpha$ -phase.

Clearly,  $G_\beta$  is higher than  $G_\alpha$  at zero combined defect fraction, however, with increasing defects concentration  $G_\beta$  decreases stronger than  $G_\alpha$  as function of  $\tilde{X}$ . At approximately  $\tilde{X} = 0.03$  (-) a cross-over takes place, which is characterized by an equal growth rate of the  $\alpha$ - and  $\beta$ -phase ( $G_\beta = G_\alpha$ ). According to literature equal growth rates for both phases take place at a critical  $\beta\alpha$ -recrystallization temperature ( $T_{\beta\alpha}$ ) of 140°C for virtually defect-free samples. This critical temperature was determined using highly isotactic (Ziegler-Natta catalyzed) polypropylene samples. At a crystallization temperature  $T_c = 130^\circ\text{C}$  and at a combined defect fraction of 0.03 (-) the growth rates for the  $\alpha$ - and  $\beta$ -phases are equal. Consequently, for samples exhibiting a combined defect fraction of 0.03 (-) the  $T_{\beta\alpha}$  is lowered from 140°C to 130°C.

A lowering of the  $T_{\beta\alpha}$  has a profound influence on the formation of the  $\beta$ -phase under shear. The following section will discuss the formation and the consequences of increasing defect fraction on the formation of the  $\beta$ -phase under shear.

### 3.3.6 The shear induced formation of the $\beta$ -phase

The relative growth rates of the  $\alpha$ - and  $\beta$ -phases are important for the formation of the  $\beta$ -phase. In the previous section we saw that at the crystallization temperature of 130°C the ratio of  $G_\beta/G_\alpha$  decreases with increasing defect fraction and above  $\tilde{X} \approx 0.03$  (-),  $G_\beta < G_\alpha$ . In this section we study the consequences of the decreasing  $\beta\alpha$ -recrystallization temperature ( $T_{\beta\alpha}$ ) on the formation of the  $\beta$ -phase under shear conditions.

A cylindrical morphology is formed by crystallization of a melt under mechanical load (shear, elongation). The mechanical load can be introduced by pulling a fiber through a (under-cooled) melt at a certain temperature  $T_{\text{pull}}$ . The shear stress generated by fiber pulling produces row nuclei consisting of the  $\alpha$ -phase that induce the growth of a cylindrical growth front [53]. These row nuclei surround the fiber in a cylindrical fashion thus the growth front is cylindrical and proceeds in radial directions. The row nuclei likely consist of extended chain crystals [14,20,54] which act as nucleants for the  $\beta$ -phase. On these structures, if  $G_\beta > G_\alpha$ ,  $\beta$ -phase crystallites can nucleate (although at a lower nucleation density as compared with the nucleation density of the  $\alpha$ -phase). Figure 3.21 gives a schematic representation of such a cylindrical morphology.

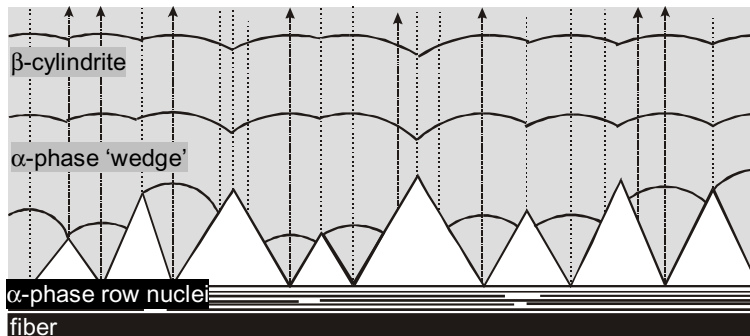


Figure 3.21. Schematic representation of the cylindrical morphology as described in literature [20,54]. The arrows indicate the direction of growth.

In typical shear-induced crystallization experiments performed in this research, a fiber was pulled at a controlled rate ( $v_{\text{pull}}$ ) for a predetermined time ( $t_{\text{pull}}$ ) (see section Experimental). The polymer was kept at 220°C for 5 min to remove the thermal-rheological history and then cooled to the temperature of crystallization ( $T_c = 130^\circ\text{C}$ ) within approximately 1 min. The temperature of pulling ( $T_{\text{pull}}$ ) was set to

be equal to  $T_c$ . The formation of the cylindritic morphology was followed with polarized light microscopy (LM). Figure 3.22 shows a typical morphology as revealed by LM of two fiber-pull experiments in which the time of pulling ( $t_{\text{pull}}$ ) was varied (1 and 8 sec).

The  $\beta$ -cylindritic structure as schematically presented in Figure 3.21 can be clearly seen in Figure 3.22B. An  $\alpha$ -phase ‘wedge’ is indicated with a white arrow. Due to the variation in  $t_{\text{pull}}$ , the morphology shows several differences, which can be seen best at the upper side of the fiber. The number of  $\beta$ -nuclei ( $N_\beta$ ) is much lower after a shorter shear time (1 sec). The  $\alpha$ -phase grows much longer unperturbed as can be seen by the larger ‘wedges’ (arrow in Figure 3.22B). In case of higher shearing times ( $t_{\text{pull}}$ ) more  $\beta$ -nuclei are generated, and as a consequence the  $\alpha$ -phase ‘wedges’ are smaller.

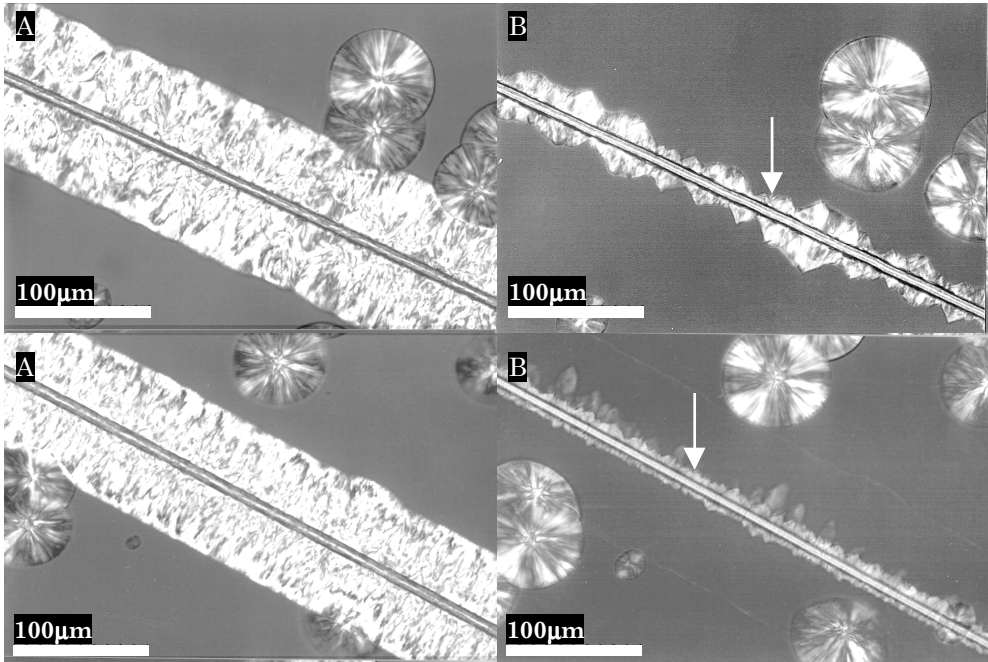


Figure 3.22. LM micrographs of cylindritic morphologies formed in typical shear experiments with  $t_{\text{pull}} = 1$  sec (A) and  $t_{\text{pull}} = 8$  sec (C). Micrographs (B) and (D) show the morphology after selective melting of the  $\beta$ -phase.

From the LM-micrographs we could quantify the number of  $\beta$ -nuclei. This was done by counting the number of “wedges” for a certain length of the fiber. The length of the fiber for which the number of nuclei was counted was chosen such that adding length to the already counted length did not change the mean value of  $N_\beta$  per unit length anymore. As the number of nuclei ( $N_\beta$ ) strongly increases with  $t_{\text{pull}}$  and  $v_{\text{pull}}$ , the distance between the nuclei becomes less and as a result the

determination of  $N_\beta$  becomes more difficult. This will increase the absolute error in the number of counted nuclei and limits the range in experimentally accessible values of  $t_{\text{pull}}$  and  $v_{\text{pull}}$ .

The number of  $\beta$ -nuclei ( $N_\beta$ ) was found to increase strongly with increasing  $v_{\text{pull}}$ , as seen in Figure 3.23 (note the logarithmic scale). The solid line in the figure is the most probable fit through the data points. Figure 3.23 gives an indication of a minimum shear rate for  $\beta$ -nucleus formation for the experimental conditions used (see the dashed line). The  $N_\beta$  per length will not reach zero because of the presence of sporadic nucleation of the  $\beta$ -phase in the crystallization of isotactic polypropylene. The limit is approximated by a line at  $v_{\text{pull}} \approx 1$  mm/s.

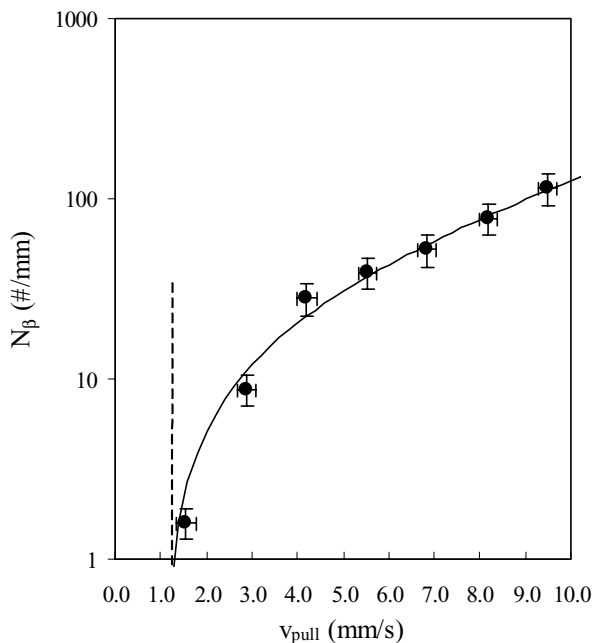


Figure 3.23. Number of  $\beta$ -nuclei as function of fiber pull speed ( $v_{\text{pull}}$ ).

The growth rate of the cylindrites was determined for various samples mentioned in Table 3.1. Growth rates of the cylindrites were determined by measuring the increase of the diameter perpendicular to the fiber direction as function of time (see the arrows in Figure 3.21). The size of the cylindrites increased linearly with time and remained linear over the measured time.

The following figure (Figure 3.24) shows the growth rates of the cylindritic structures as function of the combined defect fraction ( $\tilde{X}$ ). In this graph only samples with  $\tilde{X} < 0.06$  (-) are plotted. The growth rate of the cylindrites is linearly decreasing with increasing  $\tilde{X}$ . At  $\tilde{X} \approx 0.03$  (-), a distinct change in the slope can be seen. At this point the growth rates of the  $\alpha$ -phase equals that of the  $\beta$ -phase ( $G_\alpha = G_\beta$ ). As the upper recrystallization temperature ( $T_{\beta\alpha}$ ) is defined by the condition of

equal growth rates, we can state the condition ( $T_{\alpha\beta} < T_{\text{pull}} = T_c < T_{\beta\alpha}$ ) for the formation of  $\beta$ -cylindrites under shear is no longer fulfilled for samples containing more than  $\tilde{X} < 0.03$  defects (for  $\tilde{X} < 0.03$ ,  $T_{\beta\alpha} < T_c$ ). From LM observation we could determine that a  $\beta$ -cylindritic morphology was formed after shear in the samples with  $\tilde{X} < 0.03$  (-). However, samples containing more than  $\tilde{X} \approx 0.03$  (-) defect fraction showed simple  $\alpha$ -transcrystallization. The growth rates of the  $\beta$ - and  $\alpha$ -cylindrites were found the same as the growth rates of the  $\beta$ - and  $\alpha$ -spherulites, respectively (see Figure 3.20). The growth rates of the spherulites ( $\alpha$ - and  $\beta$ -phase) are indicated as dashed lines in Figure 3.24. An obvious question arises whether the transition at  $\tilde{X} \approx 0.03$  depends on the speed of the fiber or on the shearing time. We found the transition independent of both parameters, which implies that the condition  $T_{\alpha\beta} < T_c < T_{\beta\alpha}$  is a necessary condition to be fulfilled for the formation of the  $\beta$ -phase under shear.

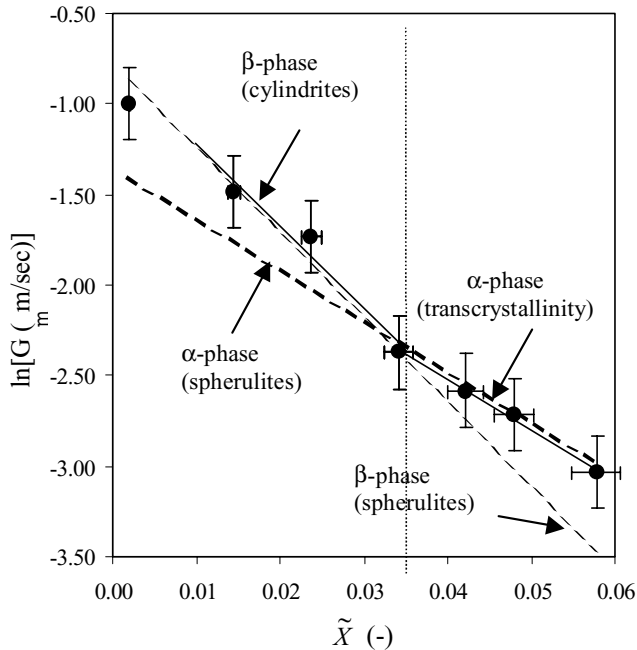


Figure 3.24. Growth rates of cylindrites after shearing as function of combined defect fraction. Indicated dashed lines are the trend-lines of the growth data from Figure 3.20 i.e. the growth data measured on spherulites.

### 3.4 Discussion

During the course of crystallization, defects will be partitioned among the amorphous and crystalline phases. It is not possible to establish a priori by theory the actual ratio of the amount of defects incorporated in the two phases [39], but two extreme cases can be distinguished: complete exclusion and uniform inclusion

of defects in the crystal phase [39]. In case of inclusion, the defect can either enter the lattice as an equilibrium requirement, or be located within the lattice as a non-equilibrium defect [39].

Several types of crystal defects can be distinguished [27] such as: dislocations, chain disorder, and amorphous defects. Dislocations occur when the periodicity of the crystal is interrupted along a certain direction. Chain disorder is specified as a point defect. It includes chain ends, kinks, and chain torsion. Amorphous defects can be described as an inclusion of a disordered region within the crystal. Obviously, the borderlines between the different crystal defects are not sharp and they vary in the energy, which is needed to incorporate such defects into the crystal, i.e. a point like chain disorder defect may result in an amorphous defect when the chain disorder is high enough.

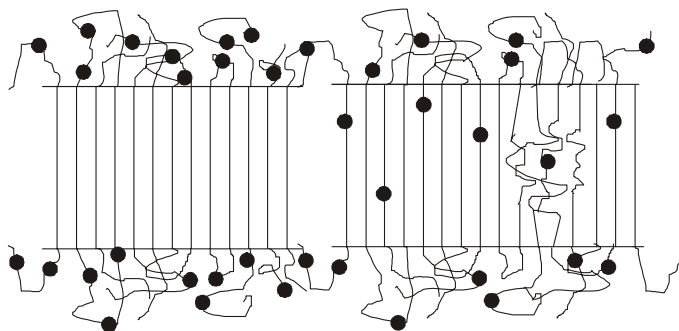


*Figure 3.25. Schematic representations showing the two limiting cases of crystallization of a polymer with defects; exclusion (left) and uniform inclusion (right). In the case of uniform inclusion several point like defects and one amorphous defect are schematically presented. Original scheme is made after Sanchez and Eby [55].*

As indicated in section 3.2.1 the samples listed in Table 3.1 contain two different types of defects e.g. regio- and stereo-defects with different characteristics. We saw from growth rate measurements that the regio-defects have a more pronounced influence on the crystallization rate as compared to the stereo-defects. As the crystallization of polypropylene involves the formation of a  $3_1$ -helix, we expect a larger influence of the regio-defects on the helical conformation of the iPP chain as compared with stereo defects.

In order to obtain a better understanding of the influence of the amount and different types of defects on the growth rate we analyzed our data with a theory originally developed by Lauritzen and Hoffman (LH-theory) [56], and later modified by Sanchez and Eby [55,57]. Although the LH-theory served as the basis for the derivation the theory, the final result will be independent of the exact molecular mechanisms (and thus the molecular background for the theory) involved for the particular case studied.

### 3.4.1 Crystallization of homo-polymers

In the LH-polymer crystallization theory the spherulitic growth rate ( $G$ ) at a given undercooling  $\Delta T = (T_m^0 - T)$  is given by the relation:

$$G = G_0 \exp\left(-\frac{U^*}{R(T - T_\infty)}\right) \exp\left(-\frac{K_g}{T\Delta T}\right) \text{ or } \ln G = \ln G_0 - \frac{U^*}{R(T - T_\infty)} - \frac{K_g}{T\Delta T}, \quad (3.19)$$

where  $U^*$  is the (material independent) activation energy for polymer diffusion across the phase boundary. For  $U^*$  the value of 6.28 kJ/mol was suggested by Hoffman *et al.* [58].  $R$  is the universal gas constant;  $K_g$  is called the secondary nucleation constant for a given regime;  $T_\infty$  is the temperature below diffusion of polymer segments is negligible ( $T_\infty = T_g - 30$  K) [58];  $T$  is the crystallization temperature and  $T_m^0$  is the equilibrium melting temperature for the completely defect-free (homo) polymer with infinite lamellar thickness and molar mass. The term  $G_0$  is a pre-exponential factor, which may slightly depend on temperature. However, its contribution to the temperature dependence of  $G$  is negligible relative to that of the transport term ( $U^*/R(T - T_\infty)$ ) and the nucleation free energy term ( $K_g/T\Delta T$ ), respectively [58]. The expression for the secondary nucleation constant is expressed by [1]:

$$K_g = \frac{n\sigma_u\sigma_e b_0 T_m^0}{R\Delta H^0}. \quad (3.20)$$

In this equation  $\sigma_u$  and  $\sigma_e$  are the interfacial lateral free energy and the interfacial surface free energy, respectively. The interfacial free energies defined here are related to nucleation (like all other terms) and cannot a priori be identified with characteristics of the mature crystallites that subsequently develop [1]. In equation (3.20) the term  $b_0$  is the layer thickness;  $n$  is a coefficient which depends on the growth regime:  $n = 4$  in regimes I and III and  $n = 2$  in regime II. For a description of the various regime we refer to the literature [59].

Inserting equation (3.20) into equation (3.19) yields the following equation for the secondary nucleation rate of homo-polymers (regime III) [60]:

$$\ln G = \ln G_0 - \frac{U^*}{R(T - T_\infty)} - \frac{4\sigma_u\sigma_e b_0 T_m^0}{R\Delta H^0 \Delta T T}. \quad (3.21)$$

As one can see, the growth rate depends exponentially on  $T_m^0/\Delta T T$ , according to equation (3.21). The spherulitic growth rate ( $G$ ) strongly depends on molar mass (MM). At a given temperature, the rate decreases when the molar mass increases up to a value where the growth is not affected by the length of the polymer chain, any further. If the kinetic nucleation theory is used in the infinite molecular weight approximation, the free energy of nucleation is given by equation (3.20).

### 3.4.2 Crystallization of copolymers

Crystallization kinetics are influenced by the molar mass and chemical structure of the macromolecules, pressure, strain, and by changes in chain architecture. Modifications of the sequence distribution and tacticity of the polymers chains lead to different crystallization kinetics and thus to different properties of the resulting crystallites. As far as crystallization kinetics are concerned, isomerism, stereo irregularities, and branching impart a co-polymeric character to the chain. The theory for copolymer crystallization (and melting) therefore can be applied for defect containing systems, as well.

The spherulitic growth-rate, as well as the overall crystallization rate, are reduced by increasing concentration of the chain defects in the polymer chain. Sanchez and Eby [61] derived a general expression for the spherulitic growth rate  $G$  (assuming a coherent surface nucleus and regime III growth):

$$\ln G = \ln G_0 - \frac{U^*}{R(T - T_\infty)} - \frac{2\sigma_u b_0 l_{c,i}^0 [1 + f(X, T)]}{RT}. \quad (3.22)$$

It is possible to express the nucleation rate of the copolymer in terms of the homo-polymer nucleation rate plus a term that contains the co-monomer concentration if the following function is defined:

$$f(X, T) \equiv \frac{\Delta G^0}{\Delta G^*} - 1. \quad (3.23)$$

The term  $\Delta G^0$  is the bulk free energy difference for the complete defect-free (homo) polymer with infinite lamellar thickness and molar mass comparable to the defect containing “real” lamella of infinite thickness and is usually approximated by

$$\Delta G^0 = \Delta H^0 (1 - T/T_m^0). \quad (3.24)$$

For  $\Delta G^0$  it is assumed that at moderate super-cooling the heat of fusion ( $\Delta H^0$ ) and entropy of fusion ( $\Delta S^0$ ) are temperature independent [62]. From nucleation theory [62] it follows that:

$$l_{c,i} = 2\sigma_e / \Delta G^0 + \delta l_c, \quad (3.25)$$

where  $l_{c,i}$  is the initial crystal thickness and  $\sigma_e$  is the surface free energy.  $\delta l_c$  is the extra thickness a crystal needs to be stable above the crystallization temperature. The minimum crystal thickness possible at the particular crystallization temperature is given by  $2\sigma_e / \Delta G^0$ . Under the assumption that  $\delta l_c = 0$ , we get for crystallized polymers with a finite lamellar thicknesses:  $l_{c,i}^0 = 2\sigma_e / \Delta G^0$ .

The term  $\Delta G^*$  is the bulk free energy difference between a crystal with partially included defects with concentration  $X_c$  and the melt with a concentration of defects equal to the overall defect composition  $X$ .



$\Delta G^*$  is given by [39]:

$$\Delta G^* = \Delta G^0 - RT \left( \frac{\varepsilon X_c}{RT} + (1 - X_c) \ln \left[ \frac{1 - X_c}{1 - X} \right] + X_c \ln \left[ \frac{X_c}{X} \right] \right). \quad (3.26)$$

The excess free energy of the defect, created by incorporating a defect in the crystalline lattice is labeled by  $\varepsilon$ .

The tendency to enter the lattice depends on the excess free energy of the defect ( $\varepsilon$ ). It was shown [39] that under equilibrium conditions the fraction of defects, which enter the crystal lattice with a penalty  $\varepsilon$  can be calculated using [63]:

$$X_c^{eq} = \frac{X e^{-\varepsilon/RT}}{(1 - X) + X e^{-\varepsilon/RT}}. \quad (3.27)$$

The parameter  $X_c^{eq}$  is the equilibrium fraction of defects in the crystal and  $X$  is the global defect fraction of the melt prior to crystallization. Insertion of equation (3.27) into equation (3.26) yields the free energy of crystals with an equilibrium defect concentration [39]:

$$\Delta G^* = \Delta G^0 + RT \ln(1 - X + X e^{-\varepsilon/RT}). \quad (3.28)$$

When the concentration of defects is negligible ( $X_c = 0$ ) then equation (3.26) is reduced to the exclusion limit:

$$\Delta G^* = \Delta G^0 + RT \ln(1 - X). \quad (3.29)$$

Equation (3.29) can also be obtained from equation (3.28) by increasing  $\varepsilon$  to infinity ( $\varepsilon \rightarrow \infty$ ). Using the equations for the bulk free energy difference between a crystal with partially included defects and the copolymer melt ( $\Delta G^*$ ) in conjunction with equation (3.23) we obtain for the parameter  $f(X, T)$ :

$$f(X, T) = \frac{-RT \ln(1 - X + X e^{-\varepsilon/RT})}{\Delta G^0 + RT \ln(1 - X + X e^{-\varepsilon/RT})} = \lim_{X \rightarrow 0} \frac{RT \cdot X}{\Delta G^0} (1 - e^{-\varepsilon/RT}) \quad (3.30)$$

and

$$f(X, T) = \frac{-RT \ln(1 - X)}{\Delta G^0 + RT \ln(1 - X)} = \lim_{X \rightarrow 0} \frac{RT \cdot X}{\Delta G^0} \quad (3.31)$$

for the equilibrium and total exclusion limit, respectively.

Since the expressions for  $f(X, T)$  are given for the different cases, we can continue with the general expression for the spherulitic growth rate  $G$  (equation (3.22)). As  $f(X, T)$  incorporates the influence of the defects on the crystallization, it is possible to separate the terms referring to the copolymer and the homopolymer,

respectively. Under the assumption that the transport term is independent of the copolymer composition for low defect fractions ( $X < 0.15$ ), the separation of terms results in the following equation for  $\ln(G)$  [55].

$$\ln G = \ln G^0 - \frac{-2\sigma_u b_0 I_{c,i}^0 f(X, T)}{RT} \quad \text{or} \quad \ln G = \ln G^0 - \frac{-4\sigma_u \sigma_e b_0 T_m^0 f(X, T)}{RT\Delta H^0 \Delta T}, \quad (3.32)$$

where  $G^0$  is the growth rate of the homo-polymer (not the pre-exponential factor  $G_\theta$ ). Inserting the expressions for  $f(X, T)$  (i.e. equation (3.30) or (3.31)) into equation (3.32) yield the growth rate in case of equilibrium inclusion of defects into the crystal:

$$\ln G = \ln G^0 - \frac{4\sigma_u \sigma_e b_0 T_m^0 \cdot RT \ln(1 - X + X e^{-\varepsilon/RT})}{R\Delta H^0 \Delta T \cdot (\Delta G^0 + RT \ln(1 - X + X e^{-\varepsilon/RT}))} \quad (3.33)$$

and the growth rate in the case of total exclusion of defect in given by:

$$\ln G = \ln G^0 - \frac{4\sigma_u \sigma_e b_0 T_m^0 \cdot RT \ln(1 - X)}{R\Delta H^0 \Delta T \cdot (\Delta G^0 + RT \ln(1 - X))}. \quad (3.34)$$

Equation (3.34) is the same expression for the co-polymer crystallization as described by Helfand [63] and Mandelkern [1]. In case  $X = 0$  equations (3.33) and (3.34) reduce to the homo-polymer case as described above, see equation (3.21).

### 3.4.3 Analysis of the crystallization behavior of the $\alpha$ - and $\beta$ -phases of polypropylene

In this section we analyze the results of the dependence of the growth rates on the fraction of defects with the theory described in the sections above. At the crystallization temperature used in the experiments, isotactic polypropylene crystallizes in regime III [59], which makes it possible to use equations (3.33) or (3.34) given in the previous analysis. In the equations (3.33) or (3.34) the expression for  $\Delta G^0$  is given by equation (3.24) and the remaining parameters can be found in literature [2,64,65]. However, the values, especially for  $\sigma_u$  and  $\sigma_e$ , which are reported in the literature are widely scattered [14]. Therefore, the parameters were determined independently using the growth rate expression for the *homo*-polymer, see equation (3.21). As a representative for a homo-polymer we took the polymer with the least amount of defects (M4). The growth rate of this polymer as function of temperature was determined.

From a plot of  $\ln(G) + U^*/(R(T - T_\infty))$  against  $1/T\Delta T$  we obtain from equation (3.21) the following term from the slope:

$$\frac{4\sigma_u \sigma_e b_0 T_m^0}{R\Delta H^0} = K_g, \quad (3.35)$$

which contains all the necessary parameters (including  $\sigma_u$  and  $\sigma_e$ ) for the calculation of  $\ln(G)$ , see equation (3.32). The growth rates were measured for temperatures between 396 K and 408 K. Figure 3.26 shows the result. From the slope we obtain the following values for the  $\alpha$ -phase:  $K_g = 3.68 \cdot 10^5 \text{ K}^2$  and  $\beta$ -phase:  $K_g = 2.46 \cdot 10^5 \text{ K}^2$ , respectively. The only unknown parameter, which is left for the calculation of  $\ln(G)$  as function of  $X$  is the excess free energy ( $\epsilon$ ) needed to incorporate a stereo defect into a crystal lattice. This parameter is used as a fitting parameter.

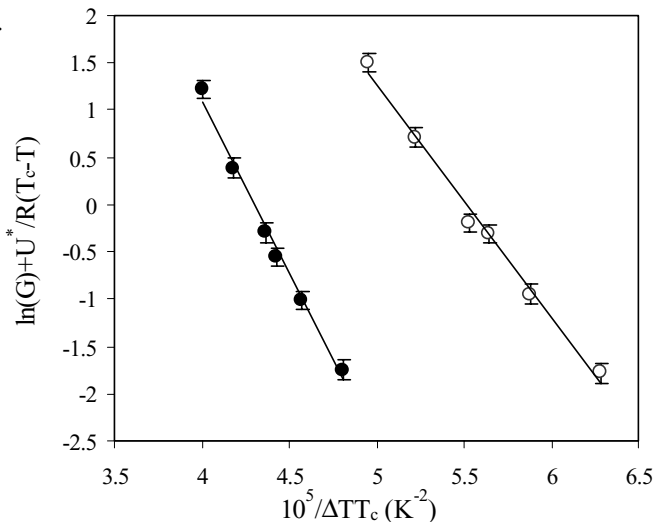


Figure 3.26. Plot of  $\ln(G)+U^*/(R(T-T_\infty))$  against  $1/T\Delta T$ . Closed symbols (●) represent the  $\alpha$ -phase, open symbols (○) indicate the  $\beta$ -phase.

The fitting using equations (3.33) and (3.34) was performed for the  $\alpha$ - as well as for the  $\beta$ -phase. Figure 3.27 shows the result for the calculation of  $\ln(G)$  as function of  $X$ . An excellent agreement is found between the calculated growth rates using the equilibrium inclusion of defects and the observed growth rate data for samples containing only a variation in the amount of stereo-defects. It is found that the growth rates of the defected polymer samples are decreased compared to the homopolymer samples. The model correctly predicts a critical defect fraction for which  $G_\alpha = G_\beta$ .

In the fitting we assumed a value of the excess free energy value for including a *stereo*-defect into an  $\alpha$ -phase crystal of  $\epsilon = 1.6 \text{ kJ mol}^{-1}$ . The value for the excess energy for including a *stereo*-defect into the  $\beta$ -phase lattice is  $\epsilon = 1.2 \text{ kJ mol}^{-1}$ . The excess free energy is thus lower for the trigonal crystal as compared to the monoclinic crystal.

For the fitting of the samples with regio-defects we maximized the excess defect free energy ( $\epsilon \rightarrow \infty$ ), which means that under equilibrium conditions virtually no regio-defects are included in the crystal (conform with equation (3.34)). The growth rate data of the samples with a varying amount of regio defects could be

less satisfactorily fitted with the model. Nevertheless, the model accounts for the much larger decrease in the growth rate due to the expelling of defects from the lattice. The model also rightly predicts the growth rate of the  $\beta$ -phase relative to the  $\alpha$ -phase, i.e. the model shows a lower growth rate for the  $\beta$ -phase instead of the  $\alpha$ -phase.

As the total exclusion of defects cannot account for the strong deceleration of the spherulitic growth rate in polymers exhibiting regio-defects, we can conclude that a certain amount of the total fraction of regio-defect will be included into the crystal as non-equilibrium defects, provided that the theory we used can be applied. The fraction of regio defects in the crystal phase will be lower as compared to the fraction of stereo-defect, as the excess free energy of regio defects is much higher.

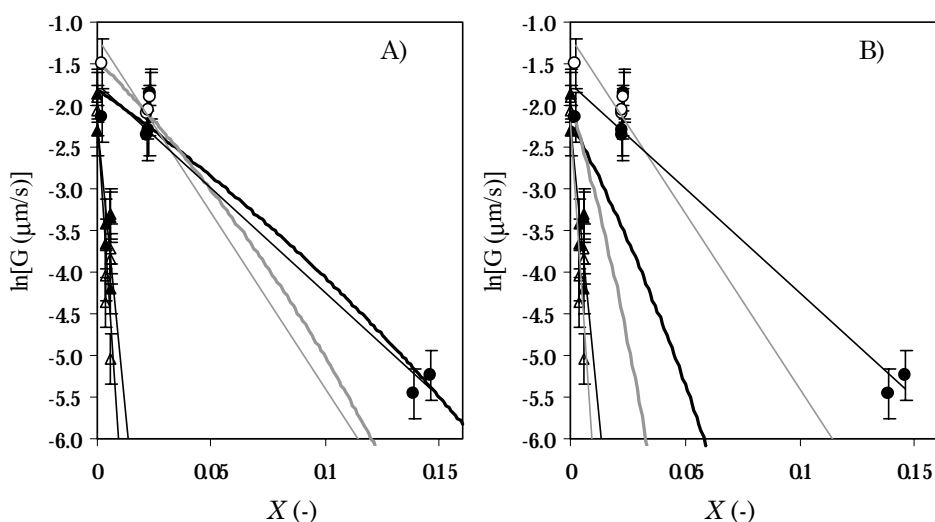


Figure 3.27. Calculated and measured growth rates of the  $\alpha$ - and  $\beta$ -phases. A) Calculated and measured growth rates in the case of equilibrium inclusion of defects B) Calculated and measured growth rates in the case of total exclusion of defects. The thick black-lines (—) and thick gray-lines (—) label the results for the  $\alpha$ -phase and  $\beta$ -phase, respectively. Indicated are the measured growth rate data (and trend lines) for the stereo-defected samples (group 1); ( $\circ$ ) =  $\beta$ -phase; ( $\bullet$ ) =  $\alpha$ -phase and the regio-defected samples (group 2); ( $\blacktriangle$ ) =  $\beta$ -phase; ( $\triangle$ ) =  $\alpha$ -phase.

In principle, the distribution of defects between the amorphous and crystalline regions might depend on both the crystallization kinetics and on the crystal characteristics. It is not possible to establish a priori by theory the actual ratio of the amount of defects among the two phases [39]. Mandelkern *et al.* [66] made large progress in determining the partitioning of several types of defects experimentally for stereo- and regio-defects of isotactic polypropylene ( $\alpha$ -phase) using  $^{13}\text{C}$ -NMR. They demonstrated that the partitioning of the defects do not depend on the kinetics of crystallization.

For clarity we plotted  $f(X, T)$  for the total exclusion and equilibrium inclusion as function of  $X$  (for the  $\alpha$ - and  $\beta$ -phases, respectively). As expected  $f(X, T)$  increases with increasing defect fraction, see Figure 3.28. The figure shows that for small  $X$  the parameter  $f(X, T)$  is approximately a linear function of the fraction of defects. However,  $f(X, T)$  diverts from linearity for larger defect fraction. Obviously this has consequences for the prediction of the growth rate depression (see Figure 3.27). In the original derivation for  $f(X, T)$  by Sanchez and Eby [55], the expressions for  $f(X, T)$  were expanded in a power series under the assumption of small  $X$  ( $X < 0.1$  (-)). Although mathematically correct the expansion in power series is not required and in this thesis use was made of the basic expressions of  $f(X, T)$  for copolymers.

The parameter  $f(X, T)$  was calculated separately for both total exclusion of defects as well as for uniform inclusion, the latter for the  $\alpha$ - as well as for  $\beta$ -phases. The results of the calculation of  $f(X, T)$  is graphically presented in Figure 3.28.

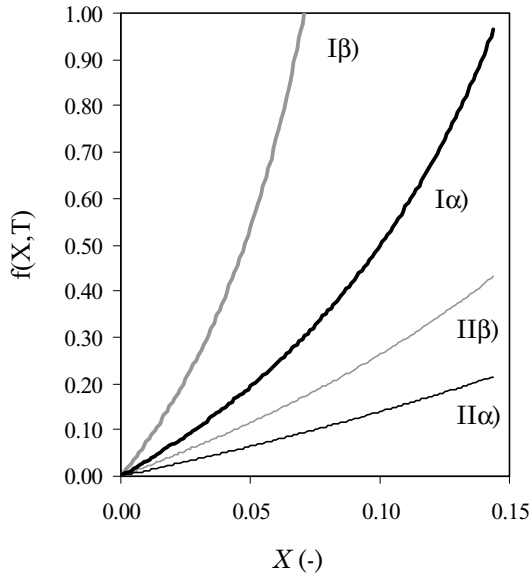


Figure 3.28. The parameter  $f(X, T)$  as function of  $X$  for the  $\alpha$ - and  $\beta$ -phases, respectively. I)  $f(X, T)$  in case of total exclusion (equation (3.13)), II)  $f(X, T)$  in the case of equilibrium inclusion (equation (3.30)).

The product of  $K_g$  with  $f(X, T)$  determines the growth rate dependence on  $X$ . From Figure 3.26 it was concluded that the value of  $K_g$  for the  $\beta$ -phase is smaller as compared to the  $\alpha$ -phase, however, from Figure 3.20 we saw that the growth rate of the  $\beta$ -phase is a stronger function of  $X$ . As a consequence we may conclude that  $f(X, T)$  predominantly determines the growth rate dependence on  $X$  compared with the effect of  $K_g$ . In turn, the trend of  $f(X, T)$  with  $X$  (especially for small  $X$ ) is very sensitive on the value of the bulk free energy of the homo-polymer ( $\Delta G^0$ ), see equations (3.30) and (3.31). It follows from the theory that the excess free energy

determines largely the magnitude of the growth rate dependence ( $G$ ) on  $X$ . The higher the value of  $\varepsilon$  the larger the dependence of the growth rate on the number of defects. The influence of  $X$  on the growth rate is maximum when the energy of inclusion is infinite. A higher value of  $\varepsilon$  would result in a lower content of defects in the lattice. The prevention of inclusion of defects will retard the rate of crystallization. Under non-equilibrium conditions some of the defects will be introduced into the lattice. Energetically the inclusion of such defects is very unfavorable and therefore will retard, or even cease, the crystallization at that point.

In the section Results of this chapter we defined the following function (equation (3.14a/b)) for the growth rate of the  $\alpha$ -phase:

$$\ln(G_{\alpha,s/r}) = -(2.5 \pm 0.2) \cdot 10^1 \tilde{X} - (1.74 \pm 0.22) \quad \text{where } \tilde{X} = X_s + (11.1 \pm 3.1)X_r. \quad (3.36a/b)$$

A combined defect fraction ( $\tilde{X}$ ) was introduced and defined as the sum of the number of stereo-defects and the number of regio-defects multiplied by a given *regio-error coefficient* with a certain value ( $11.1 \pm 3.1$ ). With the current copolymer crystallization theory an expression for the regio-error coefficient can be found. Similarly as in section 3.4.3 we construct a linear combination of the expression describing the (theoretically found) growth rates of samples containing stereo- and regio-defects:

$$\ln(G_{\alpha,s/r}) = -\frac{2\sigma_u\sigma_e b_0}{R\Delta H^0 T\Delta T} f(X_r, T) - \frac{2\sigma_u\sigma_e b_0}{R\Delta H^0 T\Delta T} f(X_s, T) - \ln(G^0). \quad (3.37)$$

We can introduce the following functions:

$$f(X_r, T) = f'(X_r, T)X_r \quad \text{and} \quad f(X_s, T) = f'(X_s, T)X_s. \quad (3.38)$$

By inserting equation (3.38) in equation (3.37) the following result can be obtained:

$$\ln(G_{\alpha,s/r}) = -\left(\frac{2\sigma_u\sigma_e b_0}{R\Delta H^0 T\Delta T} f'(X_s, T)\right) \tilde{X} - \ln(G^0) \quad \text{with } \tilde{X} = \left(X_s + \frac{f'(X_r, T)}{f'(X_r, T)} X_r\right). \quad (3.39a/b)$$

Equations (3.39a/b) are mathematically similar to equations (3.14a/b) or (3.36a/b) when  $f'(X_s, T)$  is not a strong function of  $X$  and thus can be approximated by a constant. In principle this is only valid for small  $X_s$ . However, since  $f(X_s, T)$  is approximately a linear function of  $X_s$  (as was for example shown in Figure 3.28 by the curves  $\text{II}\alpha$  and  $\text{II}\beta$ ) we may assume that  $f'(X_s, T)$  is constant for larger  $X_s$ , as well. Equation (3.39a/b) gives an expression for the combined defect fraction and regio-error coefficient. The regio-error coefficient is given by:  $f'(X_r, T)/f'(X_s, T)$ . A similar analysis can be done for the  $\beta$ -phase and will yield a similar result. Equation (3.39a/b) provides us with the opportunity to describe any sample

exhibiting both stereo- and regio-defects.

### 3.4.4 The influence of secondary crystallization

The overall crystallization is made up of at least two steps, the initial crystallization, followed by the so called secondary crystallization. The secondary crystallization can be separated into at least two processes. The first process involves the further crystallization of amorphous material, the real secondary crystallization. After the initial crystallization the crystallinity still increases when the sample is kept at the crystallization temperature. The second process is related to the further perfection of initially poorly crystallized macromolecules and is called crystal perfection. The slow increase in crystallinity and crystal perfection was frequently observed to have a logarithmic time dependence for many decades before ceasing and the overall rate is faster at higher crystallization temperatures. In order to keep the effect of this type of secondary crystallization comparable for all the crystallized polymers, the samples were kept at the crystallization temperature until fully crystallized, e.g. to the end of the typical crystallization bell-shape isotherm measured by DSC.

In addition to the secondary crystallization of the polymer at the isothermal crystallization temperature, the sample may also undergo secondary crystallization during cooling to room-temperature (RT). This type of secondary crystallization is a further stabilization of the material and may involve further lamellar thickening and crystallizing of material, which was not able to crystallize at the initial crystallization temperature. This type of secondary crystallization may influence the results from SAXS and WAXS measurements. It is expected that secondary crystallization takes place in both the  $\alpha/\gamma$ -phases and the  $\beta$ -phase after cooling from crystallization temperature to room temperature.

Since the WAXS determination of the  $\gamma$ -phase fraction was carried out at room temperature, the value determined for the  $\gamma$ -phase content is slightly different as the amount of  $\gamma$ -phase crystallized at crystallization temperature. The secondary crystallization (cooling down to RT) may affect, in addition to the result obtained by WAXS, also the results obtained by SAXS. Secondary crystallization may result in a population of relatively thin lamellae with small lateral dimensions [39]. The secondary crystallization may not be the same for all samples. It is possible that in the initial isothermal crystallization less material is able to crystallize in the more defected samples. We therefore expect a larger secondary crystallization of the samples with relatively high defect concentrations. The population of these small lamellae contribute to the SAXS scattering at high values of the scattering angle ( $q$ ). This could explain the observed increase in the scattering at higher values of  $q$  for samples with relatively high defect concentrations. The second type of secondary crystallization results in an increase in the amount of the crystalline phase following the initial crystallization, therefore the degree of crystallinity measured

by WAXS will be an overestimation. A change in the value of the degree of crystallinity will influence the values of the lamellar thickness, which is the product of the long-period with the weight fraction degree of crystallinity. So both the first and second type of secondary crystallization increase the value of lamellar thickness. At this moment we can not be conclusive about the magnitude of these effects. However we do not expect that these effects will change the trends and the overall conclusions made in this work.

## 3.5 Conclusions

For the research described in this chapter we collected an unprecedented group of polypropylene polymers with a wide variety of stereo- and regio-defects. The characteristics of the samples were such that we could independently investigate the influence of the type of defect on the crystallization rate and morphology of the  $\alpha$ -,  $\beta$ -, and  $\gamma$ -phases, respectively.

The long-period of the  $\beta$ -phase slightly increased with increasing defect fraction. The long-period of the  $\alpha$ -phase as measured by SAXS showed a complex behavior. The increasing amount of  $\gamma$ -phase and the bimodal distribution due to the presence of primary and cross-hatched lamellae gave rise to a complex scattering curve from which no direct analysis of the long-period distribution was possible. For the polymers with zero defect fraction, the long-period and the lamellar thickness were larger for the  $\beta$ -phase as compared with  $\alpha/\gamma$ -phases.

Growth rates of the  $\alpha$ -, and  $\beta$ -allomorphs were measured under isothermal crystallization conditions as a function of the amount and type of defects. The growth rate dependence of the  $\beta$ -phase on the number of defects was much larger as compared with the  $\alpha/\gamma$ -phases. As the growth rate of the  $\beta$ -phase is higher for pure isotactic polypropylene, but lower for more defected isotactic polypropylenes, a critical defect fraction was found for which the growth rates of both phases are the same. For samples having this specific critical defect fraction the critical upper recrystallization temperature of isotactic polypropylene is lowered to 130°C.

A combined defect fraction (CDF) was introduced to uniformly and uniquely describe all samples with a random arbitrarily amount and type of defects. The CDF is the sum of the number of stereo-defects and the number of regio-defects multiplied by a certain regio error coefficient. This coefficient showed that the influence on crystallization of regio-defects compared with stereo-defects is much larger.

Crystallization rates were analyzed according to the theory of Sanchez and Eby. The theory rightly predicts the stronger dependence of the growth rate of the  $\beta$ -phase on the defect fraction as compared with  $\alpha$ -phase. The theory also predicts the critical defect fraction for which the growth rates of the  $\alpha$ - and  $\beta$ -phases are equal.



The equilibrium conditions for which the theory initial has been developed provides the borders for the non-equilibrium crystallization of copolymers. Finally, the theory gives an analytically expression for the CDF and the belonging weighting factor.

In conclusion, we may state that polypropylene is a polymorphic polymer that provides us with a unique opportunity to study the influence of the chain architecture (regio-defects independently of stereo-defect) on the crystallization and thus on the three crystalline-phases existing in polypropylene.

## 3.6 References

- (1) Alamo, R. G.; Mandelkern, L. Crystallization kinetics of random ethylene copolymers *Macromolecules* **1991**, *24*, 6480.
- (2) Cheng, S. Z. D.; Janimak, J. J.; Zhang, A. Isotacticity effect on the crystallization and melting in polypropylene fractions: 1. Crystalline structures and thermodynamic property changes *Polymer* **1991**, *32*, 648.
- (3) Janimak, J. J.; Cheng, S. Z. D.; Giusti, P. A. Isotacticity effect on crystallization and melting in polypropylene fractions: 2. Linear crystal-growth rate and morphology study *Macromolecules* **1991**, *24*, 2253.
- (4) Fischer, D.; Mulhaupt, R. The influence of regio- and stereo-irregularities on the crystallization behaviour of isotactic polypropylenes prepared with homogeneous group IVa metallocene/methylaluminumoxane Ziegler-Natta catalysts *Macromol. Chem. Phys.* **1994**, *195*, 1433.
- (5) Yamada, K.; Matsumoto, S.; Tagashira, K.; Hikosaka, M. Isotacticity dependence of spherulitic morphology of isotactic polypropylene *Polymer* **1998**, *39*, 5327.
- (6) Suhm, J. New molecular and super molecular polymer archistructures via transition metal catalysed alkene polymerization *J. Mat. Chem.* **1998**, *8*, 553.
- (7) Thomann, R.; Wang, C.; Kressler, J.; Mulhaupt, R. On the gamma-phase of isotactic polypropylene *Macromolecules* **1996**, *29*, 8425.
- (8) Thomann, R.; Semke, H.; Maier, R. D.; Thomann, Y.; Scherble, J.; Mulhaupt, R.; Kressler, J. Influence of stereo irregularities on the formation of the gamma-phase in isotactic polypropene *Polymer* **2001**, *42*, 4597.
- (9) Radhakrishnan, J.; Ichikawa, K.; Yamada, K. Nearly pure alpha2 form crystals obtained by melt crystallization of high tacticity isotactic polypropylene *Polymer* **1998**, *39*, 2995.
- (10) Paukkeri, R.; Lehtinen, A. Thermal behaviour of polypropylene fractions: 1. Influence of tacticity and molecular weight on crystallization and melting behaviour *Polymer* **1993**, *34*, 4075.

- (11) Karger-Kocsis, J.; Varga, J.; Ehrenstein, G. W. Comparison of the fracture and failure behavior of injection-molded alfa- and beta-polypropylene in high-speed three-point bending tests *J. Appl. Polym. Sci.* **1997**, *64*, 2057.
- (12) Raab, M.; Kotek, J.; Baldrian, J.; Grellmann, W. Toughness profile in injection molded polypropylene: The effect of the beta-modification *J. Appl. Polym. Sci.* **1998**, *69*, 2255.
- (13) Varga, J.; Schulek-Toth, F. Crystallization, melting and spherulitic structure of beta-nucleated random propylene copolymers *J. Thermal Anal.* **1996**, *47*, 941.
- (14) Varga, J. *Crystallization, Melting and Supermolecular Structure of Isotactic Polypropylene*; Karger-Kocsis, J., Ed.; Chapman & Hall: London, 1995; Vol. 1.
- (15) Devaux, E.; Chabert, B. Nature and origin of the transcrystalline interphase of polypropylene glass-fiber composites after a shear-stress *Polym. Comm.* **1991**, *32*, 464.
- (16) Varga, J.; Karger-Kocsis, J. Direct evidence of row-nucleated cylindrical crystallization in glass fiber-reinforced polypropylene composites *Polym. Bull.* **1993**, *30*, 105.
- (17) Thomason, J. L.; Rooyen, A. A. v. Transcrystallized interphase in thermoplastic composites. 2. Influence of interfacial stress, cooling rate, fiber properties and polymer molecular-weight *J. Mat. Sci.* **1992**, *27*, 897.
- (18) Alfonso, G. C.; Scardigli, P. Melt memory effects in polymer crystallization *Macromol. Symp.* **1997**, *118*, 323.
- (19) Tribout, C.; Monasse, B.; Haudin, J. M. Experimental study of shear-induced crystallization of an impact polypropylene copolymer *Colloid Polym. Sci.* **1996**, *274*, 197.
- (20) Wu, C.-M.; Chen, M.; Karger-Kocsis, J. Micromorphological features of the crystallization of isotactic polypropylene after melt-shearing *Polym. Bull.* **1998**, *41*, 493.
- (21) Juhász, P.; Varga, J.; Belina, K.; Belina, G. Efficiency of  $\beta$ -nucleating agents in propylene/ $\alpha$ -olefin copolymers *J. Macromol. Sci.-Phys.* **2002**, *B41*, 1173.
- (22) Paukkeri, R.; Vaananen, T.; Lehtinen, A. Microstructural analysis of polypropylenes produced with heterogeneous Ziegler-Natta catalysts *Polymer* **1993**, *34*, 2488.
- (23) Randall, J. C. Carbon-13 nuclear magnetic resonance quantitative measurements of average sequence lengths of like stereochemical additions in polypropylene and polystyrene *J. Polym. Sci.* **1976**, *14*, 2083.
- (24) Although essentially the same procedure was followed for all samples, minor differences in the experimental details could take place. This was a consequence of the many different persons and companies who supplied the samples and who were involved in the measurements. We greatly acknowledge their contributions .

- (25) Busico, V.; Cipullo, R.; Monaco, G.; Vacatello, M. Full assignment of the  $^{13}\text{C}$  NMR spectra of regioregular polypropylenes: Methyl and methylene region *Macromolecules* **1997**, *30*, 6251.
- (26) Alexander, L. E. *X-ray Diffraction Methods in Polymer Science*; John Wiley & Sons, Inc.: New York, 1969.
- (27) Wunderlich, B. *Macromolecular Physics*; Academic Press: New York, 1973; Vol. 1.
- (28) Hindeleh, A. H.; Johnson, D. J. Crystallinity and crystallite size measurement in polyamide and polyester fibres *Polymer* **1978**, *19*, 27.
- (29) Kakudo, M.; Kasai, N. *X-ray Diffraction by Polymers*; Elsevier: Amsterdam, 1972.
- (30) Moore, E. P. *Polypropylene Handbook*; Hauser Publishers: München, 1996.
- (31) Feng, B.; Fuming, L.; Calhoun, B. H.; Quirk, R. P.; Cheng, S. Z. D. *Physical Constants of Poly(propylene)*; 4th ed.; Brandrup, J. and Immergut, E. H., Ed.; Wiley Interscience: New York, 1989, pp 21.
- (32) Turner-Jones, A.; Aizlewood, J. M.; Beckett, D. R. Crystalline forms of isotactic polypropylene *Makrom. Chem.* **1964**, *75*, 134.
- (33) Hauser, G.; Schmidtke, J.; Strobl, G. The role of co-units in polymer crystallization and melting: New insights from studies on syndiotactic poly(propene-co-octene) *Macromolecules* **1998**, *31*, 6250.
- (34) Varga, J.; Mudra, I.; Ehrenstein, G. W. A highly active thermally stable  $\beta$ -nucleating agent for isotactic polypropylene *J. Appl. Polym. Sci.* **1999**, *74*, 2357.
- (35) Bovey, F. A.; Mireau, P. A.; Blümich, B. NMR of polymers *Angew. Chem.* **1997**, *109*, 2637.
- (36) In principle the amount of  $\gamma$ -phase of the polymers with both types of defects could be plotted as function of regio-defects as well, however such an analysis would not change the interpretation of the results.
- (37) Alamo, R. G.; Kim, M. H.; Galante, M. J.; Isasi, J. R.; Mandelkern, L. Structural and kinetic factors governing the formation of the  $\gamma$ -polymorph of isotactic polypropylene *Macromolecules* **1999**, *32*, 4050.
- (38) The absolute value of the calculated concentration may be different than the actual concentration, as the overlapping areas of the (117) $\gamma$  and (130) $\alpha$  peaks were not taken into account.
- (39) Mandelkern, L. *Crystallization and Melting*; Booth, C. and Price, C., Ed.; Pergamon Press: Oxford, 1989; Vol. 2, pp 363.
- (40) Lotz, B.; Graff, S.; Straupé, C.; Wittmann, J. C. Single crystals of gamma phase isotactic polypropylene: Combined diffraction and morphological support for a structure with non-parallel chains *Polymer* **1991**, *32*, 2903.
- (41) Lotz, B.; Graff, S.; Wittmann, J. C. Crystal morphology of the gamma (triclinic) phase of isotactic polypropylene and its relation to the alpha-phase *J. Polym. Sci.: Polym. Phys. Ed.* **1986**, *24*, 2017.

- (42) Strobl, G. R.; Schneider, M. J.; Voigt-Martin, I. G. Model of partial crystallization and melting derived from small-angle X-ray scattering and electron microscopy studies on low-density polyethylene *J. Polym. Sci.: Polym. Phys. Ed.* **1980**, *18*, 1361.
- (43) Varga, J.; Garzo, G.; Ille, A. Kristallisation, umkristallisation und schmelzen der  $\beta$ -Modifikation des Polypropylens *Angew. Makromol. Chem.* **1986**, *142*, 171.
- (44) Varga, J. Supermolecular structure of isotactic polypropylene *J. Mat. Sci.* **1992**, *27*, 2557.
- (45) Mathieu, C.; Thierry, A.; Wittmann, J. C.; Lotz, B. "Multiple" nucleation of the (010) contact face of isotactic polypropylene, alpha phase *Polymer* **2000**, *41*, 7241.
- (46) Determination of the width of the distribution at half-height was complicated due to the absent of a clear base line. Therefore estimates of the base line positions were made by hand.
- (47) Albrecht, T.; Strobl, G. Temperature-dependent crystalline-amorphous structures in linear polyethylene: Surface melting and the thickness of the amorphous layers *Macromolecules* **1995**, *28*, 5827.
- (48) Crist, B.; Morosoff, N. Small-angle X-ray scattering of semi-crystalline polymers. II. Analysis of experimental scattering curves *J. Polym. Sci.: Polym. Phys. Ed.* **1973**, *11*, 1023.
- (49) Crist, B. Small-angle X-ray scattering of semi-crystalline polymers. I. Review of existing models *J. Polym. Sci.: Polym. Phys. Ed.* **1973**, *11*, 635.
- (50) Voigt-Martin, I. G.; Mandelkern, L. Numerical analysis of lamellar thickness distributions *J. Polym. Sci., Polym. Phys. Ed.* **1989**, *27*, 967.
- (51) Bond, E. B.; Spruiell, J. E.; Lin, J. S. A WAXD/SAXS/DSC study on the melting behaviour of Ziegler-Natta and metallocene catalysed isotactic polypropylene *J. Polym. Sci., Polym. Phys. Ed.* **1999**, *37*, 3050.
- (52) Trifonova, D.; Varga, J.; Vancso, G. J. AFM study of lamellar thickness distributions in high temperature melt-crystallization of beta-polypropylene *Polym. Bull.* **1998**, *41*, 341.
- (53) Wu, C.-M.; Chen, M.; Karger-Kocsis, J. The role of metastability in the micromorphologic features of sheared isotactic polypropylene melts *Polymer* **1999**, *40*, 4195.
- (54) Vancso, G. J.; Liu, G.; Karger-Kocsis, J.; Varga, J. AFM imaging of interfacial morphologies in carbon-fiber reinforced polypropylene *Colloid Polym. Sci.* **1997**, *275*, 181.
- (55) Sanchez, I. C.; Eby, R. K. Thermodynamics and crystallization of random copolymers *Macromolecules* **1975**, *8*, 638.
- (56) Lauritzen, J. I.; Hoffman, J. D. *J. Appl. Phys.* **1973**, *44*, 4340.
- (57) Sanchez, I. C.; Eby, R. K. *J. Res. Natl. Bur. Stand., Sect. A.* **1973**, *77*, 353.

- (58) Hoffman, J. D.; Davis, G.; Lauritzen, J. I. *In Treatise on Solid State Chemistry*; Hannay, N. B., Ed.; Plenum Press: New York, 1976; Vol. 3, Chapter 7.
- (59) Clark, E. J.; Hoffman, J. D. Regime III crystallization in polypropylene *Macromolecules* **1984**, *17*, 878.
- (60) Hoffman, J. D. Regime III crystallization in melt-crystallized polymers: The variable cluster model of chain folding *Polymer* **1997**, *24*, 3.
- (61) Odian, G. *Principles of Polymerization*; 3rd ed.; John Wiley & Sons, Inc.: New York, 1991.
- (62) Flory, P. J. *Principles of Polymer Chemistry*; Cornell University Press: Ithaca (N.Y.), 1953.
- (63) Helfand, E.; J. I. Lauritzen, J. Theory of copolymer crystallization *Macromolecules* **1973**, *6*, 631.
- (64) Xu, J.; Srinivas, S.; Marand, H. Equilibrium melting temperature and undercooling dependence of the spherulitic growth rate of isotactic polypropylene *Macromolecules* **1998**, *31*, 8230.
- (65) Janimak, J. J.; Cheng, S. Z. D.; Giusti, P. A.; Hsieh, E. T. Isotacticity effect on crystallization and melting in polypropylene fractions: 2. Linear crystal-growth rate and morphology study *Macromolecules* **1991**, *24*, 2253.
- (66) VanderHart, D. L.; Alamo, R. G.; Nyden, M. R.; Kim, M. H.; Mandelkern, L. Observations of resonances associated with stereo and regio defects in the crystalline regions of isotactic polypropylene: Toward a determination of morphological partitioning *Macromolecules* **2000**, *33*, 6078.

## 3.7 Acknowledgements

The author would like to thank Dr. A. Demain (Fina Research, Feloy, Belgium), Dr. I. Mingozzi (Basell, Ferrara, Italy), Dr. J. Chadwick and Dr. F. van der Burght (Technical University of Eindhoven, Eindhoven, The Netherlands) for the polymer samples. The author also greatly acknowledges Dr. S. Rastogi (Technical University of Eindhoven, Eindhoven, The Netherlands) for providing the opportunity to perform the SAXS and WAXS measurements and Dr. G. van den Velde for the NMR-measurements and useful discussions.

### 3.8 Appendix 1

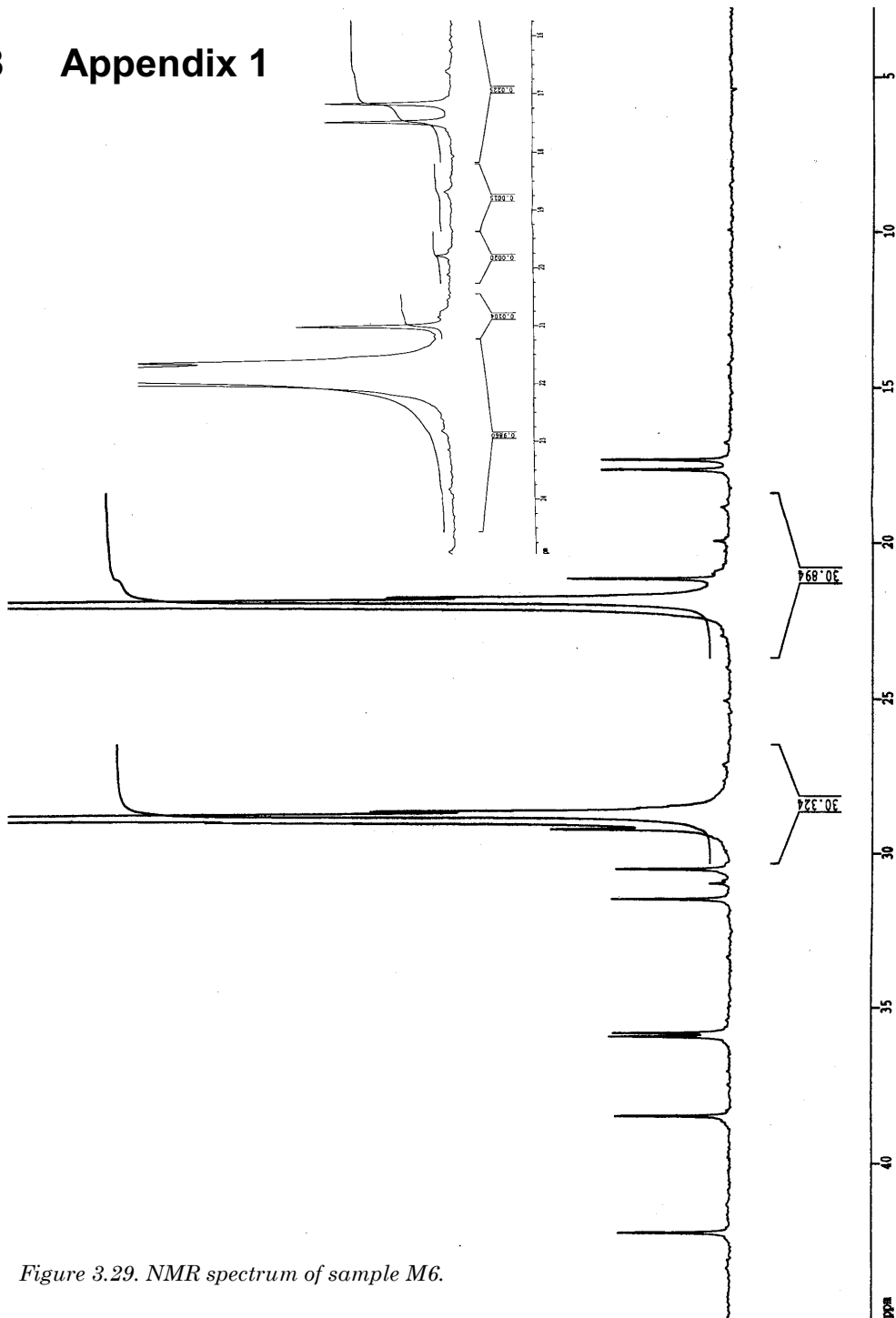


Figure 3.29. NMR spectrum of sample M6.



# Chapter 4

## The influence of chain defects on the fusion behavior of $\alpha$ -, $\beta$ -, and $\gamma$ -phases of isotactic polypropylene

The melting characteristics of the  $\alpha$ -,  $\beta$ -, and  $\gamma$ -phases of isotactic polypropylene (iPP) were studied for well-defined and fully characterized polymer samples with varying amounts of stereo- and regio-defects. The melting point, as measured by Differential Scanning Calometry (DSC), is significantly lowered by the number of defects and is much stronger influenced by regio-defects as compared with stereo-defects. A combined (unified) defect fraction was introduced as a variable which enabled us to describe the melting behavior of any iPP sample with varying amounts of stereo- and regio-defects. It was shown that in the defect-range studied, the influence of stereo-defects on the melting point is independent of the presence of regio-defects. Similar melting point depression relationships were found for all the three polymorphs ( $\alpha$ -,  $\beta$ -, or  $\gamma$ -phases) independent of the number and type of defects. No correlation was found between the melting point depression and the crystallization kinetics. An analysis of the melting point depression using the model of Sanchez and Eby for copolymer melting was found in good agreement with experiments for the samples with different amounts of stereo-defects. However, a less satisfactory agreement with experiments was found for regio-defects. From the data analysis, we concluded that it is more difficult to incorporate a regio-defect in the crystalline region than a stereo-defect. The excess free energy for incorporating a stereo-defect into the trigonal crystal lattice of  $\beta$ -phase is lower as compared with the monoclinic crystal lattice of the  $\alpha$ -phase. This results in a higher fraction of defects in the crystalline regions of the  $\beta$ -phase.

---



## 4.1 Introduction

The introduction of chain defects, or co-monomers, into an otherwise fully regular polymer chain leads in general to a broadening and lowering of the melting range. The exact melting point depression depends on the number, kind, and distribution of the defects and on the crystallization conditions [1]. It was found in many studies [2-5] that the melting point depression in semi-crystalline polymers is linear with the number of defects and often independent of the chemical nature of the defect [6]. It has been shown for example in ethylene copolymers with  $\alpha$ -olefins having uniform chemical microstructure that comonomers of several different 1-alkenes (except for the smallest comonomer 1-propene) exhibit the same melting point depression [7]. The ethylene-1-propene copolymer shows the same linear trend in the melting point as function of the number of defects only shifted to higher temperatures [1].

As the fraction of non-crystallizable units increases, a significant deterioration of the lamellar structure is observed. The thickness and lateral size of the lamellae decrease, as well as the degree of crystallinity [8,9] (see also chapter 3 of this Thesis). These changes in morphology effect both the mechanical as well as thermal properties, like the melting point of the polymer.

Several theories [10-13] were developed in order to predict and understand quantitatively the melting point depression as function of the number and kind of defects in copolymers. Experimentally however, it was often found that the depression in the melting point is much higher than predicted [1,13]. The deviation of the experimentally found melting temperatures with the predictions from theory finds its origins in the non-equilibrium aspects of crystallization and the changes in the morphology, as mentioned above [6].

In order to obtain a better insight into the exact origins and main parameters that influence the melting point depression in polymers, a random distribution of defects is highly preferred and a full characterization of the polymer microstructure and polymer morphology is indispensable. Many studies dealing with the melting point depression lack such a detailed and complete characterization of the polymer chain microstructure of the specimen used. Moreover, often use was made of Ziegler-Natta polymerized polymers. Polymers obtained by Ziegler-Natta stereospecific polymerizations produce an inhomogeneous system of molecules. The corresponding chains exhibit heterogeneous chemical and stereo-chemical distributions within one batch and within a single polymer chain and therefore structure-property relations described using ZN-polymers are of limited value.

In the present study we obtained a number of different metallocene catalyzed iPPs, with a wide variety in chain architecture. As metallocene catalyzed iPPs have randomly distributed defects a rigorous analysis of the number of defects on the

desired properties can be made. Comparisons were made also with specimens obtained by Ziegler-Natta type catalysts. All samples were fully characterized by  $C^{13}$ -NMR regarding the stereo- and regio-architecture of the corresponding macromolecules. The polymers can be divided into three groups: polymers with a varying *stereo*-defect fraction (with constant amount of regio-defect); polymers with a varying *regio*-defect fraction (with constant amount of stereo-defects); and polymers with *both* stereo- and regio-defects. With this assembly of polymers, it was possible to investigate *in a systematic manner* at different concentrations the influence of the type and the number of defects on the fusion behavior of iPP.

Isotactic polypropylene can crystallize into an  $\alpha$ -monoclinic, a  $\beta$ -trigonal, and a  $\gamma$ -orthorhombic form [14] depending on the thermal-rheological history [14-16], pressure [17] and the presence of nucleating agents [18]. Melting peak temperatures in isotactic polypropylene ( $\alpha$ -phase) may vary from 169°C to as low as 130°C depending on the amount of chain-defects [19]. A much stronger depression in melting point of the  $\alpha$ -form was found in isotactic-polypropylenes produced via metallocene polymerizations as compared to conventional Ziegler-Natta polypropylenes having similar defect concentrations. The increase in the dependence of the melting temperature on the number of defects was addressed to the incorporation of regio-defects in the chain [20-22]. Although the general trends of the melting behavior on the amount and kind of defects were clarified, the separate influence of regio- and stereo-defects on the fusion behavior of polypropylene for the different crystal phases to our knowledge, has not been systematically studied and presented in detail.

In this study we present results on the melting point depression of the  $\alpha$ -,  $\beta$ -, and  $\gamma$ -phase as function of the number of regio- and stereo-defects. A comparison was made with the copolymer crystallization theory presented by Flory [23] and Sanchez and Eby [12], complemented by the microstructural analysis presented by Mandelkern [1], which served as a starting point for the description of the observed results. In the discussion, we indicate the role of the morphology on the melting behavior of isotactic polypropylene.

## 4.2 Experimental

### 4.2.1 Samples

A collection of samples including one Ziegler-Natta catalyzed polymer (ZN), 15 different metallocene-catalyzed polymers (Mx), and 5 blends (BLx) were used in this study. Table 4.1 gives the relevant characteristics of all specimens used. The blends (BLx) were made by solution blending of M6 and ZN. Solutions of M6 and ZN in tetrachloroethene were prepared (10 wt%) at the solvent boiling point (121.1°C) and stabilized with 0.1 wt% 2,6-di-tertiar-butyl-4-methylphenol 99%

antioxidant (Aldrich). The hot solutions were mixed in the desired ratios. After 10 min stirring the polymer solution was quenched in ice-water, filtered over a glass-filter and subsequently washed with ethanol. After drying for 48 hours in a vacuum oven, the blends were ready for use.

In order to determine the tacticity of the samples,  $C^{13}$  nuclear magnetic resonance ( $C^{13}$ -NMR) measurements were performed. The samples were prepared and measured according to the procedure described in the literature [24,25]. Peak assignment was done by using the results described in reference [26]. Number average and weight average molar masses ( $\overline{M}_n$  and  $\overline{M}_w$ ) and polydispersity index values ( $\overline{M}_w / \overline{M}_n$ ) were determined by using gel permeation chromatography (GPC) measurements using a Walters-GPC set-up equipped with a differential refractometer (Walter model 410) detection system. Narrow polystyrene standards were used for calibration. Prior to the measurements, samples were solved in trichlorobenzene (TCB) at 130°C and stabilized with 0.1 wt% 2,6-di-tertiar-butyl-4-methylphenol 99% (Aldrich) [25].

### 4.2.2 Melting

The morphology and consequently the melting properties will depend on the temperature-time path taken from the melt during crystallization. To avoid any complications in interpretation due to the variety of possible pathways, we limited this study to isothermal crystallization at one temperature. Fusion behavior was studied by Differential Scanning Calometry (DSC). The DSC (A Perkin-Elmer calorimeter Pyris 1) was calibrated using gallium and indium before use. The sample chamber was kept under a constant flux of nitrogen. All samples were melted for 5 min at 220°C to erase the thermal history and subsequently cooled to the crystallization temperature of 130°C. All DSC melting scans were recorded from 110°C to 180°C with 10 °C/min. The samples were cooled down to only 110°C in order to prevent re-crystallization of the  $\beta$ -phase. To induce the  $\beta$ -phase, a selective  $\beta$ -nucleating agent, the calcium salt of suberic acid [18] (CaSub) was used, kindly supplied by Prof. J. Varga.

## 4.3 Results

### 4.3.1 Introduction

This section starts with a short overview of the significant molecular characteristics of the samples that were used in this research. Secondly, a discussion on the characteristics of the fusion behavior of isotactic-polypropylene will be described and we will provide the methods which we adopted for the determination of melting point for the  $\alpha$ -,  $\beta$ -, and  $\gamma$ -polymorphs. In the subsequent section we report on the relationships of the melting points of the  $\alpha$ -,  $\beta$ -, and  $\gamma$ -

polymorphs with the number and type of defects. The section ends with a comparison of measured data with prediction from a theory as described by Sanchez and Eby [12].

#### 4.3.2 Main sample characteristics

In order to facilitate the analyses of the relationships of the melting points of the  $\alpha$ -,  $\beta$ -, and  $\gamma$ -polymorphic forms with the number and type of defects, the samples were sorted in such a way that three groups of specimen are distinguished. The first group of samples (Group 1) contains polymers with only stereo-defects (ZN, M1-M5). Negligible amounts of regio-defects are present in these samples, therefore we can use them for investigating the influence of stereo-defects on the morphology and fusion behavior. The second group (Group 2) contains polymers with a low amount of stereo-defects, but with a strongly varying amount of regio-defects (M3-M10). The regularity of the chain of this group of polymers is mainly determined by the regio-defects. Changes in morphology and melting point are thus mainly the result of the regio-defects. The third group (Group 3) contains polymers with both a significant amounts of stereo- and regio-defects (BL15-M15).

By sub-dividing the polymer in the three groups as described above, it is possible to *separately* investigate the influence of both stereo- and regio-defects.

#### 4.3.3 Melting characteristics of the $\alpha$ -, $\beta$ - and $\gamma$ -phases as revealed by DSC and LM

##### $\alpha$ - $\gamma$ -Phase

Melting characteristics were determined by DSC. The melting curves of samples isothermally crystallized at 130°C show, in addition to a main endotherm (see the arrow assigned with  $\alpha_{\text{peak1}}$ , Figure 4.1), one or more shoulders at the low temperature side (see the arrows assigned with  $\alpha_{\text{peak2}}$  and  $\gamma$  Figure 4.1).

The main endotherm at high temperature is unequivocally associated with the melting of the  $\alpha$ -phase [27,28] and the position of the peak is often taken as the melting point of isotactic polypropylene ( $\alpha$ -phase). The assignment of the low temperature endotherm has been subject of many studies [20,27,29-35]. In this section we will give a short description and summary as far as the literature results are important for the determination of the melting points of the  $\alpha$ - and  $\gamma$ -phases in this research.

a) Molecular characteristics of samples with a varying amount of stereo defects.

Polymer Sample	$\bar{M}_n$ (*10 <sup>-4</sup> ) (g/mol)	$\bar{M}_w$ (*10 <sup>-4</sup> ) (g/mol)	$\bar{M}_w / \bar{M}_n$ (-)	Percentage [ <i>mmmm</i> ] (%)	Fraction regio defects (-)	Fraction stereo defects [r] (-)
<sup>1</sup> ZN/BL0	-	-	-	98.0	<0.0001	0.0020
<sup>2</sup> M1	1.80	3.80	2.11	83.1	<0.0001	0.1390
<sup>2</sup> M2	4.00	8.10	2.03	84.2	<0.0001	0.1460
<sup>2</sup> M3	9.90	20.0	2.02	97.6	<0.0001	0.0222
<sup>2</sup> M4	6.80	20.0	2.94	97.6	<0.0001	0.0223
<sup>2</sup> M5	2.90	8.30	2.86	97.4	<0.0001	0.0234

b) Molecular characteristics of samples with a varying amount of regio defects, and approximately constant amount of stereo defects.

Polymer Sample	$\bar{M}_n$ (*10 <sup>-4</sup> ) (g/mol)	$\bar{M}_w$ (*10 <sup>-4</sup> ) (g/mol)	$\bar{M}_w / \bar{M}_n$ (-)	Percentage [ <i>mmmm</i> ] (%)	Fraction regio defects (-)	Fraction stereo defects [r] (-)
<sup>3</sup> M6/BL100	-	15.0	-	98.5	0.0034	0.0200
<sup>3</sup> M7	-	-	-	98.0	0.0034	0.0200
<sup>2</sup> M8	28.0	83.0	2.96	97.3	0.0055	0.0010
<sup>2</sup> M9	7.50	26.0	3.47	97.3	0.0055	0.0010
<sup>2</sup> M10	-	-	-	97.3	0.0055	0.0010
<sup>2</sup> BL15	-	-	-	98.0	0.0011	0.0026

c) Molecular characteristics of samples with a varying amount of regio- and stereo defects.

Polymer Sample	$\bar{M}_n$ (*10 <sup>-4</sup> ) (g/mol)	$\bar{M}_w$ (*10 <sup>-4</sup> ) (g/mol)	$\bar{M}_w / \bar{M}_n$ (-)	Percentage [ <i>mmmm</i> ] (%)	Fraction regio defects (-)	Fraction stereo defects [r] (-)
BL20	-	-	-	98.0	0.0018	0.0036
BL30	-	-	-	98.0	0.0026	0.0054
BL50	-	-	-	98.0	0.0030	0.0092
BL70	-	-	-	98.0	0.0032	0.0128
<sup>2</sup> M11	2.00	3.90	1.95	84.6	0.0065	0.0920
<sup>3</sup> M12	6.00	12.0	2.00	95.8	0.0027	0.0500
<sup>3</sup> M13	-	18.0	-	95.0	0.0027	0.0500
<sup>3</sup> M14	10.0	23.0	2.30	95.0	0.0027	0.0500
<sup>3</sup> M15	-	-	-	-	-	-

Table 4.1a, b, c. Relevant characteristics of the polymers used. Explanations can be found in text. <sup>1</sup>DSM, Geleen, The Netherlands; <sup>2</sup>Basell, Ferrara, Italy; <sup>3</sup>Fina Research, Feloy, Belgium.

Multiple endotherms found in the melting of isotactic polypropylene samples are possibly caused by the structural reorganization of the less ordered  $\alpha$  modification to the more stable  $\alpha_{II}$  modification [30]. The  $\alpha$ - $\alpha_{II}$  transition consists of partial melting of a metastable crystal followed by renewed crystallization to a more perfect crystal. This increases the degree of order, and the melting temperature of the polymer. Especially on lowering the heating rate, the appearance of double endotherm is enhanced. At moderate (10 °C/min) and higher heating rates which we used in our experiments, usually a broad endotherm is observed [30] (see top-curve in Figure 4.1).

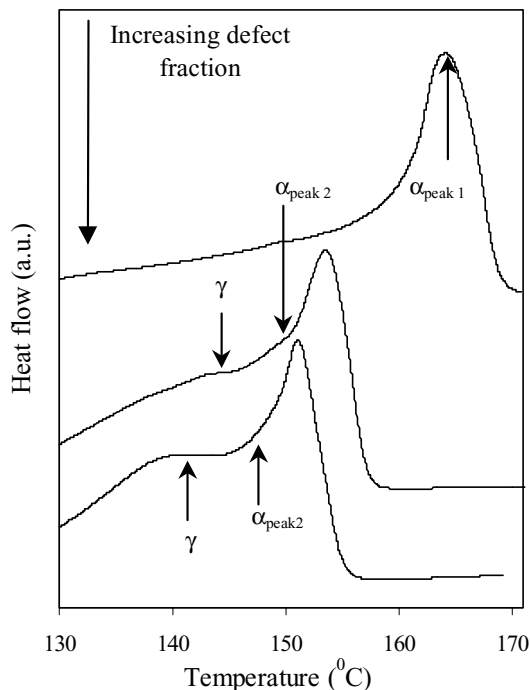


Figure 4.1. DSC heating traces of the samples M1, M2 and M11 obtained after an isothermal crystallization at 130°C. The samples have an increasing content of regio- and stereo-defects (from top to bottom). The heating rate in the DSC experiments was 10 °C/min.

Double melting peaks were also associated with the separate melting of ‘mother’ and ‘daughter’ lamellae [31]. The low-temperature melting endotherm in this case would represent the melting of thinner, transversal, cross-hatched lamellae while the higher-temperature endotherm is due to the melting of the radial (usually thicker), primary lamellae. As it was established, the number of transversal lamellae increases with decreasing crystallization temperature [31,32] and with increasing amount of defects (stereo- and regio-defects) [32]. It was shown [31,36-38] that transversal crystallites formed at crystallization temperatures less than ~140° have similar thicknesses as the radial lamellae, and therefore melt at

approximately at the same temperatures or slightly lower ( $\sim 6^\circ\text{C}$ ) [36] (see the small shoulder assigned with  $\alpha_{\text{peak2}}$  in Figure 4.1).

In addition to the  $\alpha_I$ - $\alpha_{II}$  transition or the melting of a second lamellar population, double melting can be caused by the melting of a second crystal phase, as well. Under certain circumstances, the  $\gamma$ -modification coexists with the  $\alpha$ -form [14,39]. In that case, the low temperature melting endotherm (or shoulder) may be associated with the separate (partial) melting of the  $\gamma$ -phase, which may partially recrystallize into the  $\alpha$ -phase [27]. It was shown [27,33,34] by monitoring the amount of the  $\gamma$ -phase using WAXD during recording of DSC thermograms, that the amount of the  $\gamma$ -phase is drastically decreased relative to the amount of the  $\alpha$ -phase during the temperature range bordered by the first endotherm. The conclusion from these measurements was that the lower temperature endotherm might have its origin (at least partially) in the melting of the  $\gamma$ -phase [20,27,33-35].

In summary, we can say that the lower endotherm may have different origins. However, it was clearly shown that in polymers containing a significant amount of regio- and stereo-defects the endotherm can at least partially be attributed to the melting of the  $\gamma$ -phase. The relative areas of the two endotherms are qualitatively similar to the ratio of the  $\gamma$ - to  $\alpha$ -phase contents of these samples (the ratio of the  $\gamma$ - to  $\alpha$ -phase contents was determined by wide angle x-ray scattering, see chapter 3) which is in support of this statement. With the help of results from the literature mentioned above we could explain the measured DSC-thermograms adequately (see Figure 4.1 for three examples). The values of the melting points of the  $\alpha$ - and  $\gamma$ -phases were taken at the indicated places ( $\alpha_{\text{peak1}}$  and  $\gamma$ ) on the DSC-curves.

As was mentioned in the literature [8,40], the final temperature of the melting endotherm should be used. However, the difference between the *peak*- and the *final*-melting temperature is small and approximately constant for all the polymers used. Therefore, the use of the peak temperature does not alter the results significantly. Moreover the final melting temperature of the  $\gamma$ -phase and  $\beta$ -phase (see next section) are often obscured by the overlapping melting endotherm of the  $\alpha$ -phase and therefore can be difficult to determine.

## **$\beta$ -phase**

The melting behavior of the  $\beta$ -phase is very diverse and complicated. Most of its characteristics were revealed by Varga, et.al [41]. One of the typical features in the melting behavior of the  $\beta$ -phase is the possibility of selective melting. As we will use this melting characteristic in the determination of the melting point, we give a short description of this phenomenon.

Figure 4.2 shows three LM-pictures of a  $\beta$ -nucleated ZN-PP crystallized at  $133^\circ\text{C}$ . The sample is cooled down to only  $10^\circ\text{C}$  above the critical cooling

temperature ( $T_{\alpha\beta}$ ) of 100-105°C in order to prevent a  $\beta\alpha$ -bifurcation during heating [41]. It was recently shown [42] that  $T_{\alpha\beta}$ , the critical re-cooling temperature, of propylene-ethylene co-polymers does not differ considerably from that of the homopolymer, therefore we adopted this temperature as the critical cooling temperature for our polymers, as well.

The  $\beta$ -phase exhibits a highly negative birefringent character in an optical microscope equipped with crossed polarizers. During heating the magnitude of the birefringence changes as one can see in Figure 4.2B and disappears when the melting of the  $\beta$ -phase is complete ( $\pm 158^\circ\text{C}$  in the case of this particular ZN-iPP sample). The remaining crystallites consist of the  $\alpha$ -phase [41]. One can see that the position of the  $\alpha$ -phase in the crystallized material for the majority is in spherulites, or parts of  $\beta$ -spherulites. An example of a supra-molecular entity consisting of the  $\alpha$ -phase has been circled in white, see Figure 4.2.



Figure 4.2. A polypropylene sample (ZN) nucleated with 0.01 wt.% CaSub, crystallized at 133°C, cooled to 110°C, and subsequently heated to 169°C at 10 °C/min. A, B, and C at 110, 158, and 169°C, respectively.

Some parts of the  $\beta$ -phase spherulite may incorporate  $\alpha$ -phase crystals if the  $\beta$ - $\alpha$  growth transition takes ( $T_c = 133^\circ\text{C} > T_{\alpha\beta}$ ). An example of such part can be seen in the left upper corner in Figure 4.2C. Light microscopy is able to show the selective melting of the  $\beta$ -phase, providing us with a method to determine the melting point of the  $\beta$ -phase. Melting behavior of the  $\beta$ -phase was studied by DSC, as well. Figure 4.3 shows DSC-traces of two samples with low (ZN) and higher defect fraction (M6), respectively. Each figure shows a DSC trace for a non-nucleated sample and  $\beta$ -nucleated sample, respectively. Figure 4.3 shows that the melting peak of the  $\alpha$ -phase (higher melting peak) in the  $\beta$ -nucleated samples can be superimposed on the melting peak of the  $\alpha$ -phase obtained by non-nucleated samples, which indicates a separation of the two phases. The  $\alpha$ -phase is present as a very low fraction in the  $\beta$ -nucleated ZN-sample (Figure 4.3B), but is present in a larger fraction in the more defected sample M6 (Figure 4.3A) (see also chapter 3). These results show that the selective melting of the  $\beta$ -phase can be used to determine the melting temperature range of the  $\beta$ -phase. The position of the endothermic peak is taken as the melting point for the  $\beta$ -phase.



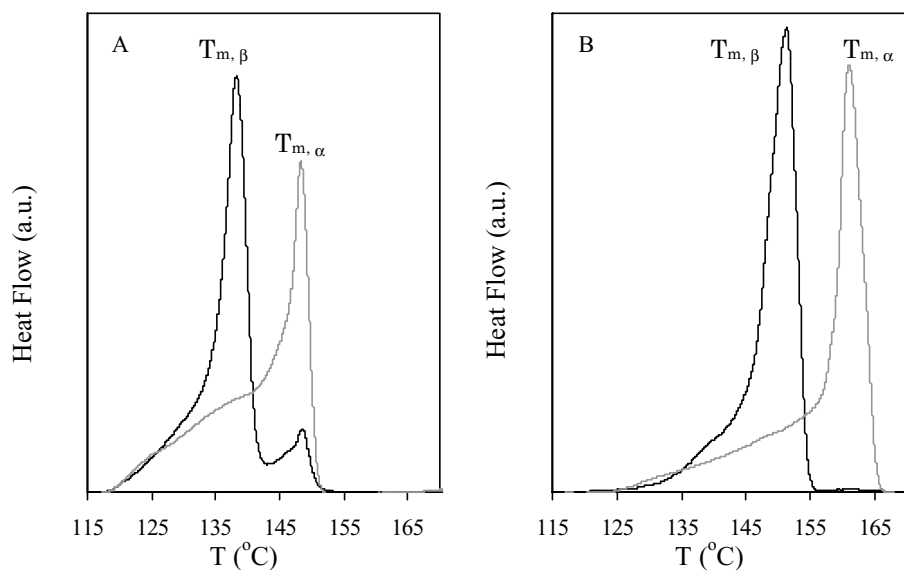


Figure 4.3. DSC heating traces of samples M6 (A) and ZN (B). The DSC heating trace of the  $\beta$ -nucleated (black line) and non-nucleated polymer samples (gray line) are shown, respectively.

#### 4.3.4 Melting points ( $\alpha$ - $\beta$ - $\gamma$ -phase) as function of type and concentration of defects

In the previous section we discussed the melting characteristics of the  $\alpha$ -  $\beta$ - and  $\gamma$ -phases of isotactic polypropylene. We concluded that the polymorphs of isotactic polypropylene separately melt and cause separate melting endotherms in a DSC experiment. The peak of the endotherm was defined as the melting point. All polymers mentioned in Table 4.1 were melted at 220 °C for 5 min, isothermally crystallized at 130°C, and cooled to 110°C to have the same thermal history. Defect fractions of both regio- and stereo-type for all polymers are given in Table 4.1

Figure 4.4 gives the melting points of isotactic-polypropylene ( $\alpha$ -phase) as a function of defect fraction. The different specimens were grouped (see section 4.3.2) and plotted according to a specific defect type as function of that defect fraction ( $X$ ). The melting points of the  $\alpha$ -phase of the polymers:

- (1) with only *stereo*-defects (ZN, M1-M5) ( $\blacklozenge$ ) are plotted as function of the fraction *stereo*-defects (group 1);
- (2) with varying fraction *regio*-defects (M3-M10) ( $\blacksquare$ ) but with approximately the same fraction of stereo-defects are plotted as function of fraction *regio*-defects (group 2);

- (3) with *both* stereo- and regio-defects (BL15-M15) ( $\circ$ ) are plotted as function of the fraction *stereo*-defects<sup>1</sup> (group 3).

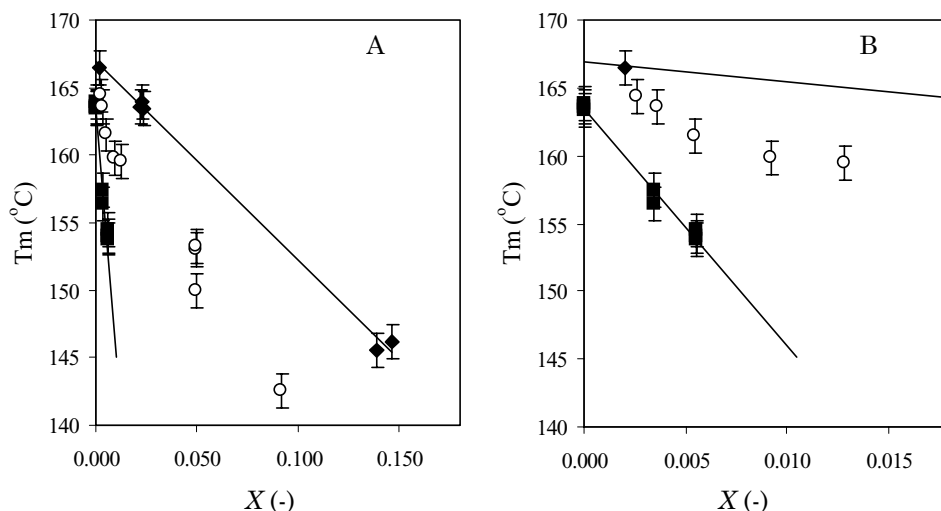


Figure 4.4. The melting points of the  $\alpha$ -phase for various samples as a function of the fraction of defects. The figure to the right (B) shows the dependence of the defect fractions with enlarged x-scale. The solid lines are fitted lines using a least squares fit through the data points. Assignments of symbols are given in the text.

As expected, the melting point is linearly depressed with increasing defect-fraction [2-5]. The samples with varying amounts of regio-defects ( $\blacksquare$ ) exhibit a much stronger depression of the melting point than samples with only a variation in stereo-defects ( $\blacklozenge$ ) [43]. The melting points of the polymers with both stereo- and regio-defects ( $\circ$ ) are scattered within the two limits of the two groups of polymers mentioned before (group 1 and group 2).

Similar plots as shown in Figure 4.4 for the  $\alpha$ -phase, were made for the  $\beta$ -phase and  $\gamma$ -phase, as well. The following figures (Figure 4.5 and Figure 4.6) present the melting point depression as function of the type and number of defects for the  $\beta$ - and  $\gamma$ -phases, respectively. The  $\beta$ - and  $\gamma$ -phases show similar relationships of the melting point depression as the  $\alpha$ -phase does. The regio-defects have a much larger influence on the melting point than the stereo-defects.

<sup>1</sup> In principle the melting point of the polymers with both types of defects could be plotted as function of regio-defects as well, however such analysis would not have any influence on the results.

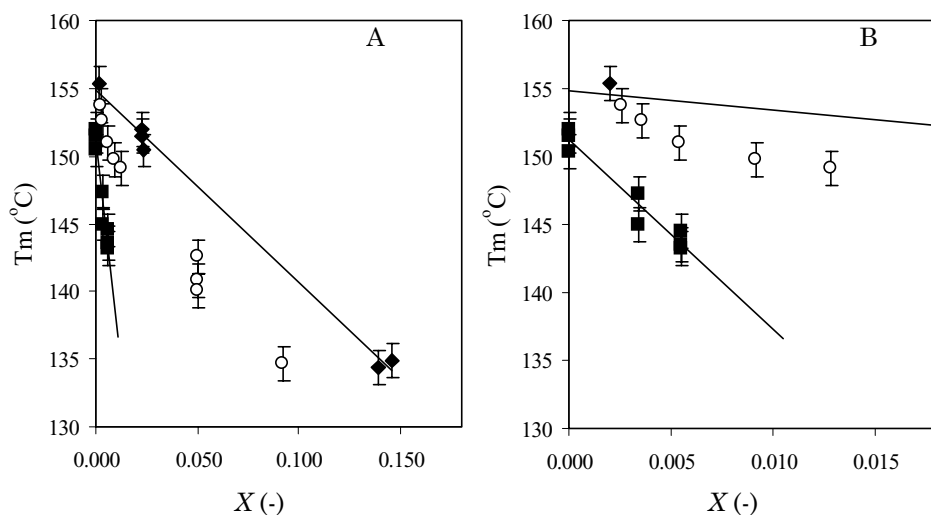


Figure 4.5. The melting points of the  $\beta$ -phase for various samples as a function of the fraction of defects. The figure to the right (B) shows the dependence of the defect fractions with enlarged x-scale. The solid lines are fitted lines using a least squares fit through the data points. Assignments of symbols are given in the text. Compare also Figure 4.4.

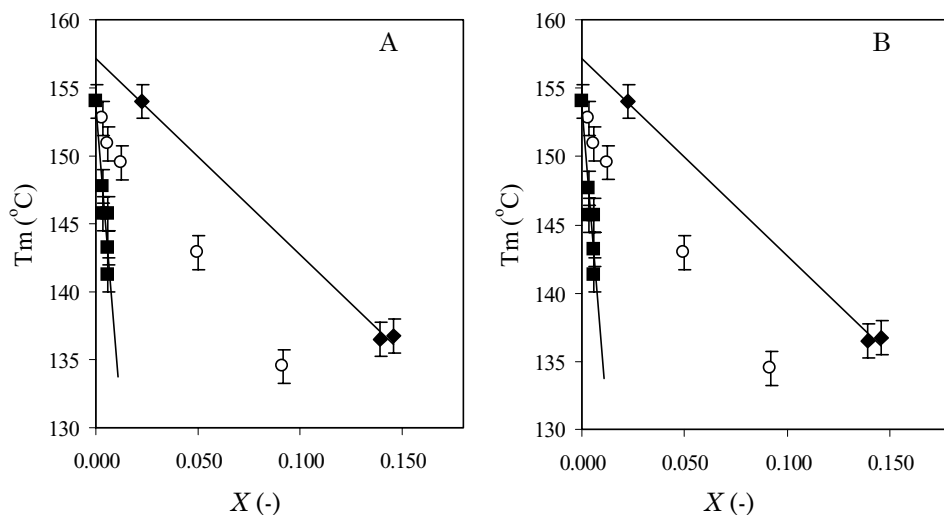


Figure 4.6. The melting point of the  $\gamma$ -phase for various samples as a function of the fraction of defects. The figure to the right (B) shows the dependence of the defect fractions with enlarged x-scale. The solid lines are fitted lines using a least squares fit through the data points. Assignments of symbols are given in the text. Compare also Figure 4.4.

As it can be seen in each of the figures (Figure 4.4, Figure 4.5, and Figure 4.6) two approximately linear dependences on the number of regio- and stereo-defects, respectively are shown. The observed relationships between the melting point as a function of the two different types (regio/stereo) of defects were fitted with a linear

dependence using a standard least-squares fit procedure. The following numerical formulas were obtained (for the  $\alpha$ -phase):

$$(T_{m,s}^{\alpha})_{X_r=0} = (166.9 \pm 0.4) - (147 \pm 4)X_s, \quad (4.1a)$$

$$(T_{m,r}^{\alpha})_{X_s=0} = (164.2 \pm 0.6) - (1.90 \pm 0.15) \cdot 10^3 X_r, \quad (4.1b)$$

where  $(T_{m,s}^{\alpha})_{X_r=0}$  corresponds to the melting point of the  $\alpha$ -phase as function of stereo-defects, while the fraction of regio-defects was kept zero.  $X_s \approx 0$  refers to approximately zero fraction of stereo-defects for the equation fitted with the regio-defects fraction used as independent variable (equation (4.1b)). One can see that the two lines have a difference in intercept at zero  $X_s$  or  $X_r$  (166.9°C vs. 164.2°C). This difference is exactly determined by the fact that in the relationship of  $T_{m,r}^{\alpha}$  the fraction of stereo defects is not exactly zero.

In order to describe also the group of polymers with both stereo- and regio-defects, a linear combination of equations (4.1a) and (4.1b) was made. This results in the following equation:

$$T_{m,s/r}^{\alpha} = (166.9 \pm 0.4) - (147 \pm 4)X_s - (1.90 \pm 0.15) \cdot 10^3 X_r. \quad (4.2)$$

Equation (4.2) can also be rewritten as:

$$\tilde{T}^{\alpha} = \frac{(T_{m,s/r}^{\alpha})}{(T_{m,s/r}^{\alpha})_{X_s=X_r=0}} = 1 - (0.89 \pm 0.03)\tilde{X}^{\alpha}, \text{ where } \tilde{X}^{\alpha} = X_s + (12.9 \pm 1.4)X_r. \quad (4.3a/b)$$

The superscript  $\alpha$  is adopted to denote the  $\alpha$ -phase. The *reduced temperature*  $\tilde{T}^{\alpha}$  is defined as the combined temperature ( $T_{m,s/r}^{\alpha}$ ) divided by the melting temperature of the polymer with zero stereo- and regio-defects ( $(T_{m,s/r}^{\alpha})_{X_s=X_r=0}$ ). The combined defect fraction ( $\tilde{X}^{\alpha}$ ) is the sum of the number of stereo-defects and the number of regio-defects multiplied by a given *regio-error coefficient* with a certain value. The value of regio-error coefficient ( $12.9 \pm 1.4$ ) was calculated using an error propagation estimation. Equations (4.2) and (4.3a/b) were derived for the  $\alpha$ -phase. With a similar data analysis as done for the  $\alpha$ -phase equations (4.3a) and (4.3b) could be derived for the  $\beta$ - and  $\gamma$ -phases as well. The results are:

$$\tilde{T}^{\beta} = 1 - (0.91 \pm 0.04)\tilde{X}^{\beta}, \text{ where } \tilde{X}^{\beta} = X_s + (11.2 \pm 1.6)X_r, \text{ and} \quad (4.4a/b)$$

$$\tilde{T}^{\gamma} = 1 - (0.92 \pm 0.06)\tilde{X}^{\gamma}, \text{ where } \tilde{X}^{\gamma} = X_s + (13.1 \pm 2.7)X_r. \quad (4.5a/b)$$

The value of regio-error coefficient in the expression for the combined defect fractions ( $\tilde{X}$ ) is the same within the experimental error for each polymorph (the  $\alpha$ - $\beta$ - $\gamma$ -phases). This suggests that the influence of defects (stereo- and regio-defects) on the melting depression is the same regardless the crystal structure or lamellar morphology.

With the introduction of the combined defect-fraction ( $\tilde{X}$ ) and the reduced temperature ( $\tilde{T}$ ) samples with both stereo- and regio-defects can be fitted within one descriptive framework. This provides us with the opportunity to study in a wider range, and for more samples, the influence of the amount and kind of defects on the parameter of interest. For example, equations (4.3a/b), (4.4a/b), and (4.5a/b) predict that the melting point depression in each of the  $\alpha$ -  $\beta$ - or  $\gamma$ -phases of isotactic polypropylene, containing any combination in the amount of stereo- and regio-defects, can be described by one “universal” parameter  $\tilde{X}$ .

For all polymer samples the combined defect fraction ( $\tilde{X}$ ) was calculated with help of equations (4.3a/b), (4.4a/b), and (4.5a/b). Subsequently, the reduced melting temperatures of the  $\alpha$ -,  $\beta$ - and  $\gamma$ -phases ( $\tilde{T}^\alpha$ ,  $\tilde{T}^\beta$ , and  $\tilde{T}^\gamma$ ) were plotted as function of combined defect fraction  $\tilde{X}^\alpha$ ,  $\tilde{X}^\beta$ ,  $\tilde{X}^\gamma$ , respectively. A remarkably good correlation was found for all of the three phases, see Figure 4.7.

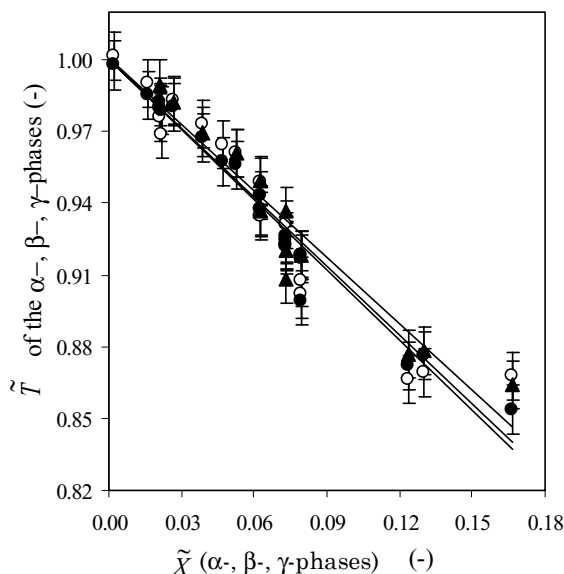


Figure 4.7. Reduced melting temperatures ( $\tilde{T}$ ) of the  $\alpha$ - ( $\circ$ ),  $\beta$ - ( $\bullet$ ), and  $\gamma$ -phases ( $\blacktriangle$ ) after isothermal crystallization at  $130^\circ\text{C}$  as a function of combined defect fractions ( $\tilde{X}$ ).

As it can be seen in Figure 4.7, the reduced melting temperatures of the  $\alpha$ -,  $\beta$ - and  $\gamma$ -phases for all samples containing any random combination of regio- and stereo-defects fall on one line. Figure 4.7 shows that the melting-lines for the three polymorphs run parallel to each other.

In order to clarify the melting points relationships between the various phases of isotactic polypropylene, melting points of the  $\beta$ - and  $\gamma$ -phase were correlated with the melting points of the  $\alpha$ -phase, see Figure 4.8. Two trend lines can be seen which run parallel within the experimental error, indicating that the melting points of the

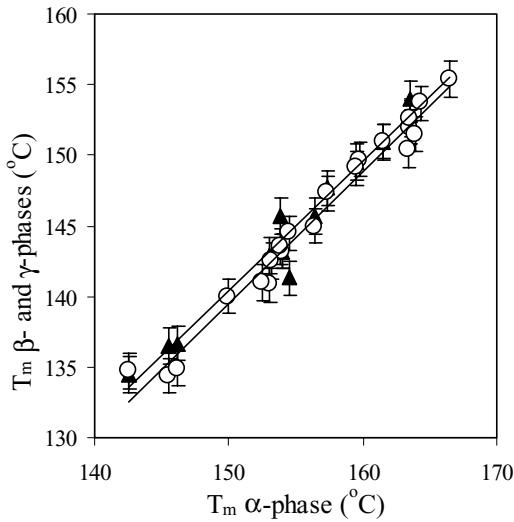
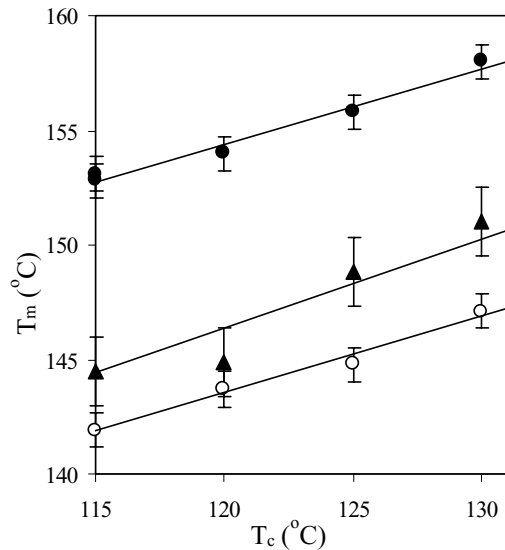


Figure 4.8. Correlation between the melting points of the  $\beta$ - and  $\alpha$ -phase ( $\circ$ ) and the  $\gamma$  and  $\alpha$ -phases ( $\blacktriangle$ ).

The conclusions mentioned above are relatively independent of the crystallization temperatures as we see in Figure 4.9. In Figure 4.9 the melting temperatures of  $\alpha$ -,  $\beta$ - and  $\gamma$ -phases as a function of the crystallization temperature is given for one polymer (M6). We see that the difference in melting temperatures between the several phases of iPP remains constant, independent of the crystallization temperature (for the range studied).

Figure 4.9. Melting temperature of the samples M6 as function of the crystallization temperature.  $\alpha$ -phase ( $\bullet$ ),  $\beta$ -phase ( $\blacktriangle$ ), and  $\gamma$ -phase ( $\circ$ ).



polymorphs are strongly related to each other. The melting temperatures of the  $\beta$ - and  $\gamma$ -phases are, on the average,  $10.9^{\circ}\text{C}$  and  $9.7^{\circ}\text{C}$  lower as compared to the melting temperatures of the  $\alpha$ -phase, the melting temperature difference being virtually independent of the combined defect fraction ( $\tilde{X}$ ). The polymorphs thus show the same dependence of melting-point depression on  $\tilde{X}^{\alpha=\beta=\gamma}$ .

## 4.4 Discussion

### 4.4.1 Comparison with theory

Several theories were developed to predict the melting point depression of copolymers. In these theories the polymer is considered to consist of crystallizable A monomer sequences which are interrupted by non-crystallizable B monomer sequences, or defects. The polymers described in these theories can also be considered, as in the case of polypropylene, as a crystallizable stereo/regio-regular polymer (A units) which is partitioned by configurational defects (B units) in the chain.

During the course of crystallization the defects (or B monomers) will be partitioned among the amorphous and crystalline phases. Two extreme cases can be distinguished: complete exclusion and uniform inclusion of defects in the crystalline phase [1]. In case of inclusion the defect can either enter the lattice as an equilibrium requirement, or be located within the lattice as a non-equilibrium defect [1].

Several types of crystal defects can be distinguished [44] including dislocations, chain disorder, and amorphous defects. Dislocations occur when the periodicity of the crystal is interrupted along a certain direction. Chain disorder is specified as a point defect. It includes chain ends, kinks, and chain torsion. The last class of defects is the amorphous defect. These defects can be described as an inclusion of a disordered region within the crystal. Obviously, the borderlines between the different crystal defects are not sharp and they vary in the energy which is needed to incorporate such defects into the crystal, i.e. a point like chain disorder defect may result in an amorphous defect when the chain disorder is high enough.

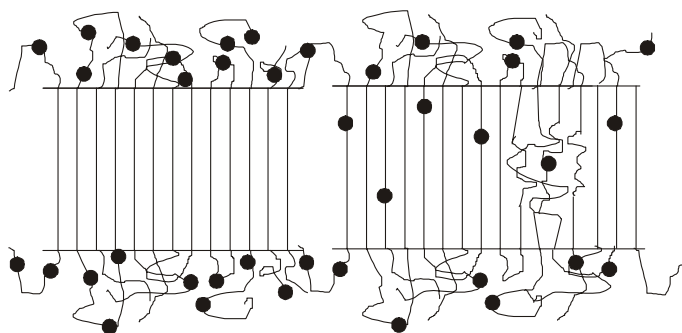


*Figure 4.10. Schematic representation showing the two limiting cases of polymer crystallization including defects; total exclusion (left) and uniform inclusion (right). In the case of uniform inclusion several point like defects and one amorphous defect are schematically presented. Original scheme is made after Sanchez and Eby [12].*

In the case if chain-defects (or B monomers) are completely excluded from the crystal, the melting point ( $T_m$ ) of polymers consisting of infinitely long, crystallizable sequences A in equilibrium with the melt having a defect fraction ( $X$ ) is described by Flory [23]. He started with the equation which gives the free energy difference,  $\Delta G$ , between the crystal and the melt:

$$\Delta G = \Delta G^0 + RT \ln \alpha, \quad (4.6)$$

where  $R$  is the universal gas constant and  $\alpha$  is the activity of the crystallizing copolymer and  $\Delta G^0$  is the bulk free energy difference for the complete defect-free polymer crystal with infinite lamellar thickness and molar mass, and is usually approximated by:

$$\Delta G^0 = \Delta H_f^0 (1 - T_m / T_m^0). \quad (4.7)$$

In the formula,  $T_m^0$  and  $H_f^0$  label the equilibrium melting temperature and equilibrium heat of fusion, respectively, for the complete defect-free polymer crystal with infinite lamellar thickness and molar mass. Using  $\alpha = \ln(1-X)$ , where  $X$  is the co-monomer (defect) fraction, the following result is found:

$$\frac{1}{T_m^0} - \frac{1}{T_m(X)} = \frac{R}{H_f^0} \ln(1-X), \quad (4.8)$$

where  $T_m(X)$  is the temperature of melting as function of  $X$  in the limit of total exclusion of defects.

Baur [11] proposed a modification of the Flory model by incorporating the constraint that only homopolymer sequences with a length of  $\zeta$  may be included into crystals exhibiting lamellar thicknesses corresponding to that length. The melting temperature of such crystals is then given by:

$$\frac{1}{T_m^0} - \frac{1}{T_m(X)} = \frac{R}{H_f^0} \left( \ln[1-X] - \langle \zeta \rangle^{-1} \right), \quad (4.9)$$

where  $\zeta = [2X(1-X)]^{-1}$  for random copolymers. A disadvantage of the Baur model is that it neglects the fact that the homopolymer sequences participating in the crystallization process are invariably fixed with other homopolymer sequences [13]. Consequently, segregation of homopolymer sequences with a length of  $\zeta$  will be difficult and equilibrium situations correspondingly difficult to reach. Moreover, the assumption of matching sequence lengths with the crystal length, which leads to an increase in the entropy of melting, is not correct [8]. As the entropy of discrete polymer sequences with lengths  $\zeta$  have not the same entropy of melting as the same polymer sequence lengths covalently bonded in a long polymer chain, we conclude that the assumption of matching sequences is not correct. Although, the Baur model and related models (e.g. the Wendling-Suter model [13]) give better



predictions of the observed melting point due to the introduction of an extra term ( $\zeta^1$ ) as compared with the Flory model, we will not proceed with these models.

The theories mentioned above were developed for the case of total exclusion of defects. Sanchez and Eby [12,45] developed a theory for the melting point of copolymers that also account for the partial inclusion of defects into the crystal lattice. As we shall use this theory to interpret our results, we give a brief account of the main points of the corresponding treatment.

The bulk free energy difference ( $\Delta G$ ) between a crystal with defects partially included and the melt with a concentration of defects equal to the overall composition ( $X$ ) of the polymer is given by [1]:

$$\Delta G = \Delta G^0 - RT \left( \frac{\varepsilon X_c}{RT} + (1 - X_c) \ln \left[ \frac{1 - X_c}{1 - X} \right] + X_c \ln \left[ \frac{X_c}{X} \right] \right). \quad (4.10)$$

The excess free energy of the defect, created by incorporating a defect in the crystalline lattice, is labeled by  $\varepsilon$ .

Setting  $\Delta G = 0$  in equation (4.10) and using equation (4.7) yields the melting temperature of an infinitely large crystal of composition  $X$ :

$$\frac{1}{T_m^0} - \frac{1}{T_m(X)} = - \frac{R}{H_f^0} \left( \frac{\varepsilon X_c}{RT} + (1 - X_c) \ln \left[ \frac{1 - X_c}{1 - X} \right] + X_c \ln \left[ \frac{X_c}{X} \right] \right). \quad (4.11)$$

From nucleation theory [10] it follows that  $l_{c,i} = 2\sigma_e/\Delta G + \delta l_c$ , where  $l_{c,i}$  is the initial crystal thickness and  $\sigma_e$  is the surface free energy. The minimum crystal thickness possible at the particular crystallization temperature is given by  $2\sigma_e/\Delta G$ . Under the assumption that  $\delta l_c = 0$ , we get for crystallized polymers with a finite lamellar thicknesses  $\Delta G - 2\sigma_e/l_{c,i} = 0$ . Incorporation of this equation in equation (4.11) yields the experimental melting point of crystals with finite thickness and in the presence of defects:

$$\frac{1}{T_m^0(1 - 2\sigma_e/\Delta H_f^0 l_{c,i})} - \frac{1}{T_m(X, l_{c,i})} = \left( \frac{R}{\Delta H_f^0 - 2\sigma_e/l_{c,i}} \right) \left( \frac{\varepsilon X_c}{RT_m(X, l_{c,i})} + (1 - X_c) \ln \left[ \frac{1 - X_c}{1 - X} \right] + X_c \ln \left[ \frac{X_c}{X} \right] \right) \quad (4.12)$$

For the inclusion limit ( $X_c = X$ ) equation (4.12) reduces to:

$$T_m(X, l_{c,i}) = T_m^0 \left( 1 - \frac{2\sigma_e}{\Delta H_f^0 l_{c,i}} - \frac{\varepsilon X}{\Delta H_f^0} \right). \quad (4.13)$$

When  $X_c = 0$  in equation (4.12) we obtain the melting point of a crystal with complete exclusion of defects:

$$\frac{1}{T_m^0(1 - 2\sigma_e/\Delta H_f^0 l_{c,i})} - \frac{1}{T_m(X, l_{c,i})} = \left( \frac{R}{\Delta H_f^0 - 2\sigma_e/l_{c,i}} \right) \ln(1 - X). \quad (4.14)$$

Note that equations (4.12), (4.13) and (4.14) reduce to the Gibbs-Thomson equation [1] when  $X \rightarrow 0$ . When  $l_{c,i} \rightarrow \infty$  equation (4.14) diverges to the equilibrium situation originally described by Flory, see equation (4.8).

The tendency for a defect to enter the lattice depends on the excess free energy of the defect ( $\varepsilon$ ). It was shown [1] that under equilibrium conditions the fraction of defects which enter the crystal lattice with a penalty  $\varepsilon$  can be calculated using [45]:

$$X_c^{eq} = \frac{Xe^{-\varepsilon/RT_c}}{(1 - X) + Xe^{-\varepsilon/RT_c}}. \quad (4.15)$$

The parameter  $X_c^{eq}$  is the equilibrium fraction of defects in the crystal and  $X$  is the global defect fraction of the melt prior to crystallization. Insertion of equation (4.15) into equation (4.12) yields the maximum melting temperature of crystals with equilibrium defect concentration and finite thickness [1]:

$$\frac{1}{T_m^0(1 - 2\sigma_e/\Delta H_f^0 l_{c,i})} - \frac{1}{T_m(X, l_{c,i})} = \left( \frac{R}{\Delta H_f^0 - 2\sigma_e/l_{c,i}} \right) \ln \left\{ (1 - X) + Xe^{\frac{-\varepsilon}{RT_c}} \right\}. \quad (4.16)$$

Originally, the development of these equations was based on the sequence propagation probability. The number of defects is then written as  $X$ . For a block copolymer  $p \gg (1-X)$ , and for an alternating copolymer  $p \ll (1-X)$ , and for a random co-polymer  $p = (1-X)$ . As the defects are distributed evenly over the chains in metallocene catalyzed polymers due to the single site character of the used metallocene catalysts, we assume  $p = (1-X)$ .

As mentioned before, the actual crystallization conditions determine the real concentration of defects ( $X_c$ ) in the crystal. A suitable parameter that denotes the fraction of concentration of defects ( $X_c$ ) in the crystal compared with the global composition  $X$ , is the partitioning coefficient ( $P_{CR}$ ). For different kinds of defects  $P_{CR}$  is defined as follows:

$$P_{CR}(i) = \frac{X_c(i)}{X(i)}, \quad (4.17)$$

where  $X_c(i)$  is the concentration of the  $i$ th kind of defect in the crystalline ( $CR$ ) region. It is not possible to establish a priori by theory the actual ratio of the amount of defects among the two phases [1]. This imposes serious problems in the analysis (or prediction) of the melting point in relation to the number and type of

defects. However, the analysis of melting point data with equilibrium theories is useful as it provides the limiting values for the partitioning coefficient and the defects excess free energy. Nevertheless, *direct* determination of the partitioning coefficient in order to fully compare the results from theory with the measured melting point data is indispensable. Alamo *et al.* [46,47] made large progress in determining the partitioning coefficients experimentally using  $^{13}\text{C}$ -NMR. They determined the values of  $P_{CR}$  for stereo- and regio-defects of isotactic polypropylene ( $\alpha$ -phase). These  $P_{CR}$ 's were used in the analysis of measured melting point data. However, in order to better comprehend the significance of this analysis, first the melting point data as function of the number and type of defects were analyzed using the aforementioned theory of Sanchez en Eby [12,45].

To achieve this goal, equations (4.12), (4.13), (4.14), and (4.16) were used to fit the melting point data for samples exhibiting a variation in the fraction of stereo-defects and samples with a variation in fraction of regio-defects, respectively (group 1 and group 2 listed in Table 4.1, respectively). The fitting was done for the  $\alpha$ -, as well as for the  $\beta$ -phases. No analysis was made for the  $\gamma$ -phase, as the melting point data for samples with low defect concentrations was not available. The material parameters which were used in the fitting procedure for the  $\alpha$ - and  $\beta$ -phases are mentioned in Table 4.2. In the case of samples with a varying amount of regio-defects we accounted for the melting point depression ( $\Delta T$ ) caused by the finite average fraction of stereo-defects ( $\pm 0.007$  (-)) present in the samples, see Figure 4.11.

	$T_m^0$ ( $^{\circ}\text{C}$ )	$\sigma_e$ ( $\text{J}/\text{m}^2$ )	$\Delta H_f^0$ ( $\text{kJ}/\text{mol}$ )	$l_{c,i}$ ( $\text{nm}$ ) <sup>1</sup>
$\beta$ -phase	177	$53 \times 10^{-3}$	5.0	19.6
$\alpha$ -phase	186	$62 \times 10^{-3}$	8.7	13.5

<sup>1</sup>Lamellar thickness values were measured for polymers with negligible amounts of defects, see Chapter 3.

Table 4.2. Summary of the parameters which were used for fitting equations (4.12), (4.13), (4.14), and (4.16).

First, the samples exhibiting only a variation in the amount of stereo-defects (group 1) were fitted according the equilibrium case of the Sanchez and Eby model using equation (4.16) and using  $\varepsilon$  as the fitting parameter. Figure 4.11 shows the results. An excellent agreement is found between the fitted equation (4.16) and the observed melting points assuming a value of the excess free energy value for including a stereo-defect into the monoclinic crystal of the  $\alpha$ -phase of  $\varepsilon = 4.5$  kJ/mol. The value for the excess energy for including a stereo-defect into the trigonal crystal of the  $\beta$ -phase is  $\varepsilon = 1.7$  kJ/mol. The energy penalty is clearly lower for the  $\beta$ -phase as compared with the  $\alpha$ -phase, see Table 4.3.

In Chapter 3 we determined the excess free energy from growth rate data. The growth rates of samples could be well described by the “equilibrium inclusion of defects” model using a value of  $\epsilon = 1.6$  kJ/mol ( $\alpha$ -phase) and of  $\epsilon = 1.2$  kJ/mol ( $\beta$ -phase), respectively. The magnitudes of the  $\epsilon$  values obtained from the growth rate data are lower than the  $\epsilon$  values obtained from the melting point analysis. However, the values of  $\epsilon$  for the  $\alpha$ -phase and the  $\beta$ -phases, respectively, show the same ratio.

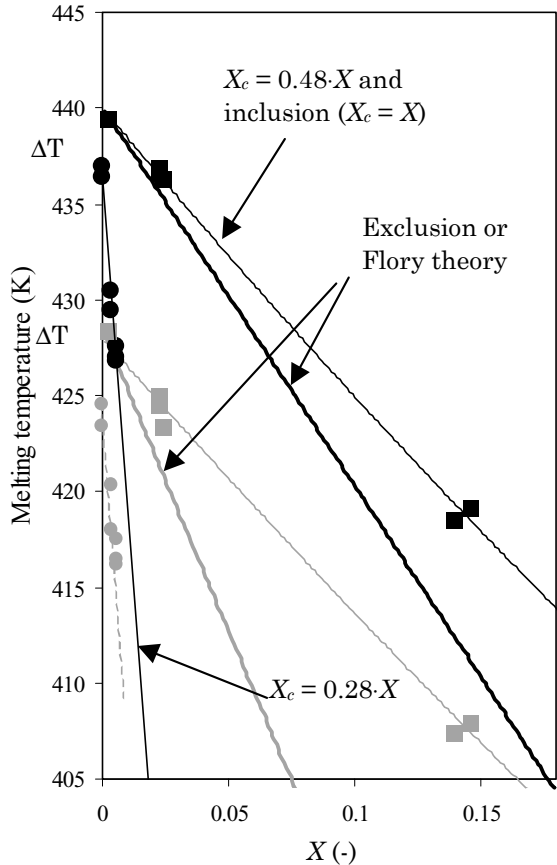


Figure 4.11. Fitting of melting points for the samples with only stereo-defects (squared symbols) and for the samples with varying amounts of regio-defects but approximately constant amount of stereo-defects (round symbols) both for the  $\alpha$ - (black symbols) and  $\beta$ -phases (gray symbols), respectively, using the Sanchez-Eby model [13] (see equations (4.12), (4.13), (4.14), and (4.16)).

Knowing the values for  $\epsilon$  it is possible to calculate  $P_{CR}$  using equation (4.15) and equation (4.10). We find for the partitioning coefficients  $P_{CR} = 0.26$  and  $P_{CR} = 0.53$  for the  $\alpha$ - and  $\beta$ -phases, respectively. The equilibrium theory predicts a higher amount of stereo-defects being included into the lattice for the  $\beta$ -phase compared with the  $\alpha$ -phase. This is in agreement with the general notion [44] that crystals with higher packing density (the  $\alpha$ -phase in this case) can tolerate less volume

addition than crystal forms with a lower density and larger disorder (the  $\beta$ -phase in this case).

The samples with stereo-defects were also fitted according to the uniform inclusion limit using equation (4.13) and  $\epsilon$  as a fitting parameter. This fit yielded a value for the defect excess free energy  $\epsilon = 3.0 \text{ kJ mol}^{-1}$  and  $\epsilon = 2.1 \text{ kJ mol}^{-1}$  for the  $\alpha$ - and  $\beta$ -phases, respectively (see Table 4.3). In addition, for the uniform inclusion limit we find a lower value of  $\epsilon$  for the  $\beta$ -phase. In the uniform inclusion limit the value of the partitioning coefficient is one ( $P_{CR} = 1$ ), per definition. A crystallization under real conditions, possibly non-equilibrium, will result in a partitioning of defects between the two limiting situations of equilibrium- and uniform-inclusion of defect:  $0.26 < P_{CR} < 1$  for the  $\alpha$ -phase and  $0.53 < P_{CR} < 1$  for the  $\beta$ -phase, respectively.

The melting points of the samples with a varying amount of regio-defects could be fitted less satisfactorily with the equilibrium model of Sanchez and Eby (equation (4.16)). In the fitting of the data for samples with regio-defects we maximized the excess defect free energy ( $\epsilon \rightarrow \infty$ ), i.e. under equilibrium conditions virtually no regio-defects are included in the crystal (which is the situation according to the Flory model). Although the fitting is clearly better for the  $\beta$ -phase as compared with the  $\alpha$ -phase (see Figure 4.11) the Flory equilibrium theory with total exclusion of defects cannot predict the observed melting temperatures. For the samples with the highest regio-defect fraction (0.0055 (-)) the difference between measured and fitted (calculated) melting points is  $11.8^\circ\text{C}$  for the  $\alpha$ -phase and  $9.9^\circ\text{C}$  for the  $\beta$ -phase, respectively.

Values of the excess free energy ( $\epsilon$ ) (kJ/mol)				
	$X_c = X$ Stereo-defect	$X_c = X_{eq}$ (eq. 4.15) Stereo-defect	$X_c = 0.48 \cdot X^1$ Stereo-defects	$X_c = 0.28 \cdot X^1$ Regio-defects
$\alpha$ -phase	3.0 ( $P_{CR} \equiv 1$ )	4.5 ( $P_{CR} = 0.26$ )	4.3 ( $P_{CR} = 0.48$ ) <sup>1</sup>	114 ( $P_{CR} = 0.28$ ) <sup>1</sup>
$\beta$ -phase	1.7 ( $P_{CR} \equiv 1$ )	2.1 ( $P_{CR} = 0.53$ )	-	-

<sup>1</sup>Measured values by Alamo et al. [46,47].

Table 4.3. Summary of the excess free energy ( $\epsilon$ ) values obtained by fitting the equations (4.12), (4.13), (4.14), and (4.16) to the observed melting points of the  $\alpha$ - and  $\beta$ -phases. The values for  $P_{CR}$ , are indicated, as well.

As the total exclusion of defects cannot account for the depression of the equilibrium melting point in polymers which exhibit regio-defects, we can conclude that a certain amount of the total fraction of regio-defects will be included into the crystal as non-equilibrium defects.

Since we know the values of  $\epsilon$  in the total exclusion- and uniform-inclusion limits, respectively, and we know the value of  $\epsilon$  under equilibrium conditions, we

can compare these values with the values of  $\varepsilon$  obtained by Alamo *et al.* [46,47]. Although, some assumptions were made in their respective NMR analyses, they obtained the following values for the partitioning coefficient:  $P_{CR}$  (stereo: mrrm) =  $0.48 \pm 0.06$  and  $P_{CR}$  (regio: 1,2-erythro) =  $0.28 \pm 0.08$  (independent of the crystallization kinetics). The values of the  $P_{CR}$  (or more precisely  $X_c$ ) for regio- and stereo-defects can be used in the general equation of the Sanchez and Eby theory (see equation (4.12)). Equation (4.12) can be fitted to the melting point data of the regio- and stereo-defects, respectively, with  $\varepsilon$  as a fitting parameter. The fitted lines are shown in Figure 4.11.

We find for the excess free energy for including a stereo-defect into the monoclinic crystal of the  $\alpha$ -phase a value of  $\varepsilon = 4.3 \text{ kJ mol}^{-1}$ . For the excess free energy required to include a regio-defect into an  $\alpha$ -phase lattice under non-equilibrium circumstances a very high value of the  $\varepsilon = 112 \text{ kJ/mol}$  is found, which is several times the value of the heat of fusion ( $\Delta H^0_f = 8.7 \text{ kJ/mol}$ ). It is clear that such high energy for including a regio-defect will lead to a modified morphology.

The results from the theory of Sanchez and Eby strongly supports the results described by Alamo *et al.* [46,47]. The regio-defects are more difficult to incorporate in the crystalline regions than the stereo-defects:  $P_{CR}$  (regio: 1,2-erythro) <  $P_{CR}$  (stereo: mrrm) and a certain amount of regio-defects is included into the crystal lattice. The value of  $P_{CR}$  directly measured by NMR will be within the limiting situations of equilibrium- and uniform-inclusion, which is in agreement what we found:  $0.26 < (P_{CR} = 0.28) < 1$ .

In Chapter 3 we studied for the same samples the crystallization rate (under isothermal crystallization conditions). We found that the linear *growth rate dependence* on the amount of defects (both stereo- and regio-defects) was *higher* for the  $\beta$ -phase as compared to the  $\alpha$ -phase. Initially, i.e. for samples with a negligible defect fraction, the growth rate of the  $\beta$ -phase ( $G_\beta$ ) is higher than the growth rate of the  $\alpha$ -phase ( $G_\alpha$ ). However, beyond a certain critical defect fraction  $G_\beta$  becomes lower than  $G_\alpha$ . On the contrary, Figure 4.7 clearly shows that the *melting point depression* as a function of the defect fraction is *linear* and the slope is the *same* for both the  $\alpha$ - and the  $\beta$ -phases. This means that the difference in melting temperature between the  $\alpha$ - and  $\beta$ -phase is constant. Therefore, we can assume, at least as a first order approximation, that the possible morphological *changes* (lamellar thickness, crystallinity) as function of the defect fraction, are of the same nature for the  $\alpha$ - and  $\beta$ -phase and that in turn the melting point depression is caused by the increase in Gibbs free energy as described by Sanchez and Eby, see equation (4.11). As the melting point dependences are linear, the partitioning coefficient which comes from equation (4.11) for the different defects must be constant (although the crystallization kinetics changes). In principle, partitioning coefficients might depend on both the crystallization kinetics and on the crystal

characteristics. We find that the crystallization kinetics do not have influence on the value of  $P_{CR}$ . However, the crystal characteristics (due to  $\Delta H^0_f$ ) determine the value of  $P_{CR}$ . This is full agreement with the findings by Alamo *et al.* [46,47] who also suggested that the kinetics of crystallization do *not* influence the value of  $P_{CR}$ .

The distribution of stereo-defects in principle may be influenced by the connectivity with regio-defects or *vice versa*. For example, if a regio-defect is excluded from the crystal-phase, the neighboring stereo-defects will have a higher chance to remain in the melt, compared with stereo-defects positioned at a larger distance from the regio-defects. The effect of connectivity on the partitioning of regio-defects will be small when the partitioning coefficient of the stereo-defects is close to 1 (uniform inclusion limit). The high value of the partitioning coefficient for stereo-defects indicates this situation. As the fraction of regio-defects is significantly lower than the fraction of stereo-defects, we do not expect an effect on the partitioning of stereo-defects due to regio-defects.

As indicated in the derivation of equations (4.12) to (4.16), except for the number of defects ( $X$ ) and the excess free energy ( $\epsilon$ ), all other parameters are assumed to be independent of the number and kind of defects. According to the aforementioned theories (the Flory and Sanchez-Eby, respectively), neither the surface free energy, nor the equilibrium heat of fusion, nor the lamellar thickness will change with increasing defect fraction. However, it is expected that some of these parameters will not remain constant with increasing defect fraction, and the exact changes would depend on the partitioning, crystal phase and temperature. In the previous chapter (see Chapter 3) we investigated the morphology of the same group of samples using small- and wide-angle X-ray scattering (SAXS and WAXD). Although, we could not be conclusive about the trend of the lamellar thickness with the number and kind of defects, we had indications of a small decrease in the lamellar thickness (see Chapter 3) with a varying amount of defects. A smaller lamellar thickness will result in a lower melting point. Therefore, a decrease in lamellar thickness would improve the agreement between the predictions of the melting point from the theory and the experiments.

#### 4.4.2 Discussion of the melting point determination by DSC

In the determination of the melting points, separate melting of the different polymorphs of iPP was assumed. The influence of the melting of one phase on the melting of another phase was implicitly neglected. For the melting of the  $\beta$ -phase this assumption is valid. Above  $T_{\alpha\beta}$  and below  $T_{\beta\alpha}$  the growth rate of the  $\alpha$ -phase ( $G_\alpha$ ) is smaller than the growth rate of the  $\beta$ -phase ( $G_\beta$ ).  $\beta$ -crystals can grow undisturbed until they impinge upon other crystals (a material with a high  $\beta$ -phase content). Below  $T_{\alpha\beta}$  and above  $T_{\beta\alpha}$ ,  $G_\beta < G_\alpha$ , this implies that once a  $\alpha$ -nucleus grows on the advancing growth front of a  $\beta$ -crystal, the  $\alpha$ -nucleus will grow into a full crystal, blocking further growth of the  $\beta$ -crystal. The  $\alpha$ - and  $\beta$ -phase are thus

macroscopically separated. We should point out that DSC scans of the  $\beta$  phase can exhibit a complex behavior if no proper precautions are taken. If  $\beta$ -nucleated samples are cooled down to below the  $\beta\alpha$ -recrystallization temperature,  $\alpha$ -crystallization begins to proceed. Upon subsequent heating complex DSC traces may be observed, depending on the thermal history. Thus, we have taken special care during the DSC studies of the  $\beta$ -modification that the samples were not cooled down to below  $T_{\alpha\beta}$ .

For the combination of the  $\alpha$ - and  $\gamma$ -phase the assumption of undisturbed melting of both phases is less straightforward. We know from the literature that the  $\gamma$ -phase is accompanied by the occurrence of the  $\alpha$ -phase [39]. Partial melting of  $\gamma$ -lamellae thus changes the direct environment of  $\alpha$ -crystals. The initially constrained melt becomes more relaxed due to the disappearance of the  $\gamma$ -crystals. During heating, the  $\alpha$ -crystals thus have more freedom to thicken and stabilize, which may result in an increase of their melting point. At the moment we cannot estimate the magnitude of this effect.

Several factors can be pointed out which influence the value of the melting point measured by DSC including melting-recrystallization-melting behavior; annealing, i.e. lamellar thickening; thermal lag; and super-heating of crystals. Each of these factors causes an increase in the melting point determined. In order to investigate the influence of the aforementioned phenomena on the determination of the melting points, several samples (M2, M7, M11) with different defect fractions (fractions = 0.02; 0.07; 0.08) were isothermally crystallized and heated at different rates (10, 1, and 0.1 °C/min), see Figure 4.12.

The polymer with the lowest fraction of defects (Figure 4.12 right) shows clear melting-recrystallization-melting behavior. The DSC trace made with the lowest heating rate (0.1 °C/min), shows two peaks associated with the (partial) melting of the original crystals and melting of the recrystallized crystals. The relative weight of the higher melting temperature peak decreases with increasing heating rate. In the curve obtained at 1 °C/min, the high temperature peak can be detected as a shoulder (at the higher temperature side) and in the curve made at 10 °C/min the shoulder can not be detected anymore. In contrary to the polymer with the lowest fraction of defects, the polymer with highest defect fraction exhibits no double peak in DSC trace made at the lowest heating rate (0.1 °C/min) (see Figure 4.12 left). However, for the sample a higher temperature shoulder can be detected at the lowest heating rate (0.1 °C/min). In conclusion, we say that melting-recrystallization-melting phenomena play a role at slow heating rates, but can practically be excluded for the determination of the melting points at 10 °C/min.

Figure 4.12 (left, middle, and right) shows for all three polymers that the position of the main melting peak at the lowest heating rate (0.1 °C/min) is shifted to higher temperatures (as compared with position of the main melting peak at



higher heating rates). The reason for this behavior is that during heating of the material (after isothermal crystallization without cooling to room temperature) the crystals continuously become more ordered and stable (an annealing effect). Higher perfection of crystals will lead to higher melting temperatures. A lower heating rate allows the initial imperfect crystals to stabilize over longer times compared with higher heating rates. Therefore, the crystals will melt at higher temperatures at lower heating rates.

The peak temperature of the main endotherms (for all three polymers) obtained at 10 °C/min shows a shift to higher temperatures compared to the endotherms obtained at 1 °C/min. The differences in melting peak temperatures between the 1 and 10 °C/min is approximately the same for all three polymers, i.e. no strong correlation with chain-architecture can be found. The increase in melting temperature can be indicative for superheating, however can also be an instrumental effects.

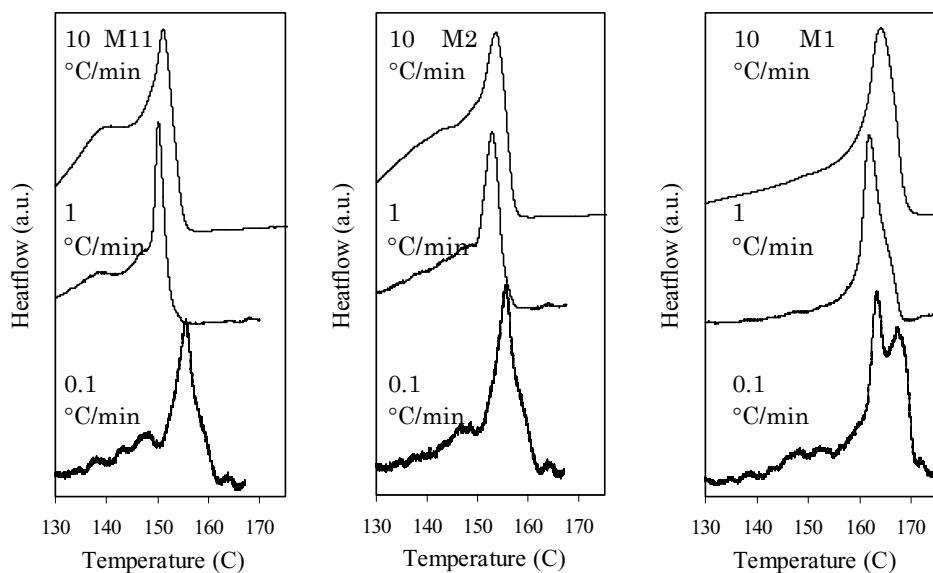


Figure 4.12. DSC traces of M11, M2 and M1 (decreasing amount of defects) obtained in measurements with different heating rates (10, 1.0, 0.1 °C/min) after isothermal crystallization at 130°C.

Obviously, it is not correct to take the position of the peak at 10 °C/min heating-rate as the melting point of the polymer. The above analysis showed that annealing- and super-heating effects take place and cause an increase in the melting point determined. However, one can draw the conclusion that the error due to these effects is much smaller than the change in melting temperatures due to the incorporation of defects into the chain.

## 4.5 Conclusions

An extensive group of samples of iPP with different primary chain (defects) structures provided us the opportunity to study separately the influence of the amount and type of defects on the crystallization, morphology, and fusion behavior of isotactic polypropylene. The melting point depression of the three polymorphs ( $\alpha$ -,  $\beta$ -, and  $\gamma$ ) was measured with DSC. Based on literature results we were able to determine the melting point of the  $\gamma$ -phase. The  $\beta$ -phase was induced by a highly selective nucleating agent which allowed us to determine the melting point of the  $\beta$ -phase even in samples with a high defect fraction.

The regio-defects have a much larger influence on melting than stereo-defects, which is in accordance with direct measurements done by Alamo *et al.* [46,47]. A combined defect fraction was introduced, which could describe samples with any combination in the relative amounts of stereo- and regio-defects. We found for the  $\alpha$ -,  $\beta$ -, and  $\gamma$ - polymorphs and for both types of defects (stereo/regio) a strong linear decrease in melting point as function of the amount of defects. The difference in melting temperature of the three crystal-phases was found constant and independent of the amount of defects. The relative melting point depression is thus independent of the crystal structure, despite the differences in morphological character of the polymorphs (cross-hatches, presence of the  $\gamma$ -phase, relative amounts of  $\alpha_I$  and  $\alpha_{II}$  crystals, or differences in chain tilt). We also concluded that the melting point depression is independent of the rate of crystallization, which is in full agreement with the results found by Alamo *et al.* [46,47]. The growth rates of the  $\alpha$ - and  $\beta$ -phases have different dependences on the defect fraction, which results in large differences in the growth rates between the two phases.

The melting point depression for the different crystal phases and types of defects were analyzed according to a theory developed by Sanchez and Eby [12]. The melting point data was fitted in the limits of total exclusion, uniform inclusion and under equilibrium conditions. It was found that exclusion (or under equilibrium conditions assuming an infinite defect free-energy) alone can not account for the melting point depression in samples exhibiting only a variation in regio-defects. Based on that observation we conclude that a certain amount of regio-defects must be partitioned into the crystal lattice as non-equilibrium defects. Alamo *et al.* [46,47] determined experimentally that the partitioning coefficient for regio-defects is indeed larger than zero. We found that stereo defects are not severely rejected from the crystal. The samples (exhibiting  $\alpha$ - or  $\beta$ -phase) with only a varying amount of stereo-defect could be fitted with both the uniform inclusion and equilibrium assumption. The two situations border the partitioning coefficient:  $0.26 < P_{CR} < 1$  for the  $\alpha$ -phase and  $0.53 < P_{CR} < 1$  for the  $\beta$ -phase. For the  $\alpha$ -phase  $P_{CR}$  was determined as 0.48 by Alamo *et al.* [46,47]. The differences in the value of the partitioning coefficients for the  $\alpha$ - and  $\beta$ -phase (0.26 and 0.53, respectively)

indicate that the excess free energy required for incorporating a stereo-defect into the trigonal lattice of the  $\beta$ -phase (1.7-2.1 kJ/mol) is lower than that for the  $\alpha$ -phase (3.0-4.5 kJ/mol).

In conclusion, isotactic polypropylenes synthesized by metallocene catalysts show unique properties in the sense that the system allows us to study the influence of two different kinds of defects on the crystallization, morphology and fusion behavior for three different crystal-phases. Moreover, with this system it is possible to study the influence of the crystal structure on the mechanisms of crystallization separately from the molecular architecture. Although, a fair amount of work was done, many possibilities and question are left open for further research.

## 4.6 References

- (1) Mandelkern, L. *Crystallization and Melting*; Booth, C. and Price, C., Ed.; Pergamon Press: Oxford, 1989; Vol. 2, pp 363.
- (2) Janimak, J. J.; Cheng, S. Z. D.; Giusti, P. A.; Hsieh, E. T. Isotacticity effect on crystallization and melting in polypropylene fractions: 2. Linear crystal-growth rate and morphology study *Macromolecules* **1991**, *24*, 2253.
- (3) Cheng, S. Z. D.; Janimak, J. J.; Zhang, A. Isotacticity effect on the crystallization and melting in polypropylene fractions: 1. Crystalline structures and thermodynamic property changes *Polymer* **1991**, *32*, 648.
- (4) Weng, J.; Olley, R. H.; Bassett, D. C. On crystallization in polypropylene-polyethylene blends *Chin. J. of Appl. Chem.* **2001**, *18*, 267.
- (5) Paukkeri, R.; Lehtinen, A. Thermal behaviour of polypropylene fractions: 1. Influence of tacticity and molecular weight on crystallization and melting behaviour *Polymer* **1993**, *34*, 4075.
- (6) Hauser, G.; Schmidtke, J.; Strobl, G. The role of co-units in polymer crystallization and melting: New insights from studies on syndiotactic poly(propene-co-octene) *Macromolecules* **1998**, *31*, 6250.
- (7) Isai, J. R.; Graham, J. A.; Mandelkern, L.; Alamo, R. G. Some aspects of the crystallization of ethylene copolymers *Polymer* **2000**, *41*, 8813.
- (8) Crist, B.; Howard, P. R. Crystallization and melting of model ethylene-butene copolymers *Macromolecules* **1999**, *32*, 3057.
- (9) Huang, J.; Lisowski, M. S.; Runt, J.; Hall, E. S.; Kean, R. T.; Buehler, N.; Lin, J. S. Crystallization and microstructure of poly(L-lactide-co-meso-lactide) copolymers *Macromolecules* **1998**, *31*, 2593.

- (10) Flory, P. J. Thermodynamics of crystallization in high polymers *J. Chem. Phys.* **1947**, *15*, 684.
- (11) Baur, H. Einfluß der Sequenzlängenverteilung auf das Schmelz-Ende von Copolymeren *Makromol. Chem.* **1966**, *98*, 297.
- (12) Sanchez, I. C.; Eby, R. K. Thermodynamics and crystallization of random copolymers *Macromolecules* **1975**, *8*, 638.
- (13) Wendling, J.; Suter, U. W. A new model describing the cocrystallization behavior of random copolymers *Macromolecules* **1998**, *31*, 2516.
- (14) Turner-Jones, A.; Aizlewood, J. M.; Beckett, D. R. Crystalline forms of isotactic polypropylene *Makrom. Chem.* **1964**, *75*, 134.
- (15) Varga, J.; Karger-Kocsis, J. Rules of super-molecular structure formation in sheared isotactic polypropylene melts *J. Polym. Sci., Polym. Phys. Ed.* **1996**, *34*, 657.
- (16) Varga, J.; Garzo, G.; Ille, A. Kristallisation, umkristallisation und schmelzen der  $\beta$ -Modifikation des Polypropylens *Angew. Makromol. Chem.* **1986**, *142*, 171.
- (17) Brückner, S.; Phillips, P. J.; Mezphani, K. On the crystallization of  $\gamma$ -isotactic polypropylene: A high pressure study *Macromol. Rapid Comm.* **1997**, *18*, 1.
- (18) Varga, J.; Mudra, I.; Ehrenstein, G. W. A highly active thermally stable  $\beta$ -nucleating agent for isotactic polypropylene *J. Appl. Polym. Sci.* **1999**, *74*, 2357.
- (19) Suhm, J. New molecular and super molecular polymer architectures via transition metal catalysed alkene polymerization *J. Mat. Chem.* **1998**, *8*, 553.
- (20) Bond, E. B.; Spruiell, J. E.; Lin, J. S. A WAXD/SAXS/DSC study on the melting behaviour of Ziegler-Natta and metallocene catalysed isotactic polypropylene *J. Polym. Sci., Polym. Phys. Ed.* **1999**, *37*, 3050.
- (21) De Rosa, C.; Auriemma, F.; Circelli, T.; Waymouth, R. M. Crystallization of the alpha and gamma forms of isotactic polypropylene as a tool to test the degree of segregation of defects in the polymer chains *Macromolecules* **2002**, *35*, 3622.
- (22) Galante, M. J.; Mandelkern, L.; Alamo, R. G.; Lehtinen, A.; Paukkeri, R. Crystallization kinetics of metallocene type polypropylenes *J. Therm. Anal.* **1996**, *47*, 913.

- (23) Flory, P. J. Theory of crystallization in copolymers *Trans. Faraday Soc.* **1955**, *51*, 848.
- (24) Randall, J. C. Carbon-13 nuclear magnetic resonance quantitative measurements of average sequence lengths of like stereochemical additions in polypropylene and polystyrene *J. Polym. Sci.* **1976**, *14*, 2083.
- (25) Although essentially the same procedure was followed for all samples, minor differences in the experimental details could take place. This was a consequence of the many different persons and companies who supplied the samples and who were involved in the measurements. We greatly acknowledge their contributions.
- (26) Busico, V.; Cipullo, R.; Monaco, G.; Vacatello, M. Full assignment of the  $^{13}\text{C}$  NMR spectra of regioregular polypropylenes: Methyl and methylene region *Macromolecules* **1997**, *30*, 6251.
- (27) Pae, K. D.  $\gamma$ - $\alpha$  Solid-solid transition of isotactic polypropylene *J. Polym. Sci.* **1968**, *6*, 657.
- (28) Fatou, J. G. Melting temperature and enthalpy of isotactic polypropylene *Eur. Polym. J.* **1971**, *7*, 1057.
- (29) Varga, J. Supermolecular structure of isotactic polypropylene *J. Mat. Sci.* **1992**, *27*, 2557.
- (30) De Rosa, C.; Guerra, G.; Napolitano, R.; Petraccone, V.; Pirozzi, B. Conditions for the  $\alpha_1$ - $\alpha_2$  transition in isotactic polypropylene samples *Eur. Polym. J.* **1984**, *20*, 937.
- (31) Alamo, R. G.; Brown, G. M.; Mandelkern, L.; Lehtinen, A.; Paukkeri, R. A morphological study of a highly structurally regular isotactic polypropylene fraction *Polymer* **1999**, *40*, 3933.
- (32) Yamada, K.; Matsumoto, S.; Tagashira, K.; Hikosaka, M. Isotacticity dependence of spherulitic morphology of isotactic polypropylene *Polymer* **1998**, *39*, 5327.
- (33) Alamo, R. G.; Kim, M. H.; Galante, M. J.; Isasi, J. R.; Mandelkern, L. Structural and kinetic factors governing the formation of the  $\gamma$ -polymorph of isotactic polypropylene *Macromolecules* **1999**, *32*, 4050.
- (34) Dai, P. S.; Cebe, P.; Capel, M. Thermal analysis and X-ray scattering study of metallocene isotactic polypropylene prepared by partial melting *J. Polym. Sci.: Polym. Phys. Ed.* **2002**, *40*, 1644.

- (35) Dai, P. S.; Cebe, P.; Capel, M.; Alamo, R. G.; Mandelkern, L. Simultaneous in-situ SAXS and WAXS study of crystallization and melting behavior of metallocene isotactic polypropylene *ACS Sym. Ser.* **2000**, *739*, 152.
- (36) Huang, T. W.; Alamo, R. G.; Mandelkern, L. Fusion of isotactic poly(propylene) *Macromolecules* **1999**, *32*, 6374.
- (37) Olley, R. H.; Basset, D. C. On the development of polypropylene spherulites *Polymer* **1989**, *30*, 399.
- (38) In Chapter 3 of this thesis we showed that that lamellar thickness of the radial 'mother' and tangential 'daughter' lamellae differ by approximately 6 nm, which corresponds to an approximate difference in melting temperature of 6°C (estimated from the Gibbs-Thomson equation) .
- (39) Lotz, B.; Graff, S.; Wittmann, J. C. Crystal morphology of the gamma (triclinic) phase of isotactic polypropylene and its relation to the alpha-phase *J. Polym. Sci.: Polym. Phys. Ed.* **1986**, *24*, 2017.
- (40) Pennings, A. J.; van der Mark, J. M. A. A.; Booij, H. C. Hydrodynamically induced crystallization of polymers from solution. II. The effect of secondary flow *Kolloid Z. Z. Polym.* **1970**, *236*, 99.
- (41) Varga, J.  $\beta$ -Modification of polypropylene and its two-component systems *J. Thermal Anal.* **1989**, *35*, 1891.
- (42) Juhász, P.; Varga, J.; Belina, K.; Belina, G. Efficiency of  $\beta$ -nucleating agents in propylene/ $\alpha$ -olefin copolymers *J. Macromol. Sci.-Phys.* **2002**, *B41*, 1173.
- (43) Benedict, G. M.; Goodall, B. L. *Metallocene Catalysed Polymers*; William Andrew Inc.: Norwich, NY, 1998.
- (44) Wunderlich, B. *Macromolecular Physics*; Academic Press: New York, 1973; Vol. 1.
- (45) Helfand, E.; J. I. Lauritzen, J. Theory of copolymer crystallization *Macromolecules* **1973**, *6*, 631.
- (46) Alamo, R. G.; VanderHart, D. L.; Nyden, M. R.; Mandelkern, L. Morphological partitioning of ethylene defects in random propylene-ethylene copolymers *Macromolecules* **2000**, *33*, 6094.
- (47) VanderHart, D. L.; Alamo, R. G.; Nyden, M. R.; Kim, M. H.; Mandelkern, L. Observations of resonances associated with stereo and regio defects in the crystalline regions of isotactic polypropylene: Toward a determination of morphological partitioning *Macromolecules* **2000**, *33*, 6078.



# Chapter 5

## Structure-Property Relations in Different Nucleated Polypropylenes<sup>1</sup>

The correlation between impact resistance and crystalline morphology was studied on specimens prepared from three different polypropylene homo- and copolymers, obtained by injection molding. The crystalline morphology was varied using three different nucleating agents. Linear elastic fracture mechanics was applied for the description of fracture resistance. The results indicate that morphological characteristics strongly influence the mechanical performance of the polymers. According to Young's theory for yielding the resistance to crack initiation, represented by  $K_{Ic}$ , correlates with the thickness of the lamellae. This suggests that the onset for yield can be described by a dislocation mechanism. The total energy absorbed during impact,  $G_{Ic}$ , is a complex function of the morphology with no single identifiable morphological characteristic that dominates its value. The heterogeneous, dispersed morphology of the polypropylene block copolymer initiates an additional energy absorption mode compared to the homo-polymer and the random-copolymer.

---

<sup>1</sup> Parts of this Chapter were published in:

Meer, D. W. v. d.; Pukánszky, B.; Vancso, G. J. On the dependence of impact behavior on the crystalline morphology in polypropylenes. *J. Macromol. Sci.-Phys.* **2002**, *B41*, 1105.



## 5.1 Introduction

A variety of commercial polypropylene polymers, including homo-polymers, as well as random- and block-copolymers of propylene and ethylene are prepared by different technologies (1). The production of these polypropylenes, now complemented by polymers polymerized using metallocene single-site catalysts, increases rapidly. These polymers are widely used as structural engineering commodity plastics (2, 3). A considerable amount of polypropylenes is processed by injection molding e.g. as automotive parts, houseware articles, and appliance parts (1). The structure and morphology of such injection-molded PP products is often complicated. Morphology varies significantly through the cross section of the part; the corresponding typical skin-core structures have been investigated by several research groups (4, 5). Karger-Kocsis and coworkers (6) have shown that as many as six layers can be distinguished as we proceed from the skin, in which crystalline structure cannot be detected by optical methods, towards the coarse spherulitic core. Crystal type, size, orientation, degree of crystallinity, lamellar thickness and LP, all can change throughout the sample, and the properties vary accordingly. The inhomogeneous structure often leads to inferior properties. Hence strength and impact-resistance often do not reach the required performance levels, or warpage of the product occurs.

The structure and morphology of polymers have often been tailored to achieve improved materials performance. Possibilities of tailoring the primary chemical structure of polypropylenes are provided by the use of different stereospecific Ziegler-Natta (7) or single-site metallocene catalysts (8). Higher order crystalline morphology can be tuned by the use of various nucleating agents (2, 3). Although the application of nucleating agents improves the homogeneity of the structure, the exact effect of these additives on crystalline morphology is difficult to predict.

Numerous studies were carried out concerning structure-property relationships in polypropylenes, however often contradictory conclusions were reached (2, 3). Attempts were made to identify the most important features of the crystalline structure and their effects on the mechanical properties. For example, a maximum was found in the yield stress of PP as a function of the size of the spherulites (9, 10). A similar correlation was observed between spherulite size and impact resistance (11). Maiti *et al.* (12) claimed that the tensile modulus and yield strength of particulate filled PP mainly depend on the degree of crystallinity of the matrix, while Hutley and Darlington (13, 14) found a very close correlation between the crystallization temperature and the falling weight impact resistance of some filled PP's. However, general correlations between crystalline structure and mechanical properties have not been established. The main reason for the lack of such general relationships is due to the existence of several levels of structural hierarchy. In principle, each of the corresponding structural features may influence the

mechanical behavior. In addition, it is practically impossible to change only one of these structural features without affecting the others. This makes identifying the dominating structural feature, which determines a given property, often an impossible task.

The effect of nucleation on the stiffness of three polypropylenes, i.e., an isotactic homo-polymer, and a random-polymer and a block-copolymer, was described in an earlier paper (15). It was shown that crystallinity and lamellar thickness are the main factors that influence Young's modulus. A single correlation described the relationship between the modulus and structure, irrespectively of the type of the polymer and the nucleating agents, or the amount of these nucleating agents in the polymer. The present paper discusses the impact resistance of the same materials and the effect of morphological changes induced by nucleation on this impact resistance.

## 5.2 Experimental

A polypropylene homo-polymer (homo-PP), as well as a random- (random-PP), and a block-copolymer (block-PP) (16) were investigated. All three polymers were produced by TVK, Hungary. The most important characteristics of the polymers studied are compiled in Table 5.1. In addition to the various nucleating agents, the polymer specimens contained 1000 ppm Irganox 1010 antioxidant, 1000 ppm Sandostab PEPQ co-stabilizer, and 1000 ppm calcium stearate. Polymer morphology was varied by using three different heterogeneous nucleating agents. Their most important characteristics, including their chemical structure, are collected in Table 5.2.

Nucleating agent	Trade name	Structure	$d_n^a$ ( $\mu\text{m}$ )	$A^b$ ( $\text{m}^2/\text{g}$ )
Aluminate	Sandostab 4030	I	12.5	55.6
Na benzoate	-	II	11.9	8.4
Phosphate	ADK STAB NA11	III	23.6	5.5

<sup>a</sup> number average particle size

<sup>b</sup> specific surface area

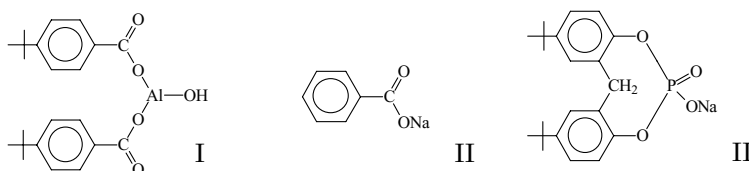


Table 5.1. Characteristics of the nucleating agents. I, II, and III: Chemical structures of the various nucleating agents used.

Polymer type	Trade name	Ethylene content (%)	$\overline{M}_w$ (g/mol)	$\overline{M}_n$ (g/mol)	$\overline{M}_w / \overline{M}_n$ (-)	MFI <sup>b</sup> (g/min)
Homo-PP	Tipplen H301	0	163	53	3.1	12
Random-PP	Tipplen R301	3.5	171	48	3.6	11
Block-PP	Tipplen K301	9.0	a	a	a	12

<sup>a</sup> Accurate data could not be obtained due to the “rubbery” phase present. Peak molar-masses however were comparable.

<sup>b</sup> Melt flow index (MFI) measured 230 °C and 21.6 N.

*Table 5.2. Characteristics of the polypropylene polymers used.*

Sodium benzoate (SB) (which is often used as reference material for numerous studies on nucleation) and two other commercial nucleating agents (NA11 and S4030) were added to the polymers in 0.05, 0.1, 0.15, and 0.3 wt%, respectively.

In order to increase homogeneity and to maintain constant properties, the nucleating agents and the stabilizers were added to the PP powder samples in a high speed, fluid mixer. The time of homogenization was 3 min. The dry-blend was compounded using a Brabender DSK 42/7 twin-screw compounder at 190 °C and 50 rpm. The polymer melt was cooled in a water bath and subsequently granulated. Injection molded bars were prepared on a Battenfeld BA 200/50 CD injection molding machine with 60 °C mold temperature. The specimens were stored under ambient conditions at least for one week prior to testing.

Crystallization characteristics of the virgin and nucleated polymers were determined by a Perkin Elmer DSC 7 instrument at 10 °C/min cooling rate. The effect of nucleation on the crystalline morphology was also studied by polarization optical microscopy (POM). Crystallization was carried out by using a Mettler FP80 hot stage with 5 °C/min cooling rate and optical micrographs were captured regularly during crystallization. Non-isothermal experiments were performed instead of isothermal measurements in order to simulate the non-isothermal conditions of processing. The samples were heated up to 200 °C and kept at this temperature for 5 min before crystallization in order to remove thermal history. Tensile yield stress and modulus were measured on a Zwick 1445 tensile testing apparatus at 50 mm/min cross-head speed. Specimens with 80 x 10 x 4 mm<sup>3</sup> dimensions were cut from injection molded bars for impact testing. The test samples were notched to different depths by a saw and sharpened by an industrial razor blade. Notch depth varied between 1 and 7.5 mm. Fracture testing was carried out on an instrumented impact tester with 2.9 m/sec velocity using a 40 mm span. Due to the high impact rate applied, dynamic effects occurred during fracture, this was compensated by the use of mechanical damping. The damper used was a 1 mm thick silicon rubber plate fixed to the force transducer. Energy absorption by the damper was corrected with a technique developed and described earlier (17). The fracture surface of the broken specimens was also characterized by

scanning electron microscopy (SEM).

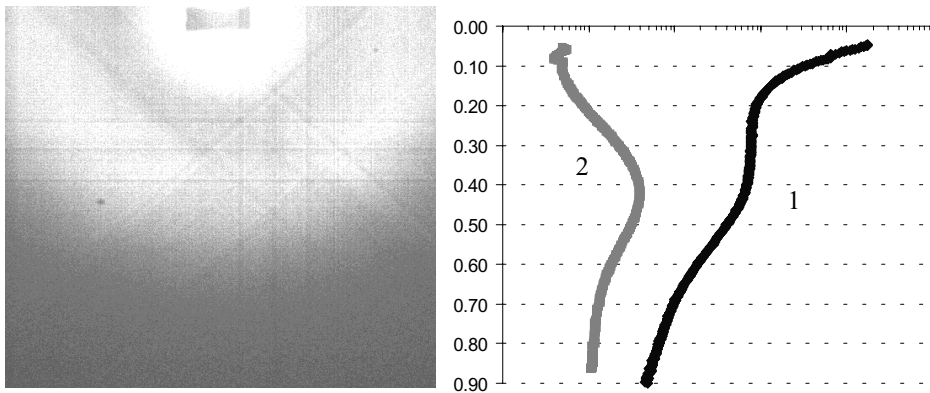


Figure 5.1 A) 2D-SAXS pattern of one of the polymers. B) line (1): integrated intensity; line (2): is intensity after background- and Lorentz-correction.

Small angle X-ray scattering (SAXS) measurements were performed on the beam-line BM26 at the European Synchrotron Radiation Facility (ESRF). In SAXS experiments, the sample to detector distance was 9 m, and an X-ray radiation wavelength of 0.1 nm was utilized. The SAXS scattering pattern obtained from an oriented specimen of wet collagen (rat-tail tendon) was used for calibration. The data was Lorenz corrected (18) and the number average distance of the diffraction peak was considered as the long-period (LP). Figure 5.1B shows the integrated (line 1), and corrected intensity (line 2). Lamellar thickness ( $d_l$ ) was estimated by multiplying the value of the LP with the crystallinity ( $\lambda_c$ ) from DSC assuming a  $\Delta H_{100\%}$  of 163 J/g for PP (2) in each sample (19).

## 5.3 Theory

### 5.3.1 LEFM and Young's dislocation theory

Fracture resistance of polymers can be characterized by standard test methods (Charpy, Izod), but these supply values, which depend on the size of the specimen and on loading conditions (20, 21). On the other hand, linear elastic fracture mechanics (LEFM) theory gives size independent fracture characteristics (22, 23). For an elaborate description of the LEFM theory see Chapter 1. One of the quantities, which can be determined by this technique is the extent of plastic deformation (plastic zone size,  $r_p$ ), which is defined as:

$$r_p = \frac{1}{2\pi} \left( \frac{K_{Ic}}{\sigma_y} \right)^2 \quad (5.1)$$

It can be assumed that the fracture resistance of a material is determined by its ability to develop a yield zone in the region of the crack tip (24).  $K_{Ic}$  represents the

critical stress intensity behind the crack tip, which is just able to initiate a crack. Using equation (5.1) and the Tresca yield criterium ( $\tau_y = \sigma_y/2$ ) we can relate  $K_{Ic}$  to the shear yield stress,  $\tau_y$ :

$$\frac{K_{Ic}}{2\sqrt{2\pi r_p}} = \frac{\sigma_y}{2} = \tau_y. \quad (5.2)$$

Young (25) proposed that the yield in crystalline polymers involves the thermal activation of screw dislocations under the action of an applied shear stress. The dependence of  $\tau_y$  on the thickness of the lamellae,  $d_l$ , can be calculated from this model. Since the theory is described by others in detail elsewhere (25-27), only its basic conclusions are mentioned here. The shear stress at which yield occurs is given by:

$$\tau_y = \frac{K}{4\pi} e^{\left[ -\left( \frac{2\pi\Delta G_c}{d_l K b^2} \right)^{n+1} \right]}, \quad (5.3)$$

where  $\Delta G_c$  is the critical energy required to activate a dislocation,  $\mathbf{b}$  is the Burgers vector of the dislocation, and  $K$  is a function of the elements of the shear modulus matrix of the crystal.

Combining equations (5.2) and (5.3) and taking the logarithm we obtain the following correlation:

$$\ln(K_{Ic}) = \left( \ln \left( \frac{K\sqrt{2\pi r_p}}{2\pi} \right) - 1 \right) - \left( \frac{2\pi\Delta G_c}{Kb^2} \right) \left( \frac{1}{d_l} \right) \quad (5.4)$$

This equation represents a direct relationship between  $K_{Ic}$  and lamellar thickness; equation (5.4) and the related theory were used to describe our experimental data quantitatively.

## 5.4 Results and discussion

### 5.4.1 Crystalline morphology

First, we describe visual features of the crystalline structure observed by POM during the crystallization experiments. In the corresponding optical micrographs, relatively large differences were captured in the structure of the three polypropylenes crystallized with different nucleating agents in non-isothermal experiments. The commercial nucleating agents appeared to be more efficient and induced the formation of much finer spherulites than sodium benzoate and talc (28). The morphology change is demonstrated in Figure 5.2, where twin slices of the virgin and a nucleated homo-polymer, crystallized at 5 °C/min cooling rate, are presented. It is obvious that much larger spherulites form in the virgin polymer, while a fine spherulitic structure can be observed in the nucleated material. The type of the polymer (chemical structure) had a much smaller influence on the

crystalline morphology than that of the nucleating agent.

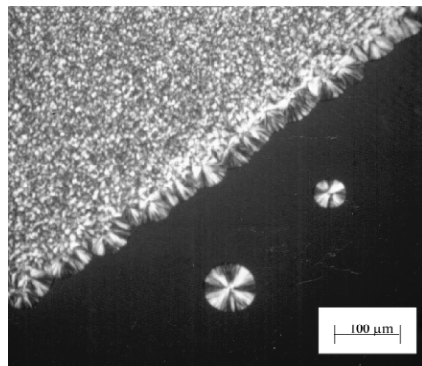


*Figure 5.2. POM of twin slices of the homo-PP crystallized at 5 °C/min cooling rate. Bottom right half: virgin polymer; top left half: polymer nucleated with 0.05 wt% NA11: The micrograph corresponds to a snapshot taken at 116 °C.*

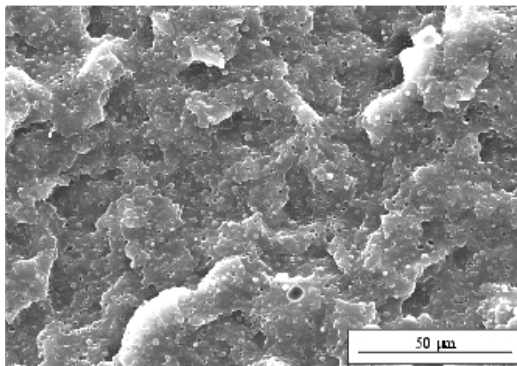


*Figure 5.3. Two-phase structure of the block-PP. SEM micrograph taken from the surface of a fractured specimen.*

An obvious question arises, though, concerning the non-isothermal experiments; one might object that the 5 °C/min cooling rate is too low and hence irrelevant for a practical injection molding operation. Practical cooling rates are higher indeed in the outer layers of the molded product, but in the core cooling rates even lower than 5 °C/min may be encountered, especially in thick molds. Therefore, we believe that our experiments are representative for the changes in the structure of nucleated PP during processing. Under non-isothermal conditions, as encountered in injection molding, the crystallization temperature will be higher when the nucleating efficiency, given by the type and concentration of the nucleating agent, is higher. In addition to the formation of finer spherulites as a result of the use of nucleating agents, DSC (15) and SAXS (see Figure 5.4) experiments indicated that the degree of crystallinity and lamellar thicknesses increase in the nucleated specimens.

The block-PP shows an extra morphological feature, which is not present in the two other polymers, i.e., a heterogeneous two-phase structure. The polymer chains with high ethylene content practically do not crystallize and phase separate into spherical domains with rubbery properties (7, 29). A representative SEM micrograph, exhibiting such a phase-separated microstructure with quasi-spherical, rubber-like domains, embedded in the PP matrix, can clearly be seen in Figure 5.3. Although not shown here, this structure could be observed also by phase contrast light microscopy.

### 5.4.2 Tensile properties

There are numerous articles dealing with correlating tensile properties with structure and a more or less a good understanding of the various aspects which determine the E-modulus, has been reached (30). Therefore it is not intended to give an extensive discussion on this subject. Moreover the treatment of the E-modulus in relation to structure is out of the scope of this thesis. Nevertheless some results and a short discussion are given.

The modulus represents the initial response of a material to energy input. Understanding this response means understanding how the stresses are transmitted through the alternating crystalline and non-crystalline regions. Connections between lamellae are provided by the direct trajectory of chains units and also by the entanglements of two (or more) long sequences, each of which returns to the crystallite of origin (32). Thus it must be the case that both the amorphous as well as the crystalline phase of the material play an important role (33). Figure 5.4 shows the correlation of the modulus with the lamellar thickness of the three polymers studied.

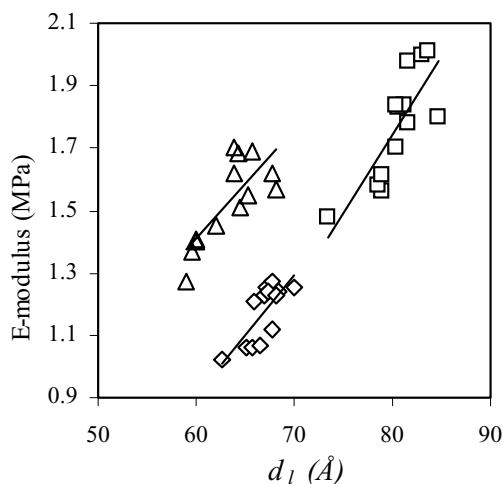


Figure 5.4. E-modulus as a function lamellar thickness ( $d_l$ );  $\square$  = homo-PP;  $\diamond$  = random-PP;  $\Delta$  = block-PP. The various points belong to different types and amounts of nucleating agents.

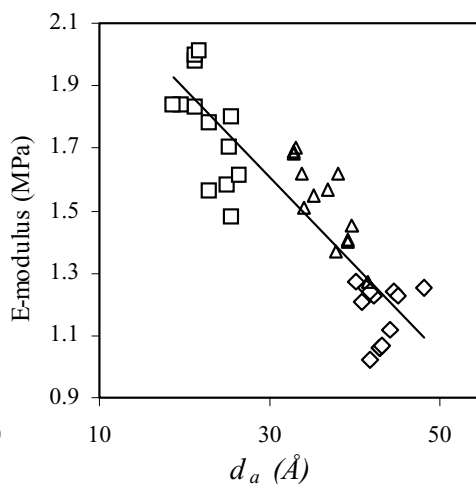


Figure 5.5. E-modulus as a function inter-lamellar thickness ( $d_a$ ); Symbols are the same as in Figure 5.4.

No clear overall correlation could be found between the E-modulus and lamellar thickness. However considering the polymers separately it appears that the thicker the lamellae the higher the E-modulus. The level of crystallinity has been quantitatively identified with the ratio of the lamellar thickness to the sum of the thicknesses of the crystalline and non-crystalline (amorphous) inter-lamellar regions ( $d_a$ ). In formula (31):

$$\lambda_c = \frac{d_l}{LP} = \frac{d_l}{d_l + d_a}. \quad (5.5)$$

Therefore, at a constant lamellar thickness the average interlamellar distance ( $d_a$ ) is reduced as the crystallinity increases. A decrease in the amorphous interlamellar distance (with constant lamellar thickness) will increase the E-modulus.

This reasoning is illustrated in Figure 5.5 where the initial modulus is plotted against the thickness of the non-crystalline region (32). A general trend can be observed. For the polymer studied, the E-modulus is monotonically decreasing with increasing inter-lamellar layer thickness. The block-PP shows a higher modulus with the same lamellar thickness compared to the random-PP, this is obviously due to smaller inter-lamellar regions in the block-PP.

The lamellar and amorphous thicknesses are probably not the only parameters that determine the E-modulus. The lateral extent of lamellae for example is severely restricted in the random-PP compared to the homo-PP. The lamellae become more and more curved and defective with increasing co-polymer content (34, 35). The boundary layer between the crystalline and amorphous region may change with crystallization conditions as well as with type of polymer (36). It is thus not surprising that in a previous study (15) on these polymers a close correlation was found between the crystallization characteristics ( $\Delta H_c$ ,  $T_{cp}$ ) and the Young's modulus of the polymers, where  $\Delta H_c$  is the enthalpy and  $T_{cp}$  peak temperature of crystallization determined with DSC.  $\Delta H_c$  is a measure for the crystallinity and  $T_{cp}$  can be associated with the lamellar thickness. From these parameters, however, no direct structure-property relation could be given. Nevertheless they hint at the importance of the crystallization conditions on the resulting morphology and thus on the value of the modulus.

### 5.4.3 Impact tests

Attempts to systematically modify the crystalline structure are usually made in isothermal crystallization experiments. The corresponding samples are crystallized, or annealed, at various temperatures resulting in very different spherulite sizes, varying between several micrometers and a few hundred micrometers. Spherulite sizes influence macroscopic properties considerably in this wide range (9, 10). A maximum observed in the yield stress as a function of spherulite size was explained by competing mechanisms between intra-spherulitic yielding and inter-spherulitic boundary failure (11). In practice, however, spherulite sizes are much smaller than in the above mentioned cases. Nucleating agents decrease the size of the spherulites even further. As a consequence, we may safely assume that in nucleated PP samples prepared by injection-molding under non-isothermal



conditions inter-spherulitic boundary failure is not of primary importance.

Several studies (33, 37, 38) have also indicated that the molar mass of the polymer strongly influences the impact properties. Thus, in order to elucidate the influence of morphology on mechanical properties, the molar mass of the polymers to be compared must be kept constant. As one can see in Table 5.2 the molar masses of the polypropylenes used in this study are very similar, hence we expect that its influence on the results of the impact tests can be neglected.

A representative example for the effect of nucleation on the impact performance is shown in Figure 5.6. The increased crystallinity and lamellar thickness of the nucleated specimen resulted in a slight increase of stiffness, i.e. the initial slope of the load vs. displacement trace, and causes an increase of the maximum force, as well. Deformation before fracture, on the other hand, decreased considerably. The figure indicates that both fracture characteristics, i.e.  $K_{Ic}$  and  $G_{Ic}$ , change as an effect of nucleation, since  $K_{Ic}$  is calculated from the maximum force, while  $G_{Ic}$  is determined from the area under the load vs. displacement trace.

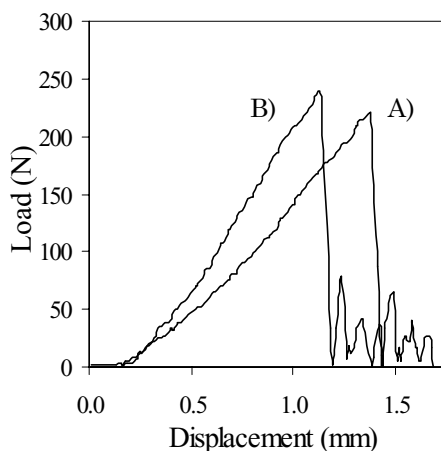


Figure 5.6. Effect of nucleation on the load vs. displacement correlation of the block-PP. Notch depth: 1.5 mm, mechanical damping: A) virgin polymer, B) nucleated sample.

#### 5.4.4 Stress intensity factor

Nucleating agents increase crystallization temperature, which results in the formation of thicker and more perfect crystallites. According to equation (5.4),  $K_{Ic}$  should decrease with increasing thickness of the lamellae. Figure 5.7 shows the logarithm of critical stress intensity factor as a function of reciprocal lamellar thickness. The measurements were performed at 23°C. The straight line is a linear fit through the data points.

As one can see, the value of  $K_{Ic}$  decreases linearly with the reciprocal value of lamellar thickness, as predicted by Young's dislocation theory (equation (5.4)). The

slope of the fitted line is  $-3.1 \pm 1.5 \cdot 10^{-3} \text{ MPa m}^{3/2}$  (39). We compared this value with the slope predicted by equation (5.4) using the assumptions and values mentioned in ref. (40). The value of the Burger's vector,  $\mathbf{b}$ , of the dislocation formed by deformation within the crystalline regions was assumed to be 0.650 nm. This value is equivalent to the  $c$ -axis of the monoclinic unit cell of isotactic PP (41). The value of  $\Delta G_c$ , i.e. the critical energy required to create a dislocation, is a function of temperature and was estimated to be in the order of 40-80 kT (42), where  $k$  is the Boltzmann's constant. In this study an average value of  $\Delta G_c = 60 \text{ kT}$  was chosen. The value of  $K$  has been reported to be in the range of 0.84 - 1.00 GPa. An average value of 0.92 GPa was used in our calculations. Using these values, a slope of  $-3.7 \pm 1.5 \cdot 10^{-3} \text{ MPa m}^{3/2}$  was estimated. The agreement with the measured slope is very good, it is within experimental error (39). Although the agreement between Young's theory and our measurements is very good, further experiments must be carried out in a much wider range in order to prove the general validity of the model.

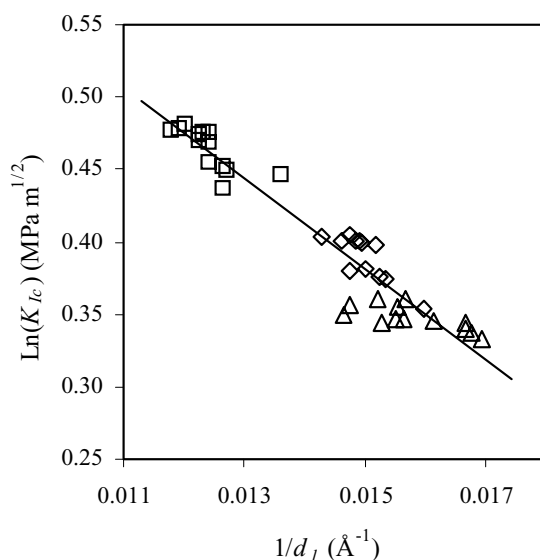


Figure 5.7.  $\text{Ln}(K_{lc})$  as a function of  $1/d_l$ ;  $\square$  = homo-PP;  $\diamond$  = random-PP;  $\Delta$  = block-PP. Data points indicated by an arrow belong to the virgin polymers, the remaining points belong to samples containing different types and amounts of nucleating agents.

Two main theories exist in the literature for the explanation of the relation between yield stress and crystal thickness (26). One claims that the dominating mechanism of yielding is partial or local melting, stretching of amorphous chains, and subsequent re-crystallization (33). The other uses the more conventional approaches of crystal plasticity. This includes stress induced crystal-crystal transformation, twinning and slip; this approach was reviewed by Bowden and Young (43). The correlation of crystal structure and yielding was extensively studied for polyethylene and the available information indicates that at, or near,

room temperature crystal plasticity, i.e. the *onset* of plastic deformation, is controlled by dislocations (34), while *post*-yield deformation, involving neck formation and stabilization, is assumed to occur by “quasi-melting” or “de-crystallization” (34).

Young’s theory was shown to have several drawbacks (33, 43), e.g. a too weak dependence on temperature and problems with the morphological reasoning behind it. Nevertheless, in our case, the theory fits the data well, which is shown also by the agreement of the calculated and measured slopes. In principle there are no a priori limitations regarding the application of this theory. Young’s theory of yield was mostly used for the evaluation of experiments carried out at low strain rates and the results could often be interpreted satisfactorily in such cases. However, since we could distinguish between the onset and propagation of cracks, we could apply Young’s theory also at high strain rates.

#### 5.4.5 Strain energy release rate

Although less clear than that for  $K_{Ic}$ , a general trend exists also for  $G_{Ic}$  as a function of lamellar thickness. At large lamellar thicknesses, the impact energy approaches a more or less constant value, while the material becomes tougher when it contains thinner lamellae. The correlation is presented in Figure 5.8 for the polypropylenes studied here.

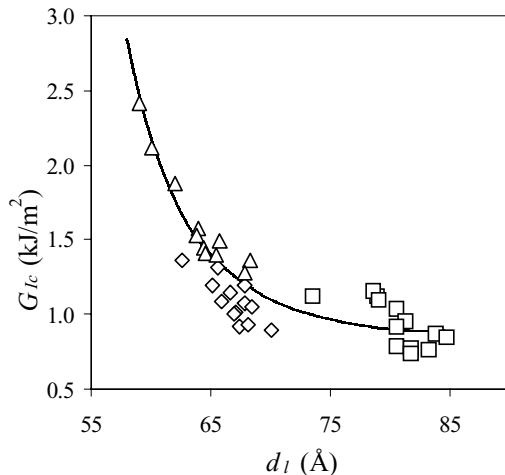


Figure 5.8.  $G_{Ic}$  as a function of  $d_l$ ;  $\square$  = homo-PP;  $\diamond$  = random-PP;  $\Delta$  = block-PP.

The results indicate that the nucleating agents induce similar changes in all three polymers, but the fracture of the block copolymer is influenced also by additional factors compared to the other two polymers. One or both factors may explain the increased total energy of fracture for the block copolymer. The elastomeric particles forming in this polymer during polymerization (see Figure 5.3) induce a heterogeneous stress distribution under the effect of external load. It

is known that stress concentration initiates local deformation processes.

In elastomer modified polypropylene the dominating deformation process is usually shear yielding, although occasionally deformation may occur by other mechanisms, as well. Increased plastic deformation leads to larger energy consumption during fracture. On the other hand, the value of the LP is the smallest in the block copolymer. The value of the LP was shown to be related to the number of tie molecules, which increases with decreasing LP (44). Tie molecules may hinder the propagation of the crack during fracture thus they may further increase the energy consumption. This tentative explanation is also supported by the results of Karger-Kocsis who claims that increased concentration of tie molecules leads to improved toughness (45). The LPs of the homo-PP and random-PP are approximately the same, which would correspond to the same concentration of tie molecules and thus the same toughness. However, due to its higher crystallinity (at approximately the same LP) the lamellar thickness is higher for the homo-PP, which in turn contributes to an increased value of  $K_{Ic}$ .

## 5.5 Conclusions

The study carried out on three different PP polymers containing three heterogeneous nucleating agents indicates that the crystalline morphology of these polymers strongly influences their fracture behavior. A close correlation was found between the resistance to crack initiation, represented by  $K_{Ic}$  and the lamellar thickness. The correlation was successfully described by the dislocation theory of Young. The total energy absorbed during impact fracture ( $G_{Ic}$ ) does not appear to depend on a single morphological parameter, nevertheless the thickness of lamellae play an important role in its value. The impact resistance of the block copolymer is significantly larger than that of the other two polymers, due to its heterogeneous two-phase structure, which induces additional plastic deformation during fracture. The relatively larger number of tie molecules may also contribute to increased fracture resistance in this polymer. In order to verify the results obtained here and prove the tentative explanation given, samples with well-defined thermal history, thus structure, must be used which can be obtained under isothermal crystallization conditions without shear. Furthermore, direct characterization of the deformation zone by various techniques is needed to identify the specific deformation mechanism, taking place in the crack tip.

## 5.6 References

1. Ulrich, H. *Introduction to Industrial Polymers*; Hanser Publishers: Munich, 1983.
2. Moore, E. P., Ed. *Polypropylene Handbook*; Hanser Publishers: Munich, 1996.
3. Karger-Kocsis, J., Ed. *Polypropylene: An A-Z Reference*; Kluwer Academic Publishers: Dordrecht, 1999.
4. Fujiyama, M.; Wakino, T. Structure of Skin Layer in Injection-Molded Polypropylene. *J. Polym. Sci., Polym. Phys.* **1988**, 35 (1), 29-49.
5. Kantz, M. R.; Newman, H. D.; Stigale, F. H. The skin-core morphology and structure-property relationships in injection-molded polypropylene. *J. Appl. Polym. Sci.* **1972**, 16, 1249-1260.
6. Karger-Kocsis, J., Skin-core morphology and failure of injection-molded specimen of impact modified polypropylene blends. *J. Polym. Eng. Sci.* **1987**, 27 (4), 241-253.
7. Lieberman, R. B.; Barbe, P. C. Propylene Polymers. In *Encyclopedia of Polymer Science and Engineering*; Kroschwitz, J. I.; Mark, H. F.; Bikales, N. M.; Overberger, C. G.; Menges, G., Eds.; John Wiley & Sons, Ltd.: New York, 1986; Vol. 13, 464-531.
8. Scheirs, J.; Kaminsky, W., Eds. *Metallocene-Based Polyolefins*; John Wiley & Sons, Ltd.: New York, 2000; Vol. 2.
9. Way, J. L.; Atkinson, J. R.; Nutting, J. The effect of spherulite size on the fracture morphology of polypropylene. *J. Mat. Sci.* **1974**, 9, 293-299.
10. Friedrich, K. Strength and fracture of crystalline isotactic polypropylene and the effect of molecular and morphological parameters. *Prog. Colloid Polym. Sci.* **1979**, 66, 299-309.
11. Karger-Kocsis, J. Microstructural Effects of Fracture in Polypropylene and its Filled, Chopped Fiber and Fiber Mat Reinforced Composites. In *Polypropylene: Structure, Blends and Composites*; Karger-Kocsis, J., Ed.; Chapman and Hall: London, 1995; Vol. 3, 142-153.
12. Maiti, S. N.; Mahapatro, P. K. Crystallization of PP in PP/Ni composites and its correlation with tensile properties. *J. Appl. Polym. Sci.* **1989**, 37 (7), 1889-1899.
13. Hutley, T. J.; Darlington, M. W. Impact strength-D.S.C. correlation in mineral filled polypropylene. *Polym. Commun.* **1984**, 25 (8), 226-228.
14. Hutley, T. J.; Darlington, M. W. Further observations on impact strength-D.S.C. correlation in mineral filled polypropylene. *Polym. Commun.* **1985**, 26 (9), 264-267.
15. Pukánszky, B.; Mudra, I.; Staniek, P. J. Relation of crystalline structure and mechanical properties of nucleated polypropylenes. *Vinyl & Additive Technology* **1997**, 3 (1), 53-57.
16. In industrial terms this polymer is also called "high impact polypropylene". The polymer consists of chains with a real block structure in the classical sense, but

- also contains a rubbery fraction with chains of high ethylene content, which is not necessarily block-like. Although not strictly correct, we call this polymer block-PP throughout the thesis.
17. Bezerédi, Á.; Vörös, G.; Pukánszky, B. J. Mechanical damping in instrumented impact testing. *J. Mat. Sci.* **1997**, 32 (24), 6601-6608.
  18. Kakudo, M.; Kasai, N. *X-ray Diffraction by Polymers*; Elsevier Publishing Company: Amsterdam, 1972; 281-286.
  19. This may be an overestimate for the statistical copolymers in view of the influence of ethylene segments built in along the polymer chain.
  20. Hertzberg, R. W.; Manson, J. A. Fracture and Fatigue. In *Encyclopedia of Polymer Science and Engineering*; Kroschwitz, J. I.; Mark, H. F.; Bikales, N. M.; Overberger, C. G.; Menges, G., Eds.; John Wiley & Sons, Ltd.: New York, 1986; Vol. 7, 328-452.
  21. Kinloch, A. J.; Young, R. J. *Fracture Behavior of Polymers*; Elsevier Applied Science Publishers: New York, 1983.
  22. Plati, E.; Williams, J. G. Determination of the fracture parameters in impact. *Polym. Eng. Sci.* **1975**, 15 (6), 470-477.
  23. Clintock, F. A.; Irwin, G. R. ASTM STP **1965**, 381, 84.
  24. McCrum, N. G.; Buckley, C. P.; Bucknall, C. B. *Principles of Polymer Engineering*; Oxford University Press Inc.: New York, 1994.
  25. Young, R. J. A dislocation theory for yield in polyethylene. *Philos. Mag.* **1974**, 30, 85-94.
  26. Crist, B. Plastic Deformation in Polymers. In *Structure and Properties of Polymers*; E. L. Thomas, Ed.; VCH: Weinheim, 1993; Vol. 12, 428.
  27. Brooks, N. W.; Duckett, R. A.; Ward, I. M. Temperature and strain-rate dependence of the yield stress of polyethylene. *J. Polym. Sci., Polym. Phys.* **1998**, 36 (12), 2177-2189.
  28. For the morphological studies, talc was used as nucleating agent. However, in view of the high degree of orientation in the injection molded specimens, SAXS measurements performed on these could not be evaluated, hence the corresponding LP was not determined. These samples were not included in the structure-impact correlation study presented here.
  29. Galli, P.; Haylock, J. C.; Simonazzi, T. Manufacturing and Properties of Polypropylene Copolymers. In *Polypropylene: Structure, Blends and Composites*; Karger-Kocsis, J., Ed.; Chapman and Hall: London, 1995; Vol. 2, 1-24.
  30. Kausch, H.H., J.A. Hassell, and R.I. Jaffee, *Deformation and fracture of high polymers*. Plenum Press.: New York, 1973.
  31. Albrecht, T. and G. Strobl.; Temperature-dependent crystalline-amorphous structures in isotactic polypropylene: Small-angle x-ray scattering analysis of edge-bounded two-phase systems. *Macromolecules*, **1995**, 28, 5267-5273.
  32. Popli, R.; Mandelkern, L. Influence of structural and morphological factors on

- the mechanical properties of the polyethylenes. *J. Polym. Sci., Polym. Phys.* **1987**, 25 (1), 441-483.
33. Kennedy, M. A.; Peacock, A. J.; Mandelkern, L. Tensile properties of crystalline polymers - linear polyethylene. *Macromolecules* **1994**, 27 (26), 7941-7941.
  34. Crist, B. and P.R. Howard, Crystallization and melting of model ethylene-butene copolymers. *Macromolecules* **1999**, 32, 3057-3067.
  35. Huang, J., et al., Crystallization and microstructure of poly(L-lactide-co-meso-lactide)copolymers. *Macromolecules* **1998**, 31, 2593-2599.
  36. Iijima, M. and G. Strobl, Isothermal crystallization and melting of isotactic polypropylene analyzed by time- and temperature-dependent small-angle X-ray scattering experiments. *Macromolecules* **2000** 33 (14), 5204-5214.
  37. Bartczak, Z.; Galeski, A.; Argon, A. S.; Cohen, R. E. On the plastic deformation of the amorphous component in semi-crystalline polymers. *Polymer* **1996**, 37 (11), 2113-2123.
  38. Avella, M.; Dell'Erba, R.; Martuscelli, E.; Ragosta, G. Influence of molecular mass, thermal treatment and nucleating agent on structure and fracture toughness of isotactic polypropylene. *Polymer* **1993**, 34 (14), 2951-2960.
  39. The experimental error was calculated as a 90% confidence limit based on a statistical error analysis, the theoretical value of the slope was calculated using a simple error propagation estimation.
  40. O'Kane, W. J.; Young, R. J.; Ryan, A. J. The effect of annealing on the structure and properties of isotactic polypropylene films. *J. Macromol. Sci.* **1995**, B34 (4), 427-458.
  41. Feng, B.; Fuming, L.; Calhoun, B. H.; Quirk, R.P.; Cheng, S. Z. D. Physical Constants of Poly(propylene). In *Polymer Handbook*, 4th Ed.; Brandrup, J.; Immergut E. H., Eds.; Wiley Interscience: New York, 1989; Part V, 21-30.
  42. Shadrake, L. G.; Guiu, F. Dislocations in polyethylene crystals: Line energies and deformation modes. *Philos. Mag.* **1976**, 34 (4), 565-581.
  43. Bowden, P. B.; Young, R. J. Deformation mechanisms in crystalline polymers. *J. Mat. Sci.* **1974**, 9, 2034-2051.
  44. Patel, R. M.; Sehanobish, K.; Knight, G. W. Theoretical prediction of tie-chain concentration and its characterization using post-yield response. *J. Appl. Polym. Sci.* **1996**, 60 (5), 749-758.
  45. Karger-Kocsis, J. Dependence of the fracture and fatigue performance of polyolefins and related blends and composites on microstructural and molecular characteristics. *Macromol. Symp.* **1999**, 143, 185-205.

## 5.7 Acknowledgements

The authors are grateful for the financial support of Clariant Huningue S.A. 68331 Huningue, Bp. 149, France and the National Scientific Research Fund of Hungary (Grant No. T 30579). The authors acknowledge prof. dr. B. Pukánszky for the mechanical measurements and samples.

# Chapter 6

## Oriented crystallization and mechanical properties of polypropylene on fibrillated polytetrafluoroethylene<sup>1</sup>

It is known that friction deposited polytetrafluoroethylene (PTFE) layers are able to nucleate crystallization of thin films of isotactic polypropylene (iPP). In order to investigate the influence of PTFE on the crystallization behavior of iPP in bulk, PTFE-particles of two different sizes ( $6 \cdot 10^2 \mu\text{m}$  and  $7 \mu\text{m}$ ) in various concentrations were blended with iPP and subsequently processed by injection molding. A strong enhancement in the nucleation rate was found. Charpy impact tests showed a large increase in the strain energy release rate ( $G_i$ ) for these PTFE nucleated samples. High resolution scanning electron microscopy (HR-SEM) combined with wide angle x-ray diffraction pole figures (WAXD) showed that this improvement in toughness depends mainly on the concentration of PTFE, and to a lesser extent dependent on the actual variation in PTFE-morphology. The measurements showed that the processing-induced oriented iPP morphology dominates the mechanical properties. Shear during processing led, in the case of 'large' PTFE-particles, to the formation of PTFE fibers in the iPP matrix. Formation of these fibers induced after melting and recrystallization an unusual morphology consisting of oriented iPP lamellar crystals. In contrary to the frequently observed (trans) crystallization, in which lamellae are directed perpendicular to the fiber direction, we found a strong overall lamellar orientation parallel to the PTFE fiber direction.

---

<sup>1</sup> Sections of this Chapter will be submitted to Journal of Polymer Science & Engineering.



## 6.1 Introduction

Enhancement of mechanical properties in polymer systems can be accomplished by self-reinforcement [1]. During processing structural anisotropy may be introduced, which can lead to improvement of mechanical properties like impact strength and/or E-modulus. The structural anisotropy can be related to molecular orientation in the amorphous and crystalline phases of the (semi-crystalline) polymer forming different types of textures [2,3], but can also be related to an additional component, e.g. fibers [4,5], liquid crystals [6], or second polymer with a fibrous morphology [7]. Another way of improving mechanical properties is the application of nucleating agents [8]. Nucleated crystallization results in changes of structural features (degree of crystallinity, lamellar thickness, fine spherulite structures) which, in turn, contribute to property enhancement [8,9]. Combination of the concepts of self-reinforcement and nucleation could lead to a synergy resulting in a strong increase in mechanical properties.

Polytetrafluoroethylene (PTFE) possesses an unique combination of properties like low bulk shear strength, low surface tension, low coefficient of friction, low yield stress, and high toughness [10,11]. When PTFE is blended with other polymers it is known to improve mechanical properties like stiffness and toughness [10]. Due to the low interfacial shear strength compared with bulk shear strength [12] PTFE can easily be fibrillated [13,14]. It has been pointed out that fibrillation of PTFE may be one of the reasons for the enhancement of the above mentioned materials properties [15]. The ability of PTFE to fibrillate was also utilized in studies of crystallization and nucleating mechanisms [16,17]. When sheared on a hot planar surface, PTFE forms highly oriented fibrils in the direction of sliding [18] with the chain direction (*c*-axis) parallel to the fibril direction [14,18]. Such sheared, anisotropic, thin PTFE films exhibit remarkable nucleating ability, e.g. in interfacial crystallization of a second polymer component on top of the PTFE film. Isotactic polypropylene (iPP) is able to epitaxially nucleate and crystallize on these (PTFE) films in its  $\alpha$ -phase [17]. Conventional PTFE-fibers were also used [4] to nucleate iPP. In this case iPP exhibited trans-crystallization on the PTFE-fibers [5,19].

The combination of the ability of PTFE to fibrillate and to act as a nucleant may result in a self-reinforced material with highly improved mechanical properties. We anticipate that in polymer melts with relatively high viscosity, PTFE-particles may fibrillate in the local direction of elongation during processing if anisotropic shear or elongation of structural elements occur. In order to look at this possibility, we melt-blended small amounts of various PTFE powder particles (with different particle diameter and molar mass) with iPP and monitored the crystallization and morphology of the resulting materials. These structural studies were complemented by investigations of the mechanical performance in order to

establish processing-structure-properties relationships. In the present study, discussion of the (fibrillar) phase morphology of the corresponding blends<sup>1</sup> is given and results obtained from impact and tensile measurements of injection-molded specimen are summarized.

## 6.2 Experimental

Polytetrafluoroethylene (PTFE) powder (Ausimont, Italy) was blended with isotactic polypropylene (iPP) (DSM, The Netherlands) ( $\bar{M}_w = 3.0 \times 10^5$  g/mol,  $\bar{M}_n = 7.7 \times 10^5$  g/mol) by extrusion on a Berstorff (ZE 25×33D) twin-screw extruder. The barrel temperature was set at 190 °C and the screw speed was 140 rpm. The length-diameter ratio of the screws was 33 ( $l/d = 33$ ), with a diameter  $d = 25$  mm. In one blend the concentration of the PTFE was set at 1 wt% and found to be 0.998%, checked by Thermo Gravimetric Analysis (TGA). PTFE-particles with two different diameters ( $d$ ) have been used: large PTFE-particles,  $d_L$  ( $d_L = 6 \cdot 10^2$   $\mu\text{m}$ ,  $\bar{M}_n = 2 \times 10^7$  g/mol) and small PTFE particles,  $d_s$  ( $d_s < 7$   $\mu\text{m}$ ,  $\bar{M}_n = 5 \times 10^5$  g/mol). In addition to the presence of PTFE, the blend contained 0.1 wt% antioxidant (Irganox). The polymer melt was cooled in a water bath, subsequently granulated and dried overnight in a vacuum oven at 40 °C. Rectangular bars (80×10×4 mm<sup>3</sup>) were injection molded on a 221-55-250 Arburg Allrounder injection molding machine. The barrel had a flat temperature profile of 220 °C, and the mould temperature was set at 40 °C. Injection and holding pressures were 55 and 45 bar, respectively.

In order to elucidate the morphology, wide angle x-ray diffraction (WAXD), polarized light microscopy (PLM), and scanning electron microscopy (SEM) were used. Samples for PLM and WAXD were prepared by cutting pieces of polymer from the injection molded bars (see Figure 6.1) and used as such or pressed between two glass cover-slides in a thermally controlled (Mettler FP80) microscope hot-stage (Mettler FP82). The polymer was kept at 220 °C for 5 min to remove the thermal-rheological history of the iPP-matrix and then cooled to the temperature of crystallization (130 °C) within approximately 1 min. Crystallization was followed on an Olympus BHSM microscope using transmitted white light and crossed polarizers. After crystallization, the glass cover-slides were removed from the hot-stage, leaving a polymer film of an estimated thickness value of 0.7 mm.

WAXD experiments were performed on a X'pert Phillips diffractometer. Pole-figures were obtained and corrected for instrumental aberrance. Additional measurements to elucidate the morphology of the blends (see Figure 6.1) were done

---

<sup>1</sup> A blend is defined as a mixture of two or more polymers in any ratio. One may argue that the term “blend” in our case could be replaced by “nucleated polymer”. However, in view of the polymeric nature of the “nucleating agent” PTFE, in this study, the term “blend” has been used to describe iPP-PTFE mixtures.

with high resolution scanning electron microscopy (HR-SEM) and energy dispersive x-ray analysis (EDX) using a LEO Gemini 1550 FEG-SEM instrument, fitted with a field emission gun and a Noran Vantage EDX system. Prior to the measurements the samples were microtomed at  $-130\text{ }^{\circ}\text{C}$  by using a Leica Ultracut-UCT device. The samples were etched using the permanganic etching procedure described in reference [20] and subsequently sputtered with platinum. The crystalline phase is less efficiently removed than the amorphous phase in these etching experiments. PTFE is believed to be essentially inert for etching.

Crystallization was studied by Differential Scanning Calorimetry (DSC). The DSC (a Perkin-Elmer calorimeter Pyrics 1) was calibrated using gallium and indium before use. The sample chamber was kept under a constant flux of nitrogen. The same procedure was followed as in the LM-experiments, i.e. the samples were melted for 5 min at  $220\text{ }^{\circ}\text{C}$  and subsequently cooled down at  $20\text{ }^{\circ}\text{C}/\text{min}$  for non-isothermal experiments or quickly cooled to the isothermal crystallization temperature of  $130\text{ }^{\circ}\text{C}$ . All DSC melting scans were recorded at  $10\text{ }^{\circ}\text{C}/\text{min}$  heating rate.

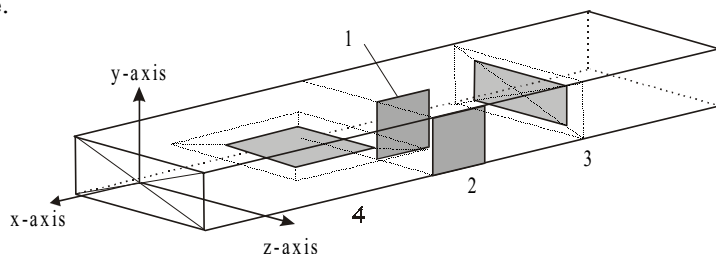


*Figure 6.1. Schematic representation of an injection molded bar. From the indicated places samples were taken for use in SEM, XRD, and PLM measurements. Indicated are four sample positions (1, 2, 3, and 4).*

Tensile yield stress and modulus values were measured using a Zwick 1445 tensile testing apparatus at  $50\text{ mm}/\text{min}$  cross-head speed. Specimens with  $80\times 10\times 4\text{ mm}^3$  dimensions were cut from the injection-molded bars for impact testing. The test samples were notched to different depths by a saw and sharpened by an industrial razor blade. Notch depth values varied between  $1.0\text{ mm}$  and  $7.5\text{ mm}$ . Fracture testing was carried out by an instrumented impact tester with  $2.9\text{ m}/\text{s}$  velocity using a  $40\text{ mm}$  span. Due to the high impact rate applied, dynamic effects occurred during fracture. This was compensated by use of mechanical damping. The damper used was a  $1\text{ mm}$  thick silicon rubber plate fixed to the force transducer. Additional Charpy non-instrumented impact tests were performed according to ASTM D256-90b. For these measurements a single-edge V-shaped notch of  $2\text{ mm}$  depth and tip radius  $0.25\text{ mm}$  was milled in the molded specimen. The error bars in the figures indicate standard deviations.

## 6.3 Results

### 6.3.1 PTFE particle morphology

The PTFE-particles ( $d_L$ ,  $d_S$ ) used in this study were made by emulsion polymerization [21]. The smaller particles ( $d_S$ ) were irradiated by  $\gamma$ - or electron-beam and ground in order to decrease the size of the particles and molar mass of the polymer [22]. This grade is commonly referred to as PTFE micro-powder [22]. Virgin particle morphology was characterized by HR-SEM. Representative results are shown in Figure 6.2.

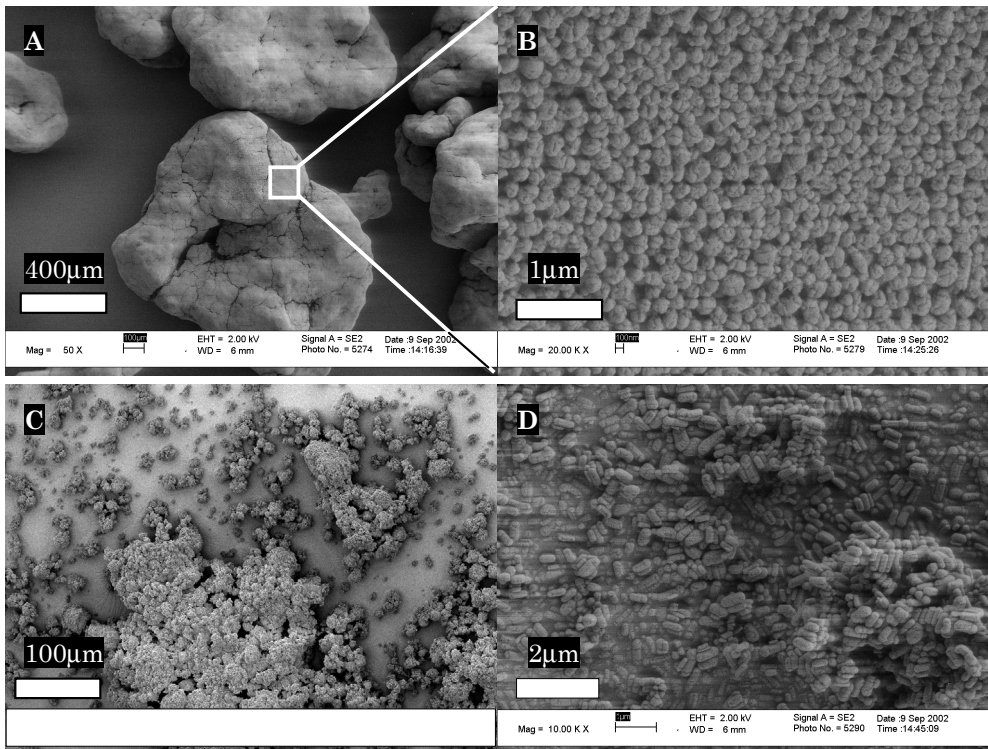


Figure 6.2. HR-SEM micrographs of PTFE-particles:  $d_L$  (A, B) and  $d_S$  (C, D). The micrographs to the right (B, D) are magnifications of the micrographs to the left (A, C).

Values of the average particle diameter of  $d_L$  and  $d_S$  were approximately  $6 \cdot 10^2 \mu\text{m}$  and  $7 \mu\text{m}$ , respectively (see Figure 6.2 A and C). The larger, as well as the smaller particles ( $d_L$  and  $d_S$ ) consist of agglomerates of primary particles. The primary particles, formed during the polymerization, can be distinguished in the micrographs (B) and (D) of Figure 6.2, respectively. The primary particles of the PTFE powder of  $d_L$  are nearly spherical and have a size of approximately  $\pm 250 \text{ nm}$ . Primary particles of  $d_S$  are approximated by cylinders with a length of  $\pm 300 \text{ nm}$

and a length-diameter ratio of approximately 2. As it can be seen, the primary particles of PTFE with  $d_L$  are clustered into large structures (Figure 6.2 A), whereas the primary particles of  $d_s$  have much less tendency to agglomerate (Figure 6.2 C).

### 6.3.2 Morphology of injection molded bars

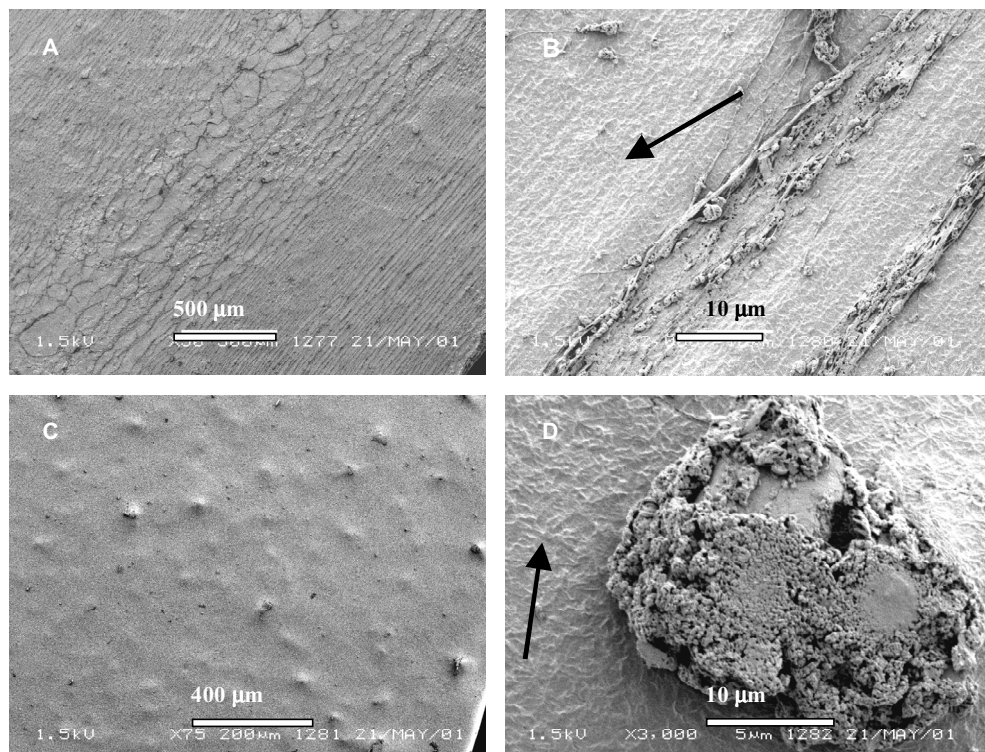
#### SEM-observations

Figure 6.3 shows the morphology of an injection molded bar (cross-section, see Figure 6.1, sample position 1) as revealed by SEM for the blends (iPP +  $d_L$ ) and (iPP +  $d_s$ ), respectively. The difference in PTFE-morphology between the blends is remarkable. Despite the good dispersion of the PTFE particles in the iPP-matrix during processing (extrusion and injection molding), in both blends large agglomerates are present. In the case of the blend with  $d_L$  particles the PTFE-agglomerates are elongated (micrograph B) and are spatially distributed over the cross-section of the bar (micrograph A). The large agglomerates of primary particles in the blend made with  $d_s$  particles are round and homogeneously distributed (micrographs C and D in Figure 6.3).

In both blends a fine-morphology can be detected between the agglomerates of PTFE (indicated by the arrows in micrographs B and D). For the blend with  $d_L$  particles oriented structures can be seen, while in the case of the blend with the smaller  $d_s$  particles no such oriented structures are visible.

The oriented fine-morphology in Figure 6.3 D is called a “fibrillar phase morphology” (FPM) typically observed in self-reinforced polymers [1]. The formation of FPM depends in general, on the deformation, break-up, and coalescence of the minority phase. These processes are influenced by several factors such as interfacial and bulk shear strength, surface tension, molar mass of the components, and the thermal rheological history of the blend during structure formation (shear, elongational stresses, flow gradients etc.). During extrusion and injection molding high shear and elongation stresses are present [23], which deform the minority phase [24,25]. The clusters of primary PTFE reactor particles break-up and are distributed into the matrix. During processing, the PTFE-particle may undergo cold drawing due to the low interfacial shear strength of PTFE compared with its bulk shear strength [13,26]. In this way elongated PTFE fibrils with high aspect ratios may form. The final size of the PTFE fibrils will depend on the break-up and coalescence of the formed structures. It is known that irradiated low molar-mass PTFE homo-polymer (powder) can easily be compounded with other polymers. However, for the corresponding blends containing low molar mass PTFE no fibrillation was observed [27].

Although at this stage not yet established, we suggest that the fine-morphology seen in the Figure 6.3 B is related to the presence of highly fibrillated ( $d_L$ ) PTFE-particles embedded in the iPP-matrix, while the fine-morphology seen in Figure 6.3 D originates from non-fibrillated,  $d_S$  PTFE-particles. The following paragraph will give a more elaborate discussion of these fine-morphologies observed. In paragraph 6.3.3 we will go deeper into the subject of fibrillation.



*Figure 6.3. Representative SEM micrographs of cross-sections of injection molded specimen of iPP-PTFE blends. Upper micrographs (A, B) exhibit structures of a blend with 1 wt%  $d_L$  particles. Lower micrographs (C, D) display a blend with  $d_S$  particles (PTFE concentration: 1 wt%). Micrographs to the right (B, D) are magnifications of the representative sections taken from the micrographs to the left (A, C). Arrows in the micrographs indicate the fine-morphology.*

### **WAXD observations**

In order to understand the fine-morphology and crystalline texture of the injection molded blends of iPP with PTFE, wide angle x-ray diffraction experiments were performed. The objective of these measurements was to obtain pole-figure distributions for representative crystal facets of the crystal phase of the iPP matrix [3]. Injection-molded blends with  $d_S$  as well as  $d_L$  particles were studied. The same

blends were analyzed by using SEM (see previous paragraph). The Bragg-angle of diffraction was taken for the (110) plane at  $2\theta \sim 14.1^\circ$  and (040) plane at  $2\theta \sim 16.8^\circ$  [28], while the azimuthal ( $\psi$ ) and polar ( $\phi$ ) angles were varied between  $0-90^\circ$  and  $0-360^\circ$ , respectively. The machine direction (MD) is defined as the main flow-direction of the polymer during processing (the x-axis in Figure 6.1). In the pole-figures, the MD is directed from bottom to top and is in the plane of view. The normal direction (ND) is perpendicular to the plane of view. The polar angle,  $\phi$ , is the angle defining rotations in the plane of view, while  $\psi$  gives the angle from the MD towards the ND ( $\psi = 0^\circ$  for the north pole and  $90^\circ$  for ND). Only the  $\alpha$ -phase of iPP was detected (diffractogram not shown). The diffraction peaks overlap to a small extent, however this does not impose any significant problems because the positions of (110) and (040) peaks differ by  $\sim 2.7^\circ$ , which is a large enough difference [29,30]. For clarity, the pole-figures before instrumental correction are displayed as well.

From Figure 6.4 we can see that the direction of the (040) plane has a distribution in the plane perpendicular to the MD and parallel to ND. For the directions of the (110) plane two modes are visible. Mode 1 is strong and concentrated close to the same plane as seen for the direction of the (040) plane (i.e. in the plane perpendicular to the MD and parallel to ND) and is homogeneously distributed. The other modes (Mode 2) are weaker and pointing towards the poles, which are parallel to the machine direction (north-south poles).

Physically we can interpret these pole-figures with a typical morphology we can find in injection molded bars [31]. As we took the samples from the middle of the injection bar, we expect a local uniaxial-like texture pointing in the MD [32,33]. Due to presence of strong flow-fields during processing polymer chains are highly oriented. These oriented chains may form a row nucleus on which lamellae can perpendicularly grow. Typically, the row nuclei are aligned parallel with the MD. These elongated structures correspond to extended chain crystals typical for crystallization under shear [34]. On these row nuclei, primary lamellar crystals of iPP can nucleate. Secondary ‘daughter’ lamellae can nucleate and grow in a subsequent process from these primary ‘mother’ lamellar crystals. Although no definitive conclusions can be reached at this point, the pole-figures seems to be in accordance with this physical picture.

First we consider mode 1 of the (110) reflection in combination with the (040) reflection. Since the directions of the (110) as well as the (040) planes are perpendicular to the crystalline  $c$ -axis of iPP and both reflections have a distribution in the plane perpendicular to the MD, the  $c$ -axis is uniquely defined and pointing in the MD. Thus, mode 1 of the (110) reflection in combination with the (040) reflection probably defines mainly the orientation of the unit-cells from lamellae perpendicular to the highly elongated backbone of the row structure and

the backbone of the row structure it self. The lamellae are homogeneously distributed around the backbone of the row-structure. Mode 2 in the (110) pole-figures, likely originates from the typical crosshatched lamellae present in the  $\alpha$ -phase. Crosshatched lamellae grow almost perpendicular ( $99^\circ$ ) to the initially grown lamellae, which explains the observation.

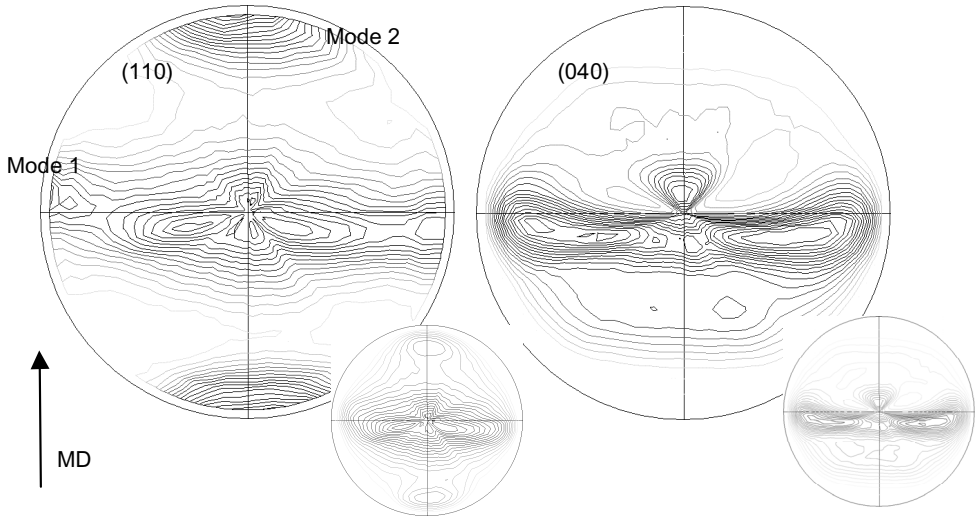


Figure 6.4. Pole-figures of a typical specimen obtained from an injection-molded blend with *ds* PTFE particles. The right figure shows the (110)- and left the (040)-plane, respectively. The pole density is indicated by dark black lines (high intensity) to light gray lines (low intensity). The machine direction (MD) is indicated by the arrow. The small inserts show the pole-figures prior to instrumental correction. Explanation of 'Mode 1' and 'Mode 2' is given in the text.

A less clear picture arises in the injection-molded blend with the *dl* particles (Figure 6.5). Roughly the same modes are visible as seen in the blend with *ds* particles, however there are a few distinct differences and distortions (asymmetries) in the corresponding pole-figures. The distribution of the *b*-axis, represented by the (040) plane, is not as homogeneous in the plane perpendicular to the MD direction as it is for the *ds* particles. Two broad 'lobes' can be observed, which smear out towards both poles (east-west poles). The (110) reflection shows the same two modes as in Figure 6.4. However, mode 1 shows, besides a strong broadening of the reflection in the plane perpendicular to the MD, an enhancement in intensity in the ND. Moreover, one strong intensity can be seen in the lower (south) pole of Figure 6.5 left (mode 2). Probably the main orientation of the material ( $MD_{\text{material}}$ ) does not coincide with the MD of the pole-figure and is rotated about  $20^\circ$  in  $\psi$  towards the north pole, which results in "congested" lines of pole intensity contours near the north pole. The situation becomes more evident when the (110) reflection of Figure 6.5 is compared with the (110) reflection of Figure 6.4.



The reflection in the south pole of Figure 6.4 becomes more visible in Figure 6.5 when rotated  $20^\circ$  in  $\psi$ , while the reflection in the north pole of Figure 6.4 disappears in Figure 6.5. The angle of rotation can also be seen in the maxima parallel with the ND, i.e. mode 1 in the (110) reflection.

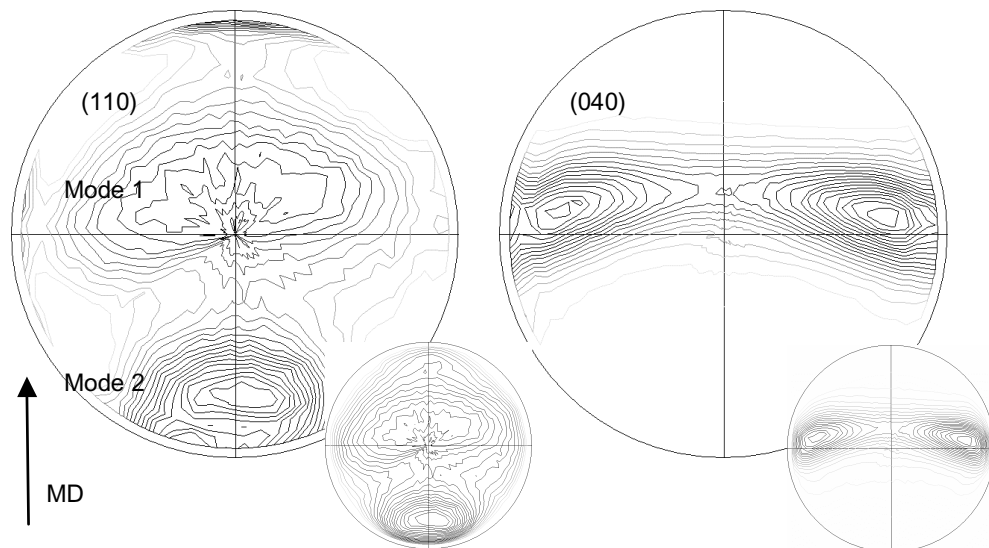


Figure 6.5. Pole-figures of a typical specimen obtained from an injection-molded blend with  $d_L$  PTFE particles. The figure to the right shows the (110)- and left the (040)-plane, respectively. The pole density is indicated by dark black lines (high intensity) to light gray lines (low intensity). The machine direction (MD) is indicated by the arrow. The small inserts show the pole-figures prior to instrumental correction. Explanation of 'Mode 1' and 'Mode 2' is given in the text.

In general, flow fields encountered in injection molding operations are complex and non-isotropic. As a result, the morphology of an injection molded specimen is highly heterogeneous (both in the x, y, and z-direction, see Figure 6.1). It is anticipated that the local flow fields of the iPP melt are influenced by the presence of elongated PTFE particles. Although the samples for the WAXD measurements for both the blend with small and large PTFE-particles are taken from the same position in the injection molded bar, local variations in the flow field of the blend with fibrillated PTFE-particles compared with the blend with small PTFE-particles may cause the rotation and asymmetries of the pole-figure as discussed above.

Regarding the major type of orientation texture we can say that the pole-figures of the sample with  $d_L$  particles are similar to pole-figures of the blend with  $d_S$  particles. Distortions and asymmetries in the pole-figures can be attributed to the presence of the PTFE-fibers in addition to self-nucleation on the iPP extended chain crystals. Local flow field changes and oriented nucleation and growth can be

caused by the PTFE-fibers, which can contribute to the differences in the pole-figures of the blend with  $d_L$  particles as compared to the blend with  $d_S$  particles.

From the SEM micrographs (Figure 6.3) we saw that the fine-morphology is different for the blend with  $d_L$  compared to the blend with  $d_S$  particles, however WAXD pole-figures show that the morphology of the *iPP*-matrix of the sample with  $d_L$  particles is similar to the blend with  $d_S$  particles. The *appearance* of the fine-morphologies in Figure 6.3 is thus related to the PTFE-phase and not to the orientation of the *iPP*-matrix.

In summary, the texture of the *iPP*-matrix of the sample with  $d_L$  particles is similar to the blend with  $d_S$  particles. In both blends processing-induced structures prevail. During injection molding the polymer melt is subjected to strong flow fields, resulting in a strongly oriented melt. During cooling of the polymer the orientation of the melt is partly preserved and probably results in *iPP*-row nuclei on which lamellae may grow perpendicularly. If a blend with added PTFE is injection-molded, the local deformation and flow may differ from that of the PTFE particles which generates a local shear field in the vicinity of the PTFE particle or fiber. This may generate extra (compared with the case when no PTFE is present) row nuclei that initiate nucleation and growth of *iPP*. It is expected that an increase in concentration of PTFE will enhance the amount of row structures in the melt.

The role of PTFE thus is twofold; firstly, it changes the local flow fields, which give rise to extra processing-induced structures, and secondly the PTFE will act as a nucleant influencing the crystallization of *iPP*. In case of the  $d_L$  particles, shear and elongation of the *iPP* matrix induce fibrillation of PTFE and in turn the fibrillated PTFE may cause oriented nucleation and crystallization of *iPP*.

### 6.3.3 Crystallization behavior of *iPP* on fibrillated PTFE

#### Introduction

As mentioned in the introduction, isotactic polypropylene (*iPP*) is able to epitaxially nucleate and crystallize on PTFE films in its  $\alpha$ -modification. We assumed that fibrillated PTFE would provide a scaffold on which *iPP* nucleates and crystallizes with preferred orientation. Such fibrillated PTFE structures may form during processing due to shear and elongation that is experienced by the (solid) PTFE particles dispersed in the *iPP* melt. In order to investigate this possibility, previously investigated injection molded samples were melted and re-crystallized, i.e. the injection molded samples are heated to above the melting point of *iPP* ( $T_{m, iPP} = 167\text{ }^\circ\text{C}$ ) [35] but below the melting point of PTFE ( $T_{m, PTFE} = 335\text{ }^\circ\text{C}$ ) [36]. By doing so, the PTFE-scaffold consisting of fibrillated PTFE in the *iPP* matrix will remain intact, but the thermal rheological history of *iPP* is removed. In this way

the effect of processing-induced nucleation and crystallization from the nucleation and crystallization due to PTFE is separated.

The morphology of the samples was investigated by high-resolution SEM (HR-SEM) and WAXD, while crystallization characteristics were investigated by light microscopy (LM) and differential scanning calorimetry (DSC). The following paragraphs give an overview of the results.

### SEM observations

First, visualization of the morphology by SEM is described. The high resolution SEM-micrographs (Figure 6.6) show the fine structure of the blend with ds particles after melting and re-crystallization. Figure 6.6 A shows the morphology parallel to the MD (sample position 3 in Figure 6.1) and Figure 6.6 B gives a magnification of another preselected location (from a different spot on the sample).

The primary reactor particles of which the ds particles consist of are homogeneously and predominantly individually distributed in the iPP matrix. There is no sign of strong deformation of these primary reactor particles. The particles act as centra for heterogeneous nucleation, giving rise to normal spherulitic growth. The boundaries of the spherulites can be nicely distinguished (see e.g. the white arrow in Figure 6.6 A). Within these spherulites the typical cross-hatched structure of iPP can be distinguished. Initially, ‘mother’ lamellae (several tens of nanometers) grow from the PTFE particles, on which shorter crosshatched daughter lamellae grow subsequently. Although not shown here, the morphology perpendicular to the MD is similar to the morphology parallel to the MD as shown in Figure 6.6. As the morphologies of the blend with ds PTFE-particles perpendicular and parallel to the MD are essentially the same, we can conclude that the material is isotropic (see next paragraph, as well).

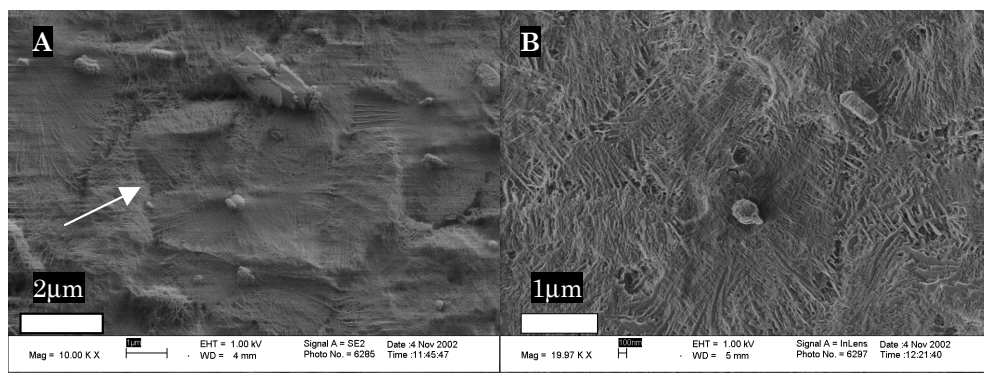


Figure 6.6. Typical high resolution SEM-micrograph of the PTFE-iPP blend with ds particles. The micrograph to the right is a magnification obtained on a different spot of the specimen. Explanation can be found in the text.

A completely different picture arises from the observation of morphology of the blend with  $d_L$  particles, as can be seen in Figure 6.7. Micrographs A and B in Figure 6.7 are micrographs taken from the sample cut parallel with the MD, micrographs C and D are micrographs from the morphology cut perpendicular to the MD (sample positions 3 and 4 in Figure 6.1, respectively). The micrographs to the right (B, D) are magnifications of the micrographs to the left (A, C).

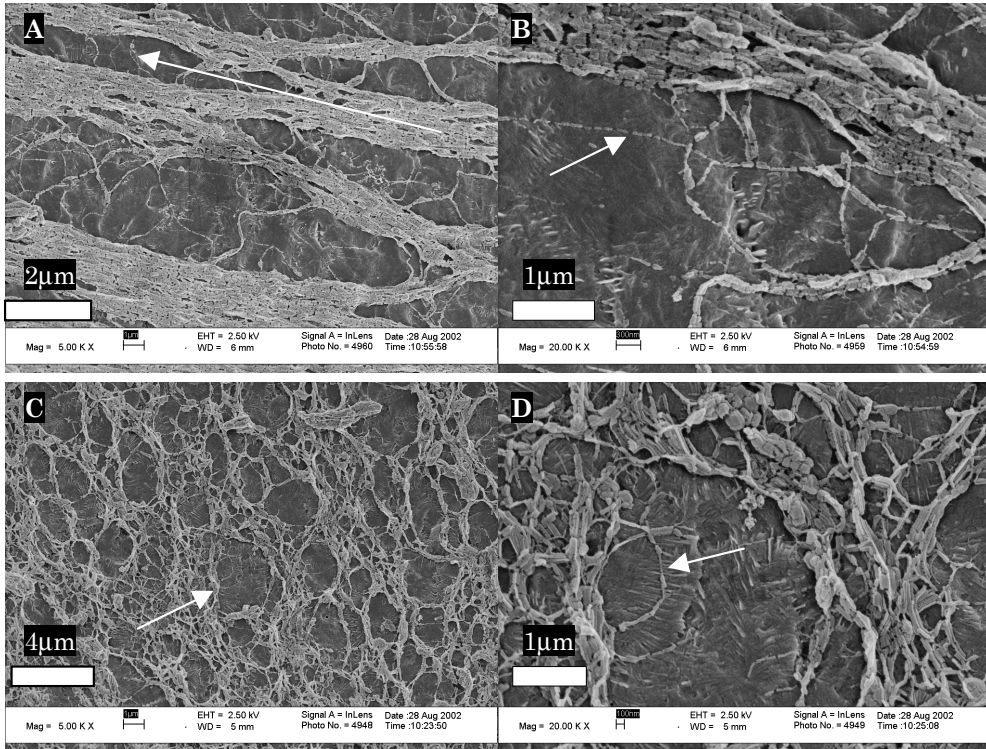
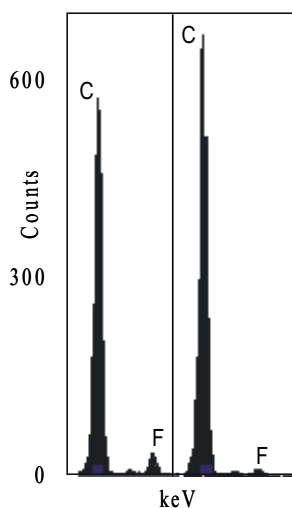


Figure 6.7. Typical high resolution SEM-micrographs of the PTFE-iPP morphology from the blend with  $d_L$  PTFE particles. Upper (A) and lower (C) micrographs show the morphology parallel and perpendicular to the MD, respectively. The micrographs to the right (C, D) are magnifications obtained on selective locations of the micrographs to the left. The white arrow in A is indicating the MD. The white arrow in D shows a clear example of the nucleation ability of PTFE.

The initial particle powder morphology (see Figure 6.2) of the  $d_L$  particles is completely destroyed during processing. The agglomerates of primary particles broke up and a strong fibrillation took place. Most of the fibrils are clustered into larger bundles, while also individual fibrils can be distinguished (indicated by the arrow in micrograph B). From HR-SEM the diameter of the individual fibrils was estimated as 20-30 nm with an aspect ratio of at least 25 (see arrow in micrograph B). The fibrils are slightly segmented. This is probably an effect of etching and/or

sputtering. One can see that the bundles of fibrils are, on the average, pointing in the MD (indicated by the arrow in micrograph A). The bundles are open PTFE structures in which iPP is present. The lower micrographs (C, D) of Figure 6.7 show circular PTFE features. The higher magnified micrograph shows that the inside of these circles consist of iPP. Predominantly edge-on lamellae can be seen, this in contrary to the upper right micrograph (A) of Figure 6.7 were significantly less edge-on lamellae are present. Typical crosshatched structures, characteristic for the  $\alpha$ -phase of polypropylene, can also be seen.

With the EDX equipment it was possible to take element specific-spectra from the fibers and the matrix separately. The EDX-spectrum (see Figure 6.8) taken from the fiber shows a significantly higher fluorine concentration at the location of the fiber, compared with the spectrum taken from the matrix. Due to the finite penetration depth of the electron beam the spectrum still shows a weak signal of fluorine coming from PTFE slightly beneath the surface. The measurements, however, clearly show that the elongated fibrillar structures consist of PTFE, while the surrounding matrix is iPP.



*Figure 6.8. EDX spectra of a fiber (left peaks) and of the matrix (right peaks). An increased fluorine concentration compared with carbon is seen when the e-beam is focused on a fiber.*

The following figure (Figure 6.9) shows a higher magnification HR-SEM-micrograph of the morphology perpendicular to the MD. Again, for the most part edge-on lamellae can be seen, which are intimately interwoven. The more ‘open’ morphology in the fourth quadrant of Figure 6.9 displays a border between two impinging spherulitic growth-fronts. On such borders more amorphous material may be present as a result of segregation during crystallization [37]. Consequently less material is able to crystallize. Etching will preferentially remove the amorphous material, resulting in the more ‘open’ morphology seen in the micrograph.

From figure 6.8 one can draw the conclusion that a clear difference in PTFE morphology exists, between the perpendicular and parallel directions (compared to MD) for re-crystallized specimens in the presence of a PTFE fibril scaffold. As a result of the difference in morphology of PTFE in the two opposite directions, the morphology of iPP also shows variations. The micrographs indicate that iPP crystallizes within the scaffold of the openly structured network of PTFE-fibers. The nucleation is strongly enhanced due to the high surface area of the highly dispersed PTFE on which the polypropylene nucleates heterogeneously.

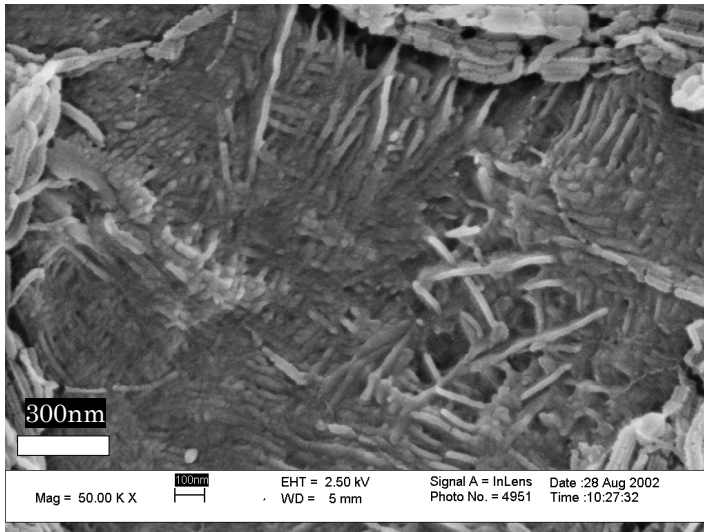


Figure 6.9. HR-SEM micrograph of a typical crosshatched structure of isotactic polypropylene ( $\alpha$ -phase). Note the 'open structure' in the fourth quadrant.

### WAXD-observations

In order to obtain more insight in the oriented overgrowth of iPP on the PTFE-scaffold in the different blends, WAXD experiments were performed and pole-figures for the crystalline iPP matrix were determined. Pole-figures and orientation distributions were studied and compared for blends of iPP with  $d_s$  and  $d_L$  PTFE-particles, respectively. Morphology was compared for the same specimen used in SEM studies earlier. The samples were taken from position 4 in Figure 6.1.

The orientation texture (based on the pole figures) of iPP after melting and re-crystallization as compared with the injection molded samples before melting and re-crystallization is completely different. Figure 6.10 shows the (110) and (040) pole-figures of the blend with  $d_s$  PTFE particles. As it can be seen, the distribution of both the (040) and the (110) planes is essentially isotropic (compared with Figure 6.4 for the same blend before melting and re-crystallization). During melting, the processing-induced orientation (due to injection molding) of iPP completely disappears. From SEM we drew the conclusion that no oriented network of PTFE was present which could have caused oriented crystallization. Thus the re-melted non-oriented iPP blends with  $d_s$  particles crystallize as in normal, quiescent crystallization.

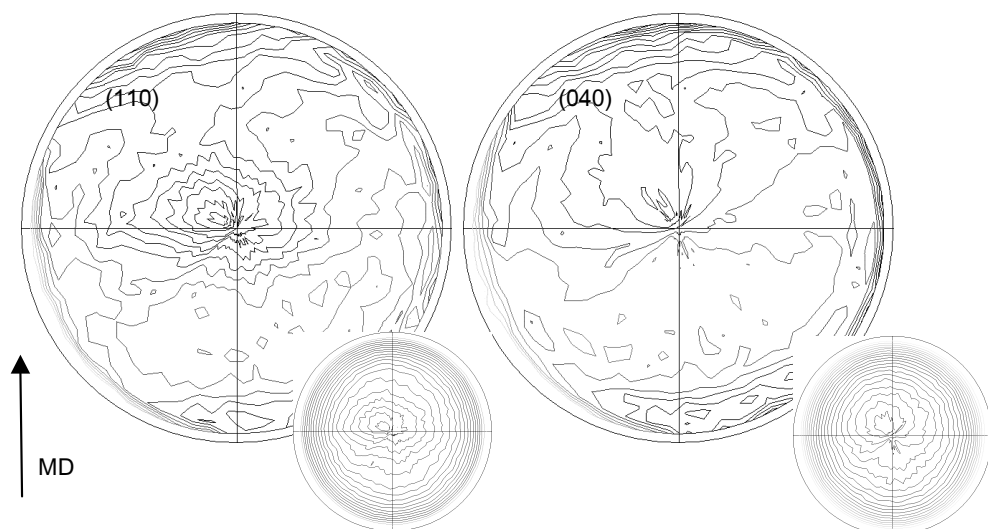


Figure 6.10. Pole-figures of a typical specimen obtained from a blend with  $d_s$  particles melted and isothermally recrystallized. The right figure shows the (110)- and left the (040)-plane, respectively. The pole density is indicated by dark black lines (high intensity) to light gray lines (low intensity). The machine direction (MD) is indicated by the arrow. The small inserts show the pole-figures prior to instrumental correction.

In contrary to the blend with  $d_s$  PTFE-particles, the pole-figure of the blend with  $d_L$  particles shows a strong orientation also *after* melting and recrystallization. See Figure 6.11 for the melted and recrystallized sample and Figure 6.5 for the original injection molded sample. The pole-figure of the (110) plane of the melted and recrystallized injection molded sample shows a broad and nearly uniform distribution in intensity over the entire hemisphere, with a slightly higher concentration in a plane perpendicular to the MD, and small splaying on the (east-west) poles. One strong and one weak mode can be seen in the pole-figure of the (040) reflection (see Figure 6.11). The first strong mode ('mode' 1) appears as two maxima between  $15^\circ < \psi < 35^\circ$  in the direction of the north and south poles, respectively. The intensities are distributed homogeneously in a plane perpendicular to the MD, forming in this way a ring around the MD with  $15^\circ < \psi < 35^\circ$ . The second mode ('mode' 2) can be detected in a plane perpendicular to the MD (at  $\psi \approx 0^\circ$ ), with an approximately isotropic distribution.

Both pole-figures (e.g. the (110) pole-figure and the strong mode in the (040) pole-figure) can be explained by first orienting an imaginary iPP unit-cell such that the  $b$ -axis (which is the normal of the (040) plane) is pointing towards the ring ('mode' 1) and the [110] direction parallel with the ND and secondly rotating the  $b$ -

axis around on the ring, in the plane perpendicular to the MD. The  $[110]$  vector then will stay in the broad plane perpendicular to the MD. As the  $c$ -axis is perpendicular to the  $[110]$  and  $[040]$  directions, this axis will also be rotated in the broad plane normal to the MD. The weak mode 2 of  $(040)$  pole-figure can be explained by orienting the iPP unit-cell such that the  $b$ -axis (which is the normal of the  $(040)$  plane) is pointing towards the west- (or east-) pole and the  $[110]$  direction becomes parallel with the ND. In this way the  $c$ -axis is pointing towards the north- (or south-) pole. Rotation of the unit cell around the  $c$ -axis will yield the results seen in the pole-figures.

Although the nucleation density of the ‘mother’ lamellae is high at the crystallization temperature employed, also growth of ‘daughter’ lamellae (cross-hatching) is expected. The ‘daughter’ lamellae will have their crystallographic  $c$ -axis approximately (angle difference =  $99.6^\circ$  between ‘mother’ and ‘daughter’ lamellae) perpendicular to the iPP  $c$ -axis and perpendicular to the PTFE  $c$ -axis, so no extra pole density due to the daughter lamellae can be seen in the pole-figures.

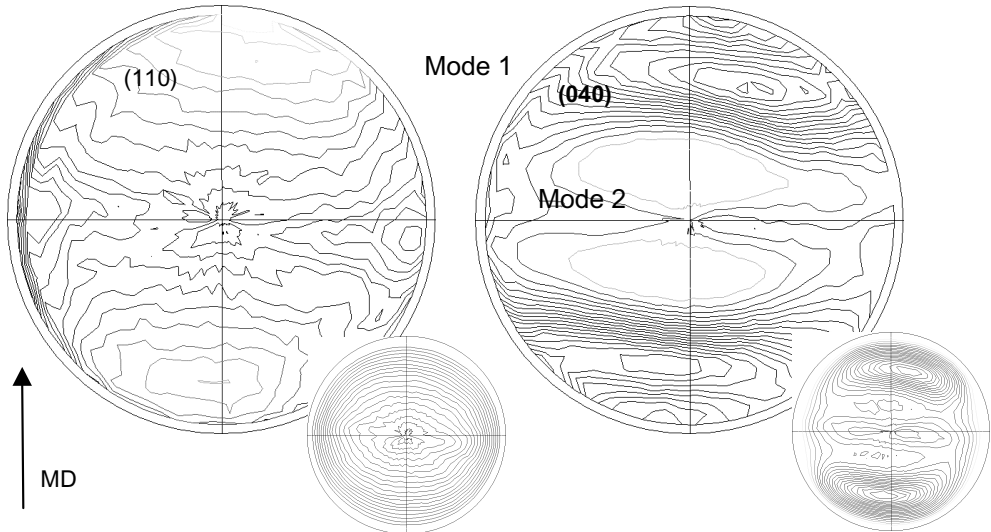


Figure 6.11. Pole-figures of a typical specimen obtained from a blend with  $d_L$  particles melted and isothermally recrystallized. The right figure shows the  $(110)$ - and left the  $(040)$ -plane, respectively. The pole density is indicated by dark black lines (high intensity) to light gray lines (low intensity). The machine direction (MD) is indicated by the arrow. The small inserts show the pole-figures prior to instrumental correction. Explanation of ‘Mode 1’ and ‘Mode 2’ is given in the text.

We can conclude that the observed orientation texture of iPP is solely due to the presence of a scaffold of oriented PTFE. The sample with  $d_s$  particles (which has no scaffold of PTFE fibrils) does not show any orientation after melting and recrystallization, while the specimen including  $d_L$  particles does show orientation.

In the paragraph concerning the oriented iPP texture of the injection molded



samples, we concluded that the *iPP*-morphology of both the injection blend with  $d_L$  and  $d_s$  particles showed similar elements of processing induced *iPP* morphology, although clear differences could be observed, as well. At this moment we can draw the conclusion that the orientated crystallization of *iPP* in the injection molded samples on the fibrillated PTFE scaffold, as we saw in the melted recrystallized samples is not the major cause of differences in morphology as observed by SEM (see figure 6.3).

### LM observations

Crystallization and nucleation of *iPP* on PTFE was also followed by polarized light microscopy experiments. The samples were subjected to the same thermal treatment as in the SEM and WAXD experiments, i.e. they were melted for 5 min at 220 °C to remove the thermal rheological history of the *iPP* matrix and quickly cooled down to the crystallization temperature (130 °C). A first-order red filter, which is placed diagonally between two crossed polarizers, can define the sign of birefringence [38]. The birefringence is defined as:

$$\Delta n = n_1 - n_2,$$

where  $n_1$ ,  $n_2$  are the refractive indices parallel and perpendicular to the slow direction of the first-order red filter, respectively [38]. The refractive indices of a material define the axis of the refractive index ellipsoid [38].

As expected from previous observations from SEM and WAXD, the melted and recrystallized blend with the  $d_s$  PTFE-particles showed normal spherulitic crystallization upon cooling. The PTFE as well as the *iPP* has no preferred orientation, so no change in birefringence can be seen upon crystallization.

The blend with the  $d_L$  PTFE-particles, however, showed different crystallization behavior. The PTFE-fibers showed a negative optical birefringence, when they are placed parallel with the first order red filter (the PTFE-fibers appeared yellow). The negative birefringence is probably the result of form and/or orientation-induced birefringence. Form-birefringence occurs in multiphase systems in which the phases have different refractive indices; at least one of the phases has dimensions in the order of the wave-length of light; and the shape of the multi-phase structure is anisotropic [39]. Orientation-induced birefringence occurs when at least one of the phases is anisotropic and has two different refractive indices perpendicular to each-other (in a Cartesian system of reference) [39]. As some of the PTFE-fibers have dimensions comparable with the wave-length of light and are aligned, both types of birefringence may occur in the blend with  $d_L$ . Upon cooling to 130 °C a strong positive birefringence arises due to the crystallization of *iPP* (the sample turned blue). The fact that the signs of birefringence of the PTFE fibrils and *iPP*-matrix are opposite (- for PTFE fibers, + for *iPP*) means that the long axis of the

refractive index ellipsoid of both phases are perpendicular to each other. Since the *c*-axis of iPP coincide with the long axis of the refractive index ellipsoid [18,38], the measurements indicate that the direction of the *c*-axis of iPP is on the *average* perpendicular to the PTFE-fiber direction.

### 6.3.4 Fibrillation

As already mentioned in the introduction, due to the low interfacial shear strength compared with the bulk value, PTFE can easily be fibrillated. Fibrillation is a strong elongation of the material in which large oriented (semi-crystalline) structures form a fibrous arrangement [40]. The morphology of fibrillated PTFE was studied in more detail by depositing  $d_L$  particles on a glass slide while exerting shear forces (see paragraph 6.2 Experimental). The result can be seen in Figure 6.12. The shear forces cause the initially large agglomerates to break up. In the micrograph left, undisturbed primary particles can be distinguished while also highly elongated structures can be seen. The elongated structures are formed from primary particles, corresponding to the actual fibrillation process. Figure 6.12 B shows a close up of a partly fibrillated particle. Individual particles are fibrillated until the particle is ‘consumed’. Several of these fibrils, formed from different primary particles, may cluster forming fibers of different sizes and lengths. The size of the fibrils is limited by the maximum drawability of the fibrils, which in turn depends on the molar mass and particle size of the PTFE. As the molar-mass of the  $d_L$ -primary particles is extremely high ( $\bar{M}_n = 2 \times 10^7 \text{g/mol}$ ), it is expected that the particles can be drawn to very high draw-ratios.

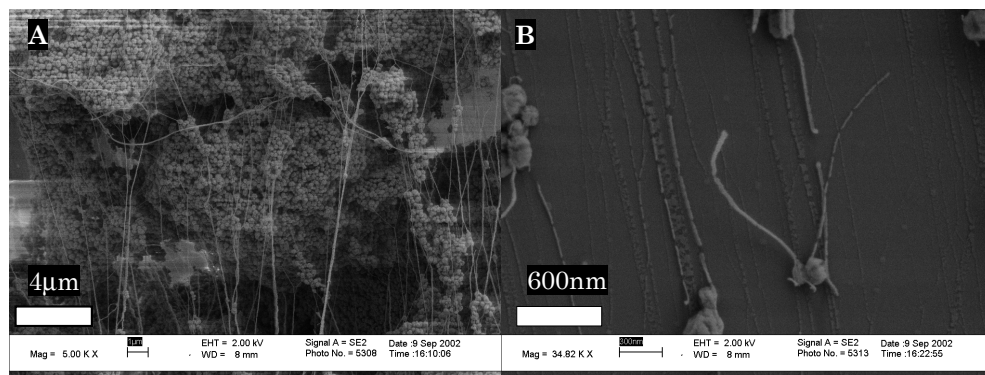


Figure 6.12. (Left) Primary particles and fibers. The fibers are formed by pull-out from the particles. Close-up of a partially fibrillated particle. The fibers are segmented due to sample preparation (thermal expansion of the matrix).

### 6.3.5 Discussion of iPP-PTFE blend morphology

The following paragraph presents a model for the melted and recrystallized blend of iPP with  $d_L$  particles. Injection molded specimen of this blend showed a

strong orientation of iPP-lamellae after melting and recrystallization. It was proved that the anisotropy is related to the oriented nucleation and crystallization on highly oriented PTFE. The fibrillated PTFE acts as a scaffold on which iPP can nucleate. We propose a model based on the epitaxial nucleation mechanism described by Lotz, *et al.* [17] which will account for the observations made by SEM, WAXD and LM.

As the epitaxial nucleation of iPP on PTFE is the basis of the model, we will shortly summarize the nucleation mechanism. It is however not the purpose to give an extensive discussion on the underlying reasonings, for this we refer to the original paper [17].

The epitaxial relationship involves the (110) contact plane of iPP with the (100) plane of PTFE. The chains of iPP and PTFE make in this case an angle of  $57^\circ$ . The initial epitaxial nucleation of iPP sets the unit-cell orientation in the initially grown lamellae:  $c_1$  parallel to the substrate of PTFE (with a  $57^\circ$  angle to the  $c$ -axis of PTFE),  $b_1$  at  $17^\circ$  to that plane, and  $a_1$  at  $80^\circ$  (or  $100^\circ$ ) to it. The lamellae grow away from the PTFE substrate mainly along the  $a$ -axis, which is by far the fastest growth direction in  $\alpha$ -iPP. The lamellae, in this case have an orientation of  $33^\circ$  to the oriented PTFE. On these initially grown ‘mother’ lamellae secondary ‘daughter’ lamellae can grow. This involves an  $\alpha$ -iPP/ $\alpha$ -iPP homo-epitaxy, which results in an interchange of  $a$ - and  $c$ -axes orientations in the mother and daughter lamellae across the contact plane, while the  $b$ -axis orientation is preserved [38,41].

Figure 6.13 shows a schematic presentation of the model, based on the nucleation mechanism described above. Two lamellae can be seen; one ‘mother’ lamella (dark gray) and one ‘daughter’ lamella (light gray). The orientation of the lamellae can be read from the figure.

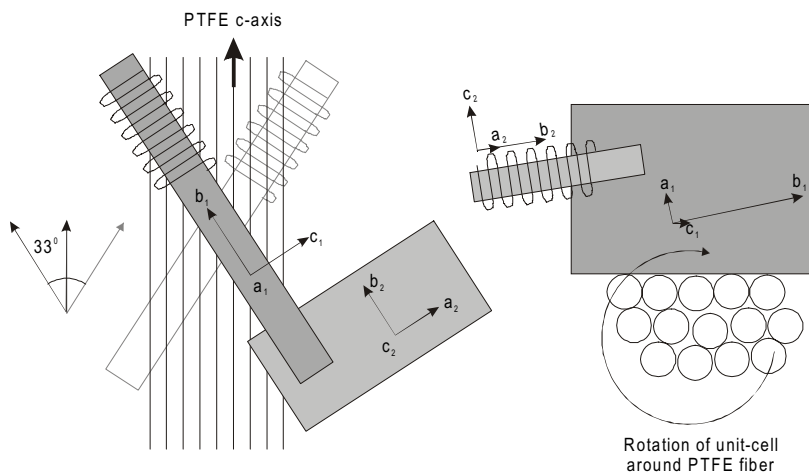


Figure 6.13. Model of epitaxial growth of iPP on PTFE fibers. Right: top-view, left: side view.

From the light-microscopy experiments we concluded that during crystallization the long axis of the refractive index ellipsoid turned into the short axis and *visa versa* (see Figure 6.14). Before crystallization the birefringence is caused due to the presence of oriented PTFE, while after crystallization the birefringence is mainly caused by the oriented iPP (which is present in the majority). Figure 6.14 shows the refractive index ellipsoid before and after crystallization.

The average orientation of the *c*-axes of iPP, which are according to the model  $57^\circ$  or  $-57^\circ$  compared with the *c*-axis of PTFE, gives an average orientation of the ellipsoid seen in Figure 6.14. The observed birefringence change during crystallization is in agreement with the proposed nucleation and crystallization mechanism of iPP on PTFE.

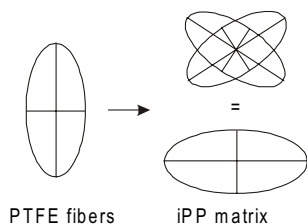


Figure 6.14. Change in refractive index ellipsoid during crystallization.

The SEM-micrographs of the melted and recrystallized samples of the blend with  $d_L$  particles show the presence of a large PTFE scaffold on which the iPP can preferentially nucleate. Indeed we see lamellae grown off the PTFE and especially in Figure 6.7 D we find a high population of edge-on lamellae as we expect from the model presented above. The SEM experiments are especially suitable to reveal to PTFE morphology, however it was not possible to obtain from the SEM-micrographs the relative orientation of the iPP-lamellae compared with the PTFE scaffold. Only in the right bottom micrograph (D) of Figure 6.7, we see the relative orientation of lamellae compared with the PTFE-fibril (indicated by a white arrow). The lamellae have an approximately perpendicular orientation compared with the fibril [4,42]. WAXD experiment results showed however that there exists no (or a very small) population of lamellae with an orientation perpendicular to MD, as described in references [5,19]. So we conclude that this nucleation mechanism appears to have a very limited impact in the overall nucleation and crystallization process of the blends studied here. We showed that the lamellae make a much smaller angle (between  $15^\circ$  and  $35^\circ$ ) with the MD. The morphological model presented accounts for these angles.

### 6.3.6 Crystallization

Isothermal crystallization experiments were performed to characterize the nucleation ability of PTFE. In a reference experiment the nucleant sodium benzoate (SB) was used. Approximately the same crystallization half-times were found for iPP nucleated by dL as well as ds PTFE-particles ( $t_{1/2}$  is between 2 min and 4 min), whereas the plain polymer has a  $t_{1/2}$  of 27 min at the same crystallization temperature. The crystallization half time for SB is similar to that of the PTFE nucleated PPs (see Figure 6.15). This clearly demonstrates the strong nucleating ability of PTFE, regardless of being present as separate particles (in the case of ds particles) or present as a fibrillated scaffold (in the case of dL particles).

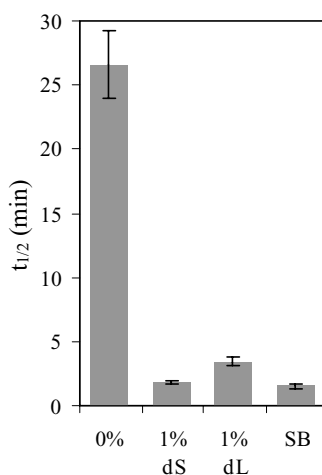


Figure 6.15. Crystallization half times of the various blends used.

### 6.3.7 Mechanical properties

#### Tensile properties

Toughness, E-modulus, and yield stress form three important parameters to characterize the mechanical properties of a material [43]. It is expected that since PTFE acts as a nucleating agent and as it modifies the morphology, its presence will modify the mechanical properties, as well. Several studies [44-46] have indicated that the molar mass of the polymer strongly influences the impact properties. Thus, in order to elucidate the influence of morphology on mechanical properties, the molar mass of the polymers compared must be kept constant. As we use the same polypropylene, the differences in mechanical properties are solely determined by the differences in morphology. To reveal the mechanical properties, instrumented impact tests [47] and tensile tests were performed. First the results from the tensile tests will be discussed and the results of the impact-tests will follow later.

Analysis of the tensile tests yielded both the E-modulus and yield stress, the results are presented in Figure 6.16. The overall trend shows an increasing E-modulus with increasing amount of added PTFE. The reasons for the increase in E-modulus are the nucleation ability of the PTFE and the enhancement of the flow-induced morphology as described in paragraph 6.3.5. The use of nucleating agents causes higher crystallinity and lamellar thickness as compared to non-nucleated samples, resulting in a higher E-modulus [8,48,49]. From the results, described in chapter 5, we found for the nucleated samples an average increase in E-modulus in the order of 0.4 MPa. The increase in E-modulus found in the blends with PTFE is approximately 0.3 MPa, which is in the same order. From DSC measurements (see Figure 6.15) we saw that the nucleation ability of PTFE is comparable among the different type of particles used, with a slightly higher nucleation ability for the fibrillated larger (d<sub>L</sub>) particles. Therefore it is expected that the increase in E-modulus, due to the change in crystallinity and lamellar thickness, is approximately the same for each blend, being slightly higher for the d<sub>L</sub> particles. Another reason for the increase in E-modulus is the presence of highly oriented row structures, which provide stiffness in the direction of the backbone of the row structure. As already said in paragraph 6.3.5, we anticipate an increase in the number of row structures with an increasing amount of PTFE, resulting in an increase in the measured E-modulus. The nucleation mechanism and processing-induced structures explain the observed general trend in E-modulus as function of the concentration of PTFE.

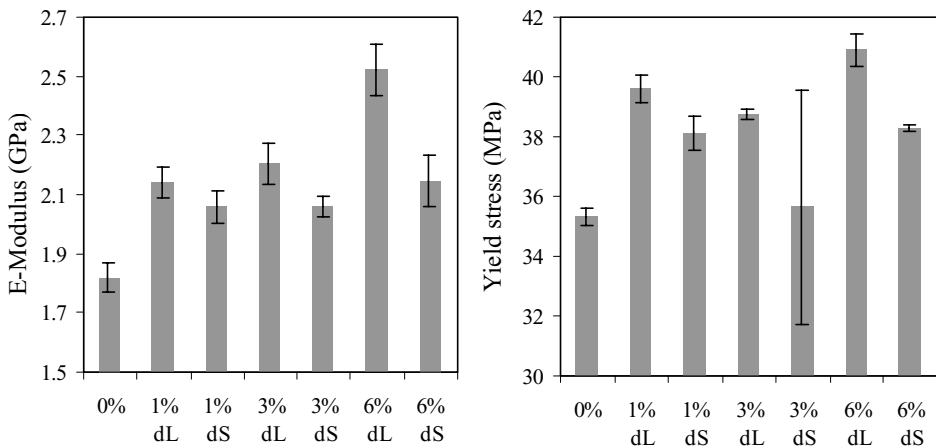


Figure 6.16. E-modulus and yield stress for several blends of PTFE with iPP. Error bars are the standard deviations. Further explanation can be found in the text.

The type of PTFE-particles has a distinct influence on the value of the E-modulus. Samples including the large particles (d<sub>L</sub>) show systematically higher values of the E-modulus. The difference in the value of the E-modulus for the blends with the same concentration of PTFE (but different particle type) is

increasing with higher concentration. This is related to the influence of the PTFE, i.e. the presence of PTFE fibers (see Figure 6.6). The fibrillated PTFE, as in traditional composite materials, acts like oriented fibers. The coupling of fiber and matrix is parallel in tension. The load is beared by the iPP matrix as well as by the PTFE-fibers. From SEM micrographs, draw ratios of the large particles are at least 25. With this particular draw ratio the E-modulus of PTFE may increase from 600 (MPa) (virgin reactor powder) to 15 (GPa) [36]. This value is significant when calculating the E-modulus in a composite using a simple linear additivity of moduli [23] and causes an increase of E-modulus of the blend with large particles ( $d_L$ ) as compared to the blend with smaller particles ( $d_S$ ).

The yield stress shows roughly the same trend as the E-modulus. The yield stress is higher for all blends compared with the plain polymer. The blends with  $d_L$  particles show a slightly higher yield stress compared with the blend with  $d_S$  particles with the same PTFE concentration. Yielding involves large plastic deformation of the iPP-matrix [50,51]. Plastic deformation takes place at higher stresses for specimen with higher yield stress. It is expected that due to the same reasons as mentioned for the E-modulus, i.e. the increase in the amount of flow-induced structures, the yield stress will be higher. Moreover, the load bearing fibrils of  $d_L$  PTFE-particles may render the yield stress higher, as well.

### Impact properties

By means of instrumented impact tests it is possible to extract strain energy release rate ( $G_I$ ) by taking the area under the force-displacement curve. For details about the analysis if the impact tests used, we refer to chapter 2, paragraph 4 of this thesis.  $G_I$  represents the total fracture energy [23]. Instrumented impact tests are preferred as compared to conventional impact tests as the force-displacement curve by these experiments can be measured, rather than the total fracture energy. The path of the stress-strain curve gives information about crack initiation and crack propagation.

Figure 6.17 shows the force-displacement curves of the blends (iPP + 1%  $d_L$ ) and (iPP + 1%  $d_S$ ). After an initial linear increase of the force the curves show a maximum.

The maximum load can be defined as the boundary between crack initiation and crack propagation [52]. Brittle fracture is characterized by zero propagation energy [52]. In contrary to brittle fracture, the curves in Figure 6.17 show pronounced crack propagation energy. The presence of this propagation energy is defined here as a sign for ductile fracture. From these curves it is clear that the blend of iPP with  $d_S$  PTFE-particles (A) shows a higher maximum force together with a much more extended propagation zone.

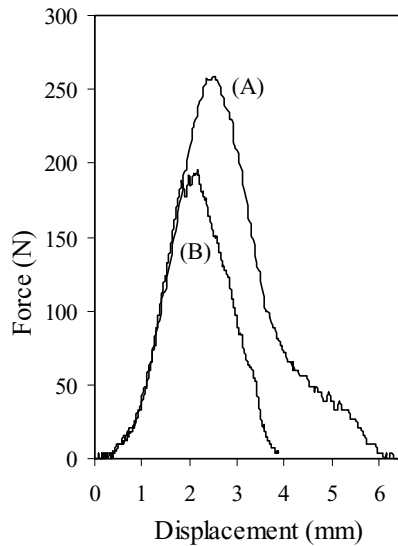


Figure 6.17. Force-displacement curve of the blends (iPP + 1% $d_L$ ) (A) and (iPP + 1%  $d_S$ ) (B).

After crack initiation, the specimen shows considerable energy uptake during crack propagation. In the first part of the force-displacement curve, elastic energy is stored and deformation can take place behind the notch. Pre-crack deformation of the notch may lead to notch blunting, resulting in higher impact energies. In both curves of Figure 6.17 a small sign of notch-blunting is seen. Although notch-blunting will increase the impact energy, it is not expected to be one of the major energy absorbing mechanisms.

Figure 6.18 gives the results of the strain energy release rate,  $G_I$  ( $\text{kJ/m}^2$ ), of several blends with two types of PTFE, both with and increasing PTFE concentration. As one can see in the figure, the blending of iPP with PTFE gives higher toughness for all specimens. The impact energy is increasing with PTFE concentration. The type of PTFE used, i.e.  $d_L$  or  $d_S$  PTFE-particles, has only a minor influence although the specimen with  $d_L$  particles yields a slightly higher toughness. The blend (iPP + 1%  $d_S$ ) behaves differently; the value of  $G_I$  is  $16.1 \text{ kJ/m}^2$ , which is significantly higher than the rest of the blends.

One of the reasons why the impact energy of the blends with PTFE is higher compared with plain iPP might be an increase in lamellar thickness due to the ability of PTFE to nucleate (see chapter 6). However no data on lamellar thicknesses is available and we can not be conclusive about this statement, moreover the increase in impact energy is higher than expected from an increase in lamellar thickness. Therefore, we anticipate also the influence of other effects. We saw from WAXD measurements (see paragraph 6.3.2) that both blends with  $d_L$  and



$d_s$  PTFE-particles showed processing-induced structures. The highly oriented row structures, which provide stiffness in the direction of the backbone, may also provide strength.

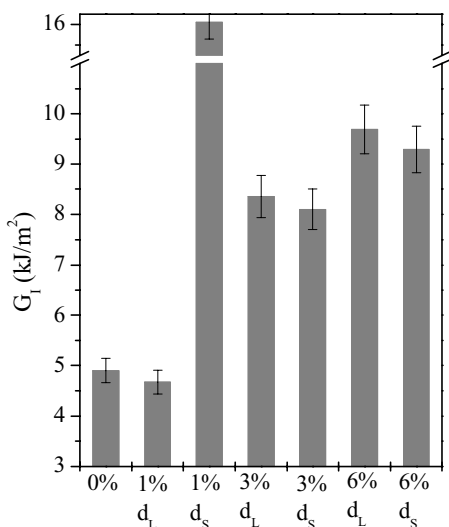


Figure 6.18. Values of strain energy release rate ( $G_I$ ) of several polymer blends. Error bars are standard deviations.

As already said in paragraph 6.3.5, we anticipate an increase in the number of row structures with an increasing amount of PTFE. The increasing number of row structures will result in higher impact energies. The enhanced nucleation and processing-induced structures explain well the observed general trend in  $G_I$  as function of the concentration of PTFE. The reason why the impact of the blends with  $d_L$  particles is slightly higher compared with the blends with  $d_s$  PTFE-particles may originate from the load bearing capacity of the PTFE-fibrils during fracture.

We believe, however, that at least one extra deformation mechanism is active, which might explain also the anomalous high impact energy of the blend with 1%  $d_s$  particles. Micro deformation of the iPP-matrix caused by cavitation [53] is well known in blends of semi-crystalline polymers blended with rubber particles [54] or rigid particles [55-57]. In our case, the PTFE may act as a stress concentrator in the iPP-matrix. Due to the extra stress, debonding will take place, leading to a different stress state. This stress state is favorable for shear yielding as opposed to crazing, which leads to higher absorption of energy during fracture. An increase in concentration provides more possibilities of iPP to cavitate, resulting in higher impact energies. It is known that the size of particles strongly influences the effectiveness of cavitation [54]. In case the particles are too small or too large they are not active. We believe that in the 1% blend of  $d_s$  particles, agglomeration of primary reactor particles is less severe compared with higher concentration blends,

and therefore more particles may have the right size to participate in the cavitation process.

Continuing the reasoning of cavitation as additional deformation mechanism, we expect that a better dispersion of PTFE particles in the iPP matrix will lead to more cavitation per unit volume and thus higher impact energies (We expect also an enhancement in nucleation, but, as said, this effect is probably of minor importance). Therefore a dispersive agent was added to the blend (iPP + 1%ds). The dispersive agent was a perfluoropolyether with an alkylamide as functional group (Fluorolink®, A10, Ausimont, Italy). It is anticipated that the dispersive agent will act as a compatibilizer between the PTFE and iPP and will cause a better dispersion of PTFE particles in the matrix, leading to higher impact energies. Moreover it is expected that a better interfacial adhesion will also improve toughness [58]. This new blend was compared with other blends in conventional non-instrumented Charpy impact tests [59]. Because the testing conditions in these tests were slightly different (different impact speed and notch shape) from the previously described instrumented Charpy impact tests, the plain iPP (0%), the blend (iPP + 1%dL), and the blend (iPP + 1%ds) were repeated in order to give a better and justified comparison with the previously described results (see Figure 6.18).

As expected the impact energy of the blends with ds-particles is indeed significantly higher, the maximum load as well as the propagation energy is higher (see Figure 6.19). In the case of well dispersed particles (iPP + 1%ds + D) the fracture energy is even higher, supporting the idea of cavitation as additional deformation mechanism.

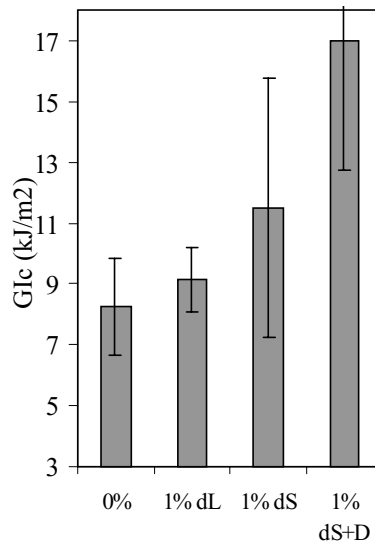


Figure 6.19.  $G_I$  values of several blends. Error-bars are standard deviations. Explanation can be found in the text.

## 6.4 Conclusions

The morphology of blends composed of iPP with PTFE is complicated and diverse. During processing agglomerates of primary PTFE reactor particles break-up under the influence of shear and elongation of the surrounding polymer melt and are as a result of processing highly distributed in the matrix. In the case of larger PTFE particles (of higher molar mass), fibrillation takes place leading to the formation of an oriented three dimensional PTFE scaffold (fibrillar phase morphology). The smaller PTFE particles of lower molar mass are well dispersed in the matrix, and do not show visible fibrillation.

The iPP-morphology of the *injection* molded blends is mainly determined by the flow-induced crystallization of iPP. Highly elongated structures are formed in the melt during processing. These act like row nuclei on which lamellae can grow perpendicularly. A large population of cross-hatched secondary lamellae is present in both blends, as well. The nucleation of iPP on fibrillated PTFE (or on PTFE particles) does not play a *major* role in the morphology of the injection molded blends, although differences in the morphology may be attributed to the role of PTFE as nucleating agent.

As shown in the samples that were melted and recrystallized, the fibrils (or bundles of fibrils) of PTFE give rise to a strong oriented overgrowth of iPP crystallized from quiescent melts. The orientation of the iPP-matrix after melting and recrystallization was solely due to the PTFE-scaffold. The orientation of the iPP-lamellae found from WAXD and LM is well explained by a model based on the epitaxial nucleation mechanism proposed by Lotz [17].

The crystallization rate of iPP blended with PTFE characterized by the crystallization half time, increased considerably. Similar crystallization halftime values were measured for sodium benzoate, which is a widely used industrial nucleating agent. Only small differences in crystallization half-time values were observed between the different types of PTFE-particles. The blend with the *dl* particles showed a slightly shorter crystallization half-time.

PTFE blended with polypropylene leads to an increase in mechanical properties. Both the total fracture energy, as well as the energy for crack propagation increases with concentration of PTFE. The increase in impact properties is not accompanied with a decrease in E-modulus. The E-modulus is higher for all concentrations and types of PTFE, compared with plain polypropylene. The yield stress shows the same trend. The enhancement in mechanical properties could be caused by an increase by the nucleation of iPP by PTFE. Nucleated crystallization results in changes of structural features (degree of crystallinity, lamellar thickness, fine spherulite structures) which, in turn, contributes to property enhancement. However, the increase in the mechanical

properties is more than expected from nucleated crystallization alone. The improvement in mechanical properties is mainly determined by the enhancement of the formation of processing-induced structures and the introduction of extra deformation mechanisms due to the incorporation of PTFE. The presence of an oriented PTFE morphology in the blend with the larger type of PTFE-particles, caused by fibrillation of the PTFE-particles, resulted in a higher E-modulus, yield stress, and toughness compared with blends containing the smaller type PTFE-particles.

## 6.5 References

- (1) Varga, J.; Breining, A.; Ehrenstein, G. W. Polymer blends with fibrillar phase morphology prepared by a self-reinforcing technique. *Intern. Polym. Process.* **2000**, *15*, 53.
- (2) Ogbonna, C. I.; Kalay, G.; Allan, P. S.; Bevis, M. J. The self-reinforcement of polyolefins produced by shear controlled orientation in injection molding. *J. Appl. Polym. Sci.* **1995**, *58*, 2131.
- (3) Alexander, L. E. *X-ray Diffraction Methods in Polymer Science*; John Wiley & Sons, Inc.: New York, 1969.
- (4) Wang, C.; Liu, C. R. Transcrystallization of polypropylene composites: nucleating ability of fibres. *Polymer* **1999**, *40*, 289.
- (5) Greso, A. J.; Phillips, P. J. Explanation of the epitaxial deposition of nylon 66 on carbon fibres and its extension to isotactic polypropylene. *Polymer* **1996**, *37*, 3165.
- (6) Meng, Y. Z.; Tjong, S. C. Effects of processing conditions on the mechanical performance of maleic-anhydride compatibilized in-situ composites of polypropylene with liquid crystalline polymers. *Polym. Composites* **1998**, *19*, 1.
- (7) Afshari, M.; Kotek, R.; Kish, M. H.; Dast, H. N.; Gupta, B. S. Effect of blend ratio on bulk properties and matrix-fibril morphology of polypropylene/nylon 6 polyblend fibers. *Polymer* **2002**, *43*, 1331.
- (8) Pukánszky, B.; Mudra, I.; Staniek, P. Relation of crystalline structure and mechanical properties of nucleated polypropylene. *J. Vinyl Addit. Techn.* **1997**, *3*, 53.
- (9) Chapter 5 of this thesis.
- (10) Akinay, A. E.; Tincer, T. Gamma-irradiated poly(tetrafluoroethylene) particle-filled low-density polyethylene. I. Effect of silane coupling agents on mechanical, thermal, and morphological properties. *J. Appl. Polym. Sci.* **1999**, *74*, 866.
- (11) Kerbow, D. L. *Poly(tetrafluoroethylene)*; Mark, J. E., Ed.; Oxford University Press: Oxford, 1999, pp 842.
- (12) Pooley, C. M.; Tabor, D. Friction and molecular structure: The behaviour of some thermoplastics. *Proc. R. Soc. Lond. A.* **1972**, *329*, 251.

- (13) Tervoort, T.; Visjager, J.; Graf, B.; Smith, P. Melt-processable poly(tetrafluoroethylene). *Macromolecules* **2000**, *33*, 6460.
- (14) Bodo, P.; Schott, M. Highly oriented polytetrafluoroethylene films: A force microscopy study. *Thin Solid Films* **1996**, *286*, 98.
- (15) Peters, W. E. *US Pat. 5,645,603*, 1997.
- (16) Damman, P.; Fischer, C.; Kruger, J. K. Oriented growth of n-alkanes crystals on nanostructured poly(tetrafluoroethylene) substrates. *J. Chem. Phys.* **2001**, *114*, 8196.
- (17) Yan, S.; Katzenberg, F.; Petermann, J.; Yang, D.; Shen, Y.; Straupe, C.; Wittmann, J. C.; Lotz, B. A novel epitaxy of isotactic polypropylene (alpha phase) on PTFE and organic substrates. *Polymer* **2000**, *41*, 2613.
- (18) Vancso, G. J.; Förster, S.; Leist, H. Nanometer-scale tribological properties of highly oriented thin films of poly(tetrafluoroethylene) studied by lateral force microscopy. *Macromolecules* **1996**, *29*, 2158.
- (19) Assouline, E.; Wachtel, E.; Grigull, S.; Lustiger, A.; Wagner, H. D.; Marom, G. Lamellar orientation in transcrystalline gamma isotactic polypropylene nucleated on aramid fibers. *Macromolecules* **2002**, *35*, 403.
- (20) Olley, R. H.; Bassett, D. C. An improved permanganic etchant for polyolefins. *Polym. Comm.* **1982**, *23*, 1707.
- (21) Rahl, F. J.; Evanco, M. A.; Fredericks, R. J.; Reimschuessel, A. C. Studies of the morphology of emulsion grade polytetrafluoroethylene. *J. Polym. Sci.: Polym. Chem. Ed.* **1972**, *10*, 1337.
- (22) Swei, G. S.; Lando, J. B.; Rickert, S. E.; Mauritz, K. A. *Poly(tetrafluoroethylene)*; 2nd ed.; Kroschwitz, J. I., Mark, H. F., Bikales, N. M., Overberger, C. G. and Menges, G., Ed.; John Wiley & Sons, Ltd: New York, 1986.
- (23) McCrum, N. G.; Buckley, C. P.; Bucknall, C. B. *Principles of Polymer Engineering*; Oxford University Press Inc.: New York, 1994.
- (24) Tsebrenko, M. V.; Rezanova, N. M.; Vinogradov, G. V. *Polym. Eng. Sci.* **1980**, *20*, 1023.
- (25) Beery, D.; Kenig, S.; Siegmann, A. Structure development during flow of polyblends containing liquid-crystalline polymers *J. Polym. Eng. Sci.* 1991, *31*, 451.
- (26) Okuyama, H.; Kanamoto, T. Solid-state deformation of polytetrafluoroethylene powder. *J. Mat. Sci.* **1994**, *29*, 6485.
- (27) Stewart, C. W. *U.S. Pat. 4,596,855*, 1986.
- (28) Turner-Jones, A.; Aizlewood, J. M.; Beckett, D. R. Crystalline forms of isotactic polypropylene. *Makrom. Chem.* **1963**, 134.
- (29) Hibi, S.; Niwa, T.; Wang, C.; Lin, J.-S. Structure and mechanical anisotropy of cold-rolled ultrahigh molecular weight polypropylene. *Polym. Eng. Sci.* **1995**, *35*, 903.

- 
- (30) Choi, D.; White, J. L. Crystal structure and orientation developemnt in tubular film extrusion of syndiotactic polypropylene and isotactic polypropylene. *Polym. Eng. Sci.* **2001**, *41*, 1743.
- (31) Kantz, M. R.; Newman, H. D.; Stigale, F. H. The skin-core morphology and structure-property relationships in injection-molded polypropylene. *J. Appl. Polym. Sci.* **1972**, *16*, 1249.
- (32) Mencik, Z.; Fitchmun, D. R. Texture of injection-molded polypropylene. *J. Polm. Sci.* **1973**, *11*, 973.
- (33) Weng, W.; Herzog, F. Injection molding of polypropylene: X-ray investigation of the skin-core morphology. *J. Appl. Polym. Sci.* **1993**, *50*, 2163.
- (34) Pennings, A. J.; van der Mark, J. M. A. A.; Booij, H. C. Hydrodynamically induced crystallization of polymers from solution. II. The effect of secondary flow. *Kolloid Z. Z. Polym.* **1970**, *236*, 99.
- (35) Moore, E. P. *Polypropylene Handbook*; Hauser Publishers: Munich, 1996.
- (36) Endo, R.; Kanamoto, T. Superdrawing of polytetrafluoroethylene virgin powder above the static melting temperature. *J. Polym. Sci., Polym. Phys. Ed.* **2001**, *39*, 1995.
- (37) Mandelkern, L. *Crystallization and Melting*; Booth, C. and Price, C., Ed.; Pergamon Press: Oxford, 1989; Vol. 2, pp 363.
- (38) Varga, J. Supermolecular structure of isotactic polypropylene. *J. Mat. Sci.* **1992**, *27*, 2557.
- (39) Gedde, U. W. *Polymer Physics*; Chapman & Hall: London, 1995.
- (40) Schönherr, H.; Vancso, G. J. The mechanism of PTFE and PE friction deposition: a combined SEM and STM study on highly oriented, polymeric sliders. *Polymer* **1998**, *39*, 5705.
- (41) Wunderlich, B. *Macromolecular Physics*; Academic Press: New York, 1973; Vol. 1.
- (42) Wu, C.-M.; Chen, M.; Karger-Kocsis, J. Transcrystallization in syndiotactic polypropylene induced by high-modulus carbon fibers. *Polym. Bull.* **1998**, *41*, 239.
- (43) Ratzsch, M. Special PPs for a developing and future market. *J. Macromol. Sci.-Pure Appl. Chem.* **1999**, *A36*, 1587.
- (44) Bartczak, Z.; Galeski, A.; Argon, A. S.; Cohen, R. E. On the plastic deformation of the amorphous component in semi-crystalline polymers. *Polymer* **1996**, *37*, 2113.
- (45) Avella, M.; Dell'Erba, R.; Martuscelli, E.; Ragosta, G. Influence of molecular weight, thermal treatment and nucleating agent on structure and fracture toughness of isotactic polypropylene. *Polymer* **1993**, *34*, 2951.
- (46) Kennedy, M. A.; Peacock, A. J.; Mandelkern, L. Tensile properties of crystalline polymers - linear polyethylene. *Macromolecules* **1994**, *27*, 5297.

- (47) Bezerédi, Á.; Vörös, G.; Pukánszky, B. Mechanical damping in instrumented impact testing. *J. Mat. Sci.* **1997**, *32*, 6601.
- (48) Popli, R.; Mandelkern, L. Influence of structural and morphological factors on the mechanical properties of the polyethylenes. *J. Polym. Sci., Polym. Phys.* **1987**, *25*, 441.
- (49) For a more elaborate study on the effect of nucleating agents on the mechanical properties we refer to chapter 5 in this thesis.
- (50) Bartczak, Z.; Galeski, A. Yield and plastic resistance of  $\alpha$ -crystals of isotactic polypropylene. *Polymer* **1999**, *40*, 3677.
- (51) Brooks, N. W.; Ghazali, M.; Duckett, R. A.; Unwin, A. P.; Ward, I. M. Effects of morphology on the yield stress of polyethylene. *Polymer* **1999**, *40*, 821.
- (52) Hertzberg, R. W.; Manson, J. A. *Fracture and Fatigue*; 2 ed.; Kroschwitz, J. I., Mark, H. F., Bikales, N. M., Overberger, C. G. and Menges, G., Ed.; John Wiley & Sons, Ltd: New York, 1986; Vol. 7, pp 328.
- (53) The study of deformation mechanisms is not one of the subjects of this thesis, therefore we give only suggestions for possible deformation mechanisms. A more elaborate study is necessary to be conclusive about the explanations proposed.
- (54) Karger-Kocsis, J. Towards understanding the morphology-related crack initiation and propagation behavior in polypropylene systems as assessed by the essential work of fracture approach. *J. Macromol. Sci.-Phys.* **1999**, *B38*, 635.
- (55) Kim, G.-M.; Michler, G. H. Micromechanical deformation processes in toughened and particle-filled semicrystalline polymers: Part1. Characterization of processes in dependence on phase morphology. *Polymer* **1998**, *39*, 5689.
- (56) Pukánszky, B. *Microstructural aspects of fracture in polypropylene and its filled chopped fiber and fiber mat reinforced composites; in Polypropylene: Structure, Blends and Composites*, Karger-Kocsis, J., Ed.; Chapman and Hall: London, 1995; Vol. 3.
- (57) Bartczak, Z.; Argon, A. S.; Cohen, R. E.; Weinberg, M. Toughness mechanisms in semi-crystalline polymer blends: II. High-density polyethylene toughened with calcium carbonate filler particles. *Polymer* **1999**, *40*, 2347.
- (58) Paul, D. R.; Bucknall, C. B. *Polymer Blends*; John Wiley & Sons: New York, 2000; Vol. Volume 2: Performance.
- (59) ASTM-standard Standard test methods for impact resistance of plastics and electrical insulating materials. *ASTM Committee on Standards* **1992**, *ASTM; D256-90b*.

# Chapter 7

## **Specimens with controlled thermo-rheological history for mechanical tests: Design and testing of a dedicated compression mold**

Accurate structure property studies of polymers necessitate the use of samples with well defined and well characterized molecular characteristics and a reproducible, well controlled thermo-rheological history of the specimens used. For studies of microstructure, thermal properties, and crystallization, characteristic specimen sizes needed can be as small as several tens of milligrams. However, for mechanical studies, e.g. for impact test, standard specimen size significantly exceeds these limits. Hence, there is need to prepare isothermally crystallized samples with large enough sizes and compare these materials processed by practice, such as injection molding.

In this chapter we discuss new possibilities to achieve the goal of producing well defined samples of sufficient size. For that purpose we designed a compression mold with which homogeneous samples could be made isothermally. Samples made with this mold were compared with injection molded specimens of polypropylene. It was shown that the process induced morphology for the injection molded samples exert a pronounced influence on the mechanical properties. Herewith we demonstrate the need for well defined samples in structure-property relationship studies and providing the basic requirements for future research.

---



## 7.1 Introduction

Numerous studies were carried out concerning structure-property relationships in polypropylenes, however often contradictory conclusions were reached [1,2]. Attempts were made to identify the most important features of the crystalline structure and their effects on the mechanical properties. For accurate structure property studies of polymers the use of samples with well defined and well characterized molecular characteristics is needed and specimens used must possess a reproducible, well controlled thermo-rheological history. Semi-crystalline polymer samples crystallized under isothermal conditions serve as model materials. Ultimately though one must be able to understand and predict structure property-function relationships for such model systems as well as for polymers obtained by processing under industrial relevant (“realistic”) processing conditions. Ill-defined thermal rheological history often obscures structure-property relationships of samples made by using conventional processing techniques.

Ideally, in order to establish rigorous structure-property relationships, the influence of processing-induced morphology and properties must be minimized. In order to extract information about the influence of process induced mechanical properties of the polymer, samples should be made:

- which are free from mechanical stresses and orientation;
- which are crystallized isothermally,

and compared with specimens prepared via conventional process methods.

To meet these requirements a device, or method of processing, is needed with which it is possible to produce such samples. Corresponding specimens must have thicknesses comparable to samples produced with conventional methods in order to map the influence of process induced structures on the mechanical properties. Sample size is of importance for the analysis of morphology, as well. Often the morphology is studied within a small section of the processed bar for which the mechanical properties are tested. Methods, like differential scanning calorimetry, x-ray scattering methods, and scanning probe and electron microscopy techniques use a very limited amount of sample. Information subtracted from such sections of limited size is often extrapolated to the whole specimen under the simplified assumption of uniformity and homogeneity of the sample’s morphology.

In this chapter, we report on a newly designed device that is able to produce samples that do not exhibit structural orientation texture. A section is included in which the validation of the design is discussed. At the end of the chapter some representative results are given which clearly show the influence of the processing induced properties. The chapter aims at providing a new approach for studying structure-property relationships.

## 7.2 Design of a dedicated compression mold

### 7.2.1 Introduction

Compression molding is a promising method to make samples under isothermal crystallization conditions which are free from mechanical stresses and orientation. However, with conventional, commercially available compression molds it is not possible to achieve completely these requirements. During a conventional compression operation, the polymer flows, introducing orientation. Moreover, isothermal crystallization is difficult, if not impossible, to reach. Thus, in order to fully satisfy the requirements defined, it is decided to design a novel compression mold equipped with some non-conventional features.

### 7.2.2 Design

#### Schematic drawing of the compression mold

Figure 7.1 shows the schematic of the compression mold. The system consists of two hollow cylinders with rubber seals on the inner sides. The two cylinders fit into an outer circular ring. The polymer is placed in the cavity confined by the two cylinders and by the outer ring. Heating of the mold occurs by heating the plates of an external press used (Fortune Holland, maximum load 450 kN), which is also used to pressurize the polymer. The polymer (and mold) is cooled by circulating a coolant through the hollow cylinders by a high temperature rotary pump. Isothermal crystallization, as one of the requirements, needs fast and accurate cooling. The cooling of the mold is thus one of the main design parameters.

A small gap is present between the insert and outer ring (see the parts assigned by 1 and 2 in Figure 7.1, respectively). When the mold is compressed, the molten polymer will flow into the gap and out of the mold. This flow can lead to material orientation in the direction of flow. The problem of flow can be avoided by using rubber seals (e.g., silicone) or Teflon placed in the gap.

The surface of the relative thick specimens used will be pulled towards the center of the sample during cooling due to the volume shrinkage in cooling process. Generally, shrinkage is caused by the initial polymer temperature, compressive properties (pressure-volume-temperature relations), and crystallinity. Shrinkage should be reduced to minimum possible, because the resulting internal stresses can be of sufficient magnitude to initiate crazes and thus introduce weak internal points in the specimens. Shrinkage can be reduced by using a suitable pressure program corresponding to the PVT diagram of the polymer and uniform cooling. Another way of reducing the consequence of shrinkage upon crystallization is the use of nucleating agents. Due to the high nucleation density spherulite size decreases significantly and the polymer crystallizes more homogeneously, resulting

in reduced internal stress points.

All molds contain air that must be removed or displaced as the mold is being filled with material. The compressed air in the mold is the cause of gas of marks and voids. In addition the entrapped air, volatile components that may come off the product during heating may give a small but significant production of gasses. The entrapped air and volatiles can be removed by applying a vacuum. The vacuum line is shown in Figure 7.1. Upon melting and pressurizing the vent line can be sealed by a screw.

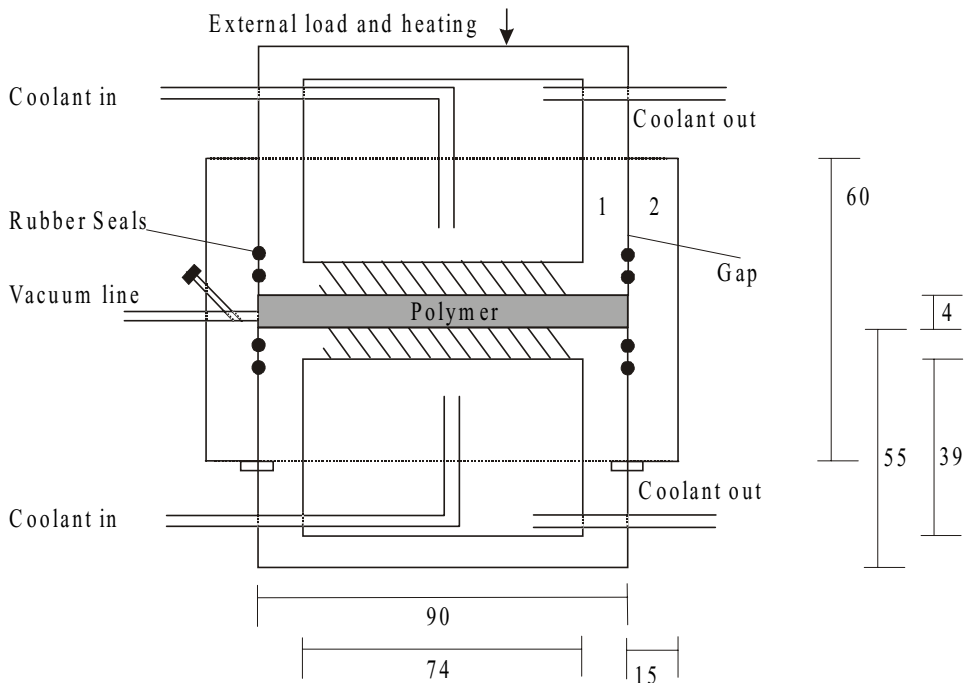


Figure 7.1. Schematic drawing of the compression mold. The dimensions are given in millimeters.

As we will see later, with this newly designed compression mold it is possible to make homogeneous samples without flow induced structures. As mentioned above, an important design variable is the cooling of the mold. The temperature must be accurate and quickly changeable to meet the requirement of isothermal crystallization. To quantify the time of cooling, calculations were performed. The following paragraphs give the outline and results.

### Cooling time: calculation for isothermal crystallization

Fast heat removal is essential in order to cool down the polymer from melt temperature to crystallization temperature prior to the onset of crystallization. Ideally, the temperature of crystallization is set instantaneously for isothermal crystallization. Practically, however, isothermal crystallization may be assumed when the temperature of the melt reaches the crystallization temperature before crystallization (nucleation) starts. The time to reach the crystallization temperature (prior to crystallization) is defined as the critical time ( $t_{crit}$ ). This time can be determined by differential scanning calorimetry (DSC), see paragraph 7.4.2.

Cooling of the polymer in this design is accomplished by conductive heat transfer through the polymer and thereafter by conduction through the mold (steel) which is surrounded by mold coolant, see Figure 7.2. The temperature profile and the change thereof in the mold-wall and polymer is a function of both the thermal properties of the mold and polymer and time. The problem can be approximated by a one-dimensional transient heat-transfer problem. The mathematical analysis of this problem in given is the appendix.

The solution of this heat-transfer problem was obtained numerically. Figure 7.3 shows the temperature profiles as functions of time and distance from the two outer sides of center of polymer to the outer surface of steel.

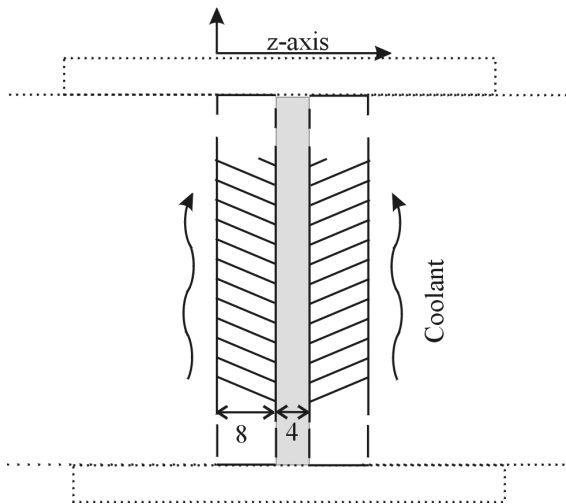


Figure 7.2. Schematic drawing of a part of the mold (see Figure 7.1). Indicated in the figure is the geometry used for the calculation of the cooling profile. Thickness values are given in millimeters. Note that the geometry is turned 90° clockwise in the plane of drawing as compared with the schematic drawing in Figure 7.1.

From the calculated temperature profiles shown in Figure 7.3, it is clear that it takes  $\pm 70$  s for the inner side of the steel (polymer side at 0.008 and 0.012 m) to cool

down from 220 °C to  $100 \pm 5$  °C. During this time, the polymer is cooled from 220 °C to  $110 \pm 5$  °C. The center of the polymer plate reaches the crystallization temperature ( $T_c = 100 \pm 2$  °C) after approximately 130 s.

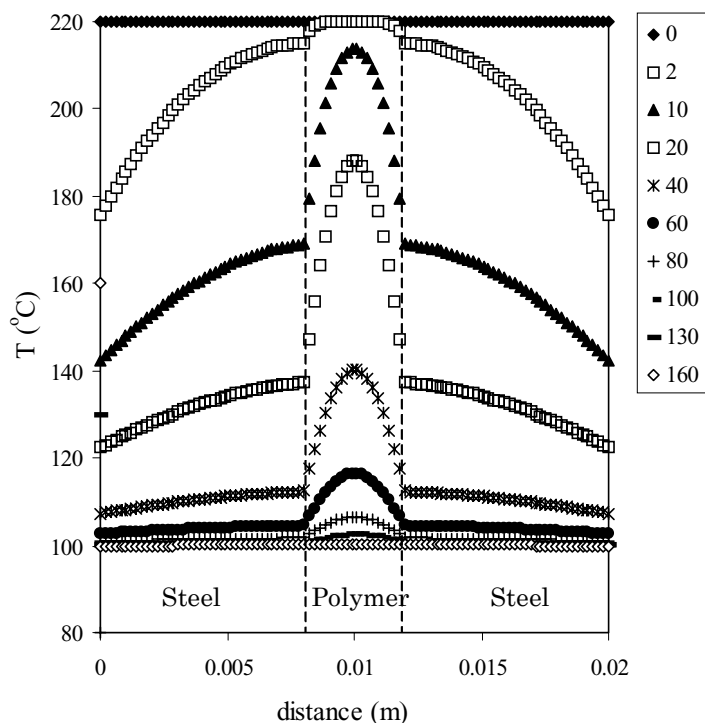


Figure 7.3. Temperature profile in the mold and polymer melt as a function of time. The times for the different profiles in the figure are assigned in the legend (unit is second).

## 7.3 Experimental

Using a Berstorff (ZE 25×33D) twin screw extruder, isotactic polypropylene (iPP) ( $\bar{M}_w = 3.0 \times 10^5$  g/mol,  $\bar{M}_n = 7.7 \times 10^5$  g/mol) (DSM, The Netherlands) was blended with an  $\alpha$ -nucleant (Irgaclear) and a  $\beta$ -nucleant in separate experiments (the  $\beta$ -nucleant was the calcium salt of suberic acid [3], kindly supplied by Prof. J. Varga). In addition to the presence of the nucleating agent the blend contained 0.1 wt% antioxidant (Irganox). The barrel temperature was set to 190 °C and the screw speed was 140 rpm. The length-diameter ratio of the screws was 33 ( $l/d = 33$ ), with a diameter  $d = 25$  mm. The concentration of the nucleating agents was set at 1 wt%. The polymer melt was cooled in a water bath, subsequently granulated and dried overnight in a vacuum oven at 40 °C. For compression molding the granules were pulverized on a Fritsch pulversette using liquid nitrogen.

Rectangular bars ( $80 \times 10 \times 4$  mm<sup>3</sup>) were injection molded on a 221-55-250 Arburg Allrounder injection molding machine. The barrel had a flat temperature profile of

205 °C, and the mould temperature was set to 100 °C. Injection and holding pressures were 70 and 30 bars, respectively. This very high mould temperature was used in order to obtain a high percentage of  $\beta$ -phase in the injection molded samples. Holding time and cooling time during injection molding were set at 80 s being enough to let the material solidify for proper mold-release. This time was determined by trial and error.

Circular plaques were compression molded using the newly designed compression mold. In a typical experiment the compression mold, filled with pulverized granules, was heated up to 220 °C in a Fortune Holland compression press. Vacuum was applied during heating, removing liberated volatiles and entrapped air. The mold was pressurized up to 230 bar and the vacuum line was closed. After 5 min the cooling was activated. At a predetermined time the mold was cooled to room temperature. The circular plaques were processed into rectangular bars (80×10×4 mm<sup>3</sup>) for mechanical tests. The bars were polished for a smooth surface finish.

Tensile yield stress and modulus values were measured by a Zwick 1445 tensile testing apparatus at 50 mm/min cross-head speed. Charpy impact tests were performed according to ASTM D256-90b. For these measurements a single-edge V-shaped notch of 2 mm depth and tip radius 0.25 mm was milled in the molded specimens.

Crystallization was studied by Differential Scanning Calometry (DSC). The DSC setup (A Perkin-Elmer calorimeter Pyris 1) was calibrated using gallium and indium before use. The sample chamber was kept under a constant flux of nitrogen. All samples were melted for 5 min at 220 °C, and subsequently cooled to the desired crystallization temperature with a pre-set cooling rate.

Number average and weight average molar masses ( $\overline{M}_n$  and  $\overline{M}_w$ ) and polydispersity index values of the molar mass distribution ( $\overline{M}_w / \overline{M}_n$ ) were determined with gel permeation chromatography (GPC) measurements using a Walters-GPC equipped with differential refractometer (Walter model 410) detection system. Before the measurements, the samples were dissolved in trichlorobenzene (TCB) and stabilized with 0.1wt% 2,6-di-tert.-butyl-4-methylphenol 99% (Aldrich).

The fraction  $\beta$ -phase of the samples was determined using wide angle x-ray scattering (WAXS). WAXS experiments were performed on a Philips (XPert-1) using Ni-filtered Cu(K $\alpha$ ) radiation. WAXS traces were taken in the scattering angle range  $2\theta = 5^\circ \dots 35^\circ$ . The relative  $\beta$ -content ( $K$ ) was determined by the method of Turner-Jones *et al.* [4]. The parameter  $K$  is determined by the ratio between the intensity  $I_\beta$  of the peak for the (300) diffracting plane and the sum of the intensities  $I_{\alpha 1}$ ,  $I_{\alpha 2}$ , and  $I_{\alpha 3}$ , of the (110), (040), and (130) planes, respectively, as well as  $I_\beta$  of the (300) peak:

$$K = \frac{I_{\beta}}{I_{\alpha 1} + I_{\alpha 2} + I_{\alpha 3} + I_{\alpha 4}} \quad (7.1)$$

In this study anisotropy was characterized by Fourier transform infrared dichroism (FTIR-D). Specimens for FTIR-D were prepared by sawing small strips ( $\approx 0.5$  mm thick) from regions of interest from the injection molded or compression molded bar, see Figure 7.4. The thickness of the sections was decreased by a water cooled abrasion machine. The samples were mounted in a sample holder with micrometer positioner. The holder was placed in a BIO-RAD (model FTS575C) infrared spectrometer equipped with a infrared microscope. A rotatable infrared polarizer was added to enable measurements of dichroic ratios. Infrared spectra were collected in transmission with the beam polarization aligned both parallel and perpendicular to the radial direction on the sample. After collecting each spectrum the sample was moved  $250 \mu\text{m}$  in the x-axis direction; 1024 scans at a resolution of  $4 \text{ cm}^{-1}$  were averaged and a liquid nitrogen-cooled cryogenic mercury cadmium telluride (MCT) detector was used. The dichroic ratios (D's) were calculated at two perpendicular IR-bands ( $1045$  and  $841 \text{ cm}^{-1}$ ) and two orthogonal IR-bands ( $898$  and  $809 \text{ cm}^{-1}$ ) (see chapter 2). The dichroic ratio (D) is defined as:

$$D = \frac{A_{\perp}}{A_{\parallel}}, \quad (7.2)$$

where  $A_{\perp}$  and  $A_{\parallel}$  are the absorbances of the IR band under consideration when the electric field vectors are perpendicular and parallel to z-axis, respectively. The thickness of the sample (in direction of y-axis) is assumed small enough for an uniaxial texture.

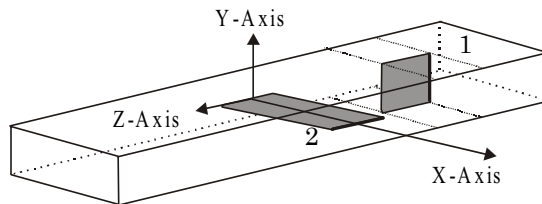


Figure 7.4. Position of specimens cut for FTIR-D from a 1) compression or 2) injection molded bar.

## 7.4 Results and Discussion

### 7.4.1 Introduction

The paragraph Results and Discussion involves two main parts. The first part discusses the validation of the mold design. Successively, orientation and cooling will be discussed. Next we want to give a short example of the possibilities of the newly designed mold. We want to emphasize that the given example is used for showing the potential of this mold, therefore no discussion will follow about the results obtained.

### 7.4.2 Validation of mold design

We correlated the numerically obtained solution of the ideal temperature drop in the center of the polymer slab with a real experiment. For this we molded a thermocouple in the center of the polymer and measured the temperature as a function of time upon cooling the mold from 220°C to 100°C. The latter temperature was taken the same as the mold-temperature used in the injection-molded operations (see section Experimental).

Figure 7.5 shows the result of the calculated temperature from the middle of the polymer slab (see Figure 7.3) and the experimentally obtained temperature, both as function of time. From Figure 7.5 we see that the experimental temperature profile does not overlap with the numerically obtained temperature profile. Instead a cooling rate of 10 °C/min was obtained. The main reason is that at the moment of writing, unfortunately, the pump capacity to meet the calculated cooling rate was not available. As a consequence the cooling of the mold was significantly slower than required. The calculated temperature drop is determined under ideal circumstances, i.e. in the calculation we assumed negligible contact resistance between the coolant and mold, a constant temperature of the coolant (see appendix). The calculated profile can thus be considered as a limiting case for the maximum obtainable cooling rate. It is expected that the experimental cooling profile will approach the calculated ideal profile with the right pump capacity.

DSC experiments were performed in order to determine the onset of crystallization ( $t_{\text{crit}}$ ) and the time to complete the crystallization ( $t_{\text{end}}$ ). In the DSC experiments the calculated cooling rate (obtained from the calculated cooling profile) and a cooling rate of 10 °C/min (obtained from the measured cooling profile) was used. The times,  $t_{\text{crit}}$  and  $t_{\text{end}}$  for both cooling rates are indicated (taken from the DSC-trace indicated in Figure 7.5, as well). In the calculated experiment the onset of crystallization starts at  $t_{\text{crit}} = 70$  s and the end of the crystallization occurred at  $t_{\text{end}} = 170$  s. For the experiment with a measured cooling rate of 10 °C/min the onset of crystallization starts at  $t_{\text{crit}} = 570$  s and the crystallization is completed at  $t_{\text{end}} = 700$  s. As can be seen, in both cases crystallization takes place in



approximately the same temperature range 100-105 °C.

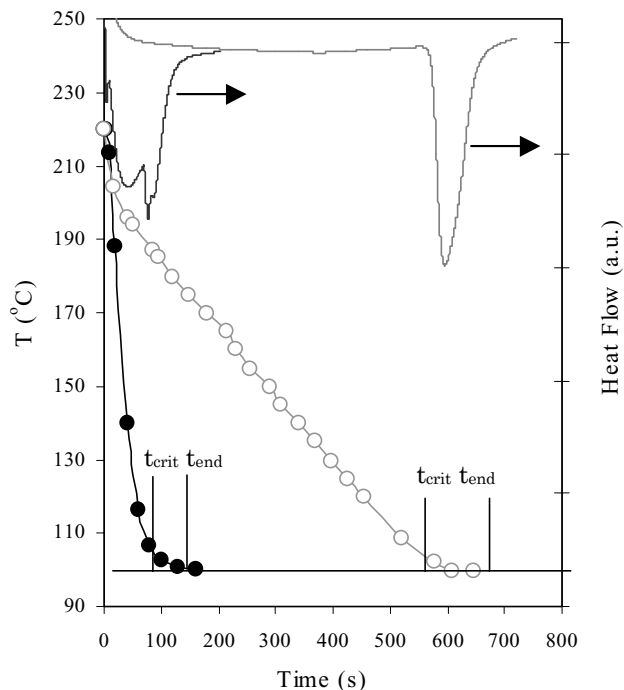


Figure 7.5. The course of temperature in the middle of the polymer sample as function of cooling time. Solid symbols (●) are (idealized) calculated values, taken from Figure 7.3. Open symbols (○) correspond to measured data.

Infrared dichroism was used to obtain information about the molecular orientation in the crystalline and amorphous regions of the material. The dichroic ratio (D) was measured at the four absorption bands, as described in the section Experimental. Figure 7.6a/b show the values of D measured through a cross-section of an injection and compression molded specimen. It can be seen that the injection molded specimen exhibits a strong morphological anisotropy (Figure 7.6a). The results show that the dichroic ratios for the perpendicular bands (see section Experimental) exhibit the opposite trend. It is also clear that the orientation is the highest near the surface of the specimen. With increasing distance to the center of the specimen the overall orientation decreases describing a complex profile which is caused by the flow and non-isothermal crystallization during the injection molding operation. The compression molded sample shows virtually no orientation (see Figure 7.6b). The compression molded sample, as required, is completely homogeneous.

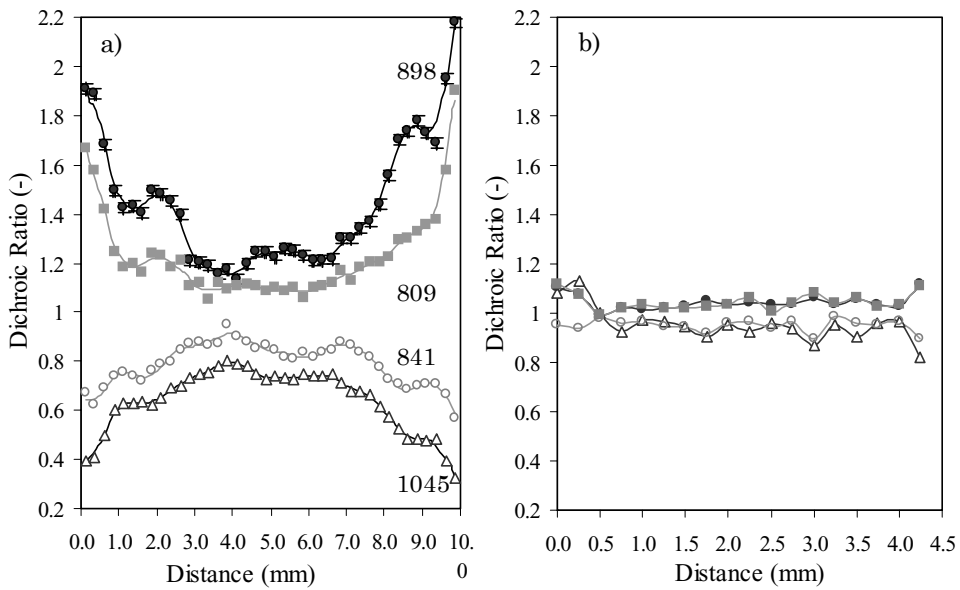


Figure 7.6. Dichroitic ratios ( $D$ 's) obtained from IR dichroism for several IR-bands. Figures a) and b) show representative samples of injection molded specimens and compression molded samples respectively.

In this section we demonstrated that it was possible to produce samples approximately at the desired temperature. IR-dichroic measurements demonstrated that the anisotropy of injection molded samples, made at the same temperature as the compression molded samples, showed a large anisotropy. In the following paragraph we will compare the mechanical properties (E-modulus and Izod impact properties) of the injection and compression molded samples.

### 7.4.3 Mechanical Properties

Samples with both  $\alpha$ -, and  $\beta$ -nucleants were used. The nucleants were used to reduce the effect of spherulite boundaries in fracture. It is known that the spherulite size significantly influences the macroscopic properties. Especially, when the spherulite size is large due to slow cooling, interspherulitic fracture readily occurs. Nucleating agents decrease the size of the spherulites considerably. Therefore, we assume that in nucleated PP samples prepared under non-isothermal conditions, inter-spherulitic boundary failure is not of primary importance. A  $\beta$ -nucleant is used in order to obtain a material with a high  $\beta$ -content, which allows us to compare the difference in toughness of the  $\beta$ -phase with the  $\alpha$ -phase. Figure 7.7 shows the WAXS traces for  $\beta$ -nucleated injection [5] and compression molded samples, respectively. The characteristic peaks at  $2\theta = 16.2^\circ$  ( $300$ ) $_{\beta}$  and  $2\theta = 21^\circ$  ( $311$ ) $_{\beta}$ , can clearly be seen. For the compression molded and injection molded samples [5] we found values for  $K = 0.92$  and  $0.87$ , respectively (for a definition of  $K$  see section Experimental). Figure 7.7 clearly shows for both the injection and

compression molded samples a high  $\beta$ -phase content. It also indicates that the amount of the  $\beta$ -phase is approximately the same for both processing methods.

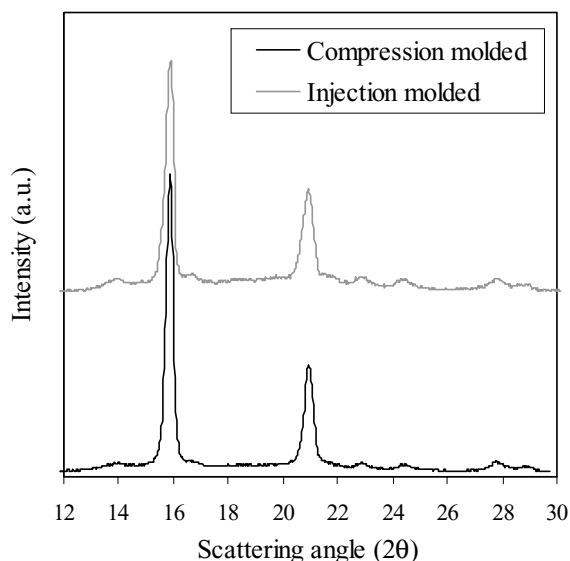


Figure 7.7. WAXS traces for the  $\beta$ -nucleated injection and compression molded samples, respectively. The curves are shifted on the y-axis for clarity.

The mechanical properties (E-modulus and impact properties) were measured for the injection- and compression molded samples for both  $\beta$ -nucleated and  $\alpha$ -nucleated cases, see Figure 7.8.

From the Figure it can be seen that the moduli of the injection molded samples are significantly higher as compared with the compression molded samples [6]. The E-modulus of the  $\beta$ -nucleated samples show a lower modulus than the  $\alpha$ -nucleated samples. Figure 7.8b shows that the compression-molded samples possess a lower toughness compared with the injection molded samples [6]. As can be seen the  $\beta$ -nucleated samples exhibit higher values for the impact energy for the compression and injection molded samples.

The results clearly show that the injection molded samples have a better mechanical performance as compared to the compression-molded samples. The main difference in morphology of these samples is the chain orientation in the crystalline and amorphous phases, respectively in the injection molded specimens. The orientation coincides with the test direction and will enhance the mechanical properties in the corresponding direction. The presence of the processing induces morphologies determine to a large extent the mechanical properties.

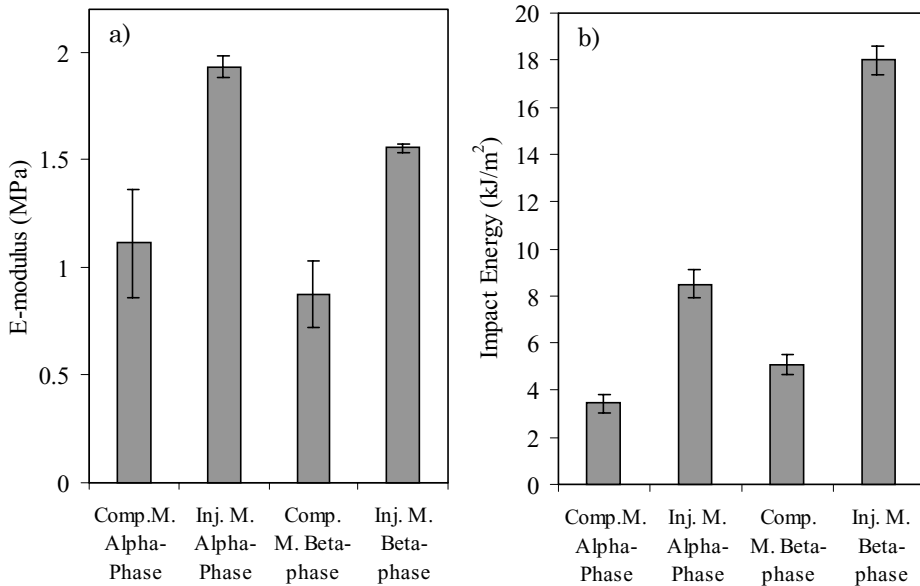


Figure 7.8. Comparison of the E-modulus and impact energy for the compression (Comp. M.) and injection molded (Inj. M.) specimens, for samples exhibiting  $\alpha$ - and  $\beta$ -phase, separately.

## 7.5 Conclusions

The aim mentioned in the beginning of this chapter was to make homogeneous, isothermally crystallized samples. The background for the need of such samples is given by the difficulties separating the properties arising from the process induced structure from the homogeneous material properties. Moreover, it was clarified that analyses of samples which are highly anisotropic is difficult due to the distribution of properties over the sample.

Given the reasons above, we attempted to overcome these problems by designing a compression mold which is able to produce homogeneous samples under isothermal conditions. A numerical analysis of the cooling characteristics of the mold was given. Samples made by the mold were compared with injection molded specimens.

IR-dichroism was used to elucidate the strong anisotropy present in the injection molded samples, which contrasted with the absence of orientation in the compression molded samples. Preliminary results showed that the process induced orientation in the samples made by injection molding strongly influenced the mechanical properties. Herewith, we demonstrated the importance of the method of processing and the related morphology and providing the basic requirements for future research.

## 7.6 References

- (1) Moore, E. P. *Polypropylene Handbook*; Hauser Publishers: Munich, 1996.
- (2) Karger-Kocsis, J. *Polypropylene: An A-Z Reference*; Kluwer Academic Publishers: Dordrecht, 1999.
- (3) Varga, J.; Mudra, I.; Ehrenstein, G. W. A highly active thermally stable  $\beta$ -nucleating agent for isotactic polypropylene. *J. Appl. Polym. Sci.* **1999**, *74*, 2357.
- (4) Turner-Jones, A.; Aizlewood, J. M.; Beckett, D. R. Crystalline forms of isotactic polypropylene. *Makrom. Chem.* **1963**, *75*, 134.
- (5) The WAXS trace for the injection molded sample was taken from the core. This not necessarily mean that this measurement is representative for the whole specimen.
- (6) Several studies indicated that the molar mass of the polymer strongly influences the impact properties. Degradation effects, which may reduce the molar-mass of the polymer, may be different for the injection molded and compression molded processes. GPC results showed however no sign of changes in molar mass (distribution).
- (7) Uryanarayana, N. V. *Engineering Heat Transfer*; West Publishing Company: New York, 1995.
- (8) Sinnott, R. K. *Chemical Engineering Design*; Coulson, J. M. and Richardson, J. F., Ed.; Butterworth Heinemann: Oxford, 1999; Vol. 6.
- (9) Kamal, M. R.; Kenig, S. Cooling molded parts. *Society of Plastics Engineers* **1970**, *26*, 50.
- (10) Isayev, A. I. *Injection and Compression Molding Fundamentals*; Marcel Dekker, Inc: New York, 1987.
- (11) McCrum, N. G.; Buckley, C. P.; Bucknall, C. B. *Principles of Polymer Engineering*; Oxford University Press Inc.: New York, 1994.

## 7.7 Acknowledgements

The authors would like to thank ir. A. Ahuja for performing parts of the work and the useful discussions and ir. L. Vogelaar for the indispensable help with the numerical analysis of the heat transfer problem.

## 7.8 Appendix: Design Calculations

In this section calculations are presented which are required to determine the cooling rate, the cooling time, and pump capacity for cooling. The symbols and the values of the parameters used in the calculation are mentioned in Table 7.1. The analysis in paragraph 1.8.1 is taken from reference [7].

### 7.8.1 Detailed calculation of the cooling time for the part

#### Assumptions

The steel and the polymer blocks are solids and hence heat transfer takes place mainly by conduction. All material properties, the convective heat transfer coefficient,  $h_f$ , and the temperature of the surrounding fluid are constant. The coolant (a circulating fluid, at constant temperature  $T_f = 100$  °C) cools the steel, which in turn cools the polymer. There is no accumulation of energy at the interfaces (polymer/steel or steel/coolant). No heat transfer to the end surfaces of the cylinder was considered. This means that the heat flux at the surfaces parallel to the z-direction is zero. No internal energy generation and negligible radiative heat transfer were assumed. The last assumption is that the temperature variation in the direction perpendicular to the z-direction is negligible so that  $T = T(z)$ .

#### Analysis

The various equations involved in this system are summarized below:

1. Heat transfer by conduction through the polymer [7]:

$$\left( \rho C_p \frac{\partial T}{\partial t} \right)_p = \frac{1}{A_z} \frac{\partial}{\partial z} \left( k A_z \frac{\partial T}{\partial z} \right)_p + \frac{1}{A_z} q_i'' \frac{dA_s}{dz} + q''' \quad (7.3)$$

In the absence of heat transfer to the surfaces parallel to the z-direction, the term containing  $q_i''$  disappears and in case there is no internal energy generation, the term  $q''' = 0$ . For polymers the thermal conductivity is relatively independent of temperature, varying by less than 1% per degree Kelvin, and a reasonable approximation to equation (7.3) is given by:

$$\left( \rho C_p \frac{\partial T}{\partial t} \right)_p = \left( k \frac{\partial^2 T}{\partial z^2} \right)_p \quad (7.4)$$

2. Next, heat transfer by conduction occurs in the steel [7]:

$$\left( \rho C_p \frac{\partial T}{\partial t} \right)_s = \frac{1}{A_z} \frac{\partial}{\partial z} \left( k A_z \frac{\partial T}{\partial z} \right)_s + \frac{1}{A_z} q_i'' \frac{dA_s}{dz} + q''' \quad (7.5)$$

With no heat transfer to the surfaces parallel to the z-direction, the term

containing  $q_i''$  drops out. Further, with no internal energy generation ( $q'' = 0$ ), a reasonable approximation to equation (7.5) is given by:

$$\left( \rho C_p \frac{\partial T}{\partial t} \right)_s = \left( k \frac{\partial^2 T}{\partial z^2} \right)_s \quad (7.6)$$

3. Convective heat transfer occurs at the coolant/steel interface. To account for this an energy balance is made at the interface that relates the energy input by conduction to the energy output by convection. Thus at any time for transport normal to the steel slab in the  $z$  direction is given by:

$$-k_s \left( \frac{\partial T}{\partial z} \right)_s = h_f (T_f - T_s) \quad (7.7)$$

### Initial and boundary conditions

To solve the above-mentioned equations, we need one initial condition and two boundary conditions.

Specified temperature:

The initial condition requires that we know the temperature distribution at some instant of time, i.e.

$$T(z, t_0) = T_0(z) = 220 \text{ }^\circ\text{C} \quad (7.8)$$

The boundary conditions for the temperatures are given below:

$$T(z_0, t) = T(z) \quad (7.9)$$

Convective boundary condition

At the interface the surface is exposed to a fluid, and heat transfer occurs between the surface and the adjacent fluid by convection. From energy balance on the surface the conductive heat flux to the surface from the interior of the solid must be equal to the convective heat flux from the surface to the surrounding fluid. That is,

$$\pm k A_z \frac{\partial T}{\partial z}(z_0, t) = h A_z [T(z_0, t) - T_\infty] \quad (7.10)$$

This equation can be recast as

$$\frac{\partial T}{\partial z}(z_0, t) \pm \frac{h}{k} [T(z_0, t) - T_\infty] = 0 \quad (7.11)$$

Positive sign if the outward normal to the surface is in the positive  $z$ -direction and negative sign if the outward normal is in the negative  $z$ -direction. Equation (7.11), in terms of steel and cooling fluid (see Figure 7.2), can be written as:

$$\text{At } z = z_s; -k_s \left( \frac{\partial T}{\partial z} \right)_s = h_f (T_f - T_s) \quad (7.12)$$

Matching heat flux and temperature.

In some cases, such as when the solid is made of two different materials or when one of the parameters in the differential equation is different in different parts of the solid body, the same differential equation cannot be used over the entire region. In such a case, solutions to each domain must be found separately. The two solutions should then satisfy certain conditions regarding the temperature and heat flux at the interface of the two domains.

As a surface cannot store energy, the heat flux at the interface must be the same whether the interface is considered as belonging to one domain or the other. Referring to Figure 7.2, polymer and steel are different materials and the solution to each domain of material must satisfy the continuity of heat flux at the interface. Denoting the location of the interface by  $z_p$ , the matching heat flux condition requires

$$k_p \left( \frac{dT_p}{dz} \right)_{z=z_p} = k_s \left( \frac{dT_s}{dz} \right)_{z=z_p} \quad (7.13)$$

The heat flux is continuous at the interface but the temperature, in general, is not. If two solids are brought together, at the interface there is contact resistance leading to discontinuity in temperature. In this analysis we assume negligible contact resistance as we have a very intimate contact between solid and polymer (the polymer has been molten). As a consequence we suppose continuity of temperature. With such an approximation, referring to Figure 7.1,

$$T_p(z = z_p) = T_s(z = z_p) . \quad (7.14)$$

## Numerical analysis

Equations (7.4) and (7.6) can be solve numerically with the boundary conditions as given by equations (7.8), (7.9), and (7.12), respectively. A commercially available software package MatLab was used. The result of the numerical analysis is given in Figure 7.3, which shows the temperature profile as function of time and distance.

### 7.8.2 Pump and Coolant

The total amount of heat to be removed during cooling is equal to the sum of the amount of heat which should be removed from the steel and the polymer. Hence, the total amount of heat that should be removed is given by:

$$Q_{total} = (V\rho c_p \Delta T)_s + (m\Delta h)_p \quad (7.15)$$

For the polymer, the amount of heat can be calculated from the specific



enthalpy needed for crystallization and cooling. Substituting the values mentioned in Table 7.1 in (7.15), the total amount of heat to be removed is:  $Q_{total} = 140$  kJ.

The flow rate of the coolant can be calculated by the expression given below:

$$\frac{Q_{total}}{t_{cool}} = \Psi c_p (T_m - T_c) \quad (7.16)$$

Assuming a linear profile of specific heat capacity with temperature and an average value for the heat capacity of the coolant, the mass flow rate of the coolant can be calculated by substituting the values of the mentioned variables into equation (7.16). The total time for cooling is determined in paragraph 7.2.2.1). The result is  $\psi = 0.005$  kg/s = 18 kg/hr. As the density of the oil = 860 kg/m<sup>3</sup>, we calculate for the volumetric flow rate of oil 0.021 m<sup>3</sup>/hr. The selection of pumps is based on the normal operating range [8]. With volumetric flow rate of 0.021 m<sup>3</sup>/hr, either diaphragm or rotary gear type pump can be selected. For high temperature applications rotary pumps are used and hence is selected for this research.

## Symbols and data

In Table 7.1 the values of various parameters are listed. These values are taken from references [9,10] and [11].

Parameter	Name	Value (steel)	Value (polymer)
$A_z$	area perpendicular to the z-direction		
$A_s$	surface area exposed to the heat flux $q''_i$		
$q''_i$	internal heat flux		
$q''$	rate of internal energy generation		
T	temperature		
k	thermal conductivity	21 W/m K	0.21 W/m K
$\rho$	density	7688 kg/m <sup>3</sup>	900 kg/m <sup>3</sup>
$c_p$	specific heat	0.46 kJ/kg K	2.10 kJ/kg K
V	total volume of steel present in the mold	$3.64 \times 10^{-4}$ m <sup>3</sup>	
$h_f$	heat transfer coefficient of coolant	2840 W/m <sup>2</sup> K	
$T_f$	temperature of coolant	100 °C	
$c_f$	specific heat capacity of the coolant	1.93 kJ/kg K	
$\psi$	mass flow rate of the coolant		0.005 kg/s
$\Delta T = T_m - T_c$	temperature difference		120 °C
$\Delta h$	enthalpy polymer		315 J/g [9]
m	weight of propylene per sample		35 g
$Q_{total}$	total amount of heat to be removed		140 kJ
$t_{cool}$	time required to cool the part		130 s

The subscript 's' refers to steel, 'p' to propylene, and 'z' to the z-direction as defined in Figure 7.2.

*Table 7.1. Values for the several constants used in the calculation of the cooling of the mold and polymer.*

# **Chapter 8**

## **Summary**



## Summary

This thesis is the result of a project initiated by the Dutch Polymer Institute (DPI)<sup>1</sup>. The general theme involves “molecular characterization and morphology development in polypropylene obtained by metallocene polymerization”. Throughout this investigation, the general theme was shaped and filled in by a variety of studies on structure-property relationships in polypropylene.

The main properties of concern were toughness, thermal properties, and structural orientation. The relationships between primary chain characteristics and morphological features, melting and crystallization and between morphology and mechanical characteristics were established on the various levels of the morphological hierarchy described in the introduction of this thesis, i.e. molecular characteristics (primary level), crystal structure (secondary level), lamellae (tertiary level), and crystal aggregates and texture (quaternary level). The levels of morphology were influenced in several ways, e.g. by changing the amount of regio/stereo defects, using copolymers, shear, and second phases. The following paragraphs give a more detailed summary of the results.

**Chapter 2** describes the basic structure of semi-crystalline materials and especially the morphology of isotactic polypropylene. The various levels of polymer morphology are treated successively: primary, secondary, tertiary, and quaternary levels. After the discussion of the morphology of isotactic polypropylene and the relationships with mechanical properties two sections discussed briefly the underlying theory concerning impact measurements and x-ray analysis.

**Chapter 3:** The crystallization characteristics and morphology of isotactic polypropylene concerning the  $\alpha$ -,  $\beta$ -, and  $\gamma$ -phases were studied for well-defined and fully characterized polymer samples with varying amounts of stereo- and regio-irregularities. The set of samples enabled us to study separately the influence of the type of defect on the parameters of interest. A combined defect fraction (CDF) was introduced to describe arbitrary samples with both a varying amount of stereo- and regio-defects. Crystal growth rates as measured by polarized light microscopy (LM) decrease linearly with the defect fraction and are much stronger influenced in samples exhibiting regio-defects as compared with stereo-defects. We found that the decreasing growth rate of the  $\beta$ -phase is higher than the  $\alpha$ -phase. We found a critical defect fraction, ( $X_{crit}$ ) for which the growth rates of the  $\alpha$ - and  $\beta$ -phase are equal. We found that the upper bifurcation temperature is lowered with increasing  $X$ . Shear induced crystallization of the samples was studied and compared with quiescent crystallization. The growth rates of the shear induced cylindrites were the same as the spherulitic growth rates. It was evidenced that due to the lowering of the upper bifurcation temperature no  $\beta$ -cylindrites could be formed above the

critical defect concentration ( $X_{\text{crit}}$ ). Analysis of the measurement data was made with the model of Sanchez and Eby. We found a good agreement for the samples with a variation in the number of stereo-defects, however a less satisfactory agreement was found for regio-defects. From the analysis it followed that regio-defects are more strongly discriminated against in the crystalline regions than are the stereo-defects. The excess free energy for incorporating a stereo-defect into the trigonal crystal lattice of the  $\beta$ -phase is lower as compared with the  $\alpha$ -phase, which results in a higher partitioning coefficient for the  $\beta$ -phase. We found from the analysis that the bulk free energy difference for the completely defect-free (homo) polymer mainly determines the differences in growth rate dependence on the defect fraction for the  $\alpha$ - and  $\beta$ -phases, respectively. The theory correctly predicts the earlier mentioned critical defect fraction for which the growth rates of the  $\alpha$ - and  $\beta$ -phases are equal. An extra factor, which decreases the growth rate, is related to the forced introduction of defects into the crystalline phase.

**Chapter 4** describes the relationships between the chain architecture of polypropylene and the fusion behavior. The melting characteristics of isotactic polypropylene concerning the  $\alpha$ -,  $\beta$ -, and  $\gamma$ -phases were studied for the same group of samples as mentioned in chapter 3. The melting point is significantly lowered by the introduction of defects in the polymer chain and is much stronger influenced by the occurrence of regio-defects than by the presence of stereo-defects. A similar melting point depression was found for all the three polymorphs ( $\alpha$ -,  $\beta$ -, or  $\gamma$ -phases) independent on the number and kind of defect, and no correlation was found to exist between the partitioning coefficient and the crystallization kinetics. The model of Sanchez and Eby for copolymer melting was used for the analysis of the melting point depression, and was found in good agreement for the samples with a variation in the number of stereo-defects, however a less satisfactory agreement was found for regio-defects. From the analysis it followed that regio-defects are more difficult to incorporate in the crystalline regions than are the stereo-defects. The excess free energy for incorporating a stereo-defect into the trigonal crystal lattice of  $\beta$ -phase is lower than in the  $\alpha$ -phase, which results in a higher partitioning coefficient for the  $\beta$ -phase.

The next chapter (**Chapter 5**) maps the correlation between crystalline morphology, i.e. the lamellar thickness and impact resistance of three different polypropylene homo- and copolymers, obtained by injection molding<sup>2</sup>. The crystalline morphology was varied using three different nucleating agents. Linear elastic fracture mechanics was applied for the description of fracture resistance. The results indicate that morphological characteristics strongly influence the

---

<sup>1</sup> Project number 120, initiated in 1999 by prof. G.J.Vancso.

<sup>2</sup> Meer, D. W. v. d.; Pukánszky, B.; Vancso, G. J., *J. Macromol. Sci.-Phys.* **2002**, *B41*, 1105.

mechanical performance of the polymers. According to Young's theory for yielding the resistance to crack initiation, represented by  $K_{Ic}$ , correlates with the thickness of the lamellae. This suggests that the onset for yield can be described by a dislocation mechanism. The total energy absorbed during impact,  $G_{Ic}$ , is a complex function of the morphology with no single identifiable morphological characteristic that dominates its value. The heterogeneous, dispersed morphology of the polypropylene block copolymer initiates an additional energy absorption mode compared to the homo-polymer and the random-copolymer.

**Chapter 6** describes structure-property relationships on the quaternary level of the morphological hierarchy. It is known that friction deposited polytetrafluoroethylene (PTFE) *layers* are able to nucleate and crystallize isotactic polypropylene (iPP). In order to investigate the influence of PTFE on the crystallization behavior of iPP in *bulk*, PTFE-particles of different sizes (500 and 7  $\mu\text{m}$ ) in various concentrations were blended with iPP and subsequently processed by injection molding. Shear during processing led, in the case of the blend with 'large' particles, to PTFE fibers. Charpy impact tests showed a large increase in the strain energy release rate ( $G_{Ic}$ ) for all PTFE nucleated samples. It was shown that this improvement in toughness was found to depend mainly on the concentration of PTFE, but less on the actual variation in PTFE-morphology. Measurements showed that the process-induced oriented iPP morphology dominates the mechanical properties for the injection-molded samples. The formation of the PTFE fibers in the blends induced, after melting and recrystallization, an unusual morphology consisting of oriented iPP lamellar crystals. In contrast to the frequently observed (trans) crystallization, in which lamellae are directed perpendicular to the fiber direction, we found a strong overall lamellar orientation *parallel* to the PTFE fiber direction.

**Chapter 7** can be considered as an outlook for further research. In this chapter a new approach to establish structure-property relationships is explored. The results in this chapter showed that based on a newly designed compression mold, it is possible to separate the influence of process induced structures on the (mechanical) properties. A comparison was made between the properties of samples made by the compression mold and samples made by injection molding. It was found that samples produced via compression molding showed negligible anisotropy in contrast to the injection-molded specimens. E-modulus and impact properties were measured for samples made with both techniques. It was shown that the processing induced morphology for the injection-molded samples exerts a pronounced influence on the mechanical properties. This illustrates the need for well-defined samples in structure-property relationship studies.

# Hoofdstuk 9

## Samenvatting



## Samenvatting

Dit proefschrift is het resultaat van een project geïnitieerd door het Dutch Polymer Institute (DPI). Het algemene thema is moleculaire karakterisering en ontwikkeling van polypropyleen structuren. In dit proefschrift heeft het algemene thema vorm gekregen door structuur-eigenschaps relaties in polypropyleen te bestuderen.

De belangrijkste eigenschappen waren slagvastheid, stijfheid, en thermische eigenschappen. De relaties tussen ketenkaracteristieken en structuurkenmerken, smelt gedrag en kristallisatie, en relaties tussen structuur en mechanische eigenschappen werden tot stand gebracht op de verschillende niveaus van de morfologische hiërarchie, zoals beschreven in de introductie van dit proefschrift.

De morfologische hiërarchie bestaat uit: de moleculaire karakteristieken (primair niveau), kristalstructuur (secondair niveau), laminaire structuur (tertiair niveau), en kristalaggregaten (quaternair niveau). De morfologische niveaus werden o.a. beïnvloed door het variëren van de hoeveelheid regio/stereo defecten, het gebruik van co-polymeren, deformatie, en de introductie van een tweede fase. De volgende paragrafen geven een gedetailleerde beschrijving van de resultaten per hoofdstuk.

**Hoofdstuk 2** beschrijft de structuur van semi-kristallijne materialen en in het bijzonder de morfologie van isotactisch-polypropyleen. Achtereenvolgens worden de primaire, secundaire, tertiaire en quaternaire niveaus beschreven. Na de discussie waarin de structuur van isotactisch-polypropyleen in relatie tot de mechanische eigenschappen werd behandeld, volgen twee paragrafen die kort de achterliggende theorie van slagvastheidsmetingen en röntgenstralingsmetingen beschrijven.

**Hoofdstuk 3.** Goed gedefinieerde en volledig gekarakteriseerde polymeer monsters, met een variërende hoeveelheid stereo- en regio-defecten, werden gebruikt voor een studie naar de kristallisatie en morfologie van isotactisch-polypropyleen ( $\alpha$ -,  $\beta$ -, en  $\gamma$ -fasen). Deze groep van monsters verschaftte ons de mogelijkheid om onafhankelijk de invloed van het type defect op de belangrijkste eigenschappen te bestuderen. Een gecalculerde defectfractie (CDF) werd geïntroduceerd om monsters met een willekeurige hoeveelheid stereo- en regio defectfractie te beschrijven. Kristalgroeisnelheden, zoals gemeten met lichtmicroscopie (LM), verminderden lineair met de hoeveelheid defecten. De groeisnelheden in monsters met alleen regiodefecten werden veel sterker beïnvloed dan in monsters met stereodefecten. De verandering in de groeisnelheid van de  $\beta$ -fase is groter in vergelijking met de  $\alpha$ -fase. We hebben een kritische defectfractie ( $X_{crit}$ ) gevonden waarbij de groeisnelheden van de  $\alpha$ - en  $\beta$ -fasen aan elkaar gelijk waren. We hebben ook ontdekt dat de bovenste overgangstemperatuur werd verlaagd met toenemende fractie aan defecten. De door afschuifspanning

geïnduceerde kristallisatie van de  $\beta$ -fase is bestudeerd en vergeleken met kristallisatie zonder afschuiving. De groeisnelheden van de door afschuiving geïnduceerde structuren bleken gelijk te zijn aan de normale spherulitsche groeisnelheden. Het is bewezen dat door het verlagen van de bovenste overgangstemperatuur geen  $\beta$ -cylindrieten gevormd kunnen worden boven de kritische defectfractie ( $X_{crit}$ ). De theorie van Sanchez en Eby is gebruikt om de meetgegevens te analyseren. Een goede overeenkomst tussen theorie en gemeten waarden werd gevonden voor monsters met een variatie in de hoeveelheid stereodefecten, een minder goede overeenkomst werd gevonden voor de monsters met regiodefecten. Uit de resultaten bleek dat de regiodefecten veel sterker worden geweerd uit de kristallijne fase dan de stereodefecten. De overtollige vrije energie om een stereodefect in te passen in een  $\beta$ -kristalrooster in vergelijking met een  $\alpha$ -kristal rooster is veel lager. Dit resulteert in een grotere verdelingscoëfficiënt voor defecten betreffende de  $\beta$ -fase. Uit de resultaten volgde dat het verschil in bulk vrije energie voor het complete defectvrije homopolymeer vooral het verschil in groeisnelheidsafhankelijkheid met het aantal defecten van de  $\alpha$ - en  $\beta$ -fase bepaalt. De theorie kon de eerder genoemde kritische defectfractie goed voorspellen. Een extra factor die de groeisnelheid verminderde is de geforceerde introductie van defecten in de kristallijne fase.

**Hoofdstuk 4** beschrijft de relaties tussen de ketenarchitectuur van polypropyleen en het smeltgedrag. De smeltkarakteristieken van isotactisch polypropyleen betreffende de  $\alpha$ -,  $\beta$ -, en  $\gamma$ -fasen zijn bestudeerd voor dezelfde monsters als in hoofdstuk 3. Door de aanwezigheid van defecten werd het smeltpunt sterk verlaagd. De smeltpunt daling was sterker voor de polymeren met regiodefecten. Voor alle drie polymorfen ( $\alpha$ -,  $\beta$ -, en  $\gamma$ -fasen) werd een vergelijkbare smeltpunt daling gevonden welke onafhankelijk was van de hoeveelheid en soort defecten. Er werd geen correlatie gevonden tussen de verdelingscoëfficiënt en de kristallisatiekinetiek. De smelttheorie voor copolymeren van Sanchez en Eby is gebruikt voor de analyse van de smeltpunt daling. De theorie toonde een goede overeenkomst met gemeten smeltpunt dalingen voor monsters met stereodefecten, echter een minder goede overeenkomst werd gevonden voor monsters met regiodefecten. Uit de meetresultaten volgt dat regiodefecten moeilijker in het kristalrooster zijn in te bouwen dan stereodefecten. De overtollige vrije energie om een stereodefect in te voegen in het trigonale kristalrooster van de  $\beta$ -fase is vergeleken met de  $\alpha$ -fase lager, wat resulteert in een grotere verdelingscoëfficiënt voor de  $\beta$ -fase.

**Hoofdstuk 5** beschrijft de correlaties tussen de kristallijne structuur (dikte van lamellen) en slagvastheid van spuitgegoten monsters bestaande uit drie verschillende polypropylenen (een homo- en twee co-polymeren). De morfologie van de kristallijne fase werd gevarieerd door gebruik te maken van verschillende kiemvormers. De theorie van de lineaire elastische breukmechanica is toegepast om



de breukresistentie te beschrijven. Uit de resultaten blijkt dat de morfologische karakteristieken de mechanische prestaties sterk beïnvloeden. Volgens de vloeitheorie van Young is de weerstand voor de breukinitiatie, weergegeven met  $K_{Ic}$ , gecorreleerd aan de dikte van de lamellen. De theorie suggereert dat het begin van de vloeï kan worden beschreven met een dislocatiemechanisme. De totale energie die wordt geabsorbeerd tijdens een slagproef,  $G_{Ic}$ , is een complexe functie van de morfologie en heeft geen eenduidige identificeerbare morfologische karakteristiek die de waarde domineert. De heterogene, gedispergeerde morfologie van het polypropyleen blokkopolymeer initieert, in vergelijking met het homopolymeer en random copolymeer, een extra manier van energie absorptie.

**Hoofdstuk 6** beschrijft structuur-eigenschaps relaties op het quaternaire niveau van de polymeerhiërarchie. Het is bekend dat *lagen* van polytetrafluoroethyleen (PTFE) die zijn aangebracht onder frictie, isotactisch polypropyleen (iPP) kunnen kiemen. Om de invloed van PTFE op het kristallisatiegedrag in de *bulk* te kunnen onderzoeken, zijn PTFE deeltjes met verschillende groottes (500 and 7  $\mu\text{m}$ ) in verschillende concentraties gemengd met iPP en vervolgens verwerkt via spuitgieten. Afschuifspanningen tijdens de verwerking waren de oorzaak, in het geval van ‘grote’ PTFE deeltjes, voor het ontstaan van PTFE vezels. Charpy slagvastheid proeven toonden voor alle PTFE gekiemde monsters een grotere toename in de rekenergie teruggaveratio ( $G_{Ic}$ ) aan. In dit hoofdstuk hebben we laten zien dat deze toename in slagvastheid vooral afhangt van de concentratie PTFE, en minder van de eigenlijke variatie in PTFE morfologie. De PTFE vezels in de mengsels met ‘grote’ deeltjes veroorzaakten, na smelten en herkristallisatie van de iPP matrix, een ongewone morfologie met georiënteerde lamellen die een gemiddelde oriëntatie *parallel* met de vezel hebben.

**Hoofdstuk 7** kan worden beschouwd als een aanbeveling voor verder onderzoek. In dit hoofdstuk werd een nieuwe benadering verkend om structuur-eigenschaps relaties te onderzoeken. De resultaten in dit hoofdstuk toonden aan dat het mogelijk is op basis van een nieuw ontworpen compressiepers de invloed van procesgeïnduceerde structuren op (mechanische) materiaal eigenschappen te bepalen. De eigenschappen van monsters gemaakt door middel van persen en spuitgieten zijn vergeleken. Wij vonden dat monsters die gemaakt waren met de compressiepers bijna geen anisotropie vertoonden in tegenstelling tot de spuitgegoten monsters. Voor de monsters, gemaakt via beide methoden, zijn de E-modulus en slagvastheid gemeten. We hebben aangetoond dat de procesgeïnduceerde morfologie een grote invloed uitoefent op de mechanische eigenschappen. Hiermee werd de behoefte aan goed gedefinieerde monsters in studies naar structuur-eigenschaps relaties geïllustreerd.

# Dankwoord

Voor u ligt een boekje met het beschreven resultaat van vier jaar werk. Alhoewel er slechts één auteur op de voorkant staat geschreven kan ik zeggen dat velen hebben bijgedragen tot de totstandkoming van dit proefschrift. Tijdens mijn promotie tijd waren er mensen die mij altijd hebben gesteund, omringt, en met interesse hebben gevolgd. Graag wil ik dan ook op deze plaats een ieder bedanken hiervoor. Het zal zeker zijn dat ik een aantal mensen vergeet die toch een plaats verdienen. Het ligt volledig aan mij dat dit niet is gebeurd. Mijn oprechte excuses.

Toronto, Canada, 1998, Tijdens een studiereis vroeg prof. dr. G. J. Vancso mij om te komen afstuderen bij de vakgroep MTP. Die vraag was het begin van een leuke en leerzame tijd, eerst als afstudeerder en later als promovendus. Julius, als persoon ben je vaak een bron van inspiratie geweest, en als hoogleraar heb je mij ook tijdens demotiverende tijden het inzicht kunnen geven om de mooie kanten van de wetenschap te zien. Bovendien, en zeker niet in het minst, zonder de hulp van jou was dit boekje niet geworden zoals het nu is! Ontzettend bedankt!

I was very fortunate to be able collaborate with Béla Pukánszky. It has been always a great pleasure and very educational talking to you. Ik wil graag Sanjay Rastogi bedanken dat hij mij de mogelijkheid heeft geboden om SAXS/WAXS metingen te doen in Grenoble. De inspirerende discussies maar ook de goede tijd (samen met Frank en Ankur) zal ik niet snel vergeten. The following people I like to thank for the scientific contributions to this thesis and the enjoyable discussions: M. Smithers (HR-SEM), V. Kogan (X-ray analysis), H. Koster (WAXS), G. van den Velde (NMR). I. Mingoze for the hospitality in Ferrara and polymer samples, A. Demain (Fina Research) for the fruitful collaboration.

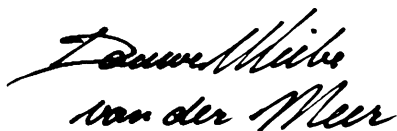
Geneviève, Karin, Gerda, Joyce, Lena (secretariaat). Jullie hebben mij soms veel ergernis en werk bespaard. In het speciaal Karin en Gen jullie waren zonder uitzondering bereid om te helpen! Ook wil ik Netty de Groot (CT-bib), L. Tiemersma (IMC), John and Zlata (Lab) voor hun bijdragen bedanken.

Clemens Padberg, als kamergenoot en zeer goede collega heb ik veel aan jou te danken. Altijd wou je me wel helpen en zonder jou zouden veel zaken niet zo soepel hebben gelopen. Maar ook de goede, grappige, leuke en alledaagse gesprekken waren altijd zeer aangenaam! Deze woorden gelden dan ook voor de andere kamer genoten (Beáta and Barbara). Thanks for standing me and thanks for the unforgettable time. During work but also besides work.

During the past four years I had the opportunity to supervise two students. Two completely different persons, Anil Ahuja and Daniel Milazzo. I'm glad that I have met you, I learnt a lot. Your contributions are part of chapter 6 and 7. Dan een paar andere personen. Laura, bedankt voor het programmeren en de goede vriendschap. Uiteindelijk ben je toch nog goed terecht gekomen (in de polymeren dan.....). Jason, afstuderen bij jou was voor mij een motivatie om te gaan promoveren, maar ook herinner ik mij de goede gesprekken, feestjes, en 'levenswijsheden'!

Working in an truly international research group was an unforgettable experience. From each of the persons of the 'group' I could tell long stories, but this would be undoable. All the borrols including eating pizza, Chinese food, etc, but also the 'groepsuitjes' and sailing trips are unforgettable. Mark (Doruve Ulube?) bedankt voor het kritisch bekijken van posters, papers, etc. Roughly in chronological order: Hans, Maria, Rob, Menno, Marçin, Dorina, Erik, Michel, Holger, Le, Beekie, Attila, Ewa, Wouter, Edgar, Igor, Nikodem, Shan, Willen-Jan, Renaud, Szczepan, Nina, Sasha, Chuanliang, Giorgio, Steffi, Henrik, Monique and Jing and all the people from the rest of the groups STEP / RBT / PBM (Ping-Pong, Triathlon, Gluhwein, Oliebollen). Many thanks for the good times!

Dan kom ik bij de twee paranimfen, Jon and Tiemen, die mij hebben geholpen met het prepareren van het proefschrift en mij kranig hebben gesteund tijdens mijn promotie. Heel veel bedankt voor de vele uurtjes nakijkwerk. Echter ik kan beter in dit respect de vele (feest) uurtjes en goede gesprekken buiten het werk noemen, daarbij denkende aan lekkere whisky, wodka en Grolsch...De tijd naast het werk werd zeker ook gedeeld met vele andere vrienden! Het plezier en de steun was en is onvervangbaar. Natuurlijk wil ik niet voorbijgaan aan mijn familie die voor mij persoonlijk in deze vier jaar veel heeft betekend. Als laatste wil ik ook mijn liefste Bea noemen. Alhoewel woorden niet toerijkend zijn wil ik je op deze plaats in het bijzonder bedanken voor de steun en wijze raad.

A handwritten signature in black ink, reading 'DouweWiebe van der Meer'. The signature is written in a cursive, flowing style with some capitalization.

DouweWiebe van der Meer

# Curriculum vitae

DouweWiebe van der Meer was born on July 14, 1975 in Sneek, The Netherlands. He passed his secondary education exam (VWO) at the Nassau College (currently Bornego College), Heerenveen, in 1993. He went on to study Chemical Engineering at the University of Twente. The industrial internship was carried out at National Starch and Chemical (ICI) in 1997. In 1998 he joined the group “Materials Science and Technology of Polymers” chaired by prof. dr. G.J. Vancso, where he carried out his masters thesis<sup>1</sup> on which he graduated in the same year.

In the same group he continued as a Ph.D. student on the research and development presented in this thesis (1999-2003). In this period he became Registered Polymer Engineer (RPK, 2002). The research project was initiated and financed by the Dutch Polymer Institute, The Netherlands (DPI) and was carried out under the supervision of prof. dr. G.J. Vancso (promotor). The results of the research were presented at several international conferences including the World Polymer Congress (1999, Warschau, Poland), EPS European conference on macromolecular physics (2002, Eger, Hungary), ISPAC (2002, Enschede, The Netherlands). Collaboration with others lead to two publications<sup>2,3</sup>, other publications related to this thesis were or will be published in several international journals<sup>4-6</sup>.

1. Pickering, J. P.; van der Meer, D. W.; Vancso, G. J. Effects of contact time, humidity, and surface roughness on the adhesion hysteresis of polydimethylsiloxane. *Journal of Adhesion Science and Technology* **2001**, 15, 1429.
2. Beekmans, L. G. M.; van der Meer, D. W.; Vancso, G. J. Crystal melting and its kinetics on poly(ethylene oxide) by in situ atomic force microscopy. *Polymer* **2002**, 43, 1887.
3. van der Meer, D. W.; Pukánszky, B.; Vancso, G. J. On the dependence of impact behavior on the crystalline morphology in polypropylenes. *Journal of Macromolecular Science-Physics* **2002**, B41, 1105.
4. van der Meer, D. W.; Milazzo, D.; Vancso, G. J. Oriented crystallization of isotactic polypropylene on oriented polytetrafluoroethylene. *Polym. Eng. Sci.*, Submitted.
5. van der Meer, D. W.; Vancso, G. J., The influence of chain architecture on the crystallization of isotactic polypropylene, In Preparation.
6. van der Meer, D. W.; Vancso, G. J., The influence of chain architecture on the melting of isotactic polypropylene, In Preparation.